

UNIVERSITY OF LATVIA  
FACULTY OF PHYSICS AND MATHEMATICS



Janis Timoshenko

**REVERSE MONTE CARLO MODELLING OF  
STRUCTURAL AND THERMAL DISORDER  
IN CRYSTALLINE MATERIALS**

Doctoral Thesis

Promotion to the Degree of Doctor of Physics  
Subbranch: Solid State Physics

Scientific advisor:  
Dr. phys. **Aleksejs Kuzmins**

Riga 2015



IEGULDĪJUMS TAVĀ NĀKOTNĒ

This work has been supported by the European Social Fund within the project "Support for Doctoral Studies at University of Latvia".

Type of the thesis: **Doctoral thesis**

Scientific advisor: *Dr. phys.* **Aleksejs Kuzmins**

Reviewers:

1) 1) *Dr. Chem.* **Girts Barinovs**, docent, Faculty of Physics and Mathematics, University of Latvia, Latvia

2) 2) *D. Sc.* **László Pusztai**, scientific advisor, Research Institute for Solid State Physics and Optics, Hungarian academy of Sciences, Hungary

3) 3) *Dr. Phys.* **Dmitry Bocharov**, researcher, Paul Scherrer Institute, Laboratory for Reactor Physics and Systems Behaviour (LRS), Switzerland

The defense of the doctoral thesis will take place in an open session of the Promotion Council of Physics, Astronomy and Mechanics of the University of Latvia on the **20th of February, 2015, at 14:00** in the conference hall of the Institute of Solid State Physics, University of Latvia.

The doctoral thesis and its summary are available at the Library of the University of Latvia (4 Kalpaka Blvd, Riga) and Latvian Academic Library (10 Rupniecibas Str, Riga).

Chairperson of the Specialized Promotion Council of the scientific section of the Physics, Astronomy and Mechanics at the University of Latvia: *Dr. habil. phys.* **Linards Skuja**.

## Acknowledgements

This work would not be possible without constant support and guidance by my supervisor Dr. Alexei Kuzmin. His professional skills, vigor and eagerness to help were a great source of inspiration for me during the whole period of my studies. I also would like to thank Dr. Juris Purans for scientific discussions and a very fruitful management of our laboratory. And, of course, many thanks to my colleagues Dr. Alexandr Kalinko and Dr. Andris Anspoks for their advices and great atmosphere they created in our laboratory in Riga and at synchrotron beamlines all around Europe. I am truly proud that I had the opportunity to be a part of this team of excellent scientists.

I am glad to say that during my studies I could also rely on people outside of our group: prof. Vyacheslavs Kashcheyevs and prof. Andris Muiznieks were great examples of successful researchers for me and never refused any kind of help or advice. I have learned a lot from them and I will always be thankful for the chance to work under their lead.

And, of course, I would never get so far without inexhaustible encouragement, patience and support of my family: my parents Janis and Faina, my sister Marina and my wife Edite.

## Abstract

In the present thesis we develop a novel simulation-based scheme to probe the local structural and thermal disorder in crystalline materials by analyzing X-ray absorption spectra. The proposed method resembles conventional reverse Monte Carlo approach, but is more computationally efficient, as it benefits from the advantages provided by evolutionary algorithm. We believe that the proposed method improves the accuracy of currently available approaches for EXAFS analysis, especially in the case of strongly distorted local environment. The proposed approach is applied to the study of several materials such as crystalline Ge,  $H_x\text{ReO}_3$ , ZnO and nanocrystalline  $\text{CoWO}_4$  and  $\text{CuWO}_4$ .

# Contents

<b>List of Figures</b>	<b>x</b>
<b>List of Tables</b>	<b>xiii</b>
<b>Glossary</b>	<b>xiv</b>
<b>1 Introduction</b>	<b>1</b>
1.1 General introduction and motivation . . . . .	1
1.2 Aim and objectives of the work . . . . .	2
1.3 Scientific novelty of the work . . . . .	3
1.4 Author's contribution . . . . .	4
1.5 Contents of the thesis . . . . .	4
<b>2 EXAFS spectroscopy</b>	<b>6</b>
2.1 Phenomenological description of X-ray absorption . . . . .	6
2.2 X-ray sources . . . . .	9
2.3 Synchrotron radiation . . . . .	10
2.4 Conventional XAS experiment . . . . .	13
2.5 Sample preparation . . . . .	14
2.6 EXAFS theory . . . . .	15
2.6.1 Introduction . . . . .	15
2.6.2 X-ray absorption by isolated atom . . . . .	16
2.6.3 Origins of EXAFS . . . . .	19
2.6.4 Many-electronic effects . . . . .	21
2.6.5 EXAFS equation within the single-scattering approximation	21
2.6.6 EXAFS equation within the multiple-scattering approxi- mation . . . . .	23
2.6.7 Thermal and static disorder . . . . .	24
2.7 Conventional EXAFS analysis . . . . .	28

2.7.1	Extraction of EXAFS data . . . . .	28
2.7.2	EXAFS curve fitting . . . . .	30
<b>3</b>	<b>Simulation-based EXAFS analysis</b>	<b>33</b>
3.1	Introduction . . . . .	33
3.2	Molecular dynamics . . . . .	34
3.3	Monte Carlo method . . . . .	36
3.4	Reverse Monte Carlo method . . . . .	37
<b>4</b>	<b>RMC/EA method for EXAFS analysis</b>	<b>43</b>
4.1	Introduction . . . . .	43
4.2	Optimization algorithms: RMC and evolutionary algorithm . . . . .	46
4.2.1	Reverse Monte Carlo basics . . . . .	46
4.2.2	Metropolis algorithm . . . . .	48
4.2.3	Simulated annealing . . . . .	50
4.2.3.1	Convergence issues . . . . .	50
4.2.3.2	Simulated annealing schemes . . . . .	52
4.2.4	Evolutionary algorithms . . . . .	54
4.2.4.1	Introduction . . . . .	54
4.2.4.2	Selection . . . . .	57
4.2.4.3	Crossover . . . . .	58
4.2.4.4	Mutation . . . . .	59
4.3	Signal processing: wavelet transform . . . . .	59
4.3.1	$k$ -, $q$ - and $R$ -spaces . . . . .	59
4.3.2	Wavelet transform . . . . .	61
4.4	Calculations of EXAFS . . . . .	66
4.4.1	<i>Ab-initio</i> calculations . . . . .	66
4.4.2	Dependency of complex scattering amplitude on interatomic distances . . . . .	70
4.4.3	Clustering algorithm . . . . .	71
4.5	Data analysis: robust statistics . . . . .	76
<b>5</b>	<b>RMC-EXAFS for crystalline germanium</b>	<b>81</b>
5.1	Introduction . . . . .	81
5.2	Application of the RMC-EXAFS method to model data . . . . .	82
5.2.1	RMC simulations for model data . . . . .	82
5.2.2	Influence of the cell size and simulation length . . . . .	86

5.2.3	Determination of the lattice parameters . . . . .	86
5.3	Application of the RMC-EXAFS method to experimental data . . .	89
5.4	Conclusions . . . . .	90
<b>6</b>	<b>RMC/EA-EXAFS for rhenium trioxide</b>	<b>92</b>
6.1	Introduction . . . . .	92
6.2	Conventional RMC simulations for the $\text{ReO}_3$ . . . . .	93
6.2.1	Simulation details and calculations for model system . . .	93
6.2.2	RMC analysis of experimental data . . . . .	95
6.2.3	Conclusions . . . . .	98
6.3	Investigations of $\text{ReO}_3$ using evolutionary algorithm . . . . .	99
6.3.1	Simulation details and calculations for model system . . .	99
6.3.2	RMC/EA analysis of experimental data . . . . .	104
6.3.3	Distant coordination shells in rhenium trioxide . . . . .	105
6.4	Conclusions . . . . .	109
<b>7</b>	<b>Hydrogen intercalation into <math>\text{ReO}_3</math></b>	<b>113</b>
7.1	Introduction . . . . .	113
7.2	Analysis of $\text{ReO}_3$ lattice distortion induced by intercalation of hydrogen ions . . . . .	114
7.3	Conclusions . . . . .	121
<b>8</b>	<b>Anisotropic dynamics of wurtzite-type zinc oxide</b>	<b>122</b>
8.1	Introduction . . . . .	122
8.2	Experimental and data analysis . . . . .	124
8.3	Revealing problems of MD force-field models . . . . .	125
8.4	RMC/EA-EXAFS calculations . . . . .	128
8.5	Discussion . . . . .	129
8.5.1	Comparison of MD and RMC/EA results . . . . .	129
8.5.2	Influence of temperature . . . . .	131
8.6	Conclusions . . . . .	134
<b>9</b>	<b>Structure of polycrystalline and nanosized tungstates</b>	<b>136</b>
9.1	Introduction . . . . .	136
9.2	Experimental data . . . . .	138
9.3	Separate analysis of the Co/Cu K-edge and W $L_3$ -edge EXAFS . . .	140
9.3.1	$\text{CoWO}_4$ case . . . . .	140

9.3.2	CuWO <sub>4</sub> case . . . . .	143
9.4	Simultaneous fit of the Co/Cu K-edge and W L <sub>3</sub> -edge EXAFS . . .	145
9.4.1	CoWO <sub>4</sub> case . . . . .	145
9.4.2	CuWO <sub>4</sub> case . . . . .	146
9.5	Local structure of nanosized tungstates . . . . .	149
9.5.1	Evolutionary algorithm for the studies of nanostructured systems . . . . .	149
9.5.2	Results and discussion . . . . .	150
9.6	Conclusions . . . . .	155
<b>10</b>	<b>Conclusions</b>	<b>157</b>
<b>11</b>	<b>Main theses</b>	<b>160</b>
	<b>References</b>	<b>161</b>
<b>A</b>	<b>EvAX code: user's guide</b>	<b>185</b>
A.1	Introduction . . . . .	185
A.2	Starting new calculation . . . . .	186
A.2.1	Required files and programs . . . . .	186
A.2.2	FEFF program . . . . .	186
A.2.3	Experimental data . . . . .	187
A.2.4	Structure file . . . . .	187
A.3	FEFF calculations . . . . .	188
A.3.1	Common FEFF keywords . . . . .	188
A.3.2	Running FEFF from EvAX code . . . . .	191
A.4	Parameters . . . . .	192
A.4.1	Example of parameter file . . . . .	192
A.4.2	Parameters for structure model construction . . . . .	195
A.4.3	Parameters for FEFF calculations: . . . . .	195
A.4.4	Parameters for spectra comparison . . . . .	196
A.4.5	Parameters for RMC and EA calculations and simulated annealing schemes . . . . .	197
A.4.6	Parameters for clustering algorithm . . . . .	198
A.4.7	Other parameters and flags . . . . .	198
A.5	Output . . . . .	198
A.5.1	Introduction . . . . .	198



A.5.2	General output files . . . . .	201
A.5.3	Spectrum-specific output files . . . . .	201
A.5.4	Restart files . . . . .	202
A.6	EvAX keywords . . . . .	202
<b>B</b>	<b>Author's publication list</b>	<b>205</b>
B.1	Published papers . . . . .	205
B.2	Papers, submitted for publication . . . . .	206
B.3	Published papers that are not related to the topic of the thesis . .	207
<b>C</b>	<b>Participation in conferences</b>	<b>208</b>
C.1	Poster presentations at international conferences . . . . .	208
C.2	Oral presentations at international conferences . . . . .	210
<b>D</b>	<b>Participation in international schools</b>	<b>211</b>
<b>E</b>	<b>Participation in experiments at synchrotron radiation facilities</b>	<b>212</b>

# List of Figures

2.1	Examples of X-ray absorption spectra . . . . .	9
2.2	Historical development of X-ray radiation sources . . . . .	11
2.3	Synchrotron radiation sources . . . . .	12
2.4	Common experimental setup for XAS experiments . . . . .	14
2.5	single-scattering and multiple-scattering paths . . . . .	25
2.6	MSD and MSRD factors . . . . .	27
2.7	Extraction of EXAFS spectra - I . . . . .	29
2.8	Extraction of EXAFS spectra - II . . . . .	32
4.1	Schematic representation of the EvAX algorithm . . . . .	46
4.2	Convergence of RMC schemes . . . . .	53
4.3	Three basic operators of evolutionary algorithm . . . . .	58
4.4	Morlet wavelet transform in action . . . . .	66
4.5	Controlling the resolution of Morlet wavelet transform . . . . .	67
4.6	Influence of the dependency of complex scattering amplitude on interatomic distances . . . . .	71
4.7	Clustering algorithm . . . . .	76
4.8	MAD estimator . . . . .	80
5.1	Crystalline germanium samples used for EXAFS measurements. . . . .	82
5.2	RMC fit of the model data . . . . .	83
5.3	RMC fit single-scattering and multiple-scattering contributions . . . . .	84
5.4	Simulated annealing parameters . . . . .	85
5.5	The radial distribution function around germanium atom for the model . . . . .	85
5.6	Influence of the cell size and simulation time . . . . .	87
5.7	Determination of the lattice constant . . . . .	88
5.8	RMC analysis of experimental Ge K-edge EXAFS spectra . . . . .	89

5.9	Temperature dependencies of MSRD factors . . . . .	91
6.1	RMC analysis of $\text{ReO}_3$ model EXAFS spectrum . . . . .	94
6.2	RMC analysis of experimental $\text{ReO}_3$ EXAFS spectra . . . . .	96
6.3	RDF's and structure parameters for $\text{ReO}_3$ . . . . .	97
6.4	EA analysis of $\text{ReO}_3$ model EXAFS spectrum . . . . .	100
6.5	RDF's and atomic displacements for $\text{ReO}_3$ model . . . . .	102
6.6	EA analysis of experimental $\text{ReO}_3$ EXAFS spectra . . . . .	106
6.7	EA analysis of SS and MS contributions to the experimental $\text{ReO}_3$ EXAFS spectra . . . . .	107
6.8	RDF's and atomic displacements for experimental $\text{ReO}_3$ sample .	108
6.9	EA analysis of temperature-dependent experimental $\text{ReO}_3$ EXAFS spectra . . . . .	109
6.10	Temperature dependence of the $\text{Re}_0\text{-Re}_4$ contribution to the total EXAFS spectrum. . . . .	110
6.11	Temperature dependence of the $\text{Re}_0\text{-O}_5$ contribution to the total EXAFS spectrum. . . . .	110
6.12	Influence of multiple-scattering effects . . . . .	111
6.13	Temperature dependence of multiple-scattering contributions . .	111
7.1	Influence of hydrogen intercalation on EXAFS spectra . . . . .	115
7.2	Influence of hydrogen intercalation on lattice structure . . . . .	117
7.3	Time-dependencies of MSRD and MSD factors in the hydrogen deintercalation process . . . . .	118
7.4	Re-O-Re angle in the hydrogen detintercalation process . . . . .	118
7.5	Distortion of $\text{ReO}_6$ and $\text{Re}(\text{Re}_2)_6$ octahedra . . . . .	120
8.1	Experimental Zn K-edge EXAFS spectra for zinc oxide . . . . .	124
8.2	EXAFS spectra obtained in MD simulations for ZnO . . . . .	126
8.3	Influence of MS effects on MD-EXAFS spectra for ZnO . . . . .	127
8.4	RMC/EA simulations for the room temperature experimental EX- AFS data . . . . .	128
8.5	Influence of MS effects on the Zn K-edge EXAFS spectrum for ZnO	130
8.6	Radial distribution function for atoms around absorbing Zn . . . .	130
8.7	Results of the RMC/EA-EXAFS calculations for the experimental Zn K-edge EXAFS spectra in crystalline ZnO at representative temperatures. . . . .	132

8.8	Structure parameters for wurtzite-type ZnO . . . . .	133
9.1	EXAFS spectra for microcrystalline CuWO <sub>4</sub> . . . . .	138
9.2	EXAFS spectra for microcrystalline CoWO <sub>4</sub> . . . . .	139
9.3	EXAFS spectra for nanocrystalline CoWO <sub>4</sub> . . . . .	139
9.4	RMC/EA analysis of the Co K-edge EXAFS spectrum for microcrystalline CoWO <sub>4</sub> . . . . .	141
9.5	Radial distribution of atoms around cobalt for microcrystalline CoWO <sub>4</sub> . . . . .	142
9.6	Checking the obtained structural model for microcrystalline CoWO <sub>4</sub>	142
9.7	RMC/EA analysis of the W L <sub>3</sub> -edge EXAFS spectrum for microcrystalline CuWO <sub>4</sub> . . . . .	144
9.8	Checking the obtained structural model for microcrystalline CuWO <sub>4</sub>	145
9.9	RMC/EA simulations for microcrystalline CoWO <sub>4</sub> using the Co K-edge and W L <sub>3</sub> -edge EXAFS data simultaneously . . . . .	147
9.10	RMC/EA simulations for microcrystalline CuWO <sub>4</sub> using the Cu K-edge and W L <sub>3</sub> -edge EXAFS spectra simultaneously . . . . .	147
9.11	Temperature-dependance of the local structure of microcrystalline CuWO <sub>4</sub> . . . . .	148
9.12	Suggested structure models of CoWO <sub>4</sub> and CuWO <sub>4</sub> nanocrystallites.	150
9.13	RMC/EA analysis of EXAFS spectra for nanocrystalline CoWO <sub>4</sub>	151
9.14	RMC/EA analysis of EXAFS spectra for nanocrystalline CuWO <sub>4</sub> at room temperature . . . . .	152
9.15	RMC/EA analysis of EXAFS spectra for nanocrystalline CuWO <sub>4</sub> at 10 K . . . . .	153
9.16	Radial distribution of atoms around W and Co/Cu in CoWO <sub>4</sub> and CuWO <sub>4</sub> nanoparticles . . . . .	155
9.17	Radial distribution of atoms (1st coordination shell) around tungsten in CoWO <sub>4</sub> and CuWO <sub>4</sub> nanoparticles . . . . .	156
A.1	Screenshot of EvAX program . . . . .	185

# List of Tables

2.1	Energies of the K and $L_3$ core levels for selected elements . . . . .	10
5.1	Structure parameters for crystalline germanium model . . . . .	84
6.1	Structure parameters for rhenium trioxide model . . . . .	95
6.2	Structure parameters for rhenium trioxide model and real $\text{ReO}_3$ sample, obtained in EA simulations . . . . .	101
6.3	Values of the mean-square relative displacements (MSRD) for the fourth and fifth coordination shells. . . . .	107
9.1	The final total residuals at both Co(Cu) K and W $L_3$ edges, characterizing the difference between simulated and experimental EXAFS data for nanocrystalline $\text{CoWO}_4$ and $\text{CuWO}_4$ and four different structural models. . . . .	154

# Glossary

<b>BADF</b>	Bonding angles distribution function
<b>CBS inequality</b>	Cauchy - Bunyakovsky - Schwarz inequality
<b>DDF</b>	Displacements distribution function
<b>DS</b>	double-scattering
<b>EA</b>	Evolutionary algorithm
<b>EXAFS</b>	Extended X-ray absorption fine structure
<b>FOJT</b>	First order Jahn-Teller effect
<b>FT</b>	Fourier transform
<b>FTIR</b>	Fourier transform infrared spectroscopy
<b>HL model</b>	Hedin-Lundqvist model
<b>LDOS</b>	Local density of states
<b>MAD</b>	Median absolute deviation
<b>MC</b>	Monte Carlo
<b>MD</b>	Molecular dynamics
<b>MS</b>	multiple-scattering
<b>MSD</b>	Mean-square displacement
<b>MSRD</b>	Mean-square relative displacement
<b>NTE</b>	Negative thermal expansion
<b>RDF</b>	Radial distribution function
<b>RF</b>	Radio frequency
<b>RMC</b>	Reverse Monte Carlo
<b>RUM</b>	Rigid unit model
<b>SOJT</b>	Second order Jahn-Teller effect

<b>SR</b>	Synchrotron radiation
<b>SS</b>	single-scattering
<b>TS</b>	Tripple scattering
<b>WT</b>	Wavelet transform
<b>XAFS</b>	X-ray absorption fine structure
<b>XANES</b>	X-ray absorption near-edge structure
<b>XAS</b>	X-ray absorption spectroscopy
<b>XFEL</b>	X-ray free electron laser

# 1. INTRODUCTION

## 1.1 General introduction and motivation

The properties of materials are strongly dependent on their structure. A detailed investigation of material structure is an essential step before any technological application of the material is possible. Two the most important experimental approaches for structure studies are diffraction and X-ray absorption spectroscopy (XAS) [1]. The first one is mainly providing information on the equilibrium atomic structure, while the latter probes the instantaneous local structure of the material.

Availability and evolution of synchrotron radiation sources has stimulated the development of XAS theory and methodology during the last decades, thus also the possibilities, provided by this method, are expanded significantly. XAS allows one to obtain the information both on local electronic structure (XANES - X-ray absorption near edge structure - spectroscopy) and atomic structure (EXAFS - Extended X-ray absorption fine structure - spectroscopy) [2]. Important advantage of XAS approach in comparison to diffraction methods is that it is element-specific, thus the information on the local environment of the atoms of particular type can be obtained. Also XAS method can be applied to studies of wide range of different samples: for concentrated and for diluted systems, for crystalline and for nanostructured, amorphous, liquid samples and even for investigations of gases [3].

EXAFS spectroscopy is the main experimental technique, used in this work. EXAFS experiment consists of X-ray absorption coefficient measurement as a function of the energy of incident radiation. If the energy of incident X-ray photon is sufficiently large, it excites an electron from the core state to an empty state above the Fermi level. The final state can be conveniently described, assuming that the excited electron - often referred to as photoelectron - is a spherical wave that gets scattered by the electrostatic potentials of neighbor atoms. The interaction of photoelectron with these neighbors modulates the value of absorption coefficient and results in an EXAFS spectrum. By analyzing such signal one can get the access to the information on average interatomic distances, relative



thermal motion of atoms and static disorder. Important aspect is that EXAFS is also sensitive to many-atom distribution functions, for example, to distributions of bonding angles. Thus an EXAFS spectrum contains an unprecedented amount of information on sample structure, but, obviously, the analysis of such complicated signal is challenging. To address this problem, several simulation-based approaches can be used, such as classical molecular dynamic (MD) simulations and Reverse Monte Carlo (RMC) method. In both cases a large amount of atomic configurations is generated, and one can calculate corresponding theoretical EXAFS spectrum, averaged over time and/or over absorbing atom sites. The obtained configuration-averaged EXAFS spectrum then can be directly compared with the experimental data. In the MD approach the atomic configurations are generated by the integration of classical Newton's equation of motion. The inter-atomic forces, required for such calculations, are given by an empirical potential function (so called force-field model) [4]. However, in the case of complicated systems with low symmetry, the construction of such force-field models is a complicated task. Additionally, classical MD cannot be applied for the analysis of data, obtained at low temperatures, due to essential neglecting of quantum effects.

To avoid this problem one can use RMC-type methods. In this case the generation of atomic configurations is not determined by any physical considerations, but is a random process. For each atomic configuration one calculates corresponding theoretical EXAFS spectrum that is then compared to experimentally obtained data. Accordingly to how close are the theoretical and experimental spectra, the proposed atomic configuration is either accepted or discarded. By choosing appropriate parameters of calculations, one can ensure that after given (and usually large) number of steps the simulated atomic configuration will represent the atomic structure of the sample [5]. This method is general and can be applied to a wide range of problems. Unfortunately, it is also computationally inefficient. Thus the further development of simulation-based approaches for the EXAFS analysis is necessary.

## 1.2 Aim and objectives of the work

The research, presented in the thesis, consists of both experimental (EXAFS measurements at synchrotron radiation sources) and theoretical (software development and computer simulations) parts.

The main goal of the thesis is to develop novel simulation-based approach (RMC/EA-EXAFS), based on the reverse Monte Carlo method and evolutionary algorithm (EA), for the analysis of EXAFS data from crystalline and nanocrystalline materials. The novel approach inherits from the RMC method its general applicability, but is more computationally efficient.

The objectives of the present work are:

- to perform temperature-dependent EXAFS studies of crystalline wurtzite type ZnO and crystalline and nanocrystalline tungstates  $\text{CoWO}_4$  and  $\text{CuWO}_4$  at synchrotron radiation sources;
- to demonstrate the potentiality of the proposed method for the analysis of experimental EXAFS spectra from crystalline materials, starting with the case of monoatomic crystalline germanium, and then applying it to more complex many-atom systems such as perovskite-type  $\text{ReO}_3$ , wurtzite-type ZnO and two wolframite-type tungstates as  $\text{CoWO}_4$  and  $\text{CuWO}_4$ ;
- to demonstrate the potentiality of the method for the analysis of experimental EXAFS spectra from nanocrystalline tungstates  $\text{CoWO}_4$  and  $\text{CuWO}_4$ ;
- to demonstrate the ability of the EXAFS technique in general to provide information on many-atom distribution functions, correlation effects and anisotropy of thermal disorder.

### 1.3 Scientific novelty of the work

Within this thesis a novel method for EXAFS analysis, based on the use of evolutionary algorithm, has been proposed and realized in the original software. The new method allowed us for the first time (i) to follow *in-situ* the development of the local structure of crystalline rhenium oxide upon intercalation of hydrogen ions and to discriminate two different effects in this process (one, related to electronic effects, and the other, related to lattice deformations); (ii) to reveal that in wurtzite-type ZnO the interactions of atoms, which lie in the same crystallographic *ab*-plane, differ significantly from the interactions of atoms, which are located at similar distances, but in different *ab*-planes, that results in the changes of the equilibrium position of oxygen atom along *c*-axis upon temperature increase; (iii) to obtain structure model for crystalline and nanocrystalline tungstates ( $\text{CoWO}_4$ ,  $\text{CuWO}_4$ ), analysing simultaneously the EXAFS data at two absorption edges (Co/Cu K-edge and W  $L_3$ -edge).

## 1.4 Author's contribution

The research, presented in the thesis, has been mostly carried out at the Institute of Solid State Physics, University of Latvia. The author also has taken part in 11 experiments using synchrotron radiation that have been carried out at the international synchrotron facilities as HASYLAB/DESY (Hamburg, Germany), ELETTRA (Trieste, Italy) and SOLEIL (Paris, France). In particular, the author participated in temperature-dependent EXAFS measurements of ZnO, CuWO<sub>4</sub> and CoWO<sub>4</sub>, which are directly relevant to the present work. The experimental EXAFS data on Ge and H<sub>x</sub>ReO<sub>3</sub> have been taken from [6] and [7], respectively.

Besides, the author participated in temperature-dependent EXAFS measurements of ZnWO<sub>4</sub>, MnWO<sub>4</sub>, SnWO<sub>4</sub>, NiO, Cu<sub>3</sub>N, ScF<sub>3</sub>, Y<sub>2</sub>O<sub>3</sub> and Fe-Cr alloys and pressure-dependent EXAFS measurements of SnWO<sub>4</sub>. The results of these studies are not included in the thesis, but allowed us to elaborate a novel simulation-based approach for the EXAFS data treatment.

The new approach for EXAFS analysis, based on the use of evolutionary algorithm, was proposed and developed by the author, and was implemented in the original software, written in C++ language. Simulations have been carried out by the author at the Latvian SuperCluster facility [8], and consequent post-processing of the obtained results has been carried out by a set of original programs, written by the author in *Wolfram Mathematica* environment.

The author has participated in 7 international summer schools during 2007-2014. The results of the research have been presented at 10 international conferences. Main results have been published in 15 SCI papers, and the author is the main contributor for 9 of them.

## 1.5 Contents of the thesis

The thesis consists of 10 chapters.

Chapter 2 is devoted to the overview of modern EXAFS spectroscopy, and gives insight in its theoretical and experimental aspects. Conventional EXAFS analysis is also discussed in Chapter 2.

Chapter 3 is devoted to the description of the state of the art of simulation-based EXAFS analysis: classical and *ab-initio* molecular dynamics, Monte Carlo and Reverse Monte Carlo methods are discussed and compared here.

Chapter 4 contains the detailed description of the developed novel method for EXAFS analysis, based on RMC and evolutionary algorithm (EA) approaches. Here the most important features of proposed method and corresponding developed software are discussed.

In the Chapters from 5 to 9 the results, obtained by the presented method, are given. In the Chapter 5 the RMC study of crystalline germanium is presented, Chapter 6 is devoted to the RMC study of crystalline rhenium trioxide, Chapter 7 - to the RMC/EA-EXAFS *in-situ* study of hydrogen intercalation process in the rhenium trioxide lattice. Chapter 8 is devoted to the RMC/EA-EXAFS studies of crystalline zinc oxide. In the Chapter 9 the results of RMC/EA studies for crystalline cobalt tungstate and crystalline copper tungstate, as well as the results, obtained in RMC/EA studies for nanosized tungstates, are given.

Chapter 10 contains the summary and the most important conclusions. Finally, the main theses of this study are given in Chapter 11.

The user's manual for the developed EvAX program for EXAFS analysis using RMC and EA methods, is given in the Appendix. Also in the Appendix the lists of publications and conferences, where the results of the research were presented, are given, and also the international schools and experiments at international synchrotron radiation facilities, where the author has participated, are listed.

## 2. EXAFS SPECTROSCOPY

### 2.1 Phenomenological description of X-ray absorption

Electromagnetic radiation can interact with matter in different ways: incident photons can, for example, be elastically or inelastically scattered, they can be absorbed by the electronic system of atoms (resulting in electron transitions from one energetic level to another) or by atomic nuclei (in this case causing transitions between the different energetic levels of absorbing nucleus). The probability of each of these processes strongly depends on the energy of incident radiation. In the case of X-rays (the radiation with photon energy above 100 eV) the electronic absorption plays very important role. Especially interesting in this case is the absorption by electrons from deep core levels (denoted usually with capital letters K, L, M, etc.).

In the absorption process the incident photon causes the transition of electron from some occupied energy level with energy  $E_i$  to some unoccupied energy level with higher energy  $E_f$ , thus the absorption is possible, only if the energy of the photon  $\hbar\omega$  is at least as large as  $E_f - E_i$ . The energy differences between deep core energy levels are much larger than those for, say, valence electrons. Therefore, while outer electrons efficiently absorb the visible light, the electrons from deep core levels participate in the absorption processes only in the case of irradiation by X-rays.

To quantitatively describe the absorption process, one can use the attenuation of the incident photon flux. If the probability to absorb photon is fixed, then the increase of the number of incident photons will lead also to the increase of the number of absorption events: the attenuation of the photon flux is proportional to the flux itself. On the other hand, obviously, the probability to absorb given photon will increase proportionally to the number of atoms along the trajectory of this photon, i.e., proportionally to the sample thickness  $d$ . Thus, according to the Beer-Lambert law, the flux of photons that are propagating through the sample decreases exponentially:

$$I(\hbar\omega) = I_0 e^{-\mu(\hbar\omega)d}, \quad (2.1)$$

where  $I_0$  is the incident photon flux,  $I(\hbar\omega)$  is the photon flux that passes through the sample (it depends on the energy of the incident photons), and  $\mu(\hbar\omega)$  is the X-ray absorption coefficient that characterizes the material [2].

The energy dependence of the X-ray absorption coefficient for homogenous monotatomic sample can be approximately described by empirical relation [9]

$$\mu(\hbar\omega) \approx \frac{\rho Z^4}{A(\hbar\omega)^3}, \quad (2.2)$$

where  $\rho$  is the density of the sample,  $Z$  is atomic number and  $A$  is relative atomic mass. Thus one can see, for instance, that the radiation with low energy will be much more attenuated than the high-energy radiation. Another important conclusion that comes from the equation above, is that X-ray absorption is element-specific, i.e., from the X-ray absorption measurements we can get some insight about the chemical composition of the sample.

However, already at the beginning of the 20th century it was shown that the energy-dependence of the absorption coefficient is not as smooth as predicted by this equation: sharp variations of the value of  $\mu$ , so called absorption edges, located at some specific energies, were observed (see Fig. 2.1).

The origin of such jump-like features now can be easily explained - when the energy of the X-ray radiation is getting sufficiently large to make another deep core level to participate in the absorption processes, the value of absorption coefficient will sharply increase. Correspondingly to the type of the deep core level that gets involved, the absorption edges are also denoted as K-edge,  $L_1$ ,  $L_2$ ,  $L_3$  edge, etc. For heavy elements the energies of these core levels are quite different, hence also the absorption edges are well separated in the energy space.

If the energy of the incident photon is close to the energy that corresponds to some absorption edge, one of the following cases will take place:

1. If the energy  $\hbar\omega$  is smaller than the energy difference between core level and the closest at least partially unoccupied energy level, the absorption by the electron from this core level will not be possible, and the attenuation of the photon flux will be caused by higher atomic energy levels only;
2. If the energy  $\hbar\omega$  corresponds to the energy difference between core level and some unoccupied and well localized energy level, the electronic transition and hence the absorption will be possible: with some probability electron will jump to the level with higher energy and will remain bonded to the

atomic nucleus; such processes are responsible for the so called pre-edge structure of the absorption spectrum;

3. If the energy  $\hbar\omega$  is larger than some reference value  $E_0$ , the electron from the core level will be excited to a delocalized state.

The latter case is the most interesting for our purposes. Indeed, if an electron is excited to a delocalized state, one may expect that the probability of such process will somehow depend on the surrounding of the absorbing atom. Taking into account that the De Broglie wavelength of the excited, delocalized electron (it is often referred to as a photoelectron) is about a few angstroms large, i.e., it is comparable with the typical interatomic distances, one may even conclude that the absorption coefficient in this case will contain some information on the atomic structure of the sample. In 1970s this idea was proven by Sayers, Stern and Lytle. In their pioneering study [10] they focused on the small oscillations of the value of X-ray absorption coefficient as a function of the energy of incident photon that can be observed, if this energy is larger than the energy of absorption edge, i.e., on so called EXAFS, Extended X-ray Absorption Fine Structure. They have shown that simple Fourier transform of these oscillations is related to the radial distribution function (RDF) around absorbing atom. Nowadays this idea turned into conventional approach to EXAFS analysis. For example, in Fig. 2.1 in the Fourier transforms of the EXAFS spectra at the Cu K-edge and W  $L_3$ -edge in crystalline  $\text{CuWO}_4$ , the first peaks are located at about 1.6 Å and 1.3 Å, respectively, which correlates with the distances between copper/tungsten atoms and their closest neighbors, oxygen atoms (shortest Cu–O distance is about 2.0 Å, shortest W–O distance is about 1.8 Å).

Conventionally, term EXAFS is referred to the oscillations of X-ray absorption coefficient in the energy range from about  $\Delta E = 30\text{...}40$  eV above  $E_0$  till a few thousands of eV above  $E_0$ , where the amplitude of the oscillations gets negligibly small. EXAFS contains information on the local atomic structure and lattice dynamics, i.e., on interatomic distances, static disorder, thermal motion of atoms. The analysis of EXAFS data will be in the focus of this thesis. In contrast, the features of X-ray absorption spectrum for energies below  $E_0 + \Delta E$ , including the pre-edge structure, are called XANES, X-ray Absorption Near Edge Structure, and they contain information on the electronic structure of absorbing atom and on local symmetry. The description and analysis of XANES spectrum is significantly more complex task, and currently is mostly qualitative.

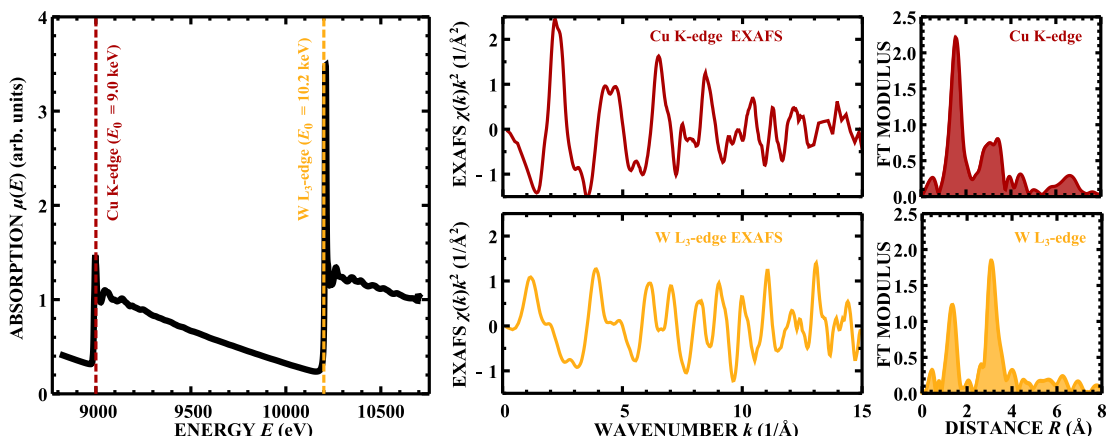


**Figure 2.1: Examples of X-ray absorption spectra**

X-ray absorption spectrum  $\mu(E)$  of crystalline copper tungstate, measured at 10 K (left panel), corresponding EXAFS spectra  $\chi(k)k^2$  at the Cu K-edge and W  $L_3$ -edge, where wavenumber  $k = \sqrt{2m_e(E - E_0)}/\hbar$ ,  $m_e$  is the electron mass and  $\hbar$  is the Planck's constant (middle panels), and their Fourier transforms (right panels).

The value of  $\Delta E$ , i.e., the border between EXAFS and XANES regions, is related to the typical plasmon excitation energy - if the energy of the photoelectron is below  $\Delta E$ , the inelastic energy losses due to electronic excitations are not pronounced and delocalization of photoelectron is much stronger, therefore the formalism, used for the description of EXAFS data (i.e., expansion in multiple-scattering paths) and that will be introduced below, is not valid for XANES analysis [11].

## 2.2 X-ray sources

EXAFS spectra were observed for the first time around 1920. Nevertheless, at least qualitatively correct theory that described this effect appeared only at the beginning of 1970s [2], and one of the reasons for such delay was the poor quality of the X-ray sources, available at the first half of the 20th century.

The requirements for the radiation sources, used for the X-ray absorption spectroscopy (XAS) experiments, are indeed remarkable: first of all, the energy of emitted radiation should be high enough to excite electrons from the atomic core levels, and often it means, it should be higher than 10 keV. As an example, in Table 2.1 the characteristic energies of the atomic core-levels for the atoms, analyzed by XAS technique in this thesis, are given.



**Table 2.1:** Energies of the K and L<sub>3</sub> core levels for selected elements [12]

Atom	Core level	Energy (keV)
Co	K	7.7
Cu	K	9.0
Zn	K	9.7
Ge	K	11.1
W	L <sub>3</sub>	10.2
Re	L <sub>3</sub>	10.5

At the same time, to obtain the energy-dependence of X-ray absorption coefficient, we should be able to continuously scan the energy of incident radiation in a wide range (typically a few thousands of eV). And, of course, for the analysis of such fine effects as XANES and EXAFS, the brightness of radiation source and its stability is of extreme importance. Hence as the main sources for the XAS experiments the synchrotron radiation (SR) sources are used.

First synchrotrons became available for scientists around 1970, and, as it have been already mentioned, almost immediately the modern theory of XAS has been developed. The conventional methods for EXAFS analysis, commonly used today, also have been proposed in the 1970s. At the same time, the development of X-ray sources at the end of the 20th century and at the beginning of 21st century is truly remarkable, and may be considered to be even faster than the exponential development of computing hardware, described by the famous Moore's law (Fig. 2.2). Consequently the quality of XAS data is also increased enormously. Hence it is clear, completely new methods for the analysis of these data are required.

### 2.3 Synchrotron radiation

In synchrotron sources X-rays are produced by bending the trajectories of fast, charged particles (electrons (as in ESRF) or positrons (as in PETRA-3)<sup>1</sup>) by strong magnetic field. Due to the acceleration of particles in this process, they emit electromagnetic radiation with the wavelength that in the reference frame,

<sup>1</sup>The use of more exotic positrons may be preferable, considering the life time of particle in the storage ring: even in the conditions of high-quality vacuum in the synchrotron ring there is always some dust, and collisions with the dust lead to losses of the orbiting particles. Particles of dust usually are positively charged, therefore the collisions with the dust are less probable for positrons than for negatively charged electrons. The drawback of the positrons is the fact that it is significantly more difficult to produce positrons than electrons.

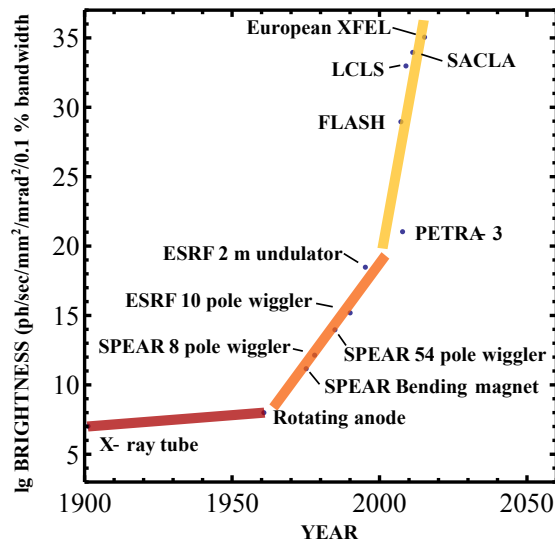


**Figure 2.2: Historical development of X-ray radiation sources**

For free-electron lasers the peak-brilliance is plotted, for European XFEL (now under construction) the expected peak-brilliance is plotted [13, p.42], [14]

associated with particles, is about 1 - 10 cm. The speed of particles circulating in the storage ring is close to the speed of light, therefore the relativistic effects become important and are responsible for that the emitted radiation is strongly collimated in the synchrotron plane, and that its wavelength is strongly reduced due to relativistic Doppler shift

In the earlier sources of the SR, the particles were just orbiting in the storage ring, and their trajectory and the emission of radiation were sustained by simple bending magnets (Fig. 2.3-A). Knowing the energy of the particles in the storage ring  $E_e$  (typically a few GeV, for instance,  $E_e$  was 6 GeV at ESRF and PETRA-3 storage rings in 2013) and their rest mass  $m$ , the relativistic factor  $\gamma = 1/\sqrt{1 - v^2/c^2}$  can be calculated as  $\gamma = E_e/mc^2$ . Then the radiation beam is collimated in the plane of synchrotron in the narrow angle that is proportional to  $1/\gamma$  [13, p.38]. Thus the beam, emitted by an accelerated particle, is seen by user of such device as a very short light pulse. Consequently, the obtained radiation has a very broad spectral range, from infra-red light up to hard X-rays.

Due to the energy losses, caused by the emission of radiation, the energy of particles circulating in the storage ring is reduced with the lapse of time. Therefore in the special section of the storage ring a radio-frequency (RF) electromagnetic field is applied to provide additional tangential acceleration to the slowest particles<sup>1</sup>. Such compensation of energy losses leads to the so called bunching of

<sup>1</sup>In fact, due to RF field all particles are accelerated, but since they have different speeds,

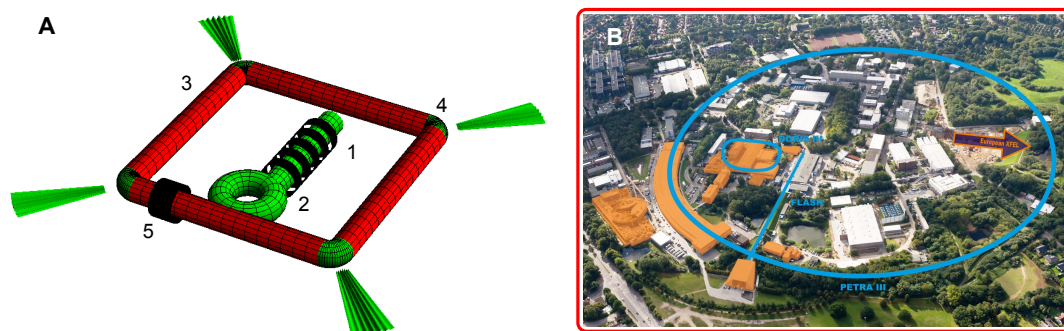


**Figure 2.3: Synchrotron radiation sources**

Panel A: schematic of SR source: electrons or positrons are created and injected in the linear accelerator (1), then in the so called booster ring (2), where they obtain additional acceleration, and then they are injected in the main storage ring (3), and the curvature of their trajectories and the radiation emission are sustained by bending magnets (4), while the energy losses are compensated in RF cavity (5). Panel B: synchrotron radiation sources DORIS and PETRA, and free electron lasers FLASH and European XFEL (under construction) in Hamburg, Germany [15].

the particles - they are not spread out homogeneously all over the storage ring, but form a few larger groups. The name "synchrotron" itself originates in the fact that the process of energy-compensation must be carefully synchronized with the orbital motion of the particles in the storage ring.

For the conventional XAS experiment the brightness, provided by bending magnet beamlines, is usually sufficient, and such beamlines have been used for all EXAFS measurements, discussed within this thesis. For more sophisticated experiments (for instance, time-resolved studies), however, one may need to have higher intensity of incident X-ray radiation. Then the beamlines, equipped with so called insertion devices (wigglers or undulators), can be used. In this case the trajectory of through-flying particles is bent by a double-row of alternating magnetic poles, aligned below and above the beam of particles, and each such wiggle of the electron or positron, flying through the insertion device, enforces the emission of electromagnetic radiation [13, p.43], and the brightness of radiation can be enhanced by several orders of magnitudes [13, p.51]. Further development of this idea, when also the interaction of the emitted radiation with the particles themselves is exploited, is realized in the so called X-ray free electron lasers (XFEL).

---

particles have also different relativistic masses, therefore, the same accelerating force will give more significant acceleration for the slower particles than for the faster ones.

## 2.4 Conventional XAS experiment

In contrast to other beamlines at SR sources, relatively simple X-ray optics are required for a conventional EXAFS beamline (Fig. 2.4), and a monochromator is probably the most important part. A single crystal, cut along specific crystallographic direction, can be used as such monochromator, and the monochromatization of the incoming beam is ensured by the diffraction of X-rays on the lattice planes. In practice, two identical and parallelly aligned crystals are used in the X-ray monochromators at SR sources to have the same direction of the outgoing monochromatized beam for all wavelengths. To filter out the higher-order harmonics that also are diffracted in the same direction as the radiation with the wavelength of interest, one may slightly skew one monochromating crystal with respect to another or, alternatively, the beam can be additionally monochromatized with totally reflecting X-ray mirrors [16, p.143]. Single crystals of silicon are usually used as monochromator, since large crystals of silicon with sufficient quality are relatively easy to manufacture, and, additionally, the crystalline silicon at temperatures, close to the temperature of liquid nitrogen, has almost negligible thermal expansion, therefore a very good stability of the monochromator can be achieved.

In the conventional XAS experiment absorption spectrum is measured point by point, and the change of the energy of photons, diffracted in the sample direction, is ensured by step-by-step rotation of monochromator crystals. Alternatively, in the so called Quick-XAFS mode the monochromator is rotated and the XAS spectra are acquired continuously, and afterwards to obtain good signal-to-noise ratio multiple obtained spectra are averaged [17, p.33].

To measure the value of absorption coefficient in the transmission XAS experiment, one needs to measure the intensity of the incident beam  $I_0$  and the intensity of the beam that has passed through the sample  $I_1$ . Optionally, after the studied sample a reference sample can be installed, and also the intensity of the beam that passed through the reference sample  $I_2$  can be measured. The intensity is measured using ionization chambers - about 10-20 cm long cylindrical reservoirs, filled with inert gases, such as helium, nitrogen, argon, xenon. High-voltage electric field is applied to the chambers. The incoming X-ray radiation ionizes the atoms in the chambers and the ions drift in the applied electric field, creating in the circuit small but measurable current. The value of the current is

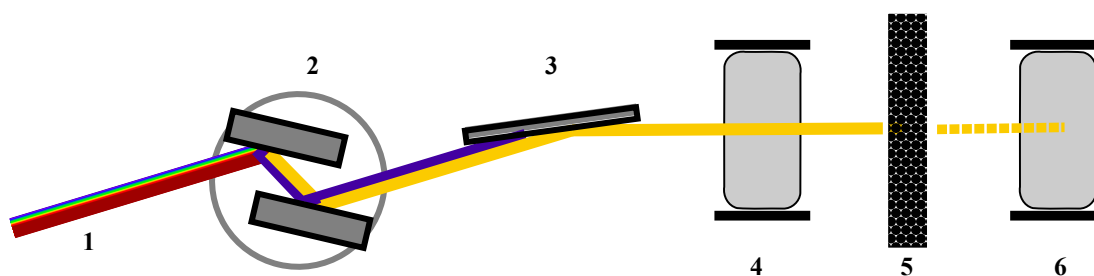


**Figure 2.4: Common experimental setup for XAS experiments**

Incident X-ray beam (1) is monochromatized in the double-crystal monochromator (2), higher-order harmonics are removed with X-ray mirror (3) with reflectivity, strongly dependent on the wavelength of the radiation, the intensity of monochromatized beam is measured in the ion-chamber (4), then X-rays pass through the sample (5) and the final intensity of the beam is measured in the second ion-chamber (6)

proportional to the intensity of the X-ray radiation. To obtain reliable absorption data, sample must be sufficiently homogenous and the concentration of the absorbing atoms should be high enough. If these conditions can be fulfilled, XAS measurements in the transmission mode will provide the highest signal-to-noise ratio.<sup>1</sup>

Finally it should be mentioned, different sample environments can be easily installed around the sample - nitrogen or helium cryostats, furnaces, high-pressure environment, equipment for different *in situ* experiments, thus it is possible to study directly the influence of temperature and different chemical and physical processes on the local structure of the sample.

## 2.5 Sample preparation

For the XAS measurements in transmission mode the thickness and concentration of the sample should be carefully adjusted, in order to ensure appropriate signal-to-noise ratio. A rule of thumb is that for the X-rays with energy slightly larger than the absorption edge the intensity after the sample (in the second ionization chamber) should be about  $e$  times weaker than the intensity of the incident radiation, measured in the first ion chamber. A very important issue in this case is also the homogeneity of the sample: even small pin-holes in the area

<sup>1</sup>The absorption coefficient can be measured not only in the direct transmission experiments. Common approach, for example, is to measure instead the intensity of X-ray fluorescence and to exploit the fact that it is proportional to the absorption coefficient [16, p.144]. Fluorescence measurements can be used, for example, when it is impossible to obtain a sufficiently homogenous sample or when the concentration of absorbing atoms in sample is very low.

of the sample can lead to the dramatic reduction of the amplitude of measured signal. A thorough review of the influence of sample thickness on the quality of the EXAFS spectra is given in [17]. The sample preparation technique that ensures probably the best homogeneity of the sample for measurements in transmission mode, is the deposition on nitrocellulose Millipore filter: the powder is ground and suspended in the water or other appropriate liquid, and then is filtered through the Millipore membrane using water pump, and then is fixed using Scotch or Kapton tape. This method is used for preparation of the most of the samples, analyzed in this work. It cannot, however, be used for high-temperature measurements, since the organic filter membrane is not heat-resistant. In this case the powder-like samples can be diluted with boron nitride that only weakly interacts with X-rays, and pressed together using conventional pelett press (similarly as in infra-red spectroscopy).

## 2.6 EXAFS theory

### 2.6.1 Introduction

The X-ray absorption edges and the oscillations of the X-ray absorption coefficient in the vicinity of absorption edges have been observed shortly after the first X-ray tubes have been developed. The very first attempts to explain the origin of such features can be attributed to Ralph Kronig, who studied this topic in the early 1930s [18]. Nevertheless, a significant development in the understanding of atomic processes and also the development of X-ray sources were necessary, to make possible the birth of modern EXAFS theory in the 1970s, when Dale Sayers, Edward Stern and Farrel Lyttle proposed a new interpretation of XAFS data, and also a new approach to the analysis of EXAFS spectra that nowadays is considered as a conventional [10, 19, 20, 21]. Detailed reviews of EXAFS theory can be found in [2] and [22], but in this section we give a brief overview of the aspects of EXAFS theory that are the most important for the understanding of further material, presented in this thesis. The insight into another approach to EXAFS theory that is based on the Green's function method and that is more convenient for the *ab-initio* calculations of EXAFS data, is given in Sec. 4.4.

### 2.6.2 X-ray absorption by isolated atom

As in many other kinds of spectroscopies, to quantitatively describe XAS, we can start with the Fermi's Golden Rule that gives the probability of transition from initial atomic state  $|i\rangle$  to some final atomic state  $|f\rangle$  upon some interaction, in this case, upon the absorption of photon, described by operator  $\hat{T}$ . Obviously, the absorption coefficient  $\mu_i$  is just proportional to this probability [2]

$$\mu_i(\hbar\omega) \sim \sum_f \left| \langle f | \hat{T} | i \rangle \right|^2 \delta(\varepsilon_f - \varepsilon_i - \hbar\omega). \quad (2.3)$$

Here Dirack function  $\delta(\varepsilon_f - \varepsilon_i - \hbar\omega)$  describes the conservation of energy during the transition, i.e., the energy of the final state  $\varepsilon_f$  is equal to the sum of the energy of initial state  $\varepsilon_i$  and the energy of incident photon  $\hbar\omega$ . The  $\left| \langle f | \hat{T} | i \rangle \right|$  term is the projection of the state, which can be obtained from the initial state by applying given interaction operator, on one of the available final states, i.e., it shows, how similar is the state, obtainable from the initial state, to one of the possible final states. If such similarity is high, then the corresponding transition will be more probable.

In the case of XAS, the initial state  $|i\rangle$  is the ground state of atom, while the final state  $|f\rangle$  is atom with one of the core-level electrons excited to one of the upper unoccupied energy levels and all other electrons rearranged due to the presence of the positively charged core hole, i.e., the transition is essentially many-electronic process. However, if the energy of the excited electron is high, i.e., if we are working in the EXAFS regime, we can effectively use the one-electron approach. In this case we factorize  $|i\rangle$  as a product of  $|\Psi_i^{N_e-1}\rangle$  and  $|\psi_i\rangle$ , where the latter term describes the initial state of the electron that will be excited, and the first term describes the initial state of remaining  $N_e - 1$  electrons. Similarly, we factorize the final state as a product of  $|\Psi_{fn}^{N_e-1}\rangle$  and  $|\psi_f\rangle$ , where index  $n$  denotes that many final states for the electronic system are possible. The additional energy, accumulated by the system of  $N_e - 1$  electrons, then will be  $\varepsilon_n$ , and the final energy of the excited electron  $\varepsilon'_f = \varepsilon_f - \varepsilon_n$ . The photon directly interacts

only with the electron, described by  $|\psi_i\rangle$  and  $|\psi_f\rangle$  [2], therefore

$$\begin{aligned}
& \left| \langle f | \hat{T} | i \rangle \right|^2 \delta(\varepsilon_f - \varepsilon_i - \hbar\omega) \approx \\
& \approx \sum_n \left| \langle \Psi_{f_n}^{N_e-1} | \Psi_i^{N_e-1} \rangle \right|^2 \left| \langle \psi_f | \hat{T} | \psi_i \rangle \right|^2 \delta(\varepsilon_n + \varepsilon'_f - \varepsilon_i - \hbar\omega) = \\
& = \sum_n S_n^2 \left| \langle \psi_f | \hat{T} | \psi_i \rangle \right|^2 \delta(\varepsilon_n + \varepsilon'_f - \varepsilon_i - \hbar\omega),
\end{aligned} \tag{2.4}$$

where  $S_n^2 = \left| \langle \Psi_{f_n}^{N_e-1} | \Psi_i^{N_e-1} \rangle \right|^2$ .

The initial state  $|\psi_i\rangle$  is the ground state of core-level electron. It is a spatially localized state, electron here is very strongly bonded to atomic nuclei and interatomic interactions (chemical bonding) do not influence it significantly. Spatial localization of the initial state means that  $|\psi_i\rangle$  is different from zero only in the area, very close to the atomic nucleus. As a result, to calculate the term  $\left| \langle \psi_f | \hat{T} | \psi_i \rangle \right|$ , we will need to carry out the integration over only very limited volume, and, consequently, we will need to know the values of  $|\psi_f\rangle$  (that, in principle, can be completely delocalized) only inside of this limited volume [2].

If the initial state is K-orbital, the wave-function, corresponding to an electron in state  $|\psi_i\rangle$ , is spherically symmetric, but generally it is not the case. The different angular orientations of the wave-function of initial state with respect to the orientation of the wave-function of final state and with respect to the direction and polarization of incident X-ray beam lead to the so called "selection rules" - due to the different overlap of initial and final states not all transitions are allowed. For the description of XANES part of X-ray absorption spectra, it is therefore important to correctly account for the angular part of electronic wave-functions. In the EXAFS region, however, it does not play significant role, as the corresponding transitions are the transitions to the continuum, where the density of states is very high and surely at given energy  $\varepsilon_f$  there will be many states with appropriate orientation. Therefore we can significantly simplify further description, neglecting angular dependencies of  $|\psi_i\rangle$  and  $|\psi_f\rangle$  states, i.e., we assign to these states wave functions  $\psi_i(r)$  and  $\psi_f(r)$ , where  $r$  is the distance to the atomic nucleus. In this approach a final state is completely characterized by its energy  $\varepsilon'_f$ . Therefore we can also replace the summation over final states with the integration over energy, introducing the density of allowed states  $\rho(\varepsilon'_f)$ .

The final state of electron, excited to a completely delocalized continuum level, (often such electron is also called as "photoelectron") can be described as a spher-



ical wave, travelling in all directions from the absorbing atom. The wavenumber  $k$  of the photoelectron is related to its energy  $\Delta E_{ph.e.}$  as  $k = \sqrt{2m_e \Delta E_{ph.e.} / \hbar^2}$ , with  $\Delta E_{ph.e.} = \hbar\omega - E_0$  ( $E_0$  - the minimal energy, required to excite core electron to the continuum level, for metals it can be considered equal to Fermi energy;  $m_e$  is the electron mass and  $\hbar$  is the Planck's constant). The life-time of such spherical wave is determined by inelastic processes in the system, which are of quite different natures: (i) inelastic scattering of the photoelectron and (ii) decay of the core-hole state (see Sec. 4.4.1 for more details on the latter aspect). Typically this life time is about  $10^{-16}$  -  $10^{-15}$  seconds [17, p.14]. To characterize the life-time of the photoelectron, commonly the so called photoelectrons effective mean free-path  $\lambda(k)$  is introduced.  $\lambda(k)$  strongly and non-linearly depends on the energy of the photoelectron. Typically, it is large in XANES region, but rapidly decreases, if the energy of the photoelectron is in EXAFS range. As will be shown later, it is one of the reasons, why the theoretical calculations of XANES spectra are much more complicated than the ones of EXAFS spectra. The effective mean free path is also the quantity that limits the range that can be probed by EXAFS in the  $R$ -space: it suppresses the contributions to the total spectrum from neighbor atoms that are more than about  $10 \text{ \AA}$  apart from the absorbing atom.

The remaining term in the Fermi's Golden rule is the interaction of electron with photon. This process is a simple interaction of a charged particle with electromagnetic field. If the intensity of electric field, associated with absorbed photon, at the moment of absorption is described by vector  $\vec{\epsilon}$ , then in the so called dipole approximation the interaction potential is proportional to  $\vec{\epsilon} \cdot \vec{r}$ , where  $\vec{r}$  is the radius vector of absorbing electron with respect to atomic nucleus. For EXAFS region the dipole approximation is completely valid, for the correct description of XANES region of heavy elements the quadruple and even higher-order corrections to the interaction operator may be required [2].

Now we put it all together:

$$\mu_i(\hbar\omega) \sim \sum_n \int_0^\infty d\varepsilon'_f S_n^2 \rho(\varepsilon'_f) \delta(\varepsilon_n + \varepsilon'_f - \varepsilon_i - \hbar\omega) |\langle \psi_f(r, \varepsilon'_f) | \vec{\epsilon} \vec{r} | \psi_i(r) \rangle|^2. \quad (2.5)$$

In principle,  $S_n^2$  terms depend on the energy of incident radiation. It can be understood, if one notes that if the energy of incident photon is exactly equal to the threshold energy  $E_0$ , only  $S_0^2$  term is non-zero, since there is just no energy

left to excite the system of  $N_e - 1$  electrons to higher states. For higher energies also the other  $S_n^2$  terms will be larger than zero. At the same time for fixed energy  $\hbar\omega$  the sum  $\sum_n S_n^2 = \sum_n |\langle \Psi_{fn}^{N_e-1} | \Psi_i^{N_e-1} \rangle|^2 = 1$  [2]. Thus  $S_0^2(\hbar\omega = E_0) = 1$ , but it is smaller than 1 for larger values of  $\hbar\omega$ . It is also worth to note here that usually  $S_n^2 \ll S_0^2$  for  $n \neq 0$ .

The result, obtained above, additionally assuming that  $\rho$  does not change rapidly in the vicinity of the threshold energy  $E_0$ , can be rewritten as a convolution [2, 23]

$$\mu_i(\hbar\omega) \sim \int_0^\infty d\varepsilon A(\varepsilon) \mu_{qp}(\hbar\omega - \varepsilon), \quad (2.6)$$

where

$$\mu_{qp}(\hbar\omega) \sim \rho(E_0) |\langle \psi_f(r, \hbar\omega) | \vec{\epsilon} \vec{r} | \psi_i(r) \rangle|^2 \quad (2.7)$$

corresponds to the absorption in the one-electron (or, more precisely, in one-quasi-particle) approximation and

$$A(\varepsilon) = \sum_n S_n^2 \delta(\varepsilon - \varepsilon_n). \quad (2.8)$$

### 2.6.3 Origins of EXAFS

The presence of neighbor atoms perturbs the final state of the electron, excited by X-ray photon, hence it modifies also the value of X-ray absorption coefficient. This results in the EXAFS oscillations of absorption spectra.

If  $\psi_f(r)$  is the wave function of the final state of the excited electron, it can now be written as

$$\psi_f(r) = \psi_{f0}(r) + \Delta\psi_f(r), \quad (2.9)$$

where  $\psi_{f0}(r)$  is the wave function of the final state for atom without neighbors, and  $\Delta\psi_f(r)$  is the perturbation, caused by the presence of neighbor atoms.

Now the term  $|\langle \psi_i(f) | \vec{\epsilon} \vec{r} | \psi_i(r) \rangle|^2$  in Eqs. (2.5) and (2.7) turns into

$$\begin{aligned}
& |\langle \psi_i(f) | \vec{\epsilon} \vec{r} | \psi_i(r) \rangle|^2 = \\
& = |\langle \psi_{f0}(r) | \vec{\epsilon} \vec{r} | \psi_i(r) \rangle|^2 \left[ 1 + \frac{|\langle \Delta \psi_f(r) | \vec{\epsilon} \vec{r} | \psi_i(r) \rangle|^2}{|\langle \psi_{f0}(r) | \vec{\epsilon} \vec{r} | \psi_i(r) \rangle|^2} + \right. \\
& \left. + \left( \frac{\langle \Delta \psi_f(r) | \vec{\epsilon} \vec{r} | \psi_i(r) \rangle}{\langle \psi_{f0}(r) | \vec{\epsilon} \vec{r} | \psi_i(r) \rangle} \right)^* + \frac{\langle \Delta \psi_f(r) | \vec{\epsilon} \vec{r} | \psi_i(r) \rangle}{\langle \psi_{f0}(r) | \vec{\epsilon} \vec{r} | \psi_i(r) \rangle} \right].
\end{aligned} \tag{2.10}$$

The second term in the square braces is negligible, since  $\Delta \psi_f$  is small. Also, for the calculations of the third and fourth terms one can recall that  $\psi_i(r)$  is strongly spatially localized state, therefore only the values of  $\Delta \psi_f(r)$  for  $r$  close to zero will have significant contribution. Thus

$$\begin{aligned}
& |\langle \psi_i(f) | \vec{\epsilon} \vec{r} | \psi_i(r) \rangle|^2 \approx \\
& \approx |\langle \psi_{f0}(r) | \vec{\epsilon} \vec{r} | \psi_i(r) \rangle|^2 \left[ 1 + \left( \frac{\langle \Delta \psi_f(0) | \psi_i(0) \rangle}{\langle \psi_{f0}(0) | \psi_i(0) \rangle} \right)^* + \frac{\langle \Delta \psi_f(0) | \psi_i(0) \rangle}{\langle \psi_{f0}(0) | \psi_i(0) \rangle} \right] = \\
& = |\langle \psi_{f0}(r) | \vec{\epsilon} \vec{r} | \psi_i(r) \rangle|^2 \left[ 1 + 2\text{Re} \left( \frac{\langle \Delta \psi_f(0) | \psi_i(0) \rangle}{\langle \psi_{f0}(0) | \psi_i(0) \rangle} \right) \right].
\end{aligned} \tag{2.11}$$

The EXAFS signal  $\chi(\hbar\omega)$  can be defined as the relative value of corresponding absorption coefficient  $\chi(\hbar\omega) = (\mu(\hbar\omega) - \mu_0(\hbar\omega)) / \mu_0(\hbar\omega)$ . Here  $\mu_0(\hbar\omega)$  is the absorption coefficient of atom, if the influence of neighbor atoms can be neglected. Similarly, in the one-electron approximation one has

$$\chi_{qp}(\hbar\omega) = \frac{\mu_{qp}(\hbar\omega) - \mu_{0,qp}(\hbar\omega)}{\mu_{0,qp}(\hbar\omega)}. \tag{2.12}$$

Here  $\mu_{0,qp}(\hbar\omega) \sim \rho(E_0) |\langle \psi_{f0}(r, k) | \vec{\epsilon} \vec{r} | \psi_i(r) \rangle|^2$  [2, 23].

Finally, we end up with

$$\chi_{qp}(\hbar\omega) \approx 2\text{Re} \left( \frac{\langle \Delta \psi_f(0) | \psi_i(0) \rangle}{\langle \psi_{f0}(0) | \psi_i(0) \rangle} \right). \tag{2.13}$$

#### 2.6.4 Many-electronic effects

From Eq. (2.6) one gets

$$\chi(\hbar\omega) = \frac{\mu(\hbar\omega) - \mu_0(\hbar\omega)}{\mu_0(\hbar\omega)} = \frac{\int_0^\infty d\varepsilon A(\varepsilon) (\mu_{qp}(\hbar\omega - \varepsilon) - \mu_{0,qp}(\hbar\omega - \varepsilon))}{\int_0^\infty d\varepsilon A(\varepsilon) \mu_{0,qp}(\hbar\omega - \varepsilon)}. \quad (2.14)$$

Now, if  $(\mu_{qp} - \mu_{0,qp}) = \chi_{qp}\mu_{0,qp}$ , and  $\mu_{0,qp}$  (smooth absorption spectrum of isolated atom) can be considered independent on  $\hbar\omega$  in the relevant range of the energies of absorbed photons, then

$$\chi(\hbar\omega) = \frac{\int_0^\infty d\varepsilon A(\varepsilon) \chi_{qp}(\hbar\omega - \varepsilon)}{\int_0^\infty d\varepsilon A(\varepsilon)} = \frac{\sum_n S_n^2 \chi_{qp}(\hbar\omega - \varepsilon_n)}{\sum_n S_n^2}. \quad (2.15)$$

Recalling that  $\sum S_n^2 = 1$  and  $S_0^2 \gg S_{n>0}^2$ , we end up with

$$\chi(\hbar\omega) \approx S_0^2 \chi_{qp}(\hbar\omega) = 2S_0^2 \text{Re} \left( \frac{\langle \Delta\psi_f(0) | \psi_i(0) \rangle}{\langle \psi_{f0}(0) | \psi_i(0) \rangle} \right). \quad (2.16)$$

The factor  $S_0^2$  is close to 1 and depends weakly on the energy  $\hbar\omega$  and interatomic distance  $R$  [2], as briefly discussed in Sec. 2.6.2. In great details the reduction of EXAFS amplitude due to many-electronic effects (or, more precisely, due to intrinsic losses, i.e. the processes, related to the formation of core-hole [17, p.276]) is explored in [23]. In practice, however, the  $S_0^2$  factor is usually assumed to be constant and equal to some effective value that is close to 1. Moreover, when treating real experimental data, the amplitude of EXAFS signal can be reduced also by the nonlinearity of detectors, by the non-homogeneity of the sample (presence of pin-holes), by the problems with EXAFS signal extraction and other experiment-related factors [24]. All of these effects are included in the effective value of  $S_0^2$  that then can be determined from the best-fit procedure of experimental data.

#### 2.6.5 EXAFS equation within the single-scattering approximation

To describe the influence of neighbor atoms, one to some extent can use the representation of the photoelectron as a spherical wave, propagating in all directions around absorbing atoms with corresponding wavenumber  $k$ . Neighbor

atoms will interact with the wave and elastically scatter it in all directions (inelastic scattering is accounted in the already mentioned mean-free paths of the photoelectron  $\lambda(k)$ ). Small part of the incident wave will be scattered back to the absorbing atom, and will interfere with the original wave. As a result, the amplitude of the final state of the photoelectron will be modulated.

It is important to remember that due to the strong spatial localization of initial state, we are interested in the amplitude of the final state  $\psi_f(r)$  only for values of  $r$  that are close to zero.

The amplitude of the original outgoing wave can be described by equation  $\psi_{f0}(r) = \psi_{f0}(0)e^{ikr}/(kr)$ . If there is some atom at the distance  $R$  from absorbing atom, then it will scatter the wave with amplitude  $\psi_{f0}(R) = \psi_{f0}(0)e^{ikR}/(kR)$ , as a result, the amplitude and phase of the wave will be changed, and this change can be described as a complex scattering function  $k\Phi(k)$ <sup>1</sup> [13, p.137]. The scattered wave that returns back to the absorbing atom thus will have the amplitude  $\Delta\psi_f(0) = \psi_{f0}(0)e^{ikR}/(kR)k\Phi(k)e^{ikR}/(kR) = \psi_{f0}(0)e^{i2kR}\Phi(k)/(kR^2)$ . To take into account inelastic losses, we multiply this expression by term  $e^{-2R/\lambda(k)}$ , where  $\lambda(k)$  is the effective mean free path of photoelectron. In programs for theoretical calculations of EXAFS signal, such as FEFF [25], this term is usually included in the  $\Phi(k)$  function, i.e., we introduce

$$\tilde{\Phi}(k, R) = \Phi(k)e^{-2R/\lambda(k)}, \quad (2.17)$$

such that  $\langle \Delta\psi_f(0)\psi_i(0) \rangle = e^{-i2kR}\tilde{\Phi}(k, R)^*\langle \psi_{f0}(0)\psi_i(0) \rangle/(kR^2)$  and

$$\chi(k) = 2S_0^2 \text{Re} \left( e^{-i2kR}\tilde{\Phi}(k, R)^* \right) / (kR^2) = S_0^2 \frac{f(k, R)}{kR^2} \sin(2kR + \phi(k, R)), \quad (2.18)$$

where the complex scattering function  $\tilde{\Phi}(k, R)$  is decomposed as  $\tilde{\Phi}(k, R) = \frac{f(k, R)}{2}e^{i(\phi(k, R) - \pi/2)}$ , with  $f(k, R)$  and  $\phi(k, R)$  being real functions that describe the changes of amplitude and phase of scattered wave.

Now if there are many atoms of the same type, located at different distances around the absorbing atoms, we can characterize their distribution with radial distribution function  $g(R)$ . The total number of neighbor atoms, for example,

<sup>1</sup>The multiplication by wavenumber  $k$  in the expression for scattering function  $k\Phi(k)$  is a convention that ensures that  $\Phi(k)$  is measured in the units of length [17, p.12]

now can be calculated simply as  $N = \int_0^{\infty} dR g(R)$ . The total EXAFS signal, defined by such distribution of neighbors, will now be just

$$\chi(k) = S_0^2 \int_0^{\infty} dR g(R) \frac{f(k, R)}{kR^2} \sin(2kR + \phi(k, R)). \quad (2.19)$$

If there are atoms of different types around the absorber, each of them will have its own amplitude and phase scattering functions. A useful rule of thumb is that for heavy atoms function  $f(k, R)$  reaches its maximum at larger values of wavenumber  $k$  than for lighter atoms. For example, oxygen atoms contribute to the total EXAFS spectrum mostly at  $k$  values below  $6 \text{ \AA}^{-1}$  [17, p.294]. The total EXAFS spectrum now will be [2]

$$\chi(k) = S_0^2 \int_0^{\infty} dR \sum_i g_i(R) \frac{f_i(k, R)}{kR^2} \sin(2kR + \phi_i(k, R)). \quad (2.20)$$

At this point we already see that from the analysis of EXAFS signal we can obtain information on the local atomic structure around the absorbing atom: information on the type of neighbor atoms and their radial distribution.

### 2.6.6 EXAFS equation within the multiple-scattering approximation

The analysis of EXAFS spectra gets significantly more complicated, if one cannot neglect the so called multiple-scattering (MS) effects. In the previous subsection we interpreted EXAFS as a result of the scattering of photoelectron wave by the potential of one of the neighbor atoms. But, of course, such scattered photoelectron can not only directly return to the absorbing atom, but it also can interact with the potentials of other atoms, thus returning to the absorbing atom via complicated path, involving three, four etc. number of atoms (Fig. 2.5). Usually, the influence of such multiple-scattering effects is small, although only rarely it is completely negligible. Moreover, if the multiple-scattering path is linear (Fig. 2.5-D), the amplitude of MS contribution can be very high, and can even exceed the amplitude of single-scattering (SS) contributions [26, 27]. This effect is called focussing effect, and it is characteristic for cubic systems, such as  $\text{ReO}_3$  [28, 29, 30],  $\text{ScF}_3$ ,  $\text{FeF}_3$  [31],  $\text{NaWO}_3$  [32],  $\text{WO}_{3-x}$  [32] But also the MS contributions from non-linear scattering paths sometimes can be quite

significant: for instance, the MS effect within the first coordination shell of the absorbing atom is strong in the case of octahedral coordination (for perovskite-type structures this effect was reported in [30, 32], for ions of the 3d-transition metals in solutions - in [33, 34]).

We can easily generalize the EXAFS equation, to account for MS scattering contributions as

$$\chi(k) = S_0^2 \int_0^\infty d\vec{R} \sum_i g_i(\vec{R}) \frac{f_i(k, \vec{R})}{kR^2} \sin(2kR + \phi_i(k, \vec{R})). \quad (2.21)$$

The summation in the equation above is carried out over all SS and MS paths,  $\vec{R}$  is the  $n$ -dimensional vector, characterizing positions of all atoms of the path with respect to the absorbing atom, and  $2R$  is the total length of this path. The distribution function  $g_i(\vec{R})$  is now many-atomic distribution function, containing information on the interatomic distances, bonding angles, etc., i.e., all structural information we are interested in. Note that scattering functions  $f_i$  and  $\phi_i$  now depend not only on wavenumber  $k$ , but also on  $\vec{R}$  - it is a consequence of the fact that scattering phase and amplitude depend on the angle, in which the photoelectron is scattered. This dependency on the positions of atoms  $\vec{R}$  is often neglected in the conventional EXAFS analysis, but it is important for the correct interpretation of MS effects.

In principle, modern *ab-initio* codes for calculations of EXAFS signal, such as FEFF [25], can calculate scattering functions  $f_i$  and  $\phi_i$  for arbitrarily complex MS paths. The main technical difficulty arises due to the fact that the number of scattering paths increases exponentially with the increase of the size of atomic cluster, whose structure we are trying to analyze.

### 2.6.7 Thermal and static disorder

Let us look at the distribution function  $g_i(\vec{R})$  in more details, and let us start with the simple case of single-scattering path, where  $g_i(R)$  is just radial distribution function (RDF) for one coordination shell. In the case of perfect crystal,  $g_i(R)$  will be equal to  $N_i\delta(R - R_i)$ , where  $\delta(R - R_i)$  is Dirac delta function that expresses the fact that all atoms in a perfect crystal are located at precisely specified distances  $R_i$ , and  $N_i$  is the number of atoms in the given coordination shell.

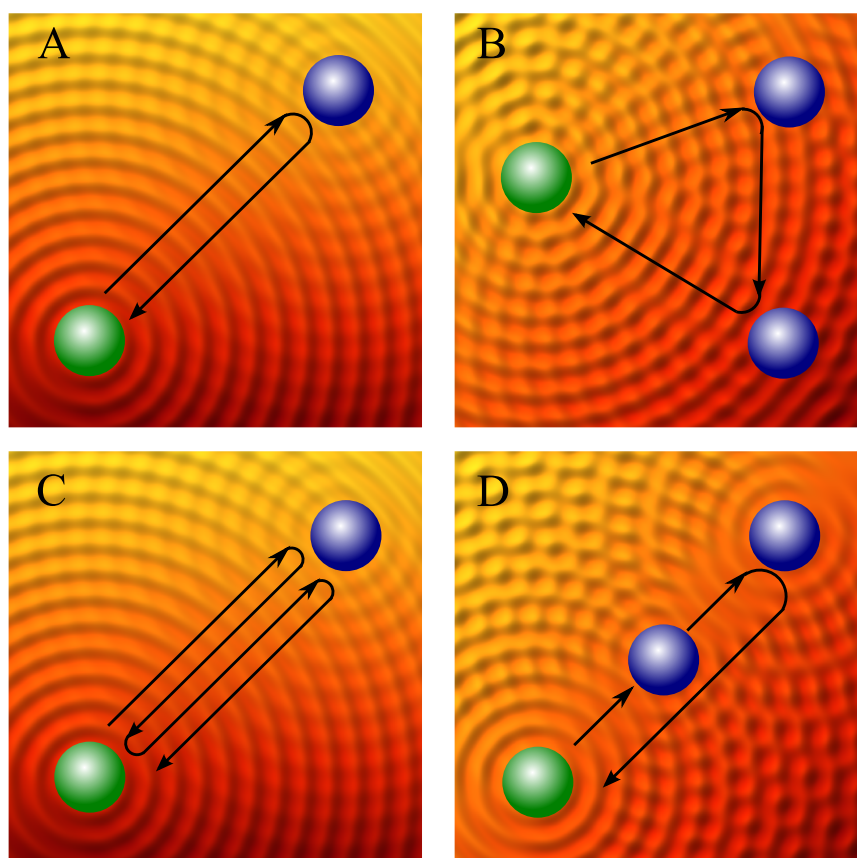


**Figure 2.5: single-scattering and multiple-scattering paths**

SS path (A) and different multiple-scattering paths: double-scattering path (B), triple-scattering path (C), linear double-scattering path (D).

However, even in crystalline materials atoms are rarely located at their equilibrium positions due to their thermal motion. In disordered materials as amorphous solids, glasses and liquids, static disorder is additionally present. As a result, the distributions of the atom positions are smeared, and so is the RDF. Note that the life-time of core-hole that is one of the factors that limits the time-scale of EXAFS formation process, is typically a few femtoseconds large [9], while the motion of atoms is much slower: the characteristic frequencies of atomic vibrations are on the scale of  $10^{13}$  Hz [17, p.14]. Thus each absorption event probes some "stroboscopic image" of the system, i.e., momentary positions of neighbor atoms, and then the total EXAFS spectrum is obtained as an average of such individual contributions over sample volume and measurement time.

Good and commonly used approximation of radial distribution function in



this case is Gaussian function [2]

$$g_i(R) = \frac{N_i}{\sqrt{2\pi\sigma_i^2}} e^{-\frac{(R-R_i)^2}{2\sigma_i^2}}. \quad (2.22)$$

Here  $R_i$  is average interatomic distance, while  $\sigma_i^2$  is mean square radial displacement (MSRD) factor. By analogy with the thermal factor in X-ray diffraction peaks,  $\sigma_i^2$  is sometimes also called as Debye-Waller factor, although this analogy is misleading: a MSRD factor for EXAFS, unlike a Debye-Waller factor for diffraction, contains information on relative, rather than absolute atomic displacements. If displacements from the equilibrium for atoms  $A$  and  $B$  are  $\vec{u}_A$  and  $\vec{u}_B$ , then the MSRD factor  $\sigma_{AB}^2$  will be  $\sigma_{AB}^2 = \langle \vec{u}_A^2 \rangle + \langle \vec{u}_B^2 \rangle - 2\langle \vec{u}_A \vec{u}_B \rangle$ , where  $\langle \vec{u}_A^2 \rangle$  and  $\langle \vec{u}_B^2 \rangle$  are corresponding mean-square displacement (MSD) factors for atoms  $A$  and  $B$  (Fig. 2.6-A). A Debye-Waller factor for diffraction characterizes MSD, rather than MSRD factor. Thus, in principle, EXAFS provides more information on atomic dynamics than diffraction - not only the information on atomic displacements, but also on the correlation of atomic motion ( $\langle \vec{u}_A \vec{u}_B \rangle$  term).

It is important to emphasize here that another difference between EXAFS and diffraction techniques is the interpretation of interatomic distance  $R_i$ : the diffraction, being sensitive to the periodic structure of the lattice, gives the *equilibrium* distance  $R_{i,eq}$ , i.e., the distance between equilibrium positions of two atoms  $A$  and  $B$ . The distance  $R_i$ , obtained from EXAFS experiment, is the *average* distance between these two atoms. Due to the thermal and static deviations of atoms from the line, defined by the equilibrium positions of atoms  $A$  and  $B$ ,  $R_i$  is always larger than  $R_{eq}$  (Fig. 2.6-B) (see [17, p.266] and [35], and [36]). This fact is sometimes used to indirectly estimate the component of the MSD factor in the direction, orthogonal to the mentioned line between  $A$  and  $B$ : if we denote this component as  $\langle u_{\perp}^2 \rangle$ , then  $R_i = \sqrt{R_{i,eq}^2 + \langle u_{\perp}^2 \rangle}$ , thus  $\langle u_{\perp}^2 \rangle \approx 2(R_i - R_{i,eq})$ .

Inserting the expression (2.22) in the EXAFS equation for SS paths (with scattering functions being independent on  $R$ , Eq. (2.20)), one obtains

$$\begin{aligned} \chi(k) &\approx \frac{4\pi S_0^2 N_i f_i(k, R) j}{k \sqrt{2\pi\sigma_i^2}} \int_0^{\infty} \frac{dR}{R^2} e^{-\frac{(R-R_i)^2}{2\sigma_i^2}} \sin(2kR + \phi_i(k, R)) \approx \\ &\approx \frac{S_0^2 N_i f_i(k, R) j}{k R_i^2} e^{-2k^2\sigma_i^2} \sin(2kR_i + \phi_i(k, R)), \end{aligned} \quad (2.23)$$

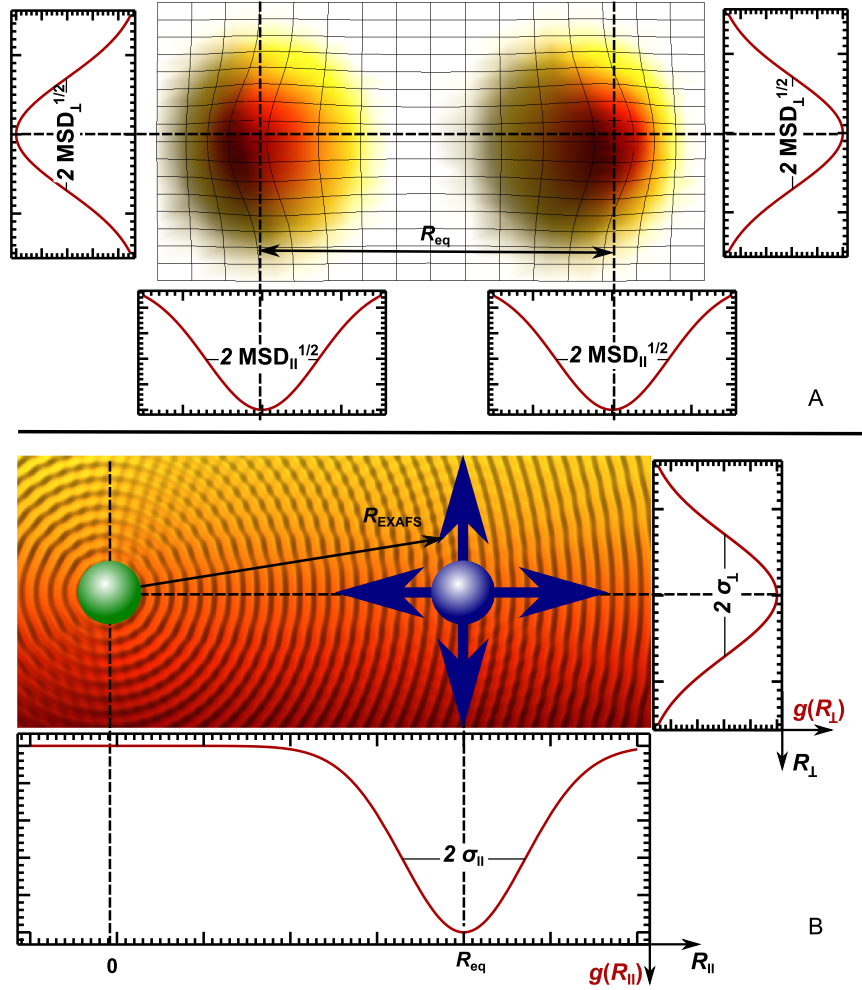


**Figure 2.6: MSD and MSRD factors**

Distributions of displacements of two atoms and their MSD factors  $\langle u^2 \rangle$  (panel A); and the distributions of their relative displacements and their MSRD factors  $\sigma^2$  (panel B).

i.e., the amplitude of EXAFS signal decreases rapidly with the increase of MSRD factor.

MSRD factors characterize both static and thermal disorder in the sample:  $\sigma_i^2 = \sigma_{i,stat}^2 + \sigma_{i,thermal}^2$ . The contribution of the static disorder  $\sigma_{i,stat}^2$  does not depend on temperature, while the contribution of the thermal part  $\sigma_{i,thermal}^2$  as a function of temperature can be calculated from the local projected density of phonon states  $\rho_i(\omega)$

$$\sigma_{i,thermal}^2(T) = \frac{\hbar}{2\mu_i} \int_0^{\omega_{max}} \frac{d\omega}{\omega} \rho_i(\omega) \coth \frac{\hbar\omega}{2k_B T}, \quad (2.24)$$

where  $\mu_i$  is reduced mass for atoms, involved in the  $i$ -th path, and  $k_B$  is Boltzmann's constant [2, 37]. Local projected density of phonon states  $\rho_i(\omega)$  can be substituted with empirical function, for instance, given by correlated Debye or correlated Einstein model [2]. For the description of EXAFS data, both models provide comparable approximation, and further we will use more simple correlated Einstein model, where  $\rho_i(\omega)$  is just Dirac delta-function:  $\rho_i(\omega) = \delta(\omega - \omega_{i,E})$ , with parameter  $\omega_{i,E}$  being so called Einstein frequency. Einstein frequency characterizes the bond strength between the atoms of the  $i$ -th paths: effective bond-stretching force constant  $\kappa_i$  can be expressed as  $\kappa_i = \omega_{i,E}^2 \mu_i$ . Thus one can approximate the temperature-dependencies of the MSRD factors with a simple expression

$$\sigma_{i,thermal}^2(T) = \frac{\hbar}{2\mu_i\omega_{i,E}} \coth \frac{\hbar\omega_{i,E}}{2k_B T}. \quad (2.25)$$

To be more general, one can use more complicated functions to model the radial distribution of atoms than Gaussian function, and use, for instance, the so called cumulant expansion [38] to describe the amplitude damping factor for EXAFS more precisely [2, 39].

Finally, to describe the reduction of the amplitude of contribution from MS paths due to thermal and static disorder, one by analogy can introduce some effective MSRD factors also for MS paths. They will depend on the distribution of atomic displacements and on the correlation of the motion of atoms, involved in the corresponding path, but also on the geometry of the path, bonding angles, etc. In this case we end up with the following EXAFS equation:

$$\chi(k) \approx S_0^2 \frac{N_i f_i(k, \vec{R}) j}{k R_i^2} e^{-2k^2 \sigma_i^2} \sin(2k R_i + \phi_i(k, \vec{R})), \quad (2.26)$$

where the summation is carried out over both SS and MS paths.

## 2.7 Conventional EXAFS analysis

### 2.7.1 Extraction of EXAFS data

Before any analysis of EXAFS is possible, the fine-structure of X-ray absorption coefficient needs to be extracted from the measured data (total absorption

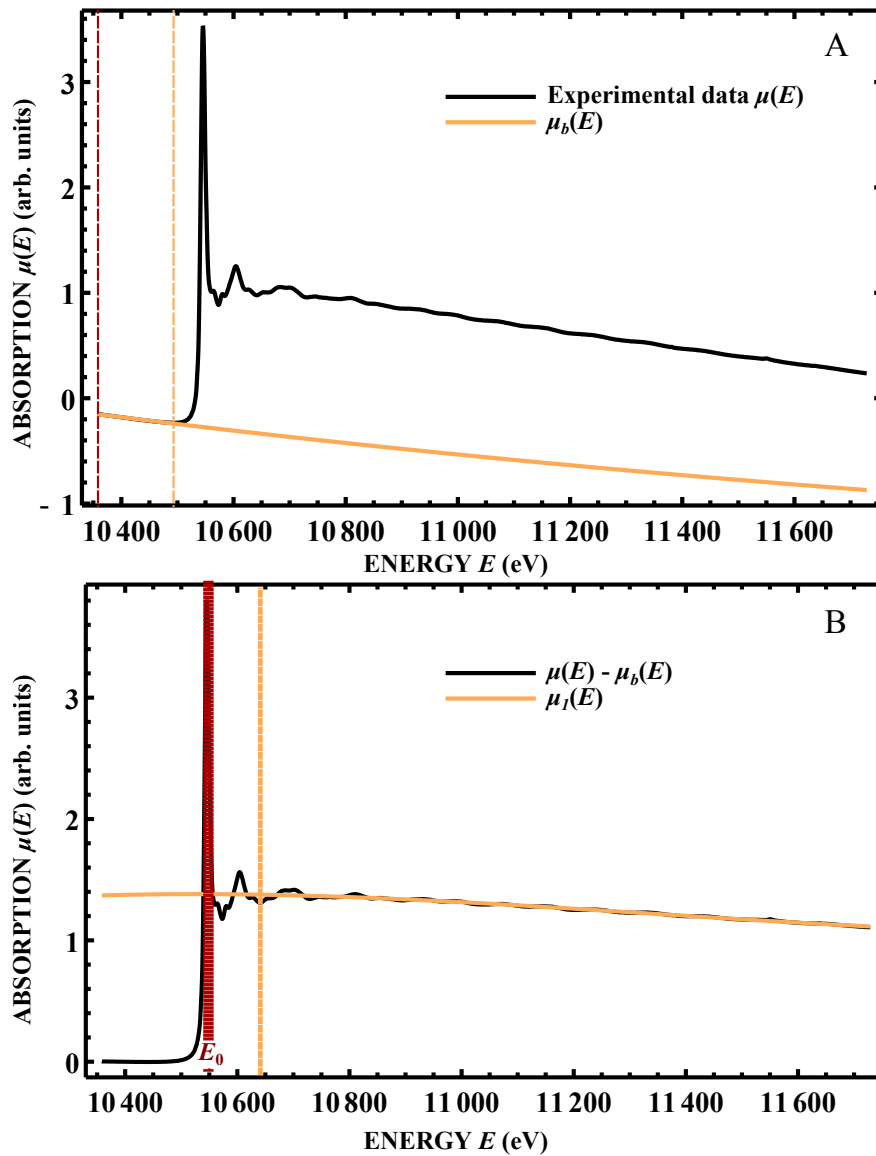


**Figure 2.7: Extraction of EXAFS spectra - I**

Extraction of the Re  $L_3$ -edge EXAFS spectrum for crystalline  $\text{ReO}_3$ : background removing (panel A) and polynomial smoothing in  $E$ -space (panel B).

coefficient as a function of the energy of incident radiation). For the cases, studied in this thesis, the extraction of EXAFS data was performed by the algorithm, implemented in EDA package by Alexei Kuzmin [40]. More interactive version of this algorithm was implemented by the author of this thesis in *Wolfram Mathematica* code.

At the first step, the contribution of all other absorption edges is removed from the absorption coefficient  $\mu(E)$ , measured near to the absorption edge of interest with corresponding energy  $E_0$ . This contribution is modelled as a function

$\mu_b = A + BE^{-3}$ , where coefficients  $A$  and  $B$  are obtained as best-fit estimates for the description of the smooth pre-edge part of measured spectrum (Fig.2.7-A).

Then the atomic-like contribution to the absorption should be removed. First of all, the data are approximated with cubic polynomial  $\mu_1(E)$  in  $E$ -space and this polynomial is subtracted (Fig.2.7-B). Then the spectrum is converted to the wavenumber ( $k$ ) space, using relation  $k = \sqrt{\frac{2m}{\hbar^2}(E - E_0)}$ . To emphasize features at large values of  $k$ , the spectrum can be multiplied with  $k^n$ , where  $n$  is usually 2 or 3. Such  $k$ -weighting also allows one to suppress oscillations in the XANES region that (i) are poorly described by the existing XAFS theory and (ii) are especially sensitive to the imperfections of the background subtraction and to the errors in the estimation of energy reference  $E_0$  [17, p.19].

Now data are approximated with another polynomial  $\mu_2(k)$ , and this polynomial is also subtracted (Fig.2.8-A). Finally, the spectrum is smoothed by Hodrick-Prescott-type filter [41] and the low-frequency contribution  $\mu_3(k)$  is removed (Fig.2.8-B).

The final EXAFS spectrum is obtained after normalization (Fig.2.8-C) as

$$\chi(k) = \frac{\mu - \mu_b - (\mu_1 + \mu_2 + \mu_3)}{\mu_1 + \mu_2 + \mu_3}. \quad (2.27)$$

### 2.7.2 EXAFS curve fitting

As conventional EXAFS analysis within this work we will refer to the curve fitting of EXAFS spectrum to experimental or theoretical standards using EXAFS equation (2.21). Radial distribution function  $g_i(\vec{R})$  in this approach is commonly approximated with Gaussian function (2.22), defined by mean value  $R_i$  and variance  $2\sigma_i^2$ . More complex approximation of RDF can be used in the so called cumulant expansion approach [2, 38, 39]. Structural parameters (interatomic distances  $R_i$  and MSD factors  $\sigma_i^2$ ), as well as amplitude correction coefficient  $S_0^2$  and photoelectron energy reference  $E_0$  are estimated from the least-squares fitting of experimental spectrum by EXAFS equation. Complex scattering function is calculated in *ab-initio* simulations, for instance, by program FEFF, or, in some cases, it can be extracted from the experimentally measured EXAFS spectrum for reference sample [6]. Fitting of the spectrum can be carried out either in  $k$ -space or in  $R$ -space. A number of computer codes exists today for such conventional approach to EXAFS analysis, for instance, EDA [40], FEFFIT [42], Artemis [43].

Due to the large number of fitting parameters and due to strong correlations between them, to obtain a stable result via conventional analysis, one should reduce the number of the degrees of freedom in the applied model [44]. As a result, (i) the contributions of distant coordination shells should be filtered out, (ii) all present thermal and static disorder effects should be described by only a few independent effective MSD factors, (iii) multiple-scattering effects should be neglected or treated using significant approximations. Therefore, as it turns out, the conventional EXAFS analysis can be reliably applied only to the treatment of EXAFS data from the first few coordination shells, often - from the first coordination shell only.

To avoid this problem and to obtain from EXAFS spectra much more information, simulation-based approaches, discussed in the next chapter, can be employed.

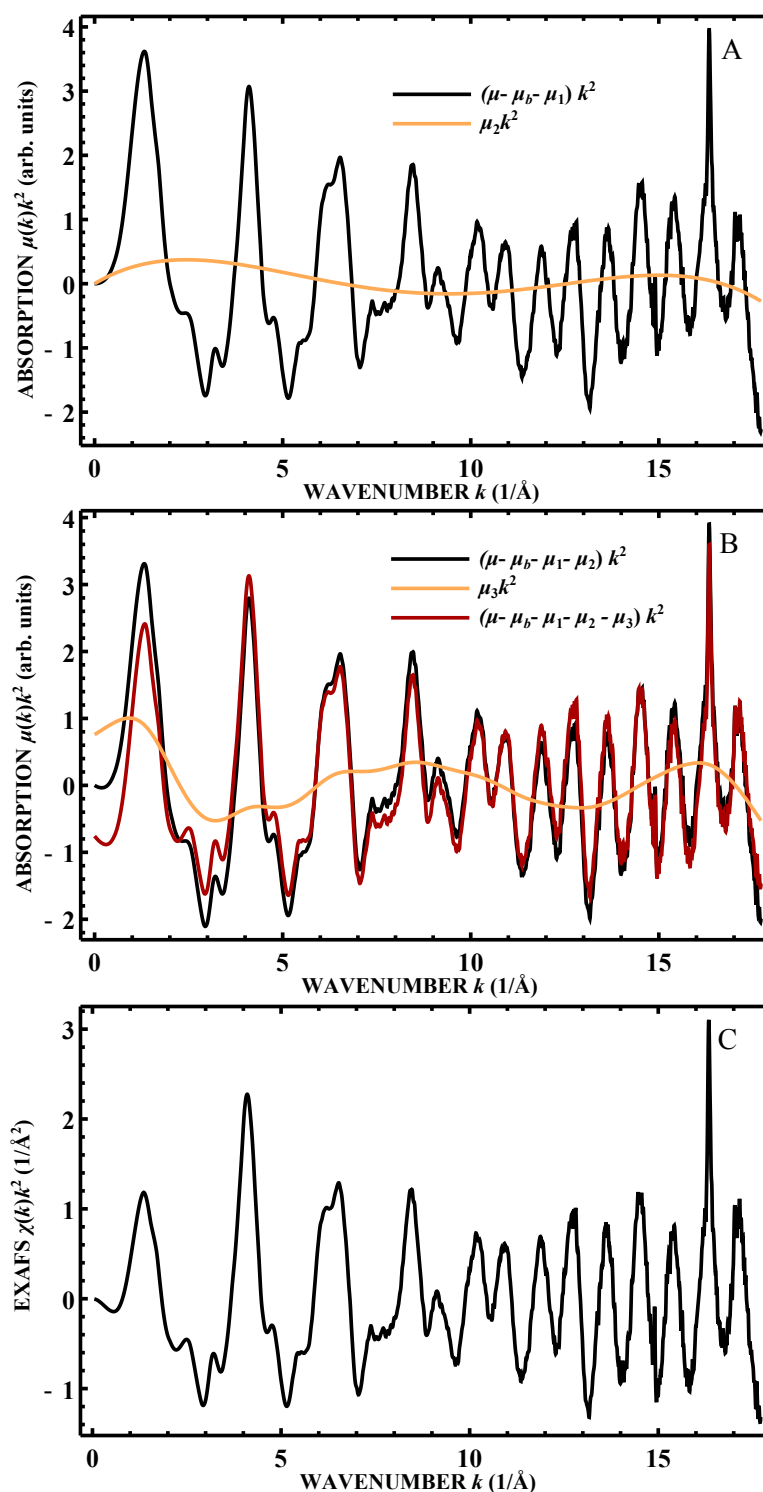


**Figure 2.8: Extraction of EXAFS spectra - II**

Extraction of the Re  $L_3$ -edge EXAFS spectrum for crystalline  $\text{ReO}_3$ : polynomial smoothing in  $k$ -space (panel A), Hodrick-Prezscott-type filtering (panel B) and final EXAFS spectrum (panel C). A narrow peak at  $\sim 16.2 \text{\AA}^{-1}$  is a glitch due to crystal monochromator.

## 3. SIMULATION-BASED EXAFS ANALYSIS

### 3.1 Introduction

The conventional EXAFS data treatment has been introduced in the previous chapter. Although this approach has been used for EXAFS analysis since 1970s, it has significant limitations, especially when applied to the studies of crystalline materials, due to the fact that EXAFS spectrum in this case may have quite complex structure, contributions of different scattering paths may overlap and thus the estimators of structural parameters are strongly correlated [44]. Therefore, as it was pointed out in the previous chapter, in most of the cases, the conventional EXAFS analysis is reliable for the studies of the first coordination shell only. Obviously, this results in the loss of significant amount of information, available, in principle, from experimental data. To make the analysis of EXAFS data more efficient and more accurate, new methods are required.

As for many other mathematically incorrect problems, to stabilize the model with many degrees of freedom that are used to parameterize EXAFS spectrum, one obviously needs to introduce some constraints. A natural set of constraints can be obtained by acknowledging that sought structural parameters are not actually independent - interatomic distances in the distant coordination shells are geometrically linked to the interatomic distances in the first coordination shells, the distributions of bonding angles are closely related to the distributions of atomic deviations, etc. To benefit from this purely geometrical information, we may reformulate the problem we are trying to solve - instead of directly fitting the average interatomic distances, MSD factors, etc., we can use as the unknown variables of our model the coordinates of atoms in a sufficiently large piece of investigated material. In this case we are trying to build a representative 3D-model of the material, for which the corresponding theoretical EXAFS spectrum can be calculated using existing *ab-initio* codes and then compared with the experimental data. If the constructed 3D model gives a good agreement between theoretically calculated and experimental spectra, then we may expect that the coordinates of atoms in the model represent the atomic configuration



of the real material. The values of structural parameters can be estimated afterwards by applying simple statistical analysis. This idea is common for all simulation-based approaches to EXAFS analysis. Due to the fact that instead of a problem with a relatively few unknowns (structural parameters) we are solving now a problem with hundreds and thousands degrees of freedom (atomic coordinates), such methods are usually much more computationally expensive than the conventional EXAFS analysis. At the same time the amount of information that one can extract by employing simulation-based approaches is essentially larger. The continuous growth of the popularity of simulation-based approaches in the last decades is closely related to the wide spread occurrence of high-performance computing systems [45].

Besides the geometrical constraints, different additional information in the analysis process can be introduced. Also the algorithms for the construction of the 3D model may be different, thus from the described basic idea very different techniques can be developed and applied to EXAFS analysis. The most well-known are molecular dynamics (MD), Monte-Carlo method (MC) and Reverse Monte-Carlo method (RMC). They are discussed in the following sections of this chapter.

## 3.2 Molecular dynamics

In a classical molecular dynamics approach a 3D time-dependent model of the investigated structure is obtained. For MD simulations one should specify an empirical force-field model  $V(\vec{r}_1, \vec{r}_2, \dots, \vec{r}_n)$ , i.e., some function that effectively describes the interactions between atoms in the materials (positions of atoms are given by vectors  $\vec{r}_1, \vec{r}_2, \dots, \vec{r}_n$ ). Force that acts on the  $i$ -th atom then can be calculated as  $\vec{F}_i = \nabla_{\vec{r}_i} V$ , and the motion of atoms can be modelled by numerical integration of classical Newton's equations, and, therefore, is fully deterministic. First MD calculations have been carried out already in 1950s [46, 47] for the simulations of phase transitions in the system of rigid spheres. Nowadays, MD is probably the most popular method for the modeling of large-scale atomic structures [48], and is widely used not only in the field of material science, but also, for instance, in biology and medicine [49].

In the early 2000's MD for the first time has been applied for the interpretation of EXAFS data. In the standard MD-EXAFS approach the results of MD

simulations - atom trajectories - are used as input for *ab-initio* calculations of EXAFS data: during the MD simulations a large number of atomic configurations is saved, and using *ab-initio* programs such as FEFF for each of these configurations one can calculate corresponding EXAFS spectrum. By averaging all these spectra a final, time-averaged EXAFS spectrum, which can be compared with the experimental data, is obtained [50, 51, 4]. Originally MD-EXAFS method has been applied to the studies of disordered systems, such as glasses [52, 53], solutions [54, 55], molten salts [50, 56]. Nevertheless, studies of our group have shown that also in the case of crystalline systems MD-EXAFS approach can be very useful: in [4] MD-EXAFS method is applied to the analysis of local structure around Ti atom in crystalline SrTiO<sub>3</sub>, in [57] - to the analysis of local structure around Co in crystalline LaCoO<sub>3</sub>, in [58] - to the analysis of local structure of crystalline germanium, in [59] - to the investigations of Re surroundings in crystalline rhenium trioxide, while in [60] - to the analysis of EXAFS data from sheelite-type compounds CaWO<sub>4</sub>, SrWO<sub>4</sub>, BaWO<sub>4</sub>. Finally, a novel trend is to apply MD-EXAFS analysis for the structure investigations of different nano-structured systems (in [61] MD calculations were combined with EXAFS analysis to investigate structure of platinum nanoparticles, while in the series of recent papers by our group [62, 63, 64, 65] MD-EXAFS method was applied to determine structure of NiO nanoparticles and to estimate the influence of oxygen vacancies).

The significant advantage of MD simulations for EXAFS analysis is that the time-dependent properties of the system, frequencies of atomic vibrations, interatomic forces can be directly accessed. The biggest problem, however, is that the precision of obtained results is fully determined by the precision of the used force-field model, and, unfortunately, for complex systems with low symmetry the precise force-field model cannot be found. Besides, since classical MD fully neglects the quantum effects in the system, it cannot be applied to model systems at low temperatures. A relatively new approach to treat these problems is to use *ab-initio* MD instead of classical MD simulations. In *ab-initio* MD the interactions between atoms are calculated from the solution of Schrodinger equation for electronic system. Obviously, such approach is extremely computationally expensive and currently can reliably be applied to investigate only small atomic clusters. For instance, in recent study [66], *ab-initio* MD-EXAFS method is applied for the structure investigations of gold nanoparticles with 147 Au atoms per particle.

### 3.3 Monte Carlo method

Monte Carlo (MC) technique incorporates a broad class of methods that can be used to solve different types of problems. The common idea of all Monte Carlo methods is to use random rather than deterministic process. The development of MC methods started in the 19th century, when random sampling has been applied to approximately solve different mathematical problems. For instance, in 1873 Asaph Hall, an American astronomer, proposed a method for the "experimental" determination of the number  $\pi$  using direct random sampling [67]. In fact, this method was based on an even older problem, the famous Buffon's needle problem, first posed in 18th century [68].

More systematic development of Monte Carlo methods began with the Second World War. In the 1930s Enrico Fermi proposed to use MC-type methods for the description of neutron diffusion in the different materials. In the 1940s Monte Carlo methods were investigated by Stanislaw Ulam and John Neumann, while both worked in Los Alamos laboratory at Manhattan Project. Significant progress in the development of MC methods started after the first electronic computer ENIAC was constructed in 1945 [69].

In 1953 Nicholas Metropolis published the paper [70] that began the applications of MC methods to the problems in the field of solid-state physics. In this paper 2D system of rigid discs has been studied. A force field, describing the interactions of such discs, was given and thus it was possible to calculate the total energy of system for each configuration of the discs. At each iteration a small and random shift of discs was proposed, and using the algorithm that later was named after Metropolis himself the proposed change of configuration was either accepted or rejected, and system slowly evolved to the state, where the distributions of discs corresponded to the Boltzmann's distribution. In the following decades the Metropolis algorithm turned to be at the heart of almost every implementation of MC method.

Nowadays MC method is widely used for the investigations of polymers and organic macromolecules (see, for instance, [71], [72]). Besides the classical Metropolis Monte Carlo very different modifications of this method have been developed, for instance, versatile quantum Monte Carlo methods that are applied to the studies of the electronic structure of different, but usually bosonic systems [73], kinetic Monte Carlo, designed for the modeling of system evolution in time, if the probabilities of different transitions are given [74], etc.

Conventional MC method suffers from the same drawbacks as classical MD: for calculations the force-field model is required. Additionally, due to the fact that the motion of atoms in MC is probabilistic rather than deterministic, the MC calculations usually are much more computationally expensive.

### 3.4 Reverse Monte Carlo method

To avoid the problems related to force-field model, at the end of 20th century a new simulation-based method for the determination of material structure has been developed - Reverse Monte Carlo (RMC). RMC was proposed by McGreevy and Pusztai in [75], where instead of the minimization of system energy, as in conventional MC, they proposed to minimize the difference between the experimental and numerically simulated X-ray diffraction data. In 1990 Keen and McGreevy published in *Nature* magazine the results of the RMC study of quartz, as experimental input simultaneously using both X-ray and neutron diffraction data [76].

RMC method has been applied for the first time to the studies of molten salts [77] and crystalline AgBr [78] from neutron diffraction data. The reconstruction of the three-dimensional structures of thirteen MX and MX<sub>2</sub> molten salts (M=metal and X=halide) allowed the authors to evidence the type of short-range order and for the first time to visualise intermediate-range order arising from a local density fluctuation [77]. The development of crystalline AgBr structure upon temperature increase from 490 K up to 703 K was investigated in [78] based on a relatively large 3D model, containing 4096 ions. RMC simulations revealed in this case the increase in distortion of the silver ions lattice, till it completely melted.

Finally, in 1990 also the paper by Gurman and McGreevy [5] was published, where instead of diffraction data the results of X-ray absorption spectroscopy have been used: for the first time the simulation-based analysis of EXAFS data using RMC approach was carried out. In this paper amorphous as well as crystalline silicon have been investigated. For RMC simulations a system with about 1000 atoms was modeled, calculations of EXAFS spectra have been carried out in single-scattering approximation. EXAFS data have been analyzed also using conventional approach (see Sec. 2.7.2). The difference between results, obtained via conventional procedure and via RMC simulations, was about 0.1 Å for inter-atomic distances and 0.002 Å<sup>2</sup> for MSRD factors.

In the following years Pusztai and McGreevy continued to employ RMC method, but mostly for highly disordered systems (liquids, glasses, amorphous samples) and for the interpretation of X-ray and neutron diffraction data [79, 80, 81]. In a recent study by Tucker et al. RMC method was applied to neutron diffraction data from  $\text{ZrW}_2\text{O}_8$  [82, 83] - a material, known for its negative thermal expansion (below room temperature its volume decreases upon heating), - and it was shown that the so called rigid unit model seems to be valid for this system<sup>1</sup>. In another very interesting paper [85] by Young et al. the neutron diffraction based RMC method was applied to study superconductor  $\text{YBa}_2\text{Cu}_3\text{O}_{6.93}$ , and it was established that two separate Cu–O bonds exists in this material [85]. In [86] this approach was applied for the studies of bismuth-based piezoelectrics. Review articles on the applications of RMC methods for the interpretation of diffraction signals from glasses were published by McGreevy in 2001 [45, 87], while a review on the applications of RMC methods for the interpretation of diffraction data from powders was published by Keen et al. in 2005 [88].

The simplicity of RMC algorithm is the reason of its widespread use, mostly for studies of disordered materials using diffraction data. For example, in [89] the RMC method is applied for the structure investigations of conductive glasses; in [90] - for the interpretation of X-ray diffraction data from amorphous hydrogenated silicon; in [91] - for the analysis of neutron diffraction data from liquid carbon and nitrogen monoxides; in [92, 93, 94] - for the X-ray diffraction analysis of Al-based alloys; in [95] - for high energy X-ray diffraction data from melts of  $\text{Ag}_2\text{Se}$  and  $\text{AgI}$ ; in [96] - for the neutron scattering study of liquid hydrogen and liquid mercury; in [97] - for the X-ray diffraction study of liquid gallium under pressure; in [98] - for the X-ray diffraction study of liquid  $\text{As}_2\text{Se}_3$  at high temperatures. In 2010 a powerful modification of the RMC method that was designed for the analysis of disordered systems with very large supercells, used to represent 3D structure model, was proposed by Cliffe and Dove in [99, 100]. Within this approach, called invariant refinement technique, the stability of solution was improved by demanding that the local environments should be similar for all atoms of given type.

A novel and very promising approach is to use RMC for the interpretation of the results of anomalous X-ray scattering data: in works by Hosokawa and

---

<sup>1</sup>The results, obtained by Tucker et al. for  $\text{ZrW}_2\text{O}_8$  have been commented recently by Bridges et al. [84]: in this paper  $\text{ZrW}_2\text{O}_8$  was investigated by means of X-ray diffraction and EXAFS at W  $L_3$  and Zr K-edges and it was concluded that the mechanisms, underlying the negative thermal expansion of this material are probably more complex.

coworkers [101, 102, 103, 104] such technique is applied for the investigations of Ge-Se alloys, amorphous  $\text{Ge}_2\text{Se}_2\text{Te}_5$ , semiconducting and metallic glasses. Recently, anomalous diffraction, combined with RMC method, was used by de Lima et al. for the determination of amorphous structure of  $\text{Ti}_{50}\text{Ni}_{25}\text{Cu}_{25}$  [105].

For the analysis of crystalline materials RMC method has been applied, for instance, in [106, 107, 108, 109, 110]. A very promising trend in the applications of RMC methods are the investigations of nanostructured materials. For example, in [111] RMC method is used together with high-energy X-ray diffraction for the investigation of ruthenium nanoparticles. Other notable examples of RMC applications to the analysis of nanopowders are [112, 113, 114]. In a recent paper [115] RMC simulations for several ferrihydrite nanoparticle models (spherical particles about 3.6 nm in diameter, containing approximately 800 iron atoms) were carried out and allowed one to find the model that gave the best agreement with available experimental (X-ray diffraction) data.

Despite the very pronounced dominance of diffraction data as input for RMC simulations, the application of RMC method to the analysis of EXAFS data also has been addressed in a number of works, for instance, [116, 117, 118, 119, 120, 121, 122, 123, 124, 125, 126, 127, 128, 129, 130]. Some of the most recent works in this field are studies by Kaban et al. [131, 132, 133, 134, 135, 136, 137, 138, 139, 140] (studies of Ge-Se-Te alloys,  $\text{AsS}_2$ -Ag glasses, Cu-doped Ge-Te glasses, AgI-doped Ge-I-S glasses, Ge-As-Se glasses, Ge-As-Te glasses, Fe-Nb-B metallic glasses, Ni-Zr and Cu-Zr alloys), works by Kumara [141] (study of superionic glass  $\text{Ag}_x(\text{GeSe}_3)_{1-x}$ ), Oliveira [142] (study of  $\text{Se}_{90}\text{P}_{10}$  alloy) and Antipas [143] (study of  $\text{GeSe}_4$  and  $\text{GeSe}_4\text{In}_5$  metallic glasses). In the works by Yang and co-workers, X-ray scattering and EXAFS data were used to run RMC simulations for the studies of atomic packing and glass-forming abilities of Cu-Zr alloys [144, 145, 146]. In [147] by Tupy et al. RMC method was applied for the analysis of EXAFS data from NiPt nanoparticles. In [148] by Kurt et al. RMC modelling of  $\text{Mn}_2\text{Ru}_x\text{Ga}$  thin films using simultaneously EXAFS data from Mn, Ga and Ru K-edges was performed. Gaseous and liquid systems ( $\text{Br}_2$ , liquid copper, liquid nickel) are investigated using RMC-EXAFS methods in works by Di Cicco et al. [119, 120, 130] (special attention in these works is paid to the many-atomic effects).

As one can see, usually in these works disordered systems are studied, and as input for RMC scheme EXAFS data are used along with the results of diffraction experiment: in the case of the systems with strong disorder EXAFS spectrum

alone contains only a very limited information [3, 121]. Also, EXAFS calculations are carried out mostly in single-scattering approximation, therefore the accurate analysis is possible for the first coordination shell around the absorber atom only (often in the case of disordered systems the contribution from the first coordination is actually the only present contribution at all, in other cases contributions from further coordination shells in SS approach need to be removed by, for instance, Fourier filtering [118]).

The importance of multiple-scattering effects was emphasized by Di Cicco and coworkers in [119] and [120]. In these studies the Cu K-edge EXAFS data from liquid copper were investigated, and it was shown, by taking into account MS effects one can access information on many-atomic distribution functions and distributions of bonding angles. One should note, however, that the MS analysis of crystalline data is computationally much more challenging task than the one of disordered systems due to the exponentially larger number of scattering paths that should be taken into account.

For perovskite-type structures RMC calculations for the first time have been carried out by Krayzman, Levin and Tucker [149, 150, 151, 152, 153]. In 2008 they published paper [149], where RMC simulations have been carried out for the solid solution  $\text{Ca}(\text{Zr},\text{Ti})\text{O}_3$ . As experimental data in this study pair-distribution functions from neutron and X-ray diffraction and also EXAFS spectra have been used. EXAFS simulations have been carried out in single-scattering approximation. The authors managed to reconstruct the pair distribution functions quite well, however, it turned out that many-atomic distribution functions, such as bonding angle distribution functions, are reproduced imprecisely. In 2009 this group of scientists published a results, obtained for another perovskite-type compound -  $\text{SrAl}_{1/2}\text{Nb}_{1/2}\text{O}_3$  [150]. For RMC simulations in this study a very large 3D model with 20480 atoms was used, and in EXAFS calculations also the influence of multiple-scattering effects was taken into account, however, in an approximate way: authors assumed that complex scattering functions are independent on the interatomic distances, and these functions for different values of bonding angles had been tabulated before the main RMC calculations, and later were just linearly interpolated. The further development of ideas, proposed in that study, was given by Nemeth et al in [152]. In 2010 Krayzman and coworkers carried out RMC simulations for perovskite  $\text{AgNbO}_3$ , with the goal to study the local displacements of Nb ion [151]. Obtained results contradicted with the existing results from electron diffraction studies, thus for the following calculations in the

list of experimental data, used for RMC simulations along with X-ray and neutron diffraction, and EXAFS data, also the results of electron diffraction were included. In 2013 this complex approach was applied to investigate the local structure of  $\text{Ba}_{1-x}\text{Ca}_x\text{TiO}_3$  and  $\text{Ba}_{1-x}\text{Sr}_x\text{TiO}_3$  solid-solutions [153].

For structure determination using RMC method a number of codes exists and are available. Most popular are RMC.POT (development of RMC++ code) [124], designed mostly for the studies of disordered systems, and RMCProfile [154], designed for the analysis of powders. Both of these codes are mostly focused on the analysis of diffraction data, however, the EXAFS data can be provided as additional information. In both of these codes EXAFS calculations are carried out neglecting the dependence of the complex scattering function on interatomic distances. The RMC code, used by Krayzman and coworkers, that allows also the approximate treatment of MS contributions, is an extension to RMCProfile [149]. Another RMC code that treats the MS effects is SpecSwap-RMC code [129]: in this case relevant local structures, for which the full EXAFS spectrum is precalculated, are chosen, and later, during the main RMC simulations, total EXAFS spectrum is expressed just as a combination of such precalculated contributions. SpecSwap-RMC code is mostly designed for RMC-EXAFS studies of disordered systems [129].

Finally, it should be mentioned that along with "pure" RMC, MC and MD methods, different combinations of these techniques exist. One of such approaches is to use RMC calculations to construct the radial distribution functions, which later can be used to estimate parameters of interatomic force-field model that can be employed for MD or MC simulations. Currently this approach is applicable only for simple systems, where the force-field can be described by combination of pair potentials. Analysis of such cases is given, for instance in [155] and [156]. At the same time, existing knowledge on interatomic interactions can be used to avoid nonphysical solutions in the conventional RMC calculations. This combined MD-RMC approach is referred as hybrid RMC or empirical potential structure refinement. It was employed, for instance, in [157, 48, 158, 159, 160, 161]. Somehow more sophisticated approach is to combine RMC method with *ab-initio* MD: in [162], for example, RMC method is employed to create initial atomic configuration of  $\text{Ga}_{11}\text{Ge}_{11}\text{Te}_{78}$  that is used as input for consequent *ab-initio* MD simulations, in [163, 164] similar approach is applied for  $\text{Ge}_x\text{As}_y\text{Se}_{1-x-y}$  glasses, in [165] - for  $\text{CaO-Al}_2\text{O}_3$  glasses. An opposite idea was realized in [166] for study



of amorphous  $\text{Ge}_{15}\text{Te}_{85}$ , where the results of *ab-initio* MD simulations provided additional constraints for X-ray and neutron diffraction-based RMC.

To conclude, RMC method is a well established approach for structure investigations. Currently, however, all existing RMC implementations are focused on the analysis of diffraction data and/or on studies of disordered systems. The possibility to apply RMC analysis to the treatment of EXAFS data from crystalline systems taking into account all MS effects, is, in turn, weakly explored due to the significant computational complexity of such task. The goal of the presented thesis is to contribute to the advancement of this field and to provide a versatile and computationally efficient tool for RMC-EXAFS analysis of the local structure of crystalline materials. The description of the developed method is given in the next chapter.

## 4. REVERSE MONTE-CARLO/EVOLUTIONARY ALGORITHM METHOD FOR EXAFS ANALYSIS

### 4.1 Introduction

In this chapter we will discuss in details the approach, developed by the author of the thesis for the analysis of EXAFS data for crystalline materials. The problem that we are trying to solve here is to obtain physically meaningful information on lattice structure and dynamics from the corresponding EXAFS spectrum, without using additional input such as empirical force-field models.

Nowadays there are a number of *ab-initio* codes available that, knowing the structure and dynamics of the system, allow one to calculate the corresponding theoretical EXAFS spectrum (FEFF [25] and GNXAS [167] codes are the most popular). The agreement between the results of such calculations and experimentally measured EXAFS data is usually good [2]. The problem that we are interested in, however, is an inverse problem: we will try to find such model of crystal structure and lattice dynamics that the corresponding calculated EXAFS spectrum is as close to the experimental data as possible.

In the conventional EXAFS analysis (Sec. 2.7.2) the model is set by specifying the distributions of distances between the absorbing atom and its closest neighbours. Usually it is assumed that these distributions are described by Gaussian functions, hence the only variables of such model are average interatomic distances and the variances of interatomic distances (MSRD, i.e., mean-square relative displacement factors).

In the simulation-based EXAFS analysis (Chapter 3) to employ the constraints set by geometrical considerations, the structure model is formulated directly in the terms of atomic coordinates: the variables are just  $x$ ,  $y$  and  $z$  coordinates of each atom in the simulated cell. The number of atoms in the cell should correspond to the experimental value of atomic number density. In the case of crystalline material such cell is often called a "supercell", since it consists of several unit cells. To avoid the surface-related effects the periodic boundary conditions (PBC) are applied. The supercell should be chosen large enough to

represent the structure of the material. The interatomic distances and MSD factors can be estimated afterwards from the sets of obtained coordinates for atoms within the supercell. As it was mentioned previously, while in the MD-EXAFS approach the variation of atomic coordinates during the simulations is governed by Newtonian equations of motion, in the RMC-type approaches the displacements of atoms are determined by a random process with the aim to minimize the disagreement between calculated and experimentally measured EXAFS data.

It is interesting to note that, in principle, the problem we are trying to solve - the extraction of relevant structural information from experimental data - is similar to the one that is treated by the so called computer vision methods, only in our case the input is not a visual image of macroscopic object, but the X-ray absorption spectrum. Nevertheless, the challenges, or so called "curses" that are formulated in the computer vision field, are also applicable for the RMC-type EXAFS analysis. The **curse of dimensionality** refers to the fact that the case we are trying to solve (i.e., the local structure of sample) is an essentially high-dimensional problem, and to completely characterize the investigated system the enormous amount of variables is required; at the same time the amount of available data is limited. The **curse of non-linearity** refers to the problem that the input data (i.e., EXAFS spectra) depends on the variables of system (atomic coordinates) in a strongly non-linear way. The problem that the disagreement between the calculated and experimental EXAFS data is a function of system variables that has many local minima, while we are interested in the global minimum only, is sometimes called the **curse of non-convexity**.

The reverse Monte Carlo/evolutionary algorithm (RMC/EA) implementation, presented in this thesis, is designed to minimize the influence of these "curses". The keys to the problem are (i) to reduce the number of involved variables and to reduce the size of configurational space to be explored (i.e., to use relatively small supercell and to constrain atomic displacements), (ii) to use efficient optimization algorithms, (iii) to employ fast algorithms to calculate theoretical EXAFS spectra as functions of atomic coordinates and (iv) to implement novel approaches of signal processing to extract from the available EXAFS spectra as much information as possible. To sum up these principles, the four main building blocks of our RMC-type method for the analysis of EXAFS data now can be identified:

1. ***Ab-initio* EXAFS calculations:** as it has been said, excellent codes for the simulations of EXAFS data are available; in our implementation we use program FEFF8 for this purpose. As it is the most time-consuming part of

simulations, it is necessary, however, to reduce the required number of FEFF calculations as much as possible. Therefore, first of all, in the present study we carefully examine the importance of all scattering paths and employ high-dimensional *clustering algorithms* to agglomerate similar paths. These issues are discussed in Sec. 4.4. Secondly, the calculations of EXAFS spectra are parallelized, to employ the potentiality of multiprocessor systems.

- 2. Signal processing:** the noise should be removed from the experimental EXAFS data; additionally, the conventional *Fourier transform* can be used to separate contributions from different coordination shells. However, in this study we demonstrate that the use of novel *wavelet transform* is preferable, since it gives the representation of the analyzed signal in real and frequency spaces simultaneously and provides more information, allowing one to better discriminate different contributions to the total EXAFS spectrum (Sec. 4.3);
- 3. Optimization algorithms:** structure model that gives the best agreement between calculated and experimentally measured EXAFS data can be obtained by performing a search for global minimum in high-dimensional space. The *reverse Monte Carlo method*, based on *Metropolis algorithm*, is a widely acknowledged tool for this purpose. In this study we employ for the first time for simulation-based EXAFS analysis a much more efficient approach based on *evolutionary algorithm* (EA). The convergence of the optimization process both in our RMC and EA implementations is controlled by *simulated annealing* scheme. See Sec. (4.2) for details;
- 4. Postprocessing of obtained results:** the information on interatomic distances, bonding angles, amplitudes and correlations of atomic motion, etc., should be extracted from the obtained set of atomic coordinates; since we are dealing with relatively small supercells, the statistics is rather poor and *robust statistics methods* should be employed at this stage (Sec. 4.5).

These four blocks are implemented in the original EvAX (Evolutionary Algorithm for XAS data analysis) code, a program, written in C++ language and designed for the efficient analysis of EXAFS data from crystalline material on high power computer systems. The basic elements of the EvAX algorithm are emphasized in Fig. 4.1. A more advanced postprocessing of obtained results is

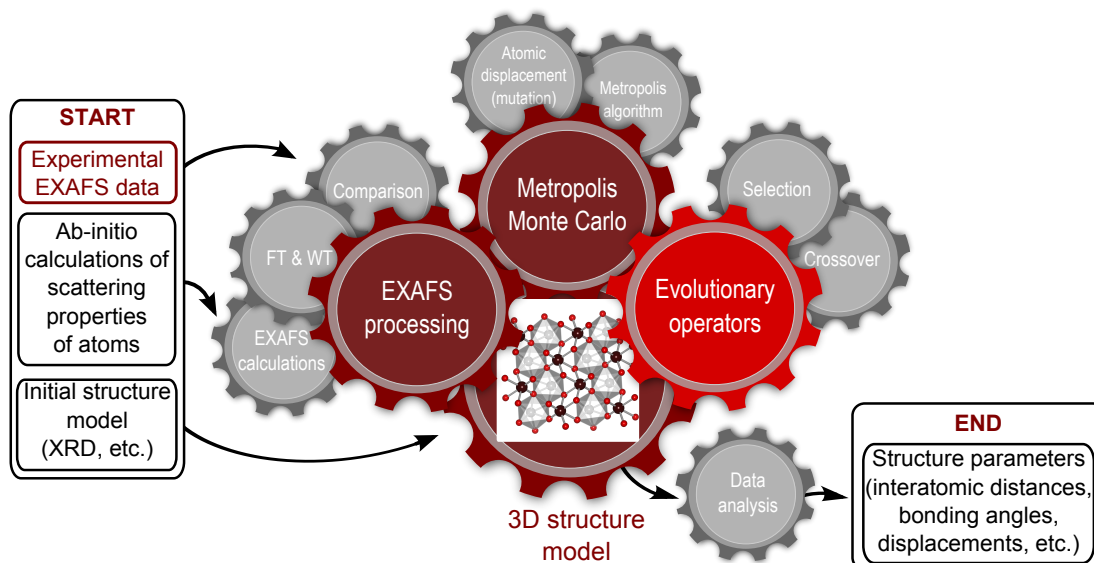


**Figure 4.1:** Schematic representation of the EvAX algorithm

also realized as a set of interactive tools, created in *Wolfram Mathematica* environment.

In further sections of this chapter we give a detailed description of the main blocks, listed above. All necessary information regarding usage of the EvAX program is given in the user's manual (Appendix A).

## 4.2 Optimization algorithms: RMC and evolutionary algorithm

### 4.2.1 Reverse Monte Carlo basics<sup>1</sup>

Reverse Monte Carlo (RMC) method is a simulation technique, proposed by McGreevy and Pusztai in the late 1980's, to determine a 3D model of the atomic structure of material by minimizing the difference between its structure-related experimental and calculated properties [75]. Here we will describe the basics of the conventional RMC algorithm, and also emphasize the peculiarities of our implementation. More details on the conventional RMC scheme can be found in [45, 168].

<sup>1</sup>The material, presented in Secs.4.2.1 - 4.2.3, has been partially published as J. Timoshenko, A. Kuzmin, J. Purans, REVERSE MONTE CARLO MODELLING OF THERMAL DISORDER IN CRYSTALLINE MATERIALS FROM EXAFS SPECTRA, *Comp. Phys. Commun.* 183 (2012) p. 1237-1245

RMC simulation starts with an arbitrary initial configuration of atoms in a cell of chosen size and shape with periodic boundary conditions, for which the total EXAFS spectrum  $\chi_{\text{tot}}(k)$  is calculated as described below in Sec. 4.4.

Next, the atomic configuration is modified by randomly changing the coordinates of one or several atoms, thus producing a new atomic configuration, for which the total EXAFS spectrum  $\chi_{\text{tot}}^{\text{new}}(k)$  is calculated. The two calculated EXAFS spectra  $\chi_{\text{tot}}^{\text{old}}(k)$  and  $\chi_{\text{tot}}^{\text{new}}(k)$  are compared with the experimental one  $\chi_{\text{exp}}(k)$ , and the new atomic configuration is either accepted or discarded depending on the results of this comparison (see the next Subsection for details). The procedure is repeated as many times as needed till the atoms in the cell will occupy such positions that the difference  $\xi$  between theoretical  $\chi_{\text{tot}}(k)$  and experimental  $\chi_{\text{exp}}(k)$  EXAFS spectra is minimized.

In the case of crystalline systems the equilibrium structure is usually known: the lattice parameters of crystalline material can be determined by diffraction techniques with much higher accuracy (better than  $10^{-3}$  Å), compared to that provided by modern EXAFS analysis (usually about  $10^{-2}$  Å). Therefore in our approach the RMC simulation of EXAFS spectrum for a crystal is performed using a fixed supercell size, defined by the lattice parameters, and by initial placing of atoms at proper Wyckoff positions. This allows us to account for the information available from diffraction data without direct simulations of diffraction pattern. However, small random initial displacements for all atoms can be given to include approximately thermal disorder and, thus, to avoid the rapid changes of residual at the beginning of RMC iteration process. The shape of the supercell is determined by the crystal symmetry and is not obligatory cubic.

EXAFS method is sensitive to the local atomic structure (usually up to 10 Å around the absorbing atom) due to the restrictions imposed by the life time of the excitation and thermal disorder. Therefore, in a periodic system one can probe and needs to account for a relatively small amount of atoms in a rather small cell, whose size should be at least twice the largest radial distance in the Fourier transform of EXAFS spectrum. This means that for the simulations of EXAFS spectra from crystalline materials a supercell containing a few hundreds of atoms should be sufficient. For the most of calculations, presented in this thesis, the supercell consisting of  $4 \times 4 \times 4$  unit cells has been used. To compare, the number of atoms, required for the RMC modelling of disordered materials, is at least 1000 [87].

Once the initial atomic configuration is chosen, one should define the procedure for its modification using random atom displacements. For this purpose at each RMC step one can either randomly pick one atom and randomly change its coordinates, or can randomly modify coordinates of all atoms. In this work the latter approach is adopted. The generation of pseudo-random numbers here and everywhere else in our program is performed using the Mersenne-Twister algorithm [169]. The Mersenne-Twister algorithm is a common choice for many Monte Carlo implementations due its speed, long repetition period and good statistical randomness of the generated numbers [170].

In the real crystals the displacements of atoms from their equilibrium positions due to thermal vibrations are normally less than a few tenths of angstrom. Therefore, in the present work we constrain the displacements of atoms from their equilibrium positions that are known from diffraction experiments to be smaller than some given value  $\delta_{\max}$ .

#### 4.2.2 Metropolis algorithm

Here we discuss the algorithm that determines, whether the atomic configuration, proposed at some RMC iteration (i.e., obtained after atomic displacements), should be accepted or discarded. For this algorithm one needs to compare the theoretically calculated and experimental EXAFS data. In Section 4.3 different approaches for such comparison are discussed in details. At this point let us just assume that the quantity, characterizing the difference between two spectra, is known and is denoted by  $\xi$ .

Let the differences between total calculated and experimental EXAFS spectra for the current and new atomic configurations be equal to  $\xi^{\text{old}}$  and  $\xi^{\text{new}}$ , respectively. It is clear, if  $\xi^{\text{new}} < \xi^{\text{old}}$ , the proposed atomic configuration is better than the previous one and should be accepted. However, if we discard all atomic configurations for which  $\xi^{\text{new}} > \xi^{\text{old}}$ , the difference  $\xi$  will always decrease and after some number of steps it will reach the *local* minimum. In order to ensure that the *global* minimum is found, it is necessary to accept some of the atomic displacements for which  $\xi^{\text{new}} > \xi^{\text{old}}$ . Such strategy is realized in the most popular algorithm of the movement acceptance/discarding, proposed by Metropolis [70]:

$$\begin{aligned}
&\text{if } \xi^{\text{new}} < \xi^{\text{old}}, \text{ the move is accepted;} \\
&\text{if } \xi^{\text{new}} > \xi^{\text{old}}, \text{ the move is accepted, if} \\
&\quad \exp(-(\xi^{\text{new}} - \xi^{\text{old}})/T) > r, \\
&\quad \text{and discarded otherwise}
\end{aligned} \tag{4.1}$$

where  $r$  is a pseudo-random number in the range between 0 and 1, and  $T$  is a scaling parameter.

It can be relatively easily shown, if one allows the atoms to move accordingly to Metropolis algorithm with fixed value of parameter  $T$  for sufficiently long time, values of the  $\xi$  will fluctuate around its minimal value accordingly to Boltzmann distribution  $P(\xi) \sim e^{-\xi/T}$  [171] (see Fig. 4.2-A). If we denote by  $w_{i \rightarrow j}$  the probability of the transition from the state  $i$  to the state  $j$ , where, for instance,  $\xi_j < \xi_i$ , then for Metropolis algorithm  $w_{i \rightarrow j}/w_{j \rightarrow i} = e^{\xi_i - \xi_j}$ , i.e., it is equal to the ratio of the probabilities to find system in states  $j$  and  $i$ , given by  $P(\xi_j)/P(\xi_i)$ . The condition  $w_{i \rightarrow j}/w_{j \rightarrow i} = P(\xi_j)/P(\xi_i)$  is known as detailed balance condition. Now if we look at the time-evolution of the probability to find system in state  $i$ , we can write  $P_i(t+1) = P_i(t) + \sum_j w_{j \rightarrow i} P_j(t) - \sum_j w_{i \rightarrow j} P_i(t)$ , where the first sum describes the probability to arrive at state  $i$  from all other possible states, while the second sum - the probability to leave the state  $i$  to any other state. From the detailed balance condition we can write now,  $P_i(t+1) = P_i(t) + \sum_j w_{i \rightarrow j} P_i(t) - \sum_j w_{i \rightarrow j} P_i(t)$ , i.e.,  $P_i(t+1) = P_i(t)$ , therefore the Boltzmann distribution indeed is the stationary distribution that corresponds to transitions, defined by Metropolis algorithm.

The fact that the distribution of  $\xi$  is Boltzmann distribution means that at some arbitrary time moment the system most likely will be close to the state where  $\xi$  is close to its minimal value. The standard deviation - the characteristic width of the Boltzmann distribution - is given by parameter  $T$ . Therefore, if  $T$  is large, the system will fluctuate around the global minimum with a large amplitude. On the other hand, if parameter  $T$  is small, we again will discard all the moves that increase the difference  $\xi$ , and the simulation will get stuck at some local minimum. For RMC simulations the conventional approach (see, for example, [5]) is to set the value of  $T$  to be proportional to the noise level of experimental data, and usually it means that the value of  $T$  is rather small. The alternative solution, implemented in our code, is to use so called simulated annealing approach.



### 4.2.3 Simulated annealing

#### 4.2.3.1 Convergence issues

In the simulated annealing approach [172], the parameter  $T$  is not fixed but decreases slowly. One starts with a large value of  $T$  to stimulate a fast approach to the global minimum. Then the parameter  $T$  decreases, so that the fluctuations of the system are damped. At the end of the simulation,  $T$  is equal to 0 and, if the annealing has been carried out slowly enough, the system reaches the global minimum. The efficiency of this approach strongly depends on the so-called "cooling schedule" - the function that controls the decrease of  $T$  during the simulation. Popular cooling schedules are, for instance, the so-called Boltzmann annealing schedule, where  $T(t) \sim 1/\log(t)$ , or the Cauchy annealing scheme, where  $T(t) \sim 1/t$ , and many others are known [173]. For each particular problem one or another algorithm can be considered as the optimal, and also the optimal values of parameters for each schedule are different for different problems. Even if the problem we are trying to solve is only slightly modified (for example, one increases the size of the used supercell), the significant changes of the cooling schedule may be required.

Regardless of the cooling scheme we have chosen, one parameter always plays a crucial role: the length of the schedule  $t_{\max}$ , i.e., the number of iterations till the parameter  $T$  reaches zero. In fact, with any reasonable cooling scheme the global minimum can be found, if the length of the schedule is chosen long enough. Of course, since this parameter determines the length of our calculation, we are also interested to keep it as small as possible.

While some (complicated) theoretical results for special cases are available, in practice the prediction of the optimal  $t_{\max}$  value for arbitrary RMC calculation is an unsolved problem. In any case  $t_{\max}$  can be obtained empirically by trial and error method. But it obviously would be useful to have at least some insight on how the once found and good  $t_{\max}$  value should be changed, if we change some other parameters of our calculations.

One of the quantities that could characterize the  $t_{\max}$  value is the time, required to visit the global minimum at least once, starting from some arbitrary point in configuration space [174]. Let us start simple - with one variable  $x$  in one dimension (Fig. 4.2-B). The initial value of  $x$  let us denote by  $x_0$ . Additionally, let us assume that the value of  $x$  can change only discretely - at each iteration it can be increased/decreased by  $\delta$ , or remain unchanged, so there are  $d = 3$  possible

values  $x_{\text{new}}$  that can be proposed. At each iteration we calculate the difference  $\xi$  between the experimental spectrum and the theoretical spectrum. Let  $\Delta$  be the largest possible change of  $\xi$ , if  $x$  increases/decreases by  $\delta$ . Now if the global minimum of the  $\xi$  corresponds to  $x_{\text{global}}$  that is  $n = |x_{\text{global}} - x_0|/\delta$  steps away from the initial point, the probability that the system goes directly from  $x_0$  to  $x_{\text{global}}$  is  $P > (d^{-1}e^{-\Delta/T_{\text{min}}})^n$  (here  $T_{\text{min}}$  is the lowest value of scaling parameter  $T$  that we had during this process). It means, if we  $N = (d^{-1}e^{-\Delta/T_{\text{min}}})^{-n} = d^n e^{n\Delta/T_{\text{min}}}$  times put the system in  $x_0$  and allow it to perform  $n$  moves, it likely will visit the global minimum. Now, if we recall that  $x_0$  is some arbitrary point and the process, described here, is, in fact, so called Markov chain, i.e., the following value of  $x$  depends only on the current value of  $x$ , then it is not necessary after each  $n$  iterations to reset our value of  $x$  to the same  $x_0$ . We can just allow the system to move through the configuration space, and still in  $N = d^{\tilde{n}} e^{\tilde{n}\Delta/T_{\text{min}}}$  iterations we, likely, will visit the global minimum (here  $\tilde{n} = R/\delta$ , and  $R$ , in turn, is the typical distance between some point in configuration space and the point of global minimum) [174].

This argument can be easily generalized for the case of many dimensions (Fig. 4.2-C): if we have  $k$  variables, we can make  $x$  to be a point in  $k$ -dimensional space, where coordinates of the point are all the variables that characterize given system. Assuming for simplicity that all of the variables still are changing discretely and can either increase/decrease by  $\delta$  or remain the same, we obtain that the total number of all possible  $x_{\text{new}}$  points that can be reached in one iteration from given  $x$  is significantly larger than in 1D case, and is equal to  $d = 1 + 2^k \approx 2^k$  for the  $k \gg 1$  case (for the 2D case in Fig. 4.2-C these points are denoted by red frame). Now we expect the global minimum point to be visited in  $N = \frac{1}{c} d^{\tilde{n}} e^{\tilde{n}\Delta/T_{\text{min}}}$  iterations. The additional factor  $c$  refers to the fact that points  $x_0$  and  $x_{\text{global}}$  now are connected by many paths with the same length (for the 2D case in Fig. 4.2-C some of these paths are shown by black arrows). One can

obtain that this number of equivalent paths is equal to  $c = \frac{\left(\sum_{i=1}^k n_i\right)!}{\sum_{i=1}^k n_i!} \approx \frac{(\tilde{n})!}{k(\tilde{n}/k)!}$ ,

where  $n_i$  is the length of the projection of the paths on  $i$ -th dimension. For our purposes, however, one needs just to note that  $c \ll 2^{kn}$ .

One ends up with

$$\ln N \approx \frac{R}{\delta} \left[ k \ln 2 + \frac{\Delta(k, \delta)}{T_{\text{min}}} \right]. \quad (4.2)$$

From this result a number of conclusions can be drawn:

1. One can see, for example, if we perform calculations with a fixed value of scaling parameter  $T$  that is too low, the required computational time will grow as  $\sim e^{1/T}$ .
2. We can analyze the influence of the maximal change of a variable per one iteration  $\delta$ : we can expand  $\Delta(\delta, k)$  as  $\Delta(\delta, k) = \alpha_1(k)\delta + \alpha_2(k)\delta^2 + \dots$ , and now it is easy to see, if  $\delta$  is too small, the required computational time will grow rapidly as  $\sim 2^{\frac{kR}{\delta}}$ , but if, in turn,  $\delta$  is too large and with  $\alpha_2(k) > 0$ , the required computational costs will also grow (as  $\sim e^{\frac{R\alpha_2(k)\delta}{T_{\min}}}$ ). So, in order to optimize the calculation process, it is crucial to find the optimal value of parameter  $\delta$ .
3. If we increase the size of our configuration space (characterized by the quantity  $R$ ), the required computational costs will grow exponentially. Therefore the restrictions for the maximal allowed displacements of the atoms from their equilibrium positions should be applied.
4. Perhaps, an even more important conclusion that can be made from Eq. (4.2) is that the increase of the number of variables (i.e., the number of atoms)  $k$  will lead also to the exponential growth of the required computational time. Therefore the chosen supercell should be as small as possible.

#### 4.2.3.2 Simulated annealing schemes

In the EvAX program two different simulated annealing schemes are implemented: one, more conventional, is based on the adjustment of scaling parameter  $T$  with fixed maximal value for the change of parameters  $\delta$ . The second simulated annealing scheme primarily changes the value of  $\delta$ .

By looking at Eq. (4.1), one can note that parameter  $T$  is equal to  $-(\xi^{\text{new}} - \xi^{\text{old}})/\ln p$ , where  $p$  is the probability to accept a move with  $\xi^{\text{new}} > \xi^{\text{old}}$ . Now we can rewrite the equation for  $T$  as

$$T(t) = -\Delta(t)/\ln p(t), \quad (4.3)$$

where  $\Delta$  is the average change of the difference between theory and experiment per RMC/EA step and  $t_{\text{max}}$  is annealing duration. The parameter  $\Delta$  can be obtained automatically during the simulations by averaging the differences  $(\xi^{\text{new}} -$

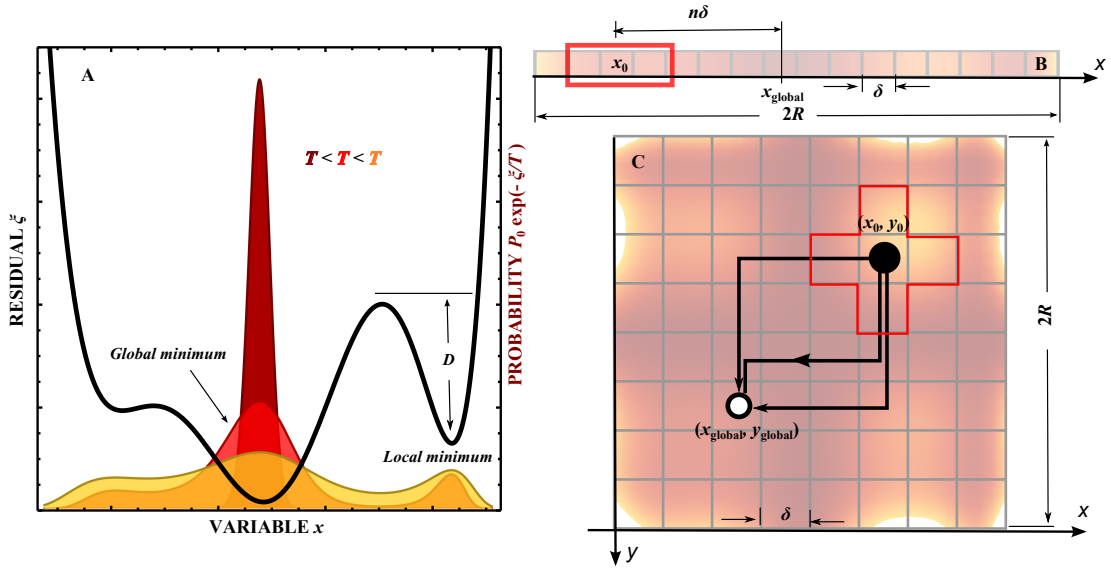


**Figure 4.2: Convergence of RMC schemes**

Residual  $\xi(x)$  for one dimensional case (black line in panel A) and corresponding stationary distributions of  $\xi$  for different values of scaling parameter  $T$  (color lines in panel A); schematic representation of discretized global-search problem in one dimension (panel B) and in two dimensions (panel C) (see details in text).

$\xi^{\text{old}}$ ). The value of  $\Delta$  depends on the system parameters (for example,  $\Delta$  is smaller for systems with larger number of atoms).

For the first simulated annealing scheme let us assume that at the beginning of simulation  $p(0)=1$ , i.e., all proposed moves are accepted, but at the end of simulation  $p(t_{\text{max}})=0$ , and in between  $p$  changes linearly:  $p(t) = 1 - t/t_{\text{max}}$ .

According to the Hajek theorem [175, 176], the simulated annealing algorithm converges if  $\sum_{t=1}^{\infty} \exp[-D/T(t)] = \infty$ , where  $D$  is a positive constant that characterizes the maximal height of the barrier that must be overcome to escape from local minima (see Fig. 4.2-A). In other words - the global minimum can be found if at any time moment there is a non-zero probability for the system to escape every local minimum. In our case, this condition can be rewritten as

$$\lim_{t_{\text{max}} \rightarrow \infty} \sum_{t=1}^{t_{\text{max}}} (1 - t/t_{\text{max}})^{D/\Delta} = \infty \quad (4.4)$$

(during the simulation the parameter  $\Delta$  changes slowly and can be considered constant). This condition is satisfied for all values of  $D$  and  $\Delta$ , hence the proposed cooling scheme is valid, if the chosen value of  $t_{\text{max}}$  is large enough. As it has been already mentioned, the required value of  $t_{\text{max}}$  grows exponentially with the

increase of investigated configuration space, and, as well, it depends on the chosen value of  $\delta_{\max}$ , the maximal allowed change of the variable (atomic coordinate) per iteration. The requirement to specify the value of  $t_{\max}$  and  $\delta_{\max}$  is the largest drawback of this scheme, as it usually leads to painful parameter studies.

The second simulated annealing scheme, implemented in EvAX code, is somehow more intelligent. Here we start with some initial, usually large value of parameter  $\delta_{\max}$ . As previously, during the simulation automatically the parameter  $\Delta$ , the average change of the difference between theory and experiment per RMC step, is estimated. Then, using Eq. (4.3), the value of parameter  $T$  is calculated, in order to make the value of  $p$  (the probability to accept a move with  $\xi^{\text{new}} > \xi^{\text{old}}$ ) to be equal to some specified, fixed value  $p_0$  (usually  $p_0 = 0.5$ ). The calculations with these values of  $\delta_{\max}$  and  $T$  are continued, till there is no significant improvement of the residual  $\xi$ . Then the value of  $\delta_{\max}$  is reduced by factor of two and the new values of parameters  $\Delta$  and  $T$  are calculated (parameter  $p_0$  is kept fixed). The process is repeated, until the reduction of  $\delta_{\max}$  does not lead to significant improvement of  $\xi$ . Thus in this scheme the computational time, as well as the value of parameter  $\delta_{\max}$  are obtained automatically. This scheme is slower than the previous one, but it can be extremely useful to obtain at least an initial idea on how large the values of  $t_{\max}$  and  $\delta_{\max}$  should be chosen.

#### 4.2.4 Evolutionary algorithms<sup>1</sup>

##### 4.2.4.1 Introduction

During the last decades the RMC method had proven to be a valuable tool for the analysis of EXAFS data (see Sec. 3.4). However, the number of applications of RMC-EXAFS approach is still rather limited. Undoubtedly, it is due to the fact that RMC method is extremely computationally inefficient. The random process that is at the heart of RMC approach usually requires many thousands of iterations till the system reaches its global minimum point. As a result, many thousands of theoretical EXAFS calculations are required, where each one of them, if all MS contributions are taken into account, may take even several minutes on modern CPUs, especially when the contributions from distant coordination shells around absorbing atom are also included. Moreover, the required computational time grows exponentially with the increase of dimensionality or

<sup>1</sup>The material, presented in Sec.4.2.4, has been published as J. Timoshenko, A. Kuzmins, J. Purans, EXAFS STUDY OF HYDROGEN INTERCALATION INTO ReO<sub>3</sub> USING THE EVOLUTIONARY ALGORITHM; J. Phys.: Condens. Matter 26 (2014) 055401 (15 pages).

characteristic length of the configuration space, over which the global minimum point is searched (Sec. 4.2.3.1).

Therefore in this thesis we present a novel approach: we propose to use for the optimization of 3D structure model of a sample the so-called evolutionary algorithm (EA). While, in principle, EA is similar to RMC method and is also based on a random process, it turns out to be significantly more efficient in the terms of required computational power. Thus the EA approach allows us to include in the analysis much larger number of photoelectron scattering paths, therefore the studies of distant coordination shells taking into account all significant MS contributions are now possible. For certain, the implementation of EA for the analysis of the total EXAFS spectra is one of the most important results, presented in this thesis.

Evolutionary algorithm is a general name for a class of similar, population-based techniques for parameter optimization that strive to mimic genetic processes in the natural systems. The most well-known type of EA is genetic algorithm, introduced by John Holland in the 1960s,[177, 178, 179, 180] for which the encoding of the variables in the form of binary strings is characteristic.

In the EA a set of current values of all parameters, which should be optimized, forms an "individual". The function of these parameters, which needs to be maximized, is called fitness function. The "population" is an ensemble of such "individuals": it consists of many sets of parameters having different values. At each iteration some manipulations with the population are carried out, so that a new population is obtained from the old one. If these manipulations, or operators, applied to the old population, are properly chosen, the fitness of the new population will be, on average, larger than for the old population. Thus, the fitness function will be maximized step by step, and the values of parameters will approach those at the global maximum point.

In the field of structure analysis EA has been already used, for instance, to interpret the results of powder diffraction [181, 182] and small-angle X-ray scattering [183, 184]. Noteworthy application of EA is the optimization of the ground-state geometries of proteins and other large molecules [185, 186]. Interestingly that evolutionary algorithm has been applied also for the EXAFS analysis, but only as a routine for the conventional best-fit of the EXAFS data, using the standard EXAFS equation (2.22) [187]. Nevertheless, to our knowledge, no attempts to use EA for the simulation-based interpretation of EXAFS data have been previously done.

When EA is applied to the interpretation of EXAFS spectra from crystalline materials, the crystalline lattice, as in conventional RMC, is modelled by a supercell and the variable parameters are the coordinates of the atoms in the supercell. An individual hence is an atomic configuration. For such individual one can perform ab initio calculations of EXAFS spectrum, and compare the obtained theoretical result with the experimental one. The fitness function is defined so that it has the maximal value, when the difference between the theoretical and experimental EXAFS spectra is the smallest. Thus, the maximization of the fitness function is equivalent to the search for the atomic configuration, which represents the atomic structure of the sample and for which the theoretical EXAFS spectrum is close to the experimental one.

The calculation of the fitness function for an atomic configuration requires the knowledge of the total theoretical EXAFS spectrum  $\chi_{\text{tot}}(k)$ , which, as in the case of RMC simulations, can be obtained by averaging EXAFS spectra  $\chi(k)$ , calculated for all absorbing atoms in the supercell by FEFF code. Using the difference between the theoretical and experimental EXAFS data  $\xi$ , already introduced for the RMC algorithm, the fitness function, required for the EA, can be simply defined as  $-\xi$ .

In the EA three operators can be usually applied to a given population: (i) selection, (ii) crossover and (iii) mutation (Fig. 4.3). In the selection process one creates a new population (i.e., a new set of atomic configurations) from the individuals of the old population, where the individual with larger fitness function has larger probability to get into the new population. Thus, there will be less atomic configurations with low values of fitness function in the new set, but instead there can be several copies of the atomic configurations with high values of the fitness function. In the crossover process one replaces two randomly selected atomic configurations ("parents") from the old population with two other atomic configurations ("children"), obtained by interchanging some parts of the "parents", i.e., we replace some atoms of one atomic configuration with atoms of the other configuration. Finally, the mutation operator applies some small and random changes to all individuals of the population: in our case, all atoms in all configurations are slightly displaced in random directions.

These three basic operators have been implemented in the EvAX code, and will be discussed below.

The convergence properties of EA is a subject of significant controversy. It is clear, however, that at least for some optimization problems the EA is much

more efficient tool than conventional simulated annealing. Intuitively it can be understood using following argument: let us assume that the fitness function  $-\xi(x_1, x_2, \dots, x_k)$  that is a function of variables  $x_1, x_2, \dots, x_k$  can be decomposed as  $-\xi(x_1, x_2, \dots, x_k) = -\xi_1(x_{11}, x_{12}, \dots) - \xi_2(x_{21}, x_{22}, \dots) - \dots - \xi_j(x_{j1}, x_{j2}, \dots)$ . Here  $(x_{11}, x_{12}, \dots)$ ,  $(x_{21}, x_{22}, \dots)$ , etc., are some (not necessarily non-overlapping) subsets of the original set of variables  $(x_1, x_2, \dots, x_k)$ . In the case of EA approach we have a population of several replicas of our system. At each iteration we select the fittest (i.e., the ones having the largest value of  $-\xi$ ) individuals to the next generation. Some of the selected individuals will be included in this next generation because they have large value of, say,  $-\xi_1$ , some others - due to the high value of  $-\xi_2$ , etc. Thus we may formulate that instead of the maximization of function  $-\xi$  of  $k$  variables, EA is solving several maximization problems, but each with a fewer number of variables [180]. As was pointed out in Sec. 4.2.3.1, the number of iterations, required to find the optimal solution to the problem using, for instance, simulated annealing, is exponentially dependent on the number of variables  $k$ . So if we are able to factorize the fitness function so that all sets  $(x_{j1}, x_{j2}, \dots)$  have a significantly fewer number of variables than  $k$ , the number of required iteration to find the optimal solution will decrease exponentially with respect to the conventional simulated annealing: in this case EA will be much more efficient.

It appears, the case of EXAFS analysis is one of those, where EA methods can be useful: the total EXAFS spectrum can be expressed as a sum of contributions from relatively small atomic clusters, and these clusters act like the "genes" of population. The "genes" that ensure high values of the fitness function survive from one generation to another, and an exchange of the "genes" between individuals efficiently maximizes the fitness of each individual.

#### 4.2.4.2 Selection

The selection operator can be implemented using different procedures: for example, the conventional proportional selection (the probability of the individual to be selected to the new generation is proportional to the value of its fitness function), truncation selection (the individuals are ranged accordingly to their fitness, and fixed number of them is selected to the new generation), etc. [188, 189]

We propose to use the so-called tournament selection: the two individuals from the old population are randomly selected, and the one with higher fitness is copied to the new population, and the process is repeated until the number of individuals in the new populations is the same as in the old population [188].



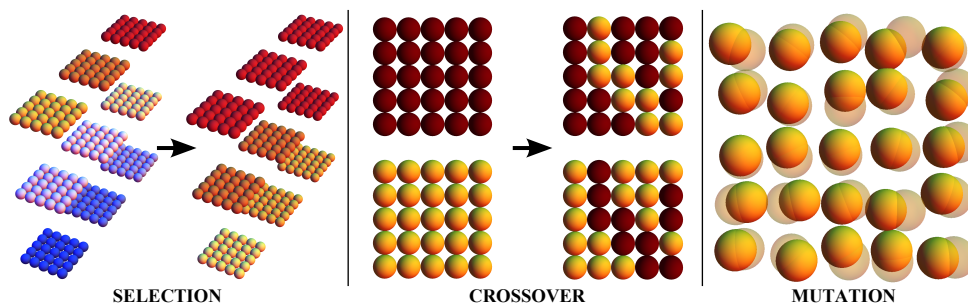


**Figure 4.3: Three basic operators of evolutionary algorithm**

Selection operator chooses the best of individuals to the next generation, keeping the total number of individuals in the population constant; crossover operator interchanges some parts of individuals in the population, while mutation operator applies some random changes to individuals.

The advantages of this scheme are that (i) it is easy to implement, and (ii) it better preserves the "genetic diversity" of the population than proportional selection. In the case of proportional selection the probability of individual with low fitness to be selected to the new population can be extremely small (if, for example, the fitness of the best individual is much higher than the fitness of all other individuals), and, therefore, all individuals will be close to each other after relatively small number of iterations, thus all advantages, provided by the use of selection and crossover operators, will be lost.

#### 4.2.4.3 Crossover

For crossover operator we split in pairs all individuals in the population, which is obtained after applying the selection operator, and then perform the "breeding" of each pair with a given probability (currently a fixed value of 50% is used). First, a pseudo-random number  $\rho_b$  ( $0 \leq \rho_b \leq 1$ ) is generated. If  $\rho_b > 0.5$ , the old pair of individuals ("parents") is replaced with a pair of new individuals ("children"). To create "children", we generate a set of pseudo-random numbers  $\rho_a$  ( $0 \leq \rho_a \leq 1$ ) for each atom in the supercell. If  $\rho_a < 0.5$ , the corresponding atom of the first of children is set at the same position as the corresponding atom of the first of parents, and the corresponding atom of the second of children is set at the same position as the corresponding atom of the second of parents. If  $\rho_a > 0.5$ , the interchange of atoms takes place: corresponding atom of the first of children now is taken from the second of parents, and the corresponding atom of the second of children is taken from the first of parents.

As the crossover changes the atomic configuration, the corresponding EXAFS spectrum should be recalculated for the bred individuals. However, an advantage of the use of the crossover operator for EXAFS analysis is based on the fact that EXAFS spectra can be expressed as a series of contributions from separate photoelectron paths, where each path contains only a few atoms. After crossover operation some of these paths are modified, but a large number of them remains unchanged, therefore one can expect, the "children" of the "parents" with good fitness will also have high values of fitness function.

#### 4.2.4.4 Mutation

In the conventional EA the mutation is a fully random change of the individuals, i.e., one should apply random displacements to all atoms of the population. In our approach, however, we propose to apply additional restriction on the mutations, defined by the Metropolis algorithm (Eq. (4.1)), thus making our EA scheme to be even closer to the RMC method.

Moreover, similarly to our RMC implementation, in the EA method we also constrain the displacements of atoms from their equilibrium positions to be smaller than a given number  $\delta_{\max}$ , thus again indirectly including in the EXAFS analysis the information obtained using diffraction technique. In the case of the EA method, however, the value of  $\delta_{\max}$  is not so crucial parameter as it was for the RMC method, and the solution can be efficiently obtained even with relatively large values of  $\delta_{\max}$ .

The usage of parameters for RMC and EA calculations and simulated annealing schemes, is described in Appendix, Sec. A.4.5.

## 4.3 Signal processing: wavelet transform

### 4.3.1 $k$ -, $q$ - and $R$ -spaces<sup>1</sup>

In this subsection we will treat EXAFS spectra as some signals in  $k$ -space, and will apply to them the methods of signal processing. Within the RMC/EA method the objectives of such signal processing is threefold: (i) to filter out both

<sup>1</sup>The material, presented in Sec.4.3.1, has been published as J. Timoshenko, A. Kuzmin, J. Purans, REVERSE MONTE CARLO MODELLING OF THERMAL DISORDER IN CRYSTALLINE MATERIALS FROM EXAFS SPECTRA, Comp. Phys. Commun. 183 (2012) p. 1237-1245

the low frequency (associated mainly with the problems of background subtraction) and high frequency noise from experimental spectra; (ii) to exclude from the experimental spectra the contributions of the further coordination shells and (iii) to perform the comparison of the experimental and theoretical EXAFS data, emphasizing signal features of interest. In all of these three cases the well-known Fourier transform (FT), providing the representation of the signal in the frequency domain, can be useful. Note that in the case of EXAFS analysis the frequencies of signal correspond to interatomic distances  $R$ . The Fourier transform, as will be shown below, can be efficiently replaced by wavelet transform (WT). WT can be more informative than the FT, since it provides 2D-representation of our signal, revealing the features of signal both in  $k$  and  $R$ -spaces simultaneously.

Let us focus now on the problem of signal comparison. Both for RMC and EA methods at each iteration we need to carry out at least two comparisons of two pairs of EXAFS spectra: we compare theoretical EXAFS spectra  $\chi_{\text{tot}}^{\text{old}}(k)$  and  $\chi_{\text{tot}}^{\text{new}}(k)$  that correspond to the old and new atomic configurations, respectively, with the experimental spectrum  $\chi_{\text{exp}}(k)$ . To measure the difference between two EXAFS spectra, we can introduce the quantity  $\xi_k$  that is defined as

$$\xi_k = \frac{\|\chi_{\text{tot}}(k)k^n - \chi_{\text{exp}}(k)k^n\|_2}{\|\chi_{\text{exp}}(k)k^n\|_2}. \quad (4.5)$$

Thus during the RMC/EA simulations we minimize the difference between the theoretical and experimental EXAFS spectra in  $k$ -space. The vertical lines  $\|\dots\|_2$  denotes here the Euclidean norm<sup>1</sup>, and  $k^n$  ( $n=1, 2$ , or  $3$ ) is the weighting factor, commonly used in EXAFS analysis to compensate the damping of spectrum.

As a rule of thumb, the agreement between experimental and theoretical spectra can be considered to be reasonably good, if  $\xi_k$  is smaller than 0.2 (see [17, p.304] and [190]).

Instead of using the full experimental EXAFS spectrum, one can also use as function  $\chi_{\text{exp}}(k)$  the spectrum, filtered by Fourier transform in the specified  $R$ -space range. In this work we define Fourier transform of some function  $\chi(k)$  as  $\text{FT}_\chi(R) = (2\pi)^{-1/2} \int_{k_{\min}}^{k_{\max}} e^{2iRk} \chi(k) dk$  and inverse Fourier transform as  $\text{BFT}_\chi(k) = (2\pi)^{-1/2} \int_{R_{\min}}^{R_{\max}} e^{-2iRk} \text{FT}_\chi(R) dR$ . If  $\chi(k)$  is now experimental EXAFS spectrum,

---

<sup>1</sup>Euclidean norm of some function  $f(k_1, k_2, \dots, k_l)$  is defined as  $\|f(k_1, k_2, \dots, k_l)\|_m = \left( \int_{-\infty}^{\infty} \int_{-\infty}^{\infty} \dots \int_{-\infty}^{\infty} |f(k_1, k_2, \dots, k_l)|^m dk_1 dk_2 \dots dk_l \right)^{1/m}$ ; it is also called as  $L_m$  norm

before the Fourier transform is carried out, function  $\chi(k)$  is multiplied by  $k^n g(k)$ , where the window-function  $g(k) = e^{-a(k-k_0)^2}$  with  $k = (k_{\min} + k_{\max})/2$  and  $a = -4 \ln 0.1 / (k_{\max} - k_{\min})^2$  damps the spectrum at  $k = k_{\min}$  and  $k = k_{\max}$  and allows us to avoid the problems that arise due to finite-length of the spectrum [17, p.111]. Thus Fourier filtering allows us to remove the contributions of scattering paths longer than  $2R_{\max}$  and also the high-frequency experimental noise. Sometimes the comparison of the Fourier-filtered spectra is called comparison in  $q$ -space.

Instead of performing inverse Fourier transform, one can also use the Fourier images of the total theoretical and experimental EXAFS spectra directly, and carry out the minimization of difference between spectra in the frequency space ( $R$ -space). In this case the difference between both spectra is defined as

$$\xi_R = \frac{\|\text{FT}_{\text{tot}}(R) - \text{FT}_{\text{exp}}(R)\|_2}{\|\text{FT}_{\text{exp}}(R)\|_2}. \quad (4.6)$$

Note that according to Parseval's theorem<sup>1</sup>,  $\xi_k$  and  $\xi_R$  should be equal. In practice, however, since the signals used for the analysis are limited both in  $k$ - and  $R$ -spaces, the  $\xi_k$  and  $\xi_R$  quantities are slightly different, and can be used to emphasize discrepancies of different features of the compared spectra.

#### 4.3.2 Wavelet transform<sup>2</sup>

Besides comparison of EXAFS spectra in either  $k$ -,  $q$ - or  $R$ -spaces, there is another possibility: we can compare EXAFS spectra in  $k$ - and  $R$ -spaces *simultaneously* using so called wavelet transform. WT is a modern technique of spectrum processing, and during the last fifteen years the advantages of its application to EXAFS analysis have been demonstrated [191, 192, 193, 194, 195, 196, 197, 198, 199, 200, 201]: WT has been found useful for EXAFS data extraction, noise filtering and de-glitching procedures and qualitative EXAFS analysis. However, to our knowledge, WT has previously never been applied to RMC-EXAFS analysis or any other quantitative treatment of EXAFS data.

Wavelet transform of a given EXAFS spectrum  $\chi(k)$  is defined as [194]

<sup>1</sup>Parseval's theorem states that Euclidean  $L_2$  norms of spectrum and its Fourier image are equal, i.e.,  $\|\chi(k)\|_2 = \|\text{FT}_\chi(R)\|_2$

<sup>2</sup>The material, presented in Sec.4.3.2, has been partially published as J.Timoshenko, A. Kuzmin, WAVELET DATA ANALYSIS OF EXAFS SPECTRA, Comp. Phys. Commun. 180 (2009) p. 920-925; and J. Timoshenko, A. Kuzmin, J. Purans, REVERSE MONTE CARLO MODELLING OF THERMAL DISORDER IN CRYSTALLINE MATERIALS FROM EXAFS SPECTRA, Comp. Phys. Commun. 183 (2012) p. 1237-1245

$$w(R, k) = \sqrt{R/R_0} \int_{-\infty}^{+\infty} \chi(k') \varphi((R/R_0)(k' - k)) dk'. \quad (4.7)$$

In fact, it is simply the inner product of the analyzed spectrum and translated by  $k$ -units and  $R/R_0$ -times distorted function  $\varphi(k)$  (this function  $\varphi(k)$  is referred as "mother-wavelet"). The basic idea behind the wavelet analysis is the Cauchy – Bunyakovsky – Schwarz (CBS) inequality that states that the inner product of two functions with fixed norms is the largest, when these functions have similar shapes<sup>1</sup>. The aim of wavelet transform is to decompose the analyzed spectrum in  $k$  and  $R$ -spaces, i.e. to reveal, which frequencies ( $R$ -values) are present in the spectrum, and, simultaneously, at which values of wavenumber  $k$  the components, corresponding to each  $R$ -value, do contribute. If as a mother-wavelet we choose such function  $\varphi(k)$  that is (i) well localized in  $k$ -space and (ii) well-localized in  $R$ -space (i.e., it has well defined characteristic frequency  $R_0$ ), the interpretation of the obtained wavelet image is rather straightforward: the absolute value of wavelet image of spectrum  $\chi(k)$  at some point  $(k_1, R_1)$  is large, if in this spectrum around wavenumber point  $k = k_1$  the amplitude of the spectral component that corresponds to frequency  $R = R_1$  is significant. Note that if we neglect the first condition and mother-wavelet is localized only in  $R$ -space, the wavelet transform gets actually equivalent to Fourier transform.

One of the possible mother-wavelet functions that have the properties, mentioned above, and that are suitable for EXAFS analysis, is the so-called Morlet wavelet [194]: for Morlet WT, function  $\varphi(k)$  is defined as

$$\varphi_{\text{Morlet}}(k) = \exp(-2iR_0k) \exp(-\sigma_0^2k^2). \quad (4.8)$$

For illustration, let us apply Morlet WT to a simple model spectrum:  $\chi(k) = \sum_{i=1}^3 \sin(2R_i k) e^{-2\sigma^2(k-k_i)^2}$  with  $R_1 = 2 \text{ \AA}$ ,  $R_2 = 6 \text{ \AA}$ ,  $R_3 = 10 \text{ \AA}$ ,  $\sigma^2 = 0.1 \text{ \AA}^2$ ,  $k_1 = 9 \text{ \AA}^{-1}$ ,  $k_2 = 15 \text{ \AA}^{-1}$ ,  $k_3 = 21 \text{ \AA}^{-1}$ . This spectrum is plotted in the upper part of Fig. 4.4, its Fourier transform - in the right panel of Fig. 4.4. The modulus of Morlet WT is shown in the central panel of Fig. 4.4. While in the case of Fourier transform any information on positions of the different components of model spectrum in  $k$ -space (i.e., the values of  $k_1, k_2, k_3$ ) is lost, wavelet transform gives us the two-dimensional representation of the studied spectrum and provides

<sup>1</sup>More precisely, CBS inequality states that for the inner product of functions  $g$  and  $h$ , denoted as  $(g, h)$ , the following relation holds:  $|(g, h)| \leq \|g\|_2 \|h\|_2$ , and the equality is achieved only if functions  $g$  and  $h$  are linearly dependent

information on localization of its components both in  $R$ - and  $k$ -spaces. This is an important advantage for the analysis of EXAFS data from samples with different types of atoms: it is known that heavy atoms usually contribute to the total EXAFS spectrum at higher values of wavenumber  $k$  than light atoms, thus the contributions of atoms of different type can be separated using wavelet analysis.

Fig. 4.4 reveals also one of the peculiarities of wavelet transform. The studied model spectrum consists of three components, and duration of each component in  $k$ -space is the same. Therefore all three peaks in the Fourier image of this spectrum are also similar. Three peaks in the wavelet image, in turn, have different shapes: peaks that correspond to higher frequencies are distorted in the direction of  $R$ -axis. This is a result of general property of the wavelet transform - it has different resolution at different frequencies. The image of low-frequency components (components with frequency  $R$  smaller than characteristic frequency of the mother-wavelet  $R_0$ ) will have high resolution in  $R$ -space and poor resolution in  $k$ -space, while the image of high-frequency components (with  $R$  larger than  $R_0$ ) will be well resolved in  $k$ -space, but in  $R$ -space their resolution will be worse [193].

To be more specific, let us look at Morlet WT of damped harmonic functions  $\chi(k) = \exp(2iR_1k) \exp(-\sigma_1^2(k - k_1)^2)$ . We put this expression into Eq. (4.7) and after integration we obtain

$$|w(R, k)| = \sqrt{\frac{\pi R R_0}{\sigma_0^2 R^2 + \sigma_1^2 R_0^2}} e^{-\frac{R_0^2(R - R_1)^2}{\sigma_0^2 R^2 + \sigma_1^2 R_0^2}} e^{-\frac{R^2 \sigma_0^2 \sigma_1^2 (k - k_1)^2}{\sigma_0^2 R^2 + \sigma_1^2 R_0^2}}. \quad (4.9)$$

The first exponent provides the localization of wavelet image in  $R$ -space: it is Gaussian function centered at  $R_1$  and with characteristic width  $\Delta_R = \sqrt{\sigma_0^2 R^2 + \sigma_1^2 R_0^2}/R_0$ . The second exponent, in turn, provides the localization of wavelet image in  $k$ -space: again it is Gaussian function now centered at  $k_1$  and with characteristic width  $\Delta_k = \sqrt{\sigma_0^2 R^2 + \sigma_1^2 R_0^2}/(R\sigma_0\sigma_1)$ . The distortion of the peak of wavelet image can now be characterized by ratio  $\Delta_R/\Delta_k = \sigma_0\sigma_1 R/R_0$ . And again, one can see, the larger is the frequency  $R$ , the more distorted is the wavelet image in the direction of  $R$ -axis.

Note also, for given value of  $R$  the  $\Delta_k$  is the larger, the larger is the parameter  $R_0$ , but  $\Delta_R$  is inversely proportional to  $R_0$ . It means, we can improve the resolution in  $k$ -space by reducing the value of parameter  $R_0$ ; however, this will result in poorer resolution in  $R$ -space, and vice versa: the resolution in  $R$ -space can be

increased by reducing the value of  $R_0$ , but, consequently, the resolution of WT in  $k$ -space will be poorer in this case [194]. We can see thus, wavelet transform can be a flexible tool for the spectrum analysis and it can easily be adapted to emphasize the spectrum features of interest.

From the practical point of view, wavelet transform has one useful property that allows an efficient implementation of WT algorithm. Note that Eq. (4.7) that defines the wavelet transform of function  $\chi(k)$ , looks similar to the convolution of functions  $\chi(k)$  and  $\phi(k)$ . Hence the result, similar to the well known convolution theorem can be obtained: the Fourier transform of the wavelet image can be written as

$$\begin{aligned}
 \text{FT}_{w(R,k)}(\omega) &= \sqrt{R/(2\pi R_0)} \int_{-\infty}^{+\infty} dk e^{i\omega k} \int_{-\infty}^{+\infty} \chi(k') \varphi((R/R_0)(k' - k)) dk' \\
 &= \sqrt{R/(2\pi R_0)} \int_{-\infty}^{+\infty} dk \int_{-\infty}^{+\infty} e^{i\omega k'} \chi(k') e^{-i\omega x(R_0/R)} \varphi(x)(R_0/R) dx \\
 &= \sqrt{R_0/(2\pi R)} \int_{-\infty}^{+\infty} dk e^{i\omega k'} \chi(k') \int_{-\infty}^{+\infty} dx e^{-i\omega x(R_0/R)} \varphi(x) dx \\
 &= \sqrt{2\pi R_0/R} \text{FT}_{\chi}(\omega) \text{FT}_{\chi}(-\omega R_0/R),
 \end{aligned} \tag{4.10}$$

and thus one gets

Thus

$$w(R, k) = \sqrt{2\pi R_0/R} \text{BFT} [\text{FT}_{\chi}(\omega) \text{FT}_{\varphi}(-\omega R_0/R)]. \tag{4.11}$$

The Fourier transform of mother-wavelet function can be calculated analytically. In the case of Morlet wavelet transform with  $\varphi(k) = e^{-2iR_0k} e^{-\sigma_0^2 k^2}$ , the corresponding result is simply Gaussian function:  $\text{FT}_{\varphi}(\omega) = \frac{1}{\sqrt{2\sigma_0}} e^{-(\omega - 2R_0)^2 / (4\sigma_0^2)}$ . The Fourier transform of the analyzed data  $\chi(k)$  and inverse Fourier transform, in turn, can be carried out using efficient fast Fourier transform algorithm (Cooley-Tukey algorithm). Besides allowing fast calculations of wavelet transform, Eq. (4.11) provides also an useful interpretation of wavelet transform: one can see, Morlet wavelet transform can be considered as Fourier filtering of spectrum with the Gaussian filter with variable width.

Other properties of wavelet transform in details are described in, for example, [202] and [203].

For the comparison of EXAFS spectra in the RMC and EA simulations, WT can be employed similarly as Fourier transform. The difference between spectra now can be calculated as

$$\xi_{k,R} = \frac{\|w_{\text{tot}}(R, k) - w_{\text{exp}}(R, k)\|_2}{\|w_{\text{exp}}(R, k)\|_2}, \quad (4.12)$$

where  $w_{\text{tot}}$  and  $w_{\text{exp}}$  are the Morlet wavelet transforms of calculated and experimental EXAFS spectra ( $\chi_{\text{tot}}(k)k^n$  and  $\chi_{\text{exp}}(k)k^n$ ), respectively.

Thus wavelet transform is an unambiguous linear transformation of signal that reflects its frequency content. In that sense it is fully analogical to the Fourier transform, widely used in the EXAFS community. A good agreement between two spectra in the wavelet space automatically means a good agreement between them in  $k$ -space and  $R$ -space. The opposite, dealing with signals, limited in  $k$ - and  $R$ -spaces, is not always true: a good agreement, for instance, in Fourier space only, does not necessarily mean a good agreement in  $k$ -space, and, consequently, also in wavelet space. Thus WT is a natural way to take into account features of signal both in  $k$ - and Fourier space simultaneously. Additionally, the advantage of WT over Fourier transform and over the representation of spectra in  $k$ -space can be seen in the case when the agreement between two spectra is *not good*: in this situation WT, providing the information on the misfit of spectra both in  $k$ - and frequency space simultaneously, allows one to identify the problem more easily.

Therefore we believe that the novel WT-based criterium for the comparison of theoretical and experimental data (Eq. (4.12)) will provide the best results during RMC/EA minimization procedure.

The additional advantage that is provided by the use of wavelet transform, is the possibility to change the sensitivity of the RMC/EA method to the different components of spectra. Instead of Eq. (4.12) we then can apply more general expression

$$\xi_{k,R}^\rho = \frac{\|w_{\text{tot}}(R, k) - w_{\text{exp}}(R, k)\|_2^\rho}{\|w_{\text{exp}}(R, k)\|_2^\rho}, \quad (4.13)$$

where  $\|\cdot\|_2^\rho$  denotes the weighted Euclidean norm, defined for some function  $f(R, k)$  as

$$\|f(R, k)\|_2^\rho = \left( \int_{-\infty}^{\infty} \int_{-\infty}^{\infty} |\rho(R, k) f(R, k)|^2 dk dR \right)^{1/m}, \quad (4.14)$$



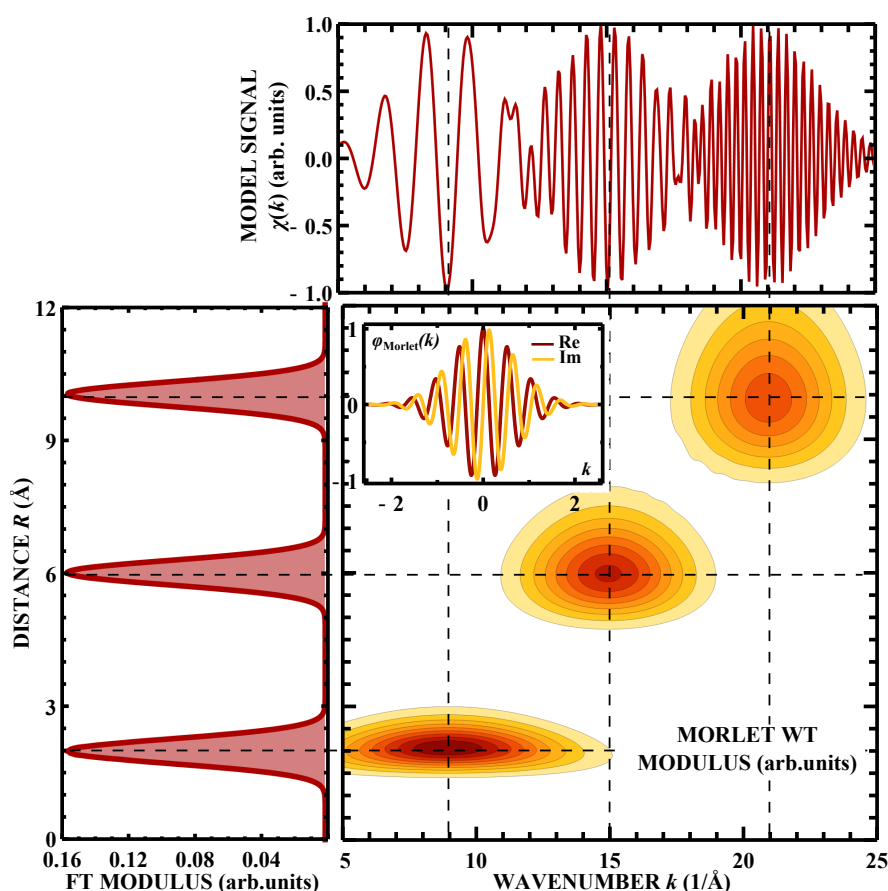


**Figure 4.4: Morlet wavelet transform in action**

Model spectrum (*upper panel*), modulus of its Fourier transform (*left panel*) and modulus of its Morlet wavelet transform (*central panel*). In the *inset* - real and imaginary parts of Morlet mother-wavelet.

and  $\rho(R, k)$  is a weight function.

The usage of parameters for the comparison of theoretical and experimental EXAFS spectrum within EvAX code, is described in Appendix, Sec. A.4.4.

## 4.4 Calculations of EXAFS

### 4.4.1 Ab-initio calculations

RMC/EA procedure requires to calculate at each iteration the total EXAFS spectrum  $\chi_{\text{tot}}(k)$ , corresponding to the current atomic configuration. This spectrum then is compared with the experimental one  $\chi_{\text{exp}}(k)$ . The total EXAFS spectrum  $\chi_{\text{tot}}(k)$  equals to the average of the EXAFS spectra  $\chi(k)$  from all absorbing atoms in the atomic configuration. These spectra can be calculated by one of the available *ab-initio* EXAFS codes as, for example, FEFF [25] or GNXAS

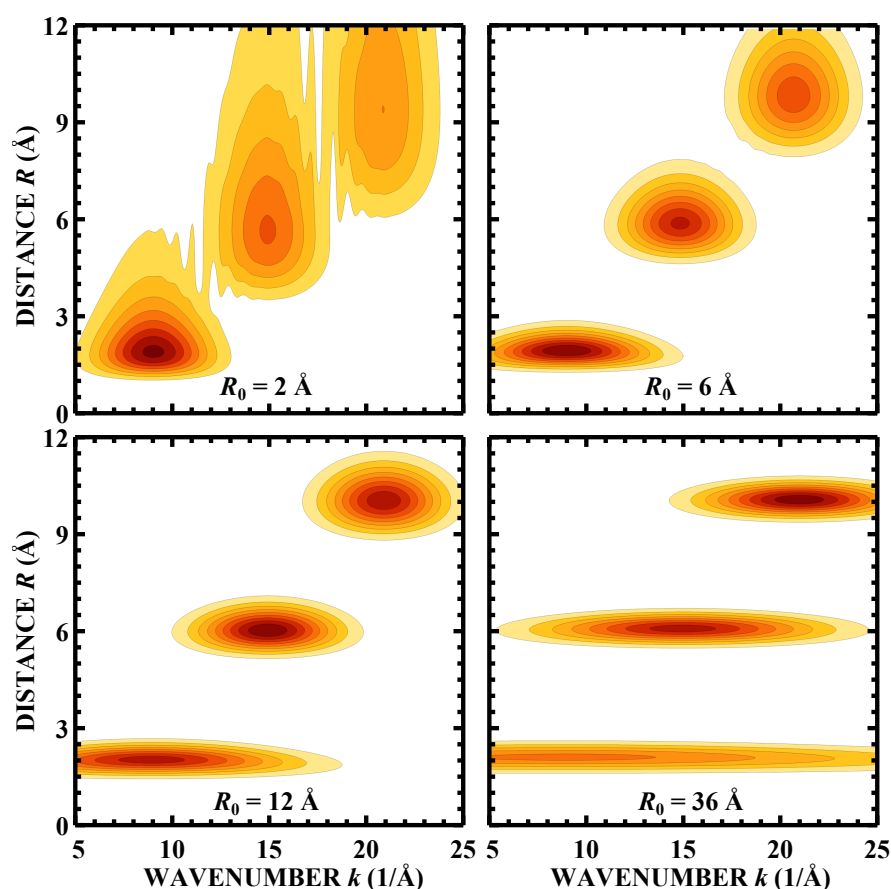


**Figure 4.5: Controlling the resolution of Morlet wavelet transform**  
 Modulus of the Morlet wavelet transform of model spectrum, calculated with different characteristic frequency values  $R_0$  for mother-wavelet.

[167]. Obviously, the accuracy of the structure model, reconstructed by RMC/EA approach, and the computational costs of such calculations are strongly related to the accuracy and efficiency of the used EXAFS code, which, without any doubts, will be improved in the future correspondingly to the progress within the EXAFS theory [11].

In this work for EXAFS calculations we use the *ab initio* self-consistent real space multiple-scattering approach as is implemented in the FEFF8 code [25, 2]. The FEFF8 program is used as an internal routine in the EvAX code. The input file *feff.inp*, required for FEFF calculations, is created and the FEFF program is started automatically by EvAX software. In this subsection we highlight some details of the *ab-initio* calculation process.

FEFF code is developed by J. Rehr et. al., for the simulations of XAS and related properties (X-ray magnetic dichroism, X-ray photoemission spectra, etc.) of given atomic cluster. Undoubtedly, currently it is one of the most popular and

reliable softwares for EXAFS calculations, which provides a good description of experimental data.

Calculations of XAS are strongly related to the calculations of local electronic density of states (LDOS). The important peculiarity of the XAS *ab-initio* calculations is that the relaxation of the electronic system of absorbing atom due to the presence of the core hole should be taken into account. On the other hand, one can exploit the fact that for the correct description of the scattering of photoelectron only the atomic potential in the region relatively close to the atomic core is actually essential, where this potential is almost spherically symmetric. Thus the *ab-initio* calculations can be significantly simplified [25]. This idea is behind the so called muffin-tin approximation, implemented in FEFF: the interatomic potential  $V_{\text{tot}}(\vec{r})$  initially is given as  $V_{\text{tot}}(\vec{r}) = V_{\text{mt}} + \sum_i V_i(\vec{r} - \vec{R}_i)$ , where  $V_i$  are spherically symmetric potentials of free atoms, located at sites  $\vec{R}_i$ , and  $V_{\text{mt}}$  is a constant potential in the interstitial region. By allowing the overlap between spherical potentials centered at neighboring sites, one can also effectively account for some deviations from spherical symmetry of charge distribution.

Solving the relativistic Dirac equation with this potential, the wave functions of the atomic electrons can be calculated, thus also the electron charge density  $\rho(\vec{r})$ . Solving Poisson equation for this density, one can calculate the potential, produced by the electrons and thus refine the total atomic potential. To preserve the muffin-tin type shape of the potential, the charge density is spherically averaged around each site and is set to a constant average value in the interstitial region [16, p.84]. The calculations then can be repeated, till the self-consistency of the atomic potentials is ensured.

The largest problem for the *ab-initio* simulations of XAS is that the Fermi Golden rule (Eq. (2.3)) cannot be applied directly due to the fact that the precise calculations of all possible final states  $|f\rangle$ , taking into account also the presence of the core hole, is a hardly accomplishable task [11]. Luckily, we are not interested in the wave functions of final states *per se*, but in the density of final electronic states only. The efficient way to perform such calculations and to avoid explicit calculations of final states is Green's function approach, implemented in FEFF code.

In this approach the summation over states  $\langle f|$  with energy  $E_f$  is replaced with one function:

$$G(E) = \frac{1}{E - h' + i\Gamma} = \sum_f \frac{1}{E - E_f + i\Gamma} \langle f |, \quad (4.15)$$

where  $\Gamma$  is the spectral broadening due to the finite core-hole lifetime,  $h'$  is effective one-electron Hamiltonian  $h' = E_{\text{kin}} + V_c + \Sigma(E)$  ( $E_{\text{kin}}$  - kinetic energy of the electron,  $V_c$  - Coulomb potential of the system with screened core hole that acts on the electron, and  $\Sigma(E)$  is energy-dependent self-energy that accounts for all other possible interactions of electrons - electron correlation and exchange energies).  $\Gamma$  is a quantity, tabulated for different chemical elements, while  $\Sigma(E)$  needs to be calculated. The common approach for such calculations is Hedin-Lundqvist (HL) model, also implemented in FEFF, that gives the complex value of  $\Sigma(E)$  [11]. One can note that the imaginary part of self-energy that is responsible for inelastic electronic interactions and that gives a finite value for electron mean free path [16, p.87], is adding up with the parameter  $\Gamma$ , and both these quantities determine the effective mean free path  $\lambda \approx k / (|\text{Im}\Sigma| + \Gamma/2)$  in the equation (2.17) [11].

Now the absorption coefficient can be expressed as

$$\mu(E) \sim -\frac{2}{\pi} \text{Im} \int_{E_F}^{\infty} dE' \langle i | \vec{\epsilon} \vec{r}_1 G(\vec{r}_1, \vec{r}, E) \vec{\epsilon} \vec{r} | i \rangle \frac{\Gamma}{\pi [(E - E')^2 + \Gamma^2]}, \quad (4.16)$$

where  $E_F$  is Fermi energy,  $|i\rangle$  is the initial core state,  $\vec{\epsilon}$  is the intensity of the electrical field of incident X-rays [25].

The Green's function can be calculated, expanding it in terms of free Green's function  $G_0(r, r', E) = -\frac{1}{4\pi} \frac{e^{ik|\vec{r}-\vec{r}'|}}{|\vec{r}-\vec{r}'|}$ ,  $k = \sqrt{\frac{2m}{\hbar^2}(E - E_0)}$  [25, 204]:

$$G(\vec{r}, \vec{r}_1, E) = G_0(\vec{r}, \vec{r}_1, E) + \int d^3r_2 G_0(\vec{r}, \vec{r}_2, E) V_{\text{tot}}(\vec{r}_2) G_0(\vec{r}_2, \vec{r}_1, E) + \dots \quad (4.17)$$

If the total potential  $V_{\text{tot}}$  now is expressed as a sum of potentials  $V_i$ , centered at  $i$ -th atom, then

$$G = G_c + \int d^3r_2 G_c \sum_{i \neq c} t_i G_c + \int d^3r_2 G_c \sum_{i \neq c} \sum_{j \neq c} t_i G_0 t_j G_c + \dots, \quad (4.18)$$

where  $G_c = G_0 + \int d^3r_2 G_0 t_c G_0$  is the Green's function, associated with the central

(absorbing) atom and  $t_i = V_i + \int d^3r_2 V_i G_0 t_i$  is a scattering matrix. The sums in the equation above corresponds to single-scattering, double-scattering, etc., events (see [25] and [204] for more details).

The usage of FEFF8 code for *ab-initio* EXAFS calculations within EvAX simulations is described in Appendix, Sec. A.3.

#### 4.4.2 Dependency of complex scattering amplitude on interatomic distances

Let us remind here, the EXAFS spectrum  $\chi(k)$  is given by equation

$$\chi(k) = S_0^2 \sum_j \frac{|f_j(k, \vec{R}_j)|}{kR_j^2} \sin(2kR_j + \phi_j(k, \vec{R}_j)). \quad (4.19)$$

Here the summation is carried out over all possible scattering paths,  $R_j$  is the half length of the  $j$ -path, and the scattering amplitude  $f_j(k, \vec{R}_j)$  and phase shift  $\phi_j(k, \vec{R}_j)$  depend on the photoelectron energy and both radial and angular characteristics of the scattering path (vector  $\vec{R}_j$  denotes the position of the atoms, involved in the  $j$ -th scattering path, with respect to the absorbing atom), see Sec. 2.6 for details. Thus the sensitivity of the total EXAFS spectrum to the many-body distribution functions, i.e., 3D atomic structure is ensured.

The calculations of the  $f_j$  and  $\phi_j$  functions in the FEFF8 code require the knowledge of the cluster potential, obtained, as explained previously, in self-consistent calculations. The cluster potential can be evaluated for the average atomic configuration only, thus neglecting the potential variation due to thermal vibrations, or recalculated at each RMC/EA step. In this work, since we deal with the crystalline compounds and disorder of the system is relatively small, the self-consistent cluster potential is evaluated only once - before the main RMC/EA run - for the average crystalline structure known from diffraction studies. This allowed us to reduce significantly the required total computation time, since the potential calculations are the most time consuming part of FEFF procedure. For the calculations of the self-consistent cluster potential the complex exchange-correlation Hedin-Lundqvist potential and default values of muffin-tin radii, as provided within the FEFF8 code [25], are used.

Nevertheless, both functions  $f_j$  and  $\phi_j$  are recalculated in our approach at each iteration, thus their dependencies on the positions  $\vec{R}_j$  of atoms, involved in the scattering path, are taken into account explicitly. This point differs the presented approach from the conventional EXAFS analysis and also from the

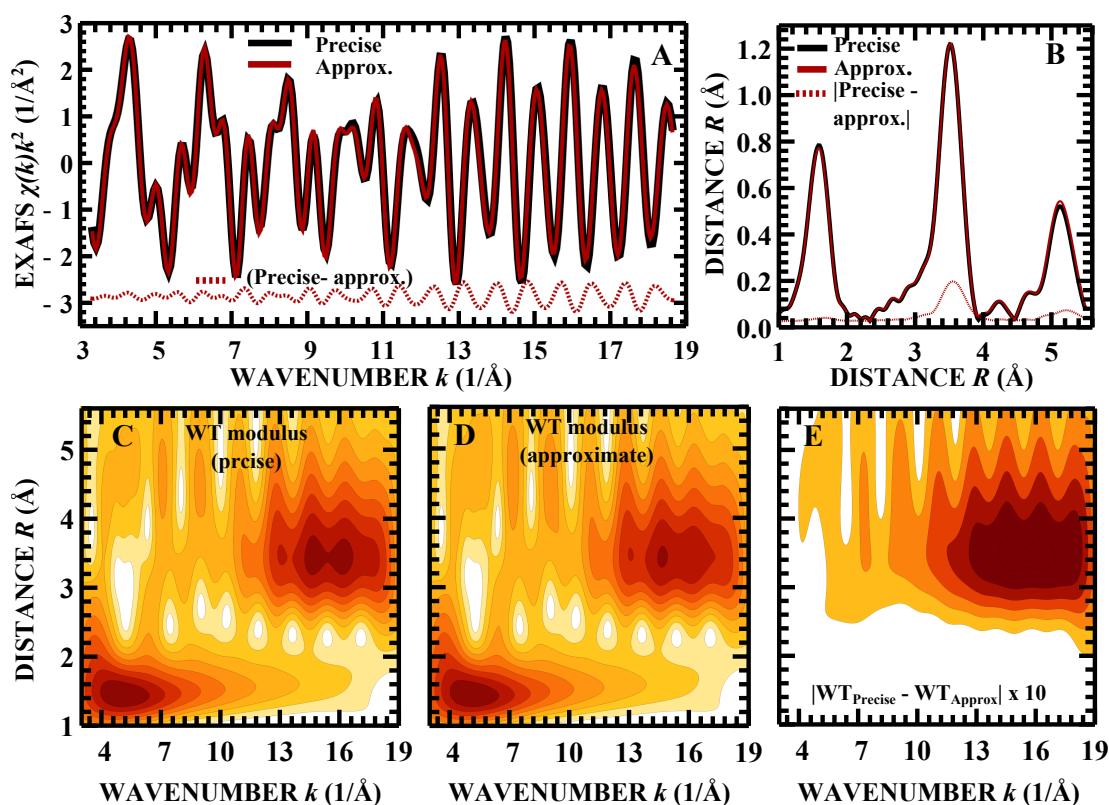


**Figure 4.6:** Influence of the dependency of complex scattering amplitude on interatomic distances

Re  $L_3$ -edge EXAFS spectrum, corresponding Fourier transforms and wavelet transforms for  $\text{ReO}_3$  model data, obtained in MD simulations (see Sec. 6.2.1), calculated (i) taking into account the dependency of complex scattering function on the positions of the atoms, involved in the scattering paths ("precise" results) and (ii) assuming that the complex scattering function for each scattering paths is the same as for the corresponding path in case of the equilibrium structure ("approximate" results).

most of the existing RMC implementations, where the influence of  $f_j$  and  $\phi_j$  on the interatomic distances and bonding angles is neglected. In Fig. 4.6 it is shown, such simplification, although it would reduce the required computational time, would lead to small but non-negligible errors.

#### 4.4.3 Clustering algorithm

For the calculations of total EXAFS spectrum we need to calculate EXAFS contribution from each scattering paths. If atoms are at least slightly displaced from their equilibrium positions, all symmetry of the system is removed and the number of non-equivalent paths is increased tremendously. Fortunately, a lot of

scattering paths still have close shapes, thus also the EXAFS contributions will be similar. Obviously, if we group such similar paths in some sets and calculate EXAFS contribution only once per each set, and then sum up the results of such calculations, applying weights that correspond to the number of atoms in a given set, we in an efficient way obtain quite precise total EXAFS spectrum.

The problem of dividing paths in groups is essentially a problem of grouping points in  $n$ -dimensional space, where  $n$  is the number of degrees of freedom for the given path ( $n = 1$  for single-scattering paths,  $n = 3$  for double-scattering paths, and  $n = 3 + 3 \cdot (p - 2)$ ) for paths with order  $p > 2$ . For example, in case of Re L<sub>3</sub> edge EXAFS from crystalline ReO<sub>3</sub> the non-linear double-scattering path Re<sub>0</sub>-O<sub>1</sub>-O<sub>2</sub> has 3 degrees of freedom: distance between Re<sub>0</sub> and O<sub>1</sub> atoms, distance between Re<sub>0</sub> and O<sub>2</sub> atoms, and distance between O<sub>1</sub> and O<sub>2</sub> atoms. Such problems are solved via so called clustering algorithms. In the EvAX code the most popular clustering algorithm, so called *K-means algorithm*, is implemented.

The idea of method relies on the following considerations. We can characterize the total error, caused by clustering, by the so called sum of squared errors:

$$\sigma_c^2 = \sum_{i=1}^K \sum_{j=1}^{m_i} (\vec{r}_i - \vec{r}_{ij})^2. \quad (4.20)$$

Here  $K$  is the number of clusters,  $m_i$  is the number of points in the  $i$ -th cluster,  $r_{ij}$  is  $j$ -th point in  $n$ -dimensional space, assigned to the  $i$ -th cluster and  $r_i = \{x_i^1, x_i^2, \dots, x_i^n\}$  is the centrum of  $i$ -th cluster. Now if we calculate the partial derivatives of  $\sigma_c^2$  with respect to  $x_i^k$ , we obtain

$$\frac{\partial \sigma_c^2}{\partial x_i^k} = 2 \sum_{i=1}^K \sum_{j=1}^{m_i} (x_i^k - x_{ij}^k). \quad (4.21)$$

In order to obtain the minimal possible value of  $\sigma_c^2$ , we set all these derivatives to zero. This can be achieved if  $\sum_{j=1}^{m_i} (x_i^k - x_{ij}^k) = 0$  and, consequently,

$$x_i^k = \sum_{j=1}^{m_i} x_{ij}^k, \quad (4.22)$$

i.e., the clustering is optimal, if  $\vec{r}_i$  is the centrum of mass for  $i$ -th cluster. The standard algorithm that allows one to achieve such clustering, sometimes referred as LLoyd's algorithm [205], is as follows:

1. Choose randomly  $K$  points in the  $n$ -dimensional space as the initial positions of cluster centra (for the clustering of  $\text{Re}_0\text{-O}_1\text{-O}_2$  paths this step is illustrated in Fig. 4.7-A:  $4 \times 4 \times 4$   $\text{ReO}_3$  supercell is used, the total number of  $\text{Re}_0\text{-O}_1\text{-O}_2$  paths is  $64 \times 24$ , number of clusters  $K = 5$ ).
2. Create  $K$  clusters by assigning all points in the  $n$ -dimensional points to the corresponding closest of cluster centra (Fig. 4.7-B).
3. Calculate centra of mass for each cluster.
4. Repeat steps 2 and 3, till the positions of cluster centra do not change significantly (Fig. 4.7-C and Fig. 4.7-D).

Obviously, the solution of clustering problem is not unique: choosing different points as initial positions for cluster centra, different clusters may be constructed. It is also worth to note that clustering problem is an example of so called  $NP$ -hard problems, i.e., with the increase of number of points, the time, required for clustering, will grow extremely non-linearly.

We can estimate the dependency of clustering error on the number of clusters  $K$  and dimensionality  $n$ . Let us assume that we have  $N$  points evenly distributed in the spherical  $n$ -dimensional region with characteristic size  $R_0$  (this quantity is somehow related to the maximal allowed displacement from the given equilibrium position). If we assume that all clusters have approximately equal sizes, then the number of points per cluster is  $N/K$ . The density of the distribution of points inside of cluster is proportional to  $\rho = N/R_0^n$ . We will assume that it is constant. The characteristic size of cluster is about  $R_K = R_0/K^{1/n}$ . The sum of the squared errors is now

$$\sigma_c^2 \approx K \rho \int_V r^2 dV \sim K \rho \int_0^{R_k} r^2 r^{n-1} dr, \quad (4.23)$$

where  $V$  is a sphere with radius  $R_k$  and we have used the fact that the surface of a surface element in  $n$ -dimensional space is proportional to  $r^{n-1}$ . Now one obtains

$$\sigma_c^2 \sim K \rho R_k^{n+2} = K \frac{N}{R_0^n} R_0^{n+2} K^{-(1+2/n)} = N R_0^2 K^{-2/n}. \quad (4.24)$$

From this result one can see, for example, that if we increase number of points  $N$  (increase the size of supercell) or the maximal allowed displacement from the



equilibrium, the number of clusters should be increased. Also it can be seen, the increase of  $K$  in the case of larger number of dimensions  $n$  reduces the sum of the squared errors less significantly: with the increase of dimensionality of problem, the clustering will work less efficiently. Luckily, in the case of EXAFS calculations, the paths with a few degrees of freedom have the most significant contribution to the total spectra.

To characterize the approximation error for EXAFS spectra (which, obviously, is strongly related to the error of clustering  $\sigma_c^2$ ) one can introduce a parameter  $\xi_c = \frac{\|\chi_{\text{app.}}(k)k^n - \chi_{\text{precise}}(k)k^n\|_2}{\|\chi_{\text{precise}}(k)k^n\|_2}$ , where  $\chi_{\text{precise}}$  and  $\chi_{\text{app.}}$  are partial contributions to the EXAFS spectra from paths of given type, calculated precisely and within clustering approximation, respectively. For the case of  $\text{Re}_0\text{-O}_1\text{-O}_2$  paths the dependency of the quantity  $\xi_c$ , as well as the time, required for clustering and consequent EXAFS calculations, on the number of clusters  $K$  are shown in Fig. 4.7-E. As one can see, the error of approximation is below 1% in this case, if  $K = 50$ , and does not improve significantly, if the number of clusters is increased. The partial contribution to the EXAFS spectra from  $\text{Re}_0\text{-O}_1\text{-O}_2$  path, calculated with 50 cluster, and difference between this approximate and precise signals are shown in Fig. 4.7-F.

In the case of evolutionary algorithm simultaneously  $M$  supercells are used. Significant improvement of calculation speed can be obtained, if one note that the positions of atoms in these supercells, hence also the corresponding sets of photoelectron scattering paths are not different, especially at the final stages of EA calculations. Therefore we propose to perform the clustering procedure for all  $M$  supercells simultaneously, following steps, listed below:

1. The lists of paths, corresponding to all supercells, are merged together, and common cluster centra, which give the good description for spectra from all supercells, are found.
2. Partial contributions to EXAFS spectra, corresponding to the obtained common cluster centra, are calculated using FEFF code.
3. The paths, corresponding to the each of the supercells, are analyzed separately again, and for each path the closest of the common cluster centra is found.

4. For each supercell the corresponding EXAFS spectrum is obtained by summing up the pre-calculated EXAFS spectra for common cluster centra, multiplied by the number of paths assigned for this supercell to the given centrum.

Thus instead of calculating EXAFS spectra for each of the  $M$  EA supercells separately, the partial contributions from the photoelectron paths to the total EXAFS spectrum are calculated only once per iteration, thus the computational time, required for EXAFS calculations, is reduced approximately  $M$  times. Unfortunately, at the same time we increase by factor of  $M$  the number of  $n$ -dimensional points, involved in the clustering problem. This leads, as was mentioned above, to a significant increase of computational time that is taken by clustering algorithm. Nevertheless, in the case of using the common centra of clusters for the EA supercells, the total time, required to perform one EA iteration still will be reduced in comparison with the case, where EXAFS for each supercell is calculated independently. Additional speed-up of calculations can be obtained, if one note that the update of cluster centra, i.e., steps (1) and (2) in the scheme above can be performed not at each iteration, but once in, say, two or three iterations (if the update of cluster centra is performed even more rarely, however, it will lead to noticeable errors in the approximation of EXAFS spectra).

For the conventional  $K$ -means clustering the number of clusters  $K$  should be specified. From the argument above (Eq. (4.24)) it is clear that this number for multiple-scattering paths with a large number of atoms involved should be much larger than for single-scattering paths to ensure the same precision. Therefore the parameter  $K$  for each path is obtained in the current version of EvAX code automatically: one starts with a small number of clusters (for example, 10) for every type of paths. Then one calculates the approximation error  $\xi_c$  and compare it with the current value of difference between theoretical and experimental EXAFS data  $\xi$ . If the ratio  $\xi_c/\xi$  is larger than some specified number  $\varepsilon$ , the number of clusters is doubled, new value of  $\xi_c$  is calculated and the procedure is repeated. Such clustering precision check and, if necessary, the increase of the number of clusters is taking place every  $T_2$  iterations. The usage of parameters for clustering algorithm within EvAX code, is described in Appendix, Sec. A.4.6.

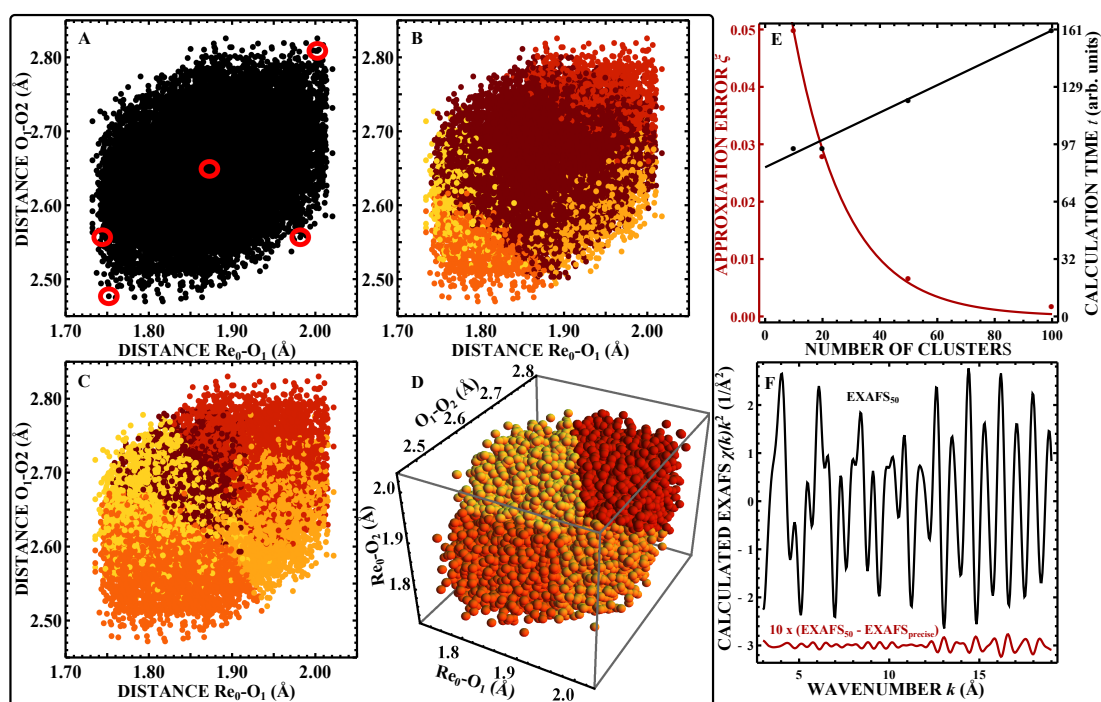


**Figure 4.7: Clustering algorithm**

Clustering of  $\text{Re}_0\text{-O}_1\text{-O}_2$  paths for Re  $L_3$  edge EXAFS from crystalline  $\text{ReO}_3$ . Projections of different steps of clustering process in  $(\text{Re}_0\text{-O}_1, \text{Re}_0\text{-O}_2)$  plane (panels A-C, see details in text), and the final result (panel D); dependencies of the time, required for clustering and consequent EXAFS calculations, and the error of approximation  $\xi_c$  on the number of clusters  $K$  (panel E); partial contribution to the EXAFS spectra from  $\text{Re}_0\text{-O}_1\text{-O}_2$  path, calculated with 50 cluster, and difference between this approximate and precise signals (panel F).

## 4.5 Data analysis: robust statistics

The solution, obtained by RMC/EA method, is a set of atomic coordinates, corresponding to the final supercell configuration. In the case of EA, when multiple supercells are used, as the final state the one, whose corresponding EXAFS spectra is the closest to the experimental data, is considered. It should be emphasized that such solution is, of course, not unique. If one repeats the simulations with the same input parameters, but employing different sequences of pseudo-random numbers, the final set of atomic coordinates will be different. However, the statistical characteristics, such as mean values and dispersions of interatomic distances and bond angles, distribution functions for distances and angles, should be close for both cases, and also close to their "experimental" analogues, if the agreement between calculated EXAFS spectra and experimental data is sufficiently good. Hence the post-processing of the results, obtained via RMC/EA

method, is important to extract physically relevant information.

The sets of interatomic distances, bonding angles and more complex structural elements, corresponding to the final configuration of supercell, can be considered as statistical samples that can be used to estimate the distributions of such elements in the population, i.e., in the investigated material. Probably the most important in our case are the distributions of interatomic distances, or so called radial distribution functions (RDFs), since they influence the EXAFS spectra through the single-scattering contributions (Eq. 2.20) that usually are dominant.

The easiest way to estimate the RDFs or distribution functions of bonding angles, etc., is to construct a **histogram** of the corresponding quantity in the statistical sample. In this case no *a-priory* knowledge on the shape of the corresponding distribution function is necessary. Similar, but more advanced approach is so called **kernel density estimation**. In this case the density distribution function  $f(x)$  is estimated as

$$f(x) = \frac{1}{nh} \sum_{i=1}^n K\left(\frac{x - x_i}{h}\right), \quad (4.25)$$

where  $x_i$  are the data values (i.e, interatomic distances, bonding angles, etc., in our final supercell),  $n$  is the size of statistical sample, parameter  $h$  is so called bandwidth and  $K$  is smoothing kernel function [206]. In this thesis for the estimation of different distribution functions the simplest kernel function - Gaussian function - was used. Kernel density estimation, similarly to the histogram approach, is also a parameter-less method. However, the bandwidth parameter  $h$  should be chosen to be much smaller than the standard deviation of the investigated population. Unlike the histogram approach, kernel density method provides smooth description of the density distribution, therefore it is much easier to compare different sets of data, for instance, the distributions, corresponding to different temperatures.

To obtain more quantitative information (average interatomic distances, MSRD factors, etc.), one needs to estimate mean values, variances, in some cases - even higher moments of investigated distributions. While the estimation of the mean value of population, having a representative statistical sample, is not a particular problem - the consistent and unbiased estimator of the population mean is just the mean value of the sample - the situation is more complicated with higher moments. The supercells that we are using for our calculations are relatively small. Therefore the variance (and, of course, higher moments) of the statistical sample

are extremely sensitive to the presence of any outliers in our data and cannot be used as estimators of the corresponding quantities of population.

To solve this problem one needs to use more robust techniques. If the shape of the distribution is known (for instance, if it can be described by Gaussian function), one can simply fit the obtained histogram of the statistical sample with the corresponding density distribution function, and hence simultaneously estimate all parameters of interest. Obviously, this approach will give a consistent estimation of structure parameters only if the underlying distribution indeed is, say, Gaussian. Sometimes this property can be even advantageous: for example, the conventional EXAFS analysis often is carried out in the Gaussian approximation. Therefore, using the fitting approach to process the RDFs from RMC/EA simulations, the obtained results are directly comparable with the results of conventional EXAFS analysis.

Alternative approach to estimate variance is so called **median absolute deviation** (MAD) method [207, 208]. The standard deviation  $\sigma$  of a distribution in this case is estimated as

$$\sigma = \text{median}(|x_1 - m|, |x_2 - m|, \dots, |x_n - m|), \quad (4.26)$$

where  $(x_1, x_2, \dots, x_n)$  is the statistical sample and  $m = \text{median}(x_1, x_2, \dots, x_n)$ . The advantage of MAD approach is that it can be applied to characterize the deviations of data, even if the shape of analyzed distribution is unknown. At the same time, MAD is an inconsistent estimator, i.e., even if the analyzed sample is infinitely large, the MAD estimator will not be equal to the true value of the standard deviation of population. On the other hand, if the approximate shape of the investigated distribution is known, one can convert MAD in a consistent estimator of  $\sigma$ , simply multiplying the MAD value by some scaling constant  $k$  that, noteworthy, is independent on the sample size (Fig. 4.8). For Gaussian distribution  $k = 1.4826$  [208]. For other distributions the corresponding value of  $k$  can be derived analytically or obtained in numerical simulations.

In Fig. 4.8 the MAD estimators for data, sampled from Gaussian distribution  $f(x) = e^{-x^2/(2\sigma^2)}/\sqrt{2\pi\sigma^2}$  with different values of scale parameters  $\sigma$  and different sample sizes  $n$  are shown. As one can see, MAD, on average, is indeed proportional to  $\sigma$  with scaling coefficient  $k = 1.4826$ .

Related to the problem of determination of MSRD factors is also the determination of MSD factors: in this case we are interested in the mean-square

displacement of atom from its equilibrium position  $\langle u^2 \rangle$ . By analogy with the previous case, we can estimate this quantity as

$$\langle u^2 \rangle = (k \times \text{median}(u))^2. \quad (4.27)$$

In the case of isotropic and harmonic atomic oscillations, atomic displacements  $u$  are distributed accordingly to Maxwell distribution  $f(u) = u^2 e^{-u^2/(2\sigma^2)} / (\sqrt{\pi/2}\sigma^3)$ . The sought quantity  $\langle u^2 \rangle$  then is equal to  $\int_0^\infty f(u)u^2 du = 3\sigma^2$ . Median of the distribution, in turn, is equal to  $\text{median}(u) = \sigma \sqrt{2Q^{-1}(3/2, 1/2)} \approx 1.538\sigma$ , where  $Q(a, b) = \Gamma(a, z)/\Gamma(a)$  is regularized incomplete gamma function. Thus the scaling coefficient  $k$  in Eq. 4.27 is equal to  $k = \sqrt{3}/1.538 = 1.126$  (in Fig. 4.8-C the numerically obtained values of coefficient  $k = \sqrt{\langle u^2 \rangle}/\text{median}(u)$  for data, sampled from Maxwell distribution with different values of scale parameters  $\sigma$  are shown).

Similar arguments can be applied to derive also the estimators for projected MSD factors. For MSD in a given direction  $f(u_{\parallel}) = e^{-u_{\parallel}^2/(2\sigma^2)} / (\sqrt{\pi/2}\sigma)$  (half-normal distribution) and

$$\langle u_{\parallel}^2 \rangle = \left( \frac{1}{\sqrt{2}\text{erf}^{-1}(1/2)} \times \text{median}(u_{\parallel}) \right)^2 \approx (1.4826 \times \text{median}(u_{\parallel}))^2 \quad (4.28)$$

(note, the scaling coefficient is the same as for the MSD correction of normally distributed data). For MSD, orthogonal to a given direction,  $f(u_{\perp}) = e^{-u_{\perp}^2/(2\sigma^2)} / \sigma^2$  (Rayleigh distribution) and

$$\langle u_{\perp}^2 \rangle = \left( \sqrt{\frac{2}{\ln 4}} \times \text{median}(u_{\perp}) \right)^2 \approx (1.201 \times \text{median}(u_{\perp}))^2. \quad (4.29)$$

From the results, shown in Fig. 4.8, one can also note that even in the ideal case of model data without any experimental noise due to the limited size of the sample the parameters of the distribution will always be estimated within some statistical uncertainty. In the case of RMC/EA simulations such statistical uncertainty can be assessed by comparing the results obtained in simulations with different sequences of pseudo-random numbers and/or different initial conditions.

Within this thesis, the quantities as average interatomic distances and average bonding angles are usually estimated as the mean values of the sets of correspond-

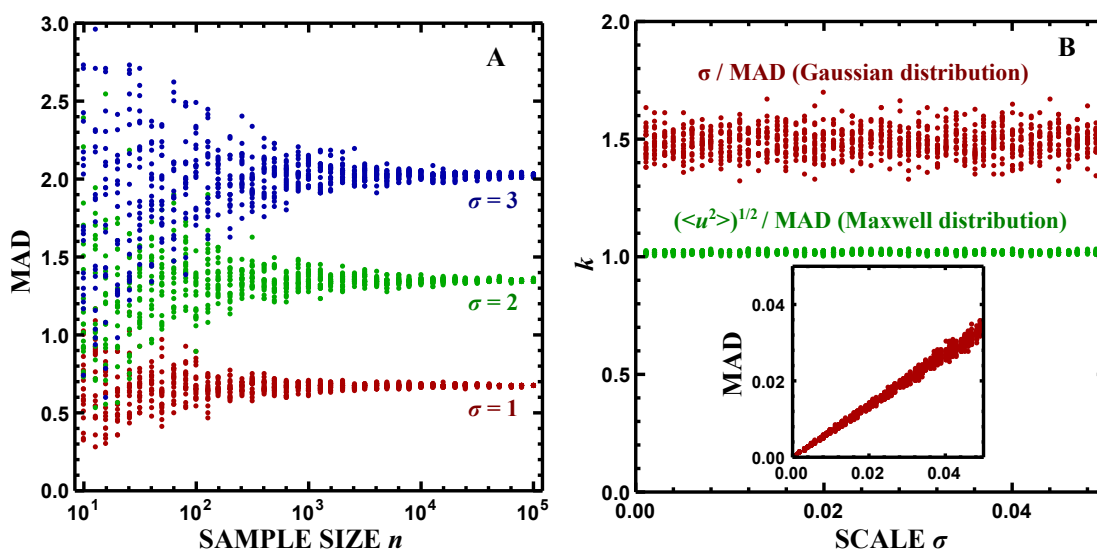


**Figure 4.8: MAD estimator**

MAD estimators, calculated for data, sampled from Gaussian distribution with scale parameters  $\sigma$  equal to 1, 2 and 3 and different sample sizes  $n$  (panel A); coefficients  $k = \sigma/\text{MAD}$  and  $k = \sqrt{\langle u^2 \rangle}/\text{MAD}$ , calculated for data, sampled from Gaussian and Maxwell distribution, correspondingly, with different values of scale parameters  $\sigma$  and sample size  $n = 1000$  (panel B); MAD estimators, calculated for data, sampled from Gaussian distribution with different values scale parameters  $\sigma$  and sample size 1000 (inset of panel B).

ing quantities in the final supercell configurations. The MSR factors (variances of RDFs), are usually estimated by fitting the peaks of RDFs with Gaussian functions. The mean-square displacements (MSD factors) are estimated using MAD approach with corresponding scaling coefficient  $k$ .

## 5. RMC-EXAFS FOR CRYSTALLINE GERMANIUM: RMC ANALYSIS FOR SIMPLE SYSTEMS

### 5.1 Introduction<sup>1</sup>

There is probably no need to emphasize the importance and possible applications of crystalline germanium. Due to its electrical properties, simple structure (space group  $Fd\bar{3}m$ ) and relatively simple manufacturing process, it is one of the most well-studied materials. At the same time it is interesting to note that the first paper, where the detailed analysis of EXAFS data from crystalline germanium was presented, appeared only in 1995 [209]. This work was followed by the paper [210], and both of these articles were devoted to the temperature-dependent study of the Ge K-edge EXAFS spectra with the focus on thermal expansion and temperature-dependencies of the amplitudes of atomic vibrations. The real success of EXAFS spectroscopy as a method for atomic structure analysis was another study of the same group of authors [211], where for the first time it was demonstrated that EXAFS measurements are sensitive and precise enough to detect tiny changes of the atomic relative vibrational amplitudes due to isotopic effect, i.e., slightly different atomic masses (in that paper the EXAFS spectra of  $^{70}\text{Ge}$  and  $^{76}\text{Ge}$  have been analyzed). The paper [211] has been devoted mainly to the analysis of isotopic effect in the first coordination shell. This work was continued in the paper [212] and also in the master-thesis of the author [213].

The simulation-based approach to the study of the dynamics and structure of crystalline germanium (as well as crystalline silicon and other similar semiconductors) originates in the works by Stillinger, Weber and Ding [214, 215]. In these papers a complicated force field model, so called Stillinger-Weber potential, was introduced that allowed to treat many-body interactions, characteristic for silicon and germanium, and to carry out classical molecular dynamics simulations for these materials. A few years later even more complicated force field model, Tersoff potential, has been presented [216, 217].

---

<sup>1</sup>The material, presented in this Chapter, has been published as J. Timoshenko, A. Kuzmin, J. Purans, REVERSE MONTE CARLO MODELLING OF THERMAL DISORDER IN CRYSTALLINE MATERIALS FROM EXAFS SPECTRA, *Comp. Phys. Commun.* 183 (2012) p. 1237-1245





**Figure 5.1:** Crystalline germanium samples used for EXAFS measurements.

In [218] and [213] it was proposed to use MD simulations for the analysis EXAFS data from crystalline Ge. In these works it has been shown, in particular, that the multiple-scattering contributions to the total EXAFS spectrum are relatively small in the case of crystalline germanium. However, they are less temperature-sensitive than single-scattering contributions, therefore the importance of MS effects is larger at higher temperatures, when the amplitude of single-scattering contributions is significantly reduced by strong atomic vibrations.

To sum up - the crystalline germanium is well-known, relatively simple material with relatively weak influence of multiple-scattering contributions. Before starting this work, we already had the results of molecular dynamics simulations, as well as EXAFS data from samples with excellent quality, used previously for the study of isotopic effect [211, 212] (Fig. 5.1). All these conditions made the crystalline germanium to be an ideal candidate for our first RMC-EXAFS investigations. In this Chapter we employ the conventional RMC scheme without Evolutionary Algorithms.

## 5.2 Application of the RMC-EXAFS method to model data

### 5.2.1 RMC simulations for model data

To test our RMC scheme, we applied it first to the model data: artificial Ge K-edge EXAFS spectrum of crystalline germanium. It was calculated using the results of molecular dynamics (MD) simulation, based on the Stillinger-Weber

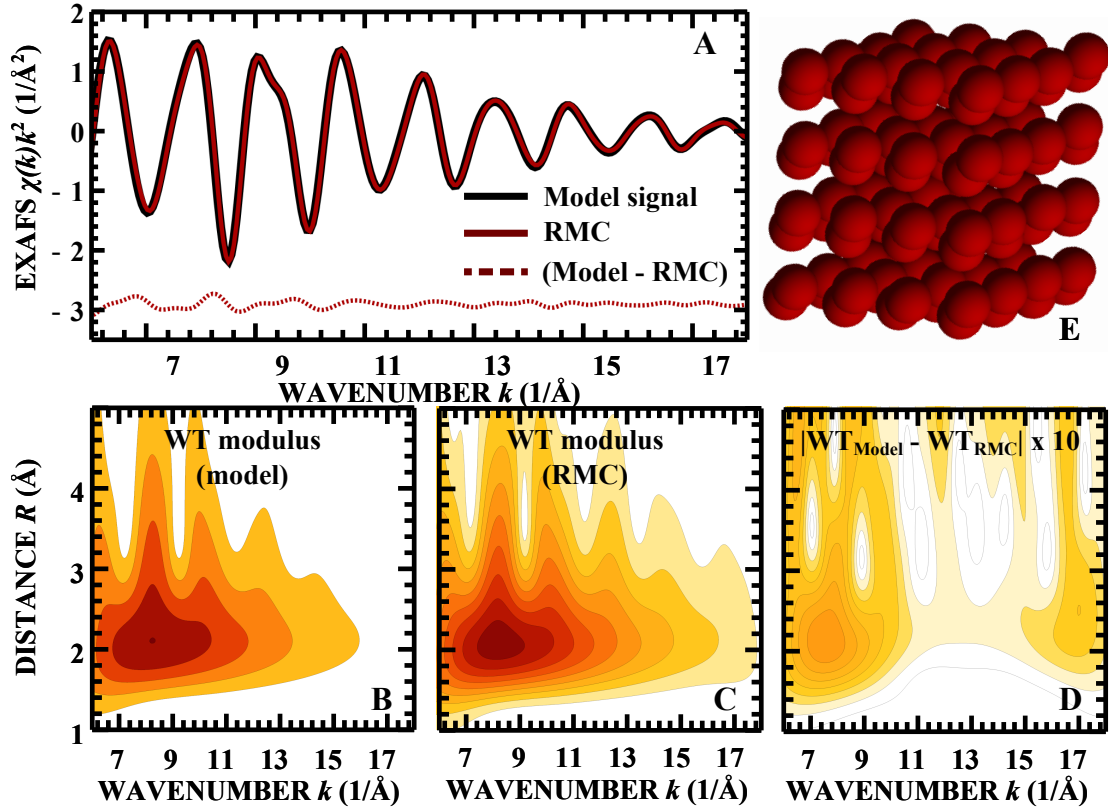


**Figure 5.2: RMC fit of the model data**

Panel A: model Ge K-edge EXAFS spectrum (black line) and EXAFS spectrum, obtained in RMC simulations (solid red line), and their difference (dashed red line). Bottom panels: WT moduli for model EXAFS spectrum (B), for EXAFS spectrum, obtained in RMC simulations (C) and for the difference between model and RMC-EXAFS spectra (D). Panel E:  $4 \times 4 \times 4$  supercell (128 atoms), used in the RMC simulations of crystalline germanium.

force field [218] and performed within the NVT ensemble for the lattice constant  $a_{\text{Ge}} = 5.658 \text{ \AA}$  [219] at the effective temperature of 395 K. It has been shown in [218] that the theoretical EXAFS spectrum, obtained within such simulation, is very similar to the real Ge K-edge EXAFS data from crystalline germanium at 300 K.

The RMC simulation cell was composed of 64 unit cells of germanium, forming a  $4 \times 4 \times 4$  supercell with 128 atoms inside. The total number of the RMC steps was 40000. The difference  $\xi_k$  between calculated by RMC and model EXAFS spectra was calculated in  $k$ -space by Eq. (4.5). The obtained result is shown in Fig. 5.2, where the supercell, both EXAFS spectra and the wavelet transforms of the model EXAFS and difference between the model and calculated spectra are presented. In Fig. 5.3 the comparison between the model and calculated spectra

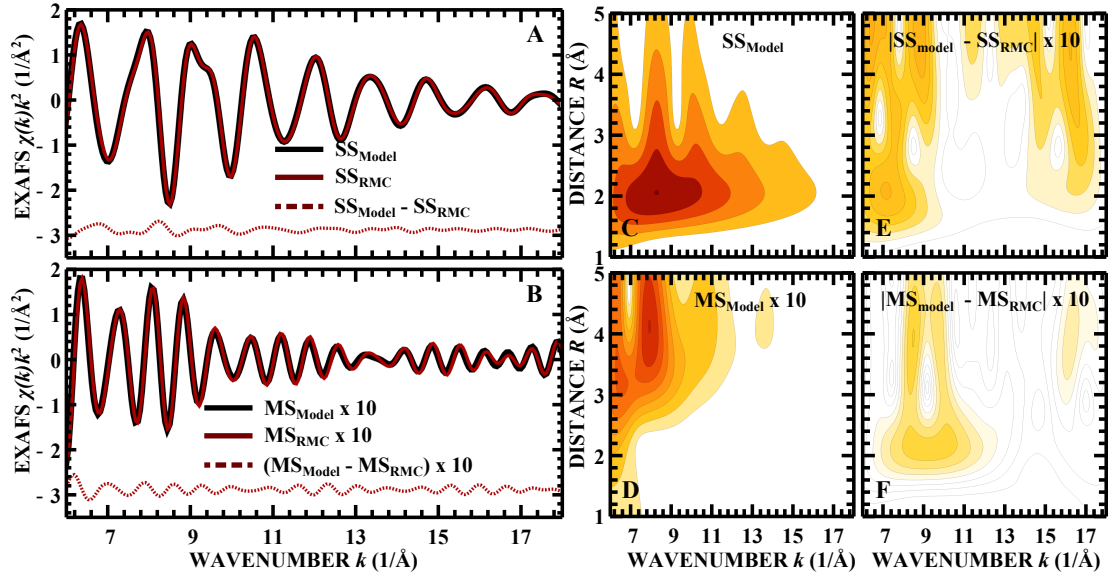


**Figure 5.3:** RMC fit single-scattering and multiple-scattering contributions

Panels A and B: model Ge K-edge EXAFS spectrum (black line) and EXAFS spectrum, obtained in RMC simulations (solid red line) for single-scattering (SS) and multiple-scattering (MS) contributions, and their difference (dashed red line). Panels C - F: WT moduli for corresponding model EXAFS spectra and corresponding differences between model and RMC-EXAFS spectra.

is separately shown for single-scattering and multiple-scattering contributions. It can be seen, although for the crystalline germanium the changes of EXAFS spectrum due to the multiple-scattering effects are relatively small, they can be accurately reconstructed and analyzed using our RMC scheme. The development of the scaling parameter for simulated annealing  $T$  and difference between calculated and model spectra  $\xi_k$  during the simulations are shown in Fig. 5.4.

**Table 5.1:** Values of mean-square displacements ( $u^2$ ), mean-square relative displacements ( $\sigma^2$ ) and the mean coordination shell radii  $\langle R \rangle$  in crystalline germanium at 395 K for the starting model and obtained by the RMC simulation for a  $4 \times 4 \times 4$  supercell.

	Starting model	RMC result
$\langle R \rangle_{1st\ shell}$ (Å)	2.45479(6)	2.454(3)
$\langle R \rangle_{2nd\ shell}$ (Å)	4.00458(6)	4.004(3)
$\langle R \rangle_{3rd\ shell}$ (Å)	4.69485(7)	4.695(2)
$\sigma_{1st\ shell}^2$ (Å <sup>2</sup> )	0.003262(5)	0.004(1)
$\sigma_{2nd\ shell}^2$ (Å <sup>2</sup> )	0.010716(1)	0.0105(3)
$\sigma_{3rd\ shell}^2$ (Å <sup>2</sup> )	0.014804(1)	0.013(1)
$u^2$ (Å <sup>2</sup> )	0.0272(6)	0.0214(7)

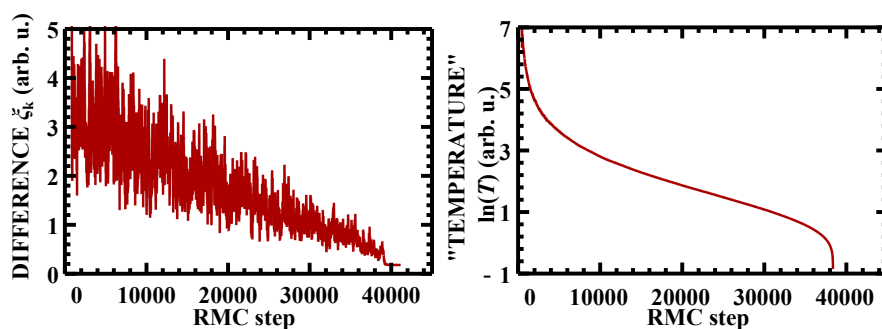


**Figure 5.4: Simulated annealing parameters**

Dependencies of the difference  $\xi_k$  and parameter  $T$  on the number of the RMC steps.

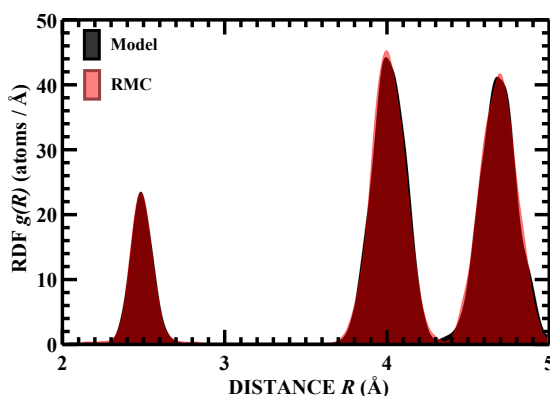


**Figure 5.5: The radial distribution function around germanium atom for the model**

Comparison of RDFs around germanium atom for the model data and for the results of the RMC simulations.

In Fig. 5.5 the radial and bonding angle distribution functions for our MD model are compared with that obtained from RMC simulations: the agreement between both sets of functions for the nearest coordination shells of germanium is very good, implying that RMC method in this case successfully reconstructs the statistical characteristics of the sample, such as mean values and dispersions of interatomic distances and bonding angles. We compare the values of the mean-square displacements (MSD or  $u^2$ ), mean-square relative displacements (MSRD or  $\sigma^2$ ) and the mean coordination shell radii  $\langle R \rangle$  for the first three coordination shells of Ge in the starting model and as obtained by the RMC simulation in Table 5.1. As one can see, our RMC method is able to recover with very good accuracy (less than 1%) the mean shell radii and reasonably well uncorrelated (MSD) and correlated (MSRD) thermal vibration amplitudes.

### 5.2.2 Influence of the cell size and simulation length

The cell size and the simulation length (number of RMC steps) are important parameters, which affect both the results of RMC simulation as well as computational resources required. Therefore, their optimal choice is crucial.

We have repeated our simulations also for two smaller supercells,  $2 \times 2 \times 2$  (16 atoms) and  $3 \times 3 \times 3$  (54 atoms), varying the number of RMC steps between 10000 and 80000. The obtained results are compared in Fig. 5.6. The agreement between calculated and model EXAFS spectra improves significantly by increasing the supercell size from  $2 \times 2 \times 2$  to  $3 \times 3 \times 3$ . Further increase of the supercell size does not lead to a notable improvement of the agreement between calculated and model EXAFS spectra. Therefore the increase of the supercell will not ensure more precise determination of structure parameters. Instead, multiple RMC calculations with the same supercell but different sequences of pseudo-random numbers can be carried out to reduce statistical error.

The results, obtained after 20000, 40000 or 80000 RMC steps, are very close to each other and to the model data. However, the shorter simulation with just 10000 RMC steps results in the EXAFS spectrum, which deviates strongly from the model one, giving the  $\xi_k$  value about five times larger than it is in the cases with longer simulations.

Finally, one can conclude that in the case of crystalline germanium, the good results can be obtained already for the size of the supercell  $3 \times 3 \times 3$  and the number of the RMC steps being at least 40000.

### 5.2.3 Determination of the lattice parameters

The RMC simulations, discussed above, were all performed at the fixed cell size. However, when the lattice parameters of the crystal are not known accurately enough (better than  $0.01 \text{ \AA}$ ), the cell size and shape could be, in principle, adjusted during the RMC run. In this case, the values of the lattice constants and angles become additional degrees of freedom and can be slightly and randomly changed at each RMC step.

For cubic crystalline germanium there is only one parameter, the lattice constant  $a_{\text{Ge}}$ , determining the cell. Therefore, it is a simple case, for which such calculations can be easily performed, and their results are shown in Fig. 5.7. The RMC simulation was performed for  $3 \times 3 \times 3$  supercell and 40000 RMC steps. It should be noted that the difference between the model and calculated EXAFS

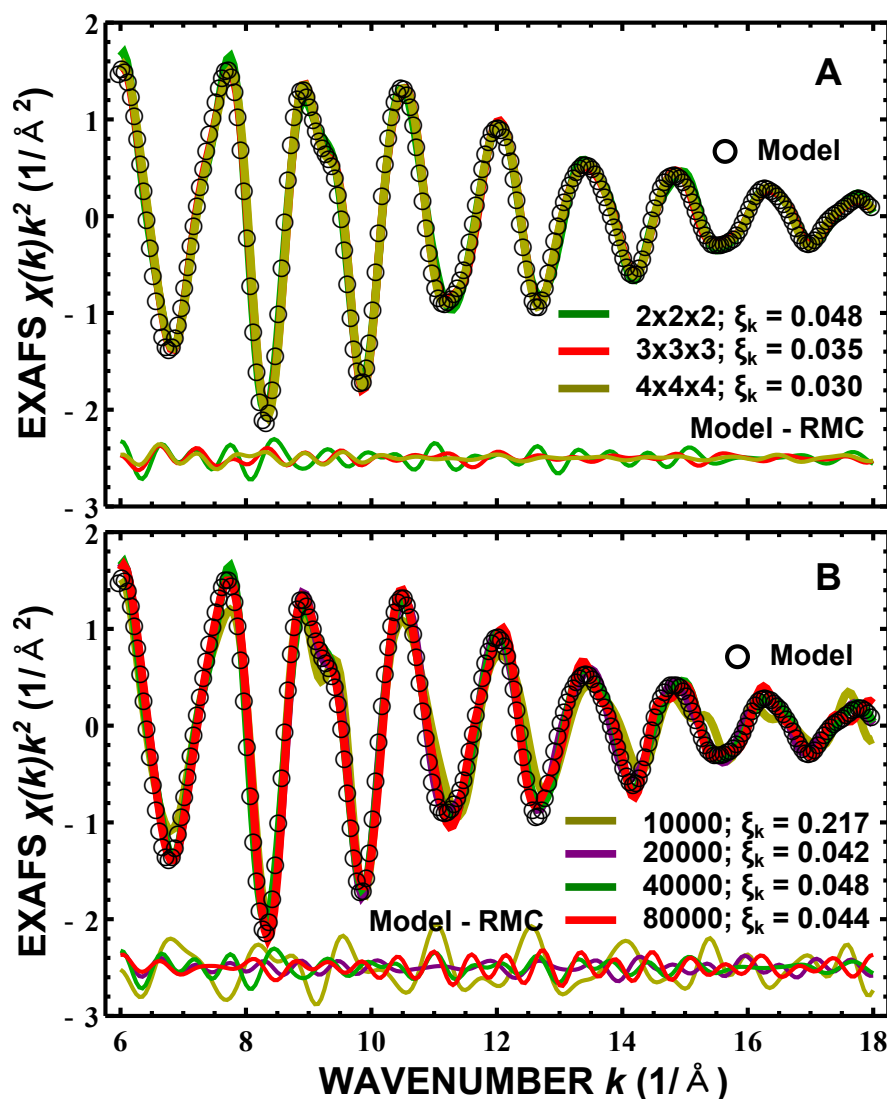


**Figure 5.6: Influence of the cell size and simulation time**

Comparison between the model Ge K-edge EXAFS spectrum (circles) and the EXAFS spectra, obtained from the RMC simulations of crystalline germanium using different parameters (thick solid lines). The corresponding differences between model spectrum and RMC spectra are shown with thin solid lines at the bottom of panels.  $\xi_k$  is the final difference, calculated by Eq. (4.5). The values of the parameters are: (panel A) the length of simulation is 40000 RMC steps and the sizes of the supercells are  $2 \times 2 \times 2$ ,  $3 \times 3 \times 3$ , and  $4 \times 4 \times 4$ ; (panel B) the size of the supercell is  $2 \times 2 \times 2$  supercell, the lengths of simulations are 10000, 20000, 40000, and 80000 RMC steps.

spectra has been evaluated using the wavelet transform (Eq. (4.12)), since we found that the calculations in  $k$ -space were less accurate in this case. This example shows that the use of the WT as a criterion for minimization has an advantage, even if it is computationally slightly more heavy.

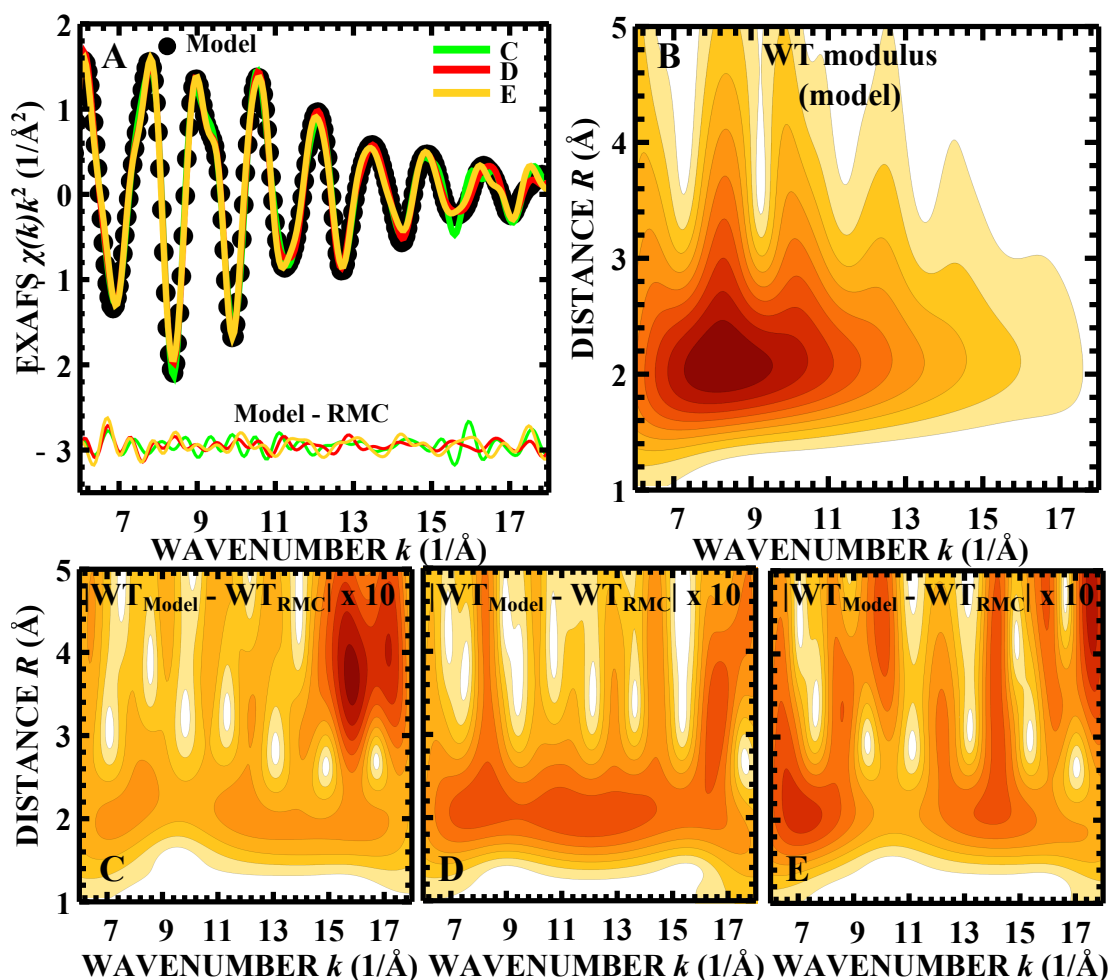


**Figure 5.7: Determination of the lattice constant**

Results of the RMC simulations with variable lattice constant for the model Ge K-edge EXAFS spectrum, obtained from the MD calculations of crystalline germanium. Ge K-edge EXAFS spectrum for the starting MD model (black dots on panel A, panel B - its wavelet image) and the result of RMC simulations with (C) fixed lattice constant  $a = 5.658 \text{ \AA}$ , the difference  $\xi_{k,R} = 0.056$ ; (D) lattice constant, varied during the simulations: initial value of the lattice constant is  $a = 5.608 \text{ \AA}$ , its final value is  $a = 5.652 \text{ \AA}$ , the difference  $\xi_{k,R} = 0.033$ ; (E) lattice constant, varied during the simulations: initial value of lattice constant is  $a = 5.708 \text{ \AA}$ , its final value is  $a = 5.679 \text{ \AA}$ , the difference  $\xi_{k,R} = 0.037$ . The corresponding differences between model spectrum and RMC spectra are shown by thin lines at the bottom of panel A, the wavelet images of the difference are shown on bottom panels C, D, E, correspondingly.

As one can see in Fig. 5.7, the variation of lattice constant  $a_{\text{Ge}}$  during the RMC process results in a good agreement between the model and calculated EXAFS spectra. The obtained value  $a_{\text{Ge}}$  agrees with the expected one within about  $0.02 \text{ \AA}$ : such accuracy is sufficient for the conventional EXAFS analysis.

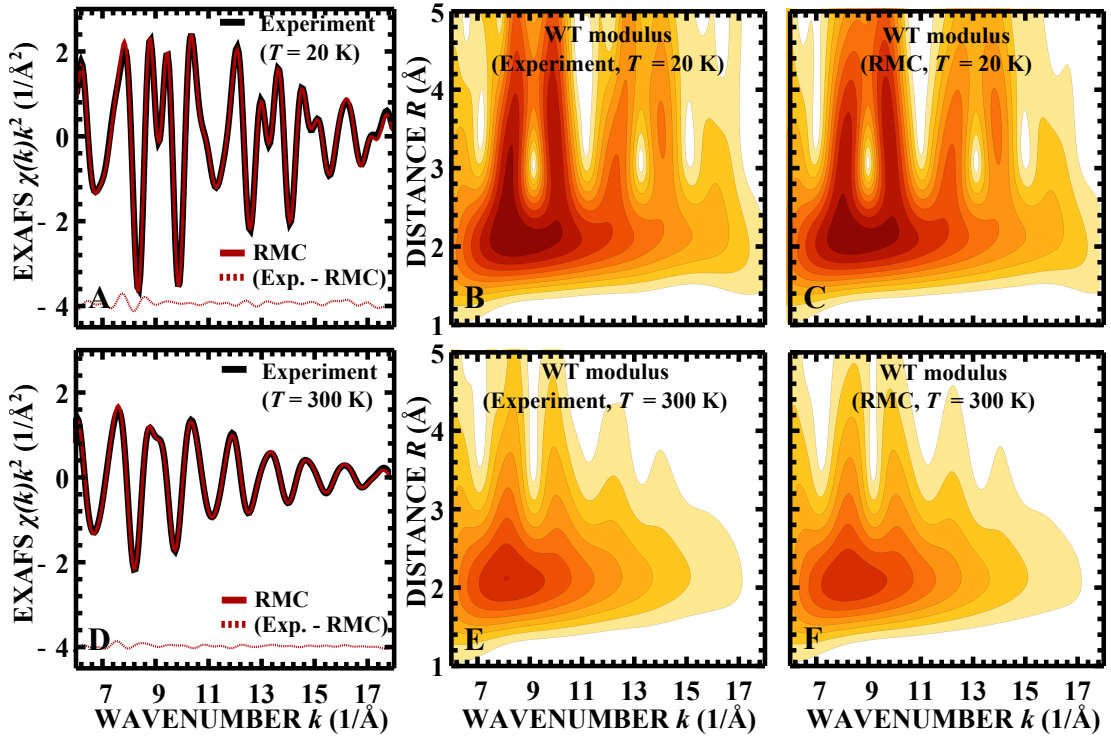


**Figure 5.8:** RMC analysis of experimental Ge K-edge EXAFS spectra. Experimental and calculated by the RMC method Ge K-edge EXAFS spectra for crystalline germanium at  $T=20$  K (panel A) and at  $T=300$  K (panel D), and their corresponding WT images (panels B, C - WT modulus of experimental spectrum and of RMC spectrum for  $T=20$  K, panels D, E - WT modulus of experimental spectrum and of RMC spectrum for  $T=300$  K). The differences between experimental and RMC spectra are  $\xi_{k,R} = 0.092$  for the low-temperature data and  $\xi_{k,R} = 0.053$  for the room-temperature case (Eq. (4.12)).

### 5.3 Application of the RMC-EXAFS method to experimental data

Next we will apply the proposed RMC scheme to the analysis of experimental Ge K-edge EXAFS in crystalline germanium [6].

While the model, discussed in Sec. 5.2, is very close to the experimental EXAFS spectrum, nevertheless, there are several differences between the analysis of model data and of real experimental EXAFS spectra: (i) the already mentioned problem with the value of the lattice parameters; (ii) the influence of experimental noise; (iii) the influence of outer coordination shells; (iv) the presence of the amplitude reduction factor  $S_0^2$ ; (v) the problem of the choice of energy reference  $E_0$ . The parameter  $E_0$  is never known precisely and, in principle, can be even different for several measurements of the same sample due to, for example,



instability of the monochromator positions during the experiment.

The first problem has been already addressed in Sec. 5.2.3. The second and third problems can be treated using the proper Fourier or wavelet filtering of the experimental data. The fourth and the fifth problems require to estimate additional parameters  $S_0^2$  and  $E_0$ . In principle, they can be calculated in the same way as the lattice parameters during the RMC simulations. However, such approach is complicated due to the strong correlations between  $S_0^2$  and the EXAFS amplitude, and between  $E_0$  and the EXAFS frequency. Therefore, in this work we did not refine  $S_0^2$  and  $E_0$  during the RMC calculations. Instead, before the simulations we carried out the conventional analysis of the EXAFS spectrum from the first coordination shell (Sec. 2.7.2), and obtained the values of  $S_0^2$  and  $E_0$ , which were fixed in the further RMC calculations.

For the analysis of the experimental EXAFS spectra of crystalline germanium [212], measured in the temperature range from 20 K to 300 K, the  $3 \times 3 \times 3$  supercell was constructed, and the RMC simulations were carried out for 40000 steps. The lattice constant was fixed during the calculations at the known experimental value  $a_{\text{Ge}} = 5.658 \text{ \AA}$  [219]. The minimization was performed using the wavelet transform criterion (Eq. (4.12)).

The experimental Ge K-edge EXAFS spectrum, measured at 20 K, and the result of the RMC simulations are compared in Fig. 5.8. Note that while the theoretical EXAFS spectrum includes all multiple-scattering contributions in the range up to 6  $\text{\AA}$  around the absorber, their importance is not crucial in this case [218]. The temperature-dependencies of the mean-square relative displacement (MSRD) for the first, second and third coordination shells, obtained from the RMC simulations and using conventional EXAFS analysis [212], are compared in Fig. 5.9. The agreement between the two results is good, so one can conclude that the accuracy of the proposed method is sufficient to analyze the thermal disorder in crystalline material.

## 5.4 Conclusions

In this chapter we applied the improved Reverse Monte Carlo (RMC) scheme for the analysis of the EXAFS spectra from crystalline germanium, using for the analysis also the Morlet continuous wavelet transform of the EXAFS spectrum and simulated annealing method to ensure the convergence of the simulations.

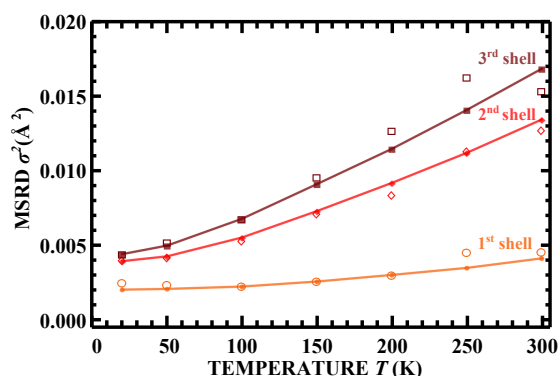


**Figure 5.9: Temperature dependencies of MSDR factors**

MSRD factors for the 1st, 2nd, and 3rd coordination shells of Ge in crystalline germanium. Results obtained by conventional EXAFS analysis [212] are shown by lines and solid symbols, MSDR factors, calculated using the proposed RMC scheme are shown by open symbols.

The use of the method is demonstrated on the example of the EXAFS spectra analysis both for the model system and for the experimental Ge K-edge EXAFS data. It is shown that the method allows one to reconstruct the 3D atomic structure of the compound taking into account the thermal disorder and to obtain the distributions of distances describing the local structure around the absorber. Also the uncorrelated (MSD) and correlated (MSRD) thermal vibration amplitudes can be recovered with reasonable accuracy.

## 6. RMC/EA-EXAFS FOR RHENIUM TRIOXIDE: TREATING MULTIPLE-SCATTERING EFFECTS

### 6.1 Introduction

Rhenium trioxide ( $\text{ReO}_3$ ) is a perovskite-type compound (space group  $Pm\bar{3}m$ ) that has a number of interesting properties. First of all, due to the delocalization of  $5d$ -electron of rhenium atoms it has a surprisingly large electrical conductivity (about  $7 \cdot 10^7 S/m$  at room temperature) that is close to the value, characteristic for silver [220, 221]. At the same time, it is also a ionic-type conductor, since the hydrogen ions can intercalate the  $\text{ReO}_3$  lattice easily [222].

Additionally, it is often considered as a model material to explain the so called negative thermal expansion (NTE) effect: rhenium atoms are bonded to the six closest oxygen atoms, located at the vertices of rhenium-centered octahedra, by strong covalent bond and Re–O distance is practically independent on temperature. Thus it is believed that the thermal motion of oxygen atoms leads to the rotation of  $\text{ReO}_6$  octahedra, connected by vertices, and consequent shrinking of Re–Re distance and the whole  $\text{ReO}_3$  lattice upon temperature increase [223, 224, 225]. At the same time, in the case of  $\text{ReO}_3$  the value of such negative expansion is very low, if compared, for instance, with scandium fluoride that has the same structure [226].

Regarding EXAFS spectroscopy, it is necessary to note that multiple-scattering (MS) effects are essential for crystals with cubic symmetry as rhenium trioxide, where the MS contributions are strongly enhanced due to the "focusing effects" within the collinear atomic chains [28, 30]. Numerous EXAFS studies on crystalline rhenium trioxide have been carried out during the last decades [30, 227, 228, 229, 230]. EXAFS studies of negative thermal expansion in  $\text{ReO}_3$  have been reported in [231]. In all of these studies the first ( $\text{Re}_0\text{--O}_1$ ) and fourth ( $\text{Re}_0\text{--Re}_4$ ) coordination shell around absorbing rhenium atom has been considered: these are the only single-scattering contributions that can be to some extent separated from the total EXAFS data and analyzed by the conventional methods of EXAFS analysis [229]. Contributions from the second, third and further coordination shells, in turn, are inaccessible for the conventional methods, because

they overlap with several strong multiple-scattering contributions [30]. Thus the simulation-based approaches for the analysis of EXAFS data are required to advance the understanding of local structure and lattice dynamics in this material. Regarding such techniques, one should mention the recent MD-EXAFS study of  $\text{ReO}_3$  by Kalinko et al [59].

In this chapter we present the results of the RMC/EA-EXAFS study of lattice dynamics in  $\text{ReO}_3$  over a broad range of temperatures from 10 K to 573 K. The results of two different studies are summarized here: (i) the results of conventional RMC simulations for the first coordination shells (up to 4.5 Å from absorbing Re atom) are given in Sec. 6.2 and (ii) the results of RMC/EA simulations with the influence of further coordination shells (up to 5.6 Å from absorbing Re atom) also taken into account are given in Sec. 6.3. Note that in the latter case due to significantly larger number of the scattering paths that should be included into analysis, the conventional RMC simulations were almost infeasible for the available computational resources and the use of evolutionary algorithms was essential.

The results of related studies, devoted to the investigation of hydrogen intercalation process in the  $\text{ReO}_3$  lattice, are given in the next chapter.

## 6.2 Conventional RMC simulations for the $\text{ReO}_3$ <sup>1</sup>

### 6.2.1 Simulation details and calculations for model system

Before applying the proposed method to experimental data, we have validated it using the model Re  $L_3$ -edge EXAFS signal for  $\text{ReO}_3$ , obtained from molecular dynamics (MD) simulations [59]. Such model spectrum will be referred further as the MD-EXAFS spectrum. In [59] the MD was performed for the  $5 \times 5 \times 5$  supercell with the unit cell size  $a_{\text{MD}} = 3.75$  Å in the NVT ensemble at the temperature  $T = 300$  K using the Buckingham and covalent exponential interatomic potentials to describe Re–O and O–O bonding as described in [59]. The Re  $L_3$ -edge EXAFS spectrum has been calculated for each of the 4000 atomic configurations, obtained in the MD simulations, and, finally, the configuration-averaged EXAFS spectrum (MD-EXAFS) has been obtained as the average of all these spectra (see [59] for

---

<sup>1</sup>The material, presented in this Section, has been published as J. Timoshenko, A. Kuzmin, J. Purans, AN EFFICIENT IMPLEMENTATION OF THE REVERSE MONTE CARLO METHOD FOR EXAFS ANALYSIS IN CRYSTALLINE MATERIALS, J. Phys.: Conf. Ser. 430 (2013) 012012 (4 pages).

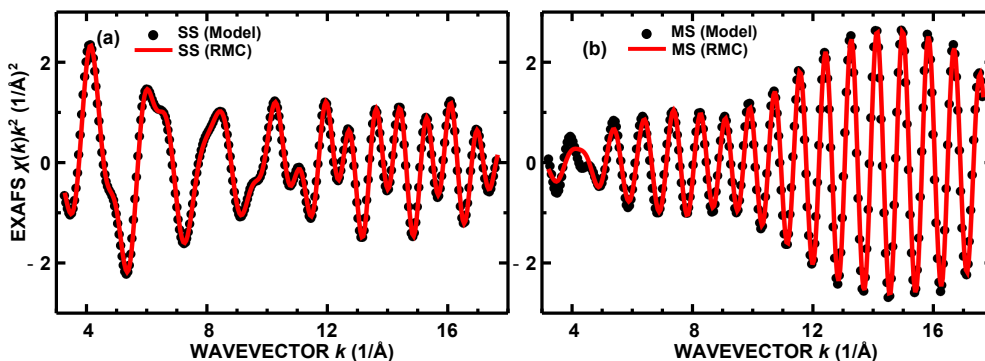


**Figure 6.1: RMC analysis of  $\text{ReO}_3$  model EXAFS spectrum**

Model (dots) and reconstructed by the RMC simulation (lines)  $\text{Re L}_3$ -edge EXAFS spectra  $\chi(k)k^2$  for  $\text{ReO}_3$ . The SS and MS contributions are shown separately.

details). Note that the MD-EXAFS spectrum agrees well with the experimental  $\text{Re L}_3$ -edge EXAFS spectrum, measured at 300 K [59].

The RMC calculations have been carried out for  $4 \times 4 \times 4$  supercell (256 atoms) and 40000 iterations. The difference between the model and RMC-EXAFS spectra has been minimized by the best fit of their wavelet transforms, i.e., simultaneously in  $k$ -space (from 3 to  $18 \text{ \AA}^{-1}$ ) and in  $R$ -space (from 0 to  $R_{\text{max}}=4.5 \text{ \AA}$ ) (see Sec. 4.3.2). As one can see in Fig. 6.1, due to the cubic perovskite-type structure of  $\text{ReO}_3$ , the contribution of MS effects to the total EXAFS signal is comparable to the one from SS paths. Moreover, our RMC scheme allows us to reconstruct and analyze simultaneously both SS and MS parts of the EXAFS spectrum.

In our RMC simulations, the maximal allowed displacement for each atom from its equilibrium position was set to  $0.2 \text{ \AA}$ : such constraint significantly increases the stability of the simulation and reduces the required computation time and does not corrupt the radial distribution functions (RDFs) and the distribution functions of bonding angles for the first two coordination shells, because due to the strong correlation between atomic displacements the amplitude of the thermal fluctuations of interatomic distances is smaller than  $0.2 \text{ \AA}$ . However, it may corrupt the distributions of atomic displacements, especially for oxygen, whose oscillation amplitude is significantly larger.

The estimated values of the mean-square radial displacements (MSRD) for the first two coordination shells ( $\text{Re}_0\text{-O}_1$  and  $\text{Re}_0\text{-Re}_2$ ) differ from that in the MD model by only about  $0.0001 \text{ \AA}^2$ , and the average value of the  $\text{Re}_0\text{-O}_1\text{-Re}_2$  angle is determined with noteworthy precision better than  $0.01^\circ$  (see Table 6.1). The MSRD value for the third coordination shell ( $\text{Re}_0\text{-O}_3$ ) shows slightly worse agreement (within about 10%) due to the fact that this MSRD value is large and

**Table 6.1:** Values of the MSRDS  $\sigma^2$  (in  $\text{\AA}^2$ ) for the first three coordination shells and the true Re–O–Re angle  $\varphi_{\text{EXAFS}}$  (in  $^\circ$ ), estimated both for the model and for the final atomic configuration, obtained in the RMC simulations.

Parameter	Model	RMC
$\sigma_{\text{Re}_0\text{-O}_1}^2$	0.00105(4)	0.0011(1)
$\sigma_{\text{Re}_0\text{-Re}_2}^2$	0.00170(6)	0.0018(1)
$\sigma_{\text{Re}_0\text{-O}_3}^2$	0.00771(7)	0.0069(10)
$\varphi_{\text{EXAFS}}$	174.19(4)	174.9(1)

therefore the contribution of the third shell to the total EXAFS spectrum is relatively small. Also the mentioned constraining of the allowed atomic displacements may give additional error for the analysis of this coordination shell.

### 6.2.2 RMC analysis of experimental data

Next we applied our method to the experimental temperature-dependent Re  $L_3$ -edge EXAFS spectra for  $\text{ReO}_3$  [231]. The experimental EXAFS spectra for  $T=10$  K and 573 K and the corresponding theoretical EXAFS spectra, calculated for the final atomic configurations obtained in the RMC simulations, are shown in Fig. 6.2. The agreement between the experimental and simulated EXAFS spectra is very good and implies that the obtained atomic configurations are representative sample of  $\text{ReO}_3$  structure. One can consider separately the SS and MS contributions and analyze for the first-time the temperature dependence of the MS effects. Note that the MS effects give the maximum contribution to the total EXAFS signal in  $\text{ReO}_3$  at about  $k=16 \text{ \AA}^{-1}$ , where it is about two times larger than the contribution of the SS effects, and this ratio is nearly independent on temperature.

The conventional EXAFS analysis can provide in  $\text{ReO}_3$  only very limited accuracy beyond the first coordination shell due to the pronounced MS effects. Using RMC simulations, in turn, the structural information can be obtained straightforwardly. The radial distribution functions (RDFs) for  $\text{Re}_0\text{-O}_1$ ,  $\text{Re}_0\text{-Re}_2$ , and  $\text{Re}_0\text{-O}_3$  pairs are shown in Fig. 6.3(a), and the temperature dependencies of the MSRDS, extracted from the RDFs, are given in Fig. 6.3(b) for the first three coordination shells. It should be emphasized that the proposed method gives us reliable information even at low temperatures - in the region where, for example, the classical molecular dynamics cannot be applied. For the first coordination

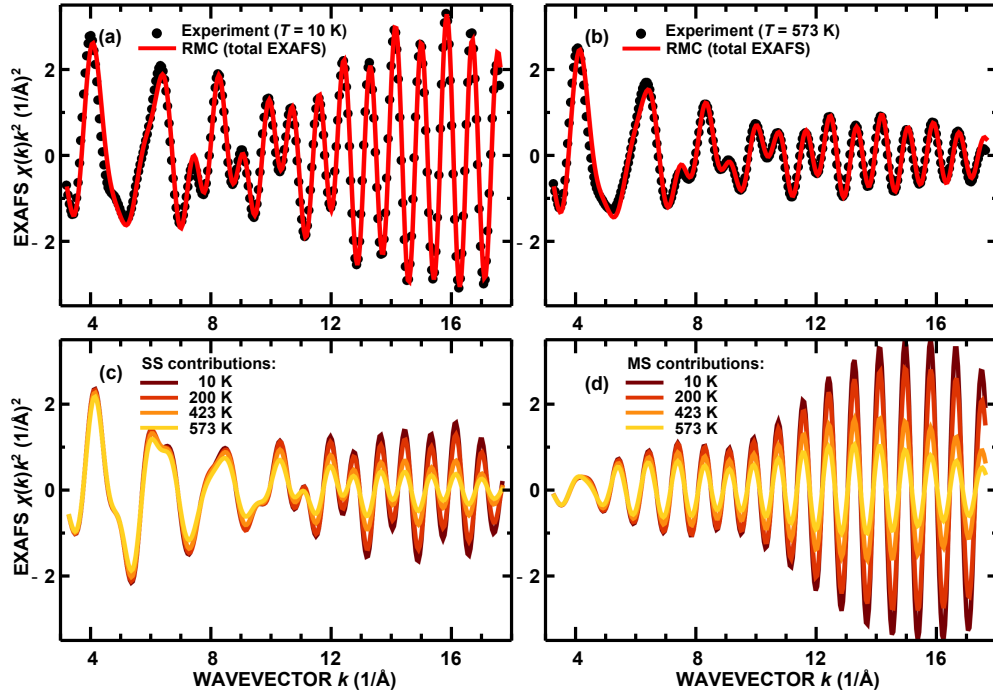


**Figure 6.2: RMC analysis of experimental  $\text{ReO}_3$  EXAFS spectra**  
 Experimental (dots) and RMC (lines)  $\text{Re L}_3$ -edge EXAFS spectra  $\chi(k)k^2$  for  $\text{ReO}_3$  at temperatures  $T=10$  K (a) and  $573$  K (b). Temperature dependencies of the SS (c) and MS (d) contributions are also shown.

shell  $\text{Re}_0\text{-O}_1$ , the RMC results are close to that obtained using the FEFFIT code [42].

Temperature dependencies of the MSRDS in Fig. 6.3(b) can be approximated using the correlated Einstein model [2]. The Einstein frequency for the first coordination shell  $\omega_E=94.9$  THz is in a good agreement with the previously published result ( $\omega_E=94.1$  THz [227]). The Einstein frequencies for the second (36.2 THz) and third (60.8 THz) coordination shells are obtained for the first time. It is important to note that while the Einstein frequency for the second shell ( $\text{Re}_0\text{-Re}_2$  pairs) is significantly smaller than for the first one, due to the larger masses of involved rhenium atoms, the effective bond-strength coefficient  $\kappa = \omega_E^2 \mu$  ( $\mu$  is the effective mass) for  $\text{Re}_0\text{-Re}_2$  pairs (203 N/m) is almost as large as for  $\text{Re}_0\text{-O}_1$  pairs (222 N/m) and is about twice larger than the effective bond-strength coefficient (91.2 N/m) for the third coordination shell.

This means that a strong correlation is present between the motion of the neighbouring  $\text{Re}_0$  and  $\text{O}_1$  atoms (the fact, usually emphasized in the explanation of negative thermal expansion (NTE) of  $\text{ReO}_3$  lattice ([232, 223]), but also between the motion of the next-neighbouring  $\text{Re}_0$  and  $\text{Re}_2$  atoms.

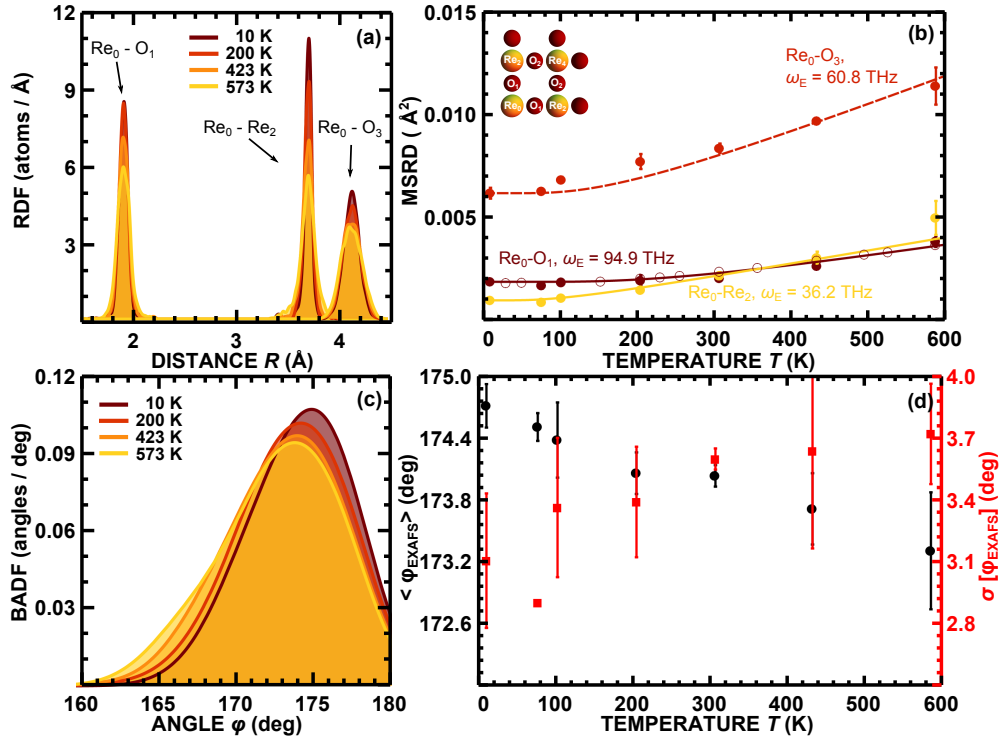


**Figure 6.3: RDF's and structure parameters for  $\text{ReO}_3$**

(a) Temperature dependent Re–O and Re–Re RDFs obtained from the RMC simulations. (b) Temperature dependencies of the MSDs for the Re–O and Re–Re pairs: filled circles - the RMC data; solid lines - approximations by Einstein model; open circles - the FEFFIT results. (c) Temperature dependency of the  $\text{Re}_0\text{-O}_1\text{-Re}_2$  bonding angle distribution function (BADF). (d) The average value of the  $\text{Re}_0\text{-O}_1\text{-Re}_2$  angle (black circles) and its statistical dispersion  $\sigma$  (red squares).

The NTE phenomenon in  $\text{ReO}_3$  is usually explained in terms of the rigid-unit model (RUM) [232]. The strong correlation in the  $\text{Re}_0\text{-O}_1$  atomic motion leads to the nearly temperature-independent  $\text{Re}_0\text{-O}_1$  bond length, thus ensuring the rigidity of the  $\text{ReO}_6$  octahedra. At the same time, an increase of temperature raises the vibration amplitude of oxygen atoms in the direction, orthogonal to  $\text{Re}_0\text{-Re}_2$  bonds. The two effects together result in a reduction of  $\text{Re}_0\text{-Re}_2$  interatomic distances. According to this model, the average value of  $\text{Re}_0\text{-O}_1\text{-Re}_2$  angle should decrease with the increasing temperature, and this effect can be accurately determined from the results of the RMC simulations. The described trend is clearly seen in Figs. 6.3(c) and (d). Let us remind that since EXAFS is sensitive to the correlated motion of atoms, a spatial and temporal average of the scattering paths within the  $\text{Re}_0\text{-O}_1\text{-Re}_2$  atom group will always result in the mean value of the true [233] (or actual [234]) Re–O–Re angle  $\phi_{\text{EXAFS}}$  being less than  $180^\circ$ , even in cubic  $\text{ReO}_3$  [230]. On the contrary to EXAFS, scattering



methods, being sensitive to an average of the atomic positions, will give the value of the apparent Re–O–Re angle  $\varphi_{\text{DIFFR}} = 180^\circ$  in cubic  $\text{ReO}_3$ , but a smaller angle value when the static tilting of  $\text{ReO}_6$  octahedra occurs.

The mean value of the true  $\text{Re}_0\text{--O}_1\text{--Re}_2$  angle decreases almost linearly from  $174.7^\circ$  at 10 K to  $173.3^\circ$  at 573 K. In turn, the statistical dispersion of  $\text{Re}_0\text{--O}_1\text{--Re}_2$  angle values increases from  $3.1^\circ$  at 10 K to  $3.7^\circ$  at 573 K. Thus, the temperature dependency of  $\text{Re}_0\text{--O}_1\text{--Re}_2$  angle agrees well with the structural model of the NTE in  $\text{ReO}_3$ .

### 6.2.3 Conclusions

We have demonstrated that reverse Monte Carlo (RMC) method can be successfully used to interpret EXAFS spectra of crystalline materials even in case, when the multiple-scattering effects are very pronounced. Moreover, the strong MS contributions are a source of valuable information, since they allow to investigate the distributions of bonding angles.

The analysis of the Re  $L_3$ -edge EXAFS data from the second and third coordination shells of rhenium in  $\text{ReO}_3$  has been carried out for the first time taking into account both thermal disorder and multiple-scattering effects. The obtained results are in agreement with the rigid unit model of lattice dynamics in  $\text{ReO}_3$ . We affirm the strong correlation between displacements of oxygen and nearest rhenium atoms. Our results reveal also the strong correlation between the motion of two nearest rhenium atoms.

Two significant limitations due to the limited available computational resources have been, nevertheless, observed in this case. First of all, the analysis was limited to the first three coordination shells, since the extension of  $R$ -space range, used for the analysis, would require to include in the calculations much more additional scattering paths. Secondly, we were forced to constrain the maximal allowed displacement for atoms for their equilibrium positions to  $0.2 \text{ \AA}$  to improve the convergence of our calculations. Such constraint is physically unreasonable for the description of oxygen vibrations in  $\text{ReO}_3$  lattice and may corrupt the results, obtained for the third coordination shell. Therefore for the further calculations we have used the much more efficient evolutionary algorithm approach.

## 6.3 Investigations of $\text{ReO}_3$ using evolutionary algorithm<sup>1</sup>

### 6.3.1 Simulation details and calculations for model system

In this section to investigate the local structure and lattice dynamics of rhenium trioxide we use the evolutionary algorithm (EA) approach. As usually, we test the RMC/EA-EXAFS method using the simulated Re  $L_3$ -edge EXAFS spectrum of  $\text{ReO}_3$ , calculated from the classical molecular dynamics (MD) results [59].

The EA calculations for the model spectrum (MD-EXAFS) have been performed using the  $4 \times 4 \times 4$  supercell (256 atoms) by the EvAX code using different number of simultaneously simulated atomic configurations, but keeping the total maximal number of the calculated EXAFS spectra constant and equal to 96000. For example, the EA calculations with 32 atomic configurations have been carried out for 1500 iterations, so the EXAFS spectrum has been recalculated one (if only mutation operator has been applied to the given configuration) or two times (if also the crossover operator has been involved) at each iteration for each of the 32 configurations, hence the maximal number of iterations is  $32 \times 1500 \times 2 = 96000$ . The EA calculations with 16 atomic configurations, in turn, have been run for 3000 iterations, etc. Note that the EA calculations with only one atomic configuration are just conventional RMC calculations for 96000 iterations, since here no selection or crossover operators can be applied.

The dependence of the final residual between the model MD-EXAFS spectrum and the one calculated by the EA method (EA-EXAFS), evaluated using Eq. (4.12), on the number of the used atomic configurations is shown in Fig. 6.4(a) (final EA-EXAFS spectrum corresponds to the one of the atomic configurations, obtained at the last iteration, which gives the best agreement between experimental and calculated EXAFS data). A comparison of the MD-EXAFS and RMC/EA-EXAFS spectra was carried out using Morlet WT in the  $k$ -space range from  $1 \text{ \AA}^{-1}$  to  $19 \text{ \AA}^{-1}$  and in the  $R$ -space range from  $0 \text{ \AA}$  to  $5.6 \text{ \AA}$ , thus taking into account the contribution of the first five coordination shells around absorbing Re atom. In the calculations of EXAFS spectrum up to 200 scattering path with maximal half-length  $6.4 \text{ \AA}$  were included and multiple-scattering effects with up to fifth order (i.e., with `nlegs` up to 6) were taken into account. Maximal allowed

---

<sup>1</sup>The material, presented in Sec.6.3.1 - 6.3.2, has been published as J. Timoshenko, A. Kuzmins, J. Purans, EXAFS STUDY OF HYDROGEN INTERCALATION INTO  $\text{ReO}_3$  USING THE EVOLUTIONARY ALGORITHM; J. Phys.: Condens. Matter 26 (2014) 055401 (15 pages).

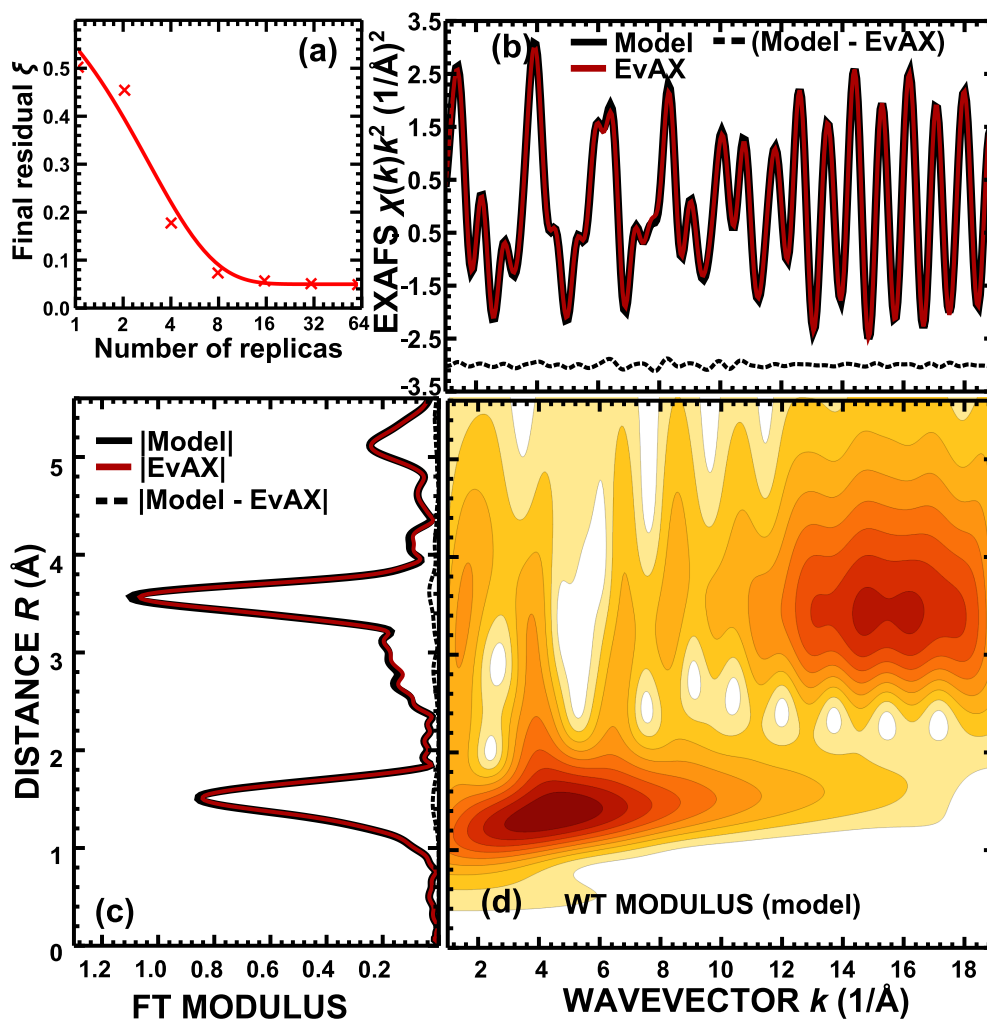


**Figure 6.4: EA analysis of  $\text{ReO}_3$  model EXAFS spectrum**

Dependence of the final residual  $\xi$  on the number of simultaneously used atomic configurations in the EA method (a). The Re  $L_3$ -edge MD-EXAFS spectrum  $\chi(k)k^2$  and the one, reconstructed by the EA method using 32 atomic configurations in the population (b), their FT moduli (c), and the WT modulus of the MD-EXAFS spectrum (d).

displacements for atoms from their equilibrium positions were set to 0.4 Å that is significantly larger than vibrational amplitudes both for Re and O atoms in the  $\text{ReO}_3$  lattice. Experimental, temperature-dependent Re  $L_3$  EXAFS data from crystalline  $\text{ReO}_3$ , the EXAFS spectra, corresponding to final RMC configuration, and their Fourier transforms are shown in Fig. 6.9, together with the calculated EXAFS spectra, obtained for the final RMC/EA configuration.

As one can see, the conventional RMC calculations were unsuccessful in this case: with only one atomic configuration the given number of iterations was too small, and the system got trapped in some local minimum, thus providing

**Table 6.2:** Values of the mean coordination shell radii  $\langle R \rangle$  (in Å), mean-square relative displacements (MSRD)  $\sigma^2$  (in Å<sup>2</sup>), mean-square displacements (MSD)  $\langle u^2 \rangle$  (in Å<sup>2</sup>), parallel (...<sub>||</sub>) and orthogonal (...<sub>⊥</sub>) to the direction, defined by the average positions of  $\text{Re}_0$  and  $\text{Re}_2$  atoms, and the average value of the  $\text{Re}_0\text{-O}_1\text{-Re}_2$  angle  $\varphi_{\text{EXAFS}}$  (in °) in crystalline  $\text{ReO}_3$  at 300 K for the MD model and obtained by the EA-EXAFS simulation for MD model (Fig. 6.4) and experimental data (Fig. 6.6).

Parameter	MD model	EA-EXAFS results for MD model	EA-EXAFS results for experimental data
$\langle R \rangle_{\text{Re}_0\text{-O}_1}$	1.8774(3)	1.879(1)	1.880(1)
$\langle R \rangle_{\text{Re}_0\text{-Re}_2}$	3.7486(5)	3.749(1)	3.749(1)
$\langle R \rangle_{\text{Re}_0\text{-O}_3}$	4.1913(3)	4.191(1)	4.192(1)
$\langle R \rangle_{\text{Re}_0\text{-Re}_4}$	5.3003(4)	5.300(1)	5.300(1)
$\sigma_{\text{Re}_0\text{-O}_1}^2$	0.00105(4)	0.0011(1)	0.0026(2)
$\sigma_{\text{Re}_0\text{-Re}_2}^2$	0.00170(6)	0.0017(1)	0.0021(1)
$\sigma_{\text{Re}_0\text{-O}_3}^2$	0.00771(7)	0.0083(1)	0.0118(15)
$\sigma_{\text{Re}_0\text{-Re}_4}^2$	0.00624(16)	0.0064(1)	0.0063(4)
$\langle u^2 \rangle_{\text{Re}  }$	0.0025(2)	0.0027(4)	0.0033(10)
$\langle u^2 \rangle_{\text{O}  }$	0.0025(2)	0.0025(2)	0.0030(2)
$\langle u^2 \rangle_{\text{O}⊥}$	0.0147(21)	0.015(1)	0.0223(59)
$\langle \varphi_{\text{EXAFS}} \rangle_{\text{Re-O-Re}}$	174.19(4)	172.8(1)	172.2(9)

the largest final residual. An increase of the number of simultaneously modelled atomic configurations leads to almost exponential improvement, and already with 8 atomic configurations the obtained difference between the MD-EXAFS and RMC/EA-EXAFS spectra is about six times smaller. In all further calculations we have simultaneously simulated 32 atomic configurations.

The MD-EXAFS and RMC/EA-EXAFS spectra and their Fourier transforms (FTs) are compared in Fig. 6.4(b) and (c). The EA method is able to reconstruct accurately the model data, therefore one may expect, the obtained atomic configuration should be also close to the atomic structure of the model. In fact, the radial distribution functions (RDFs) around absorbing Re atom, calculated for our MD model and reconstructed by the EA method, are in good agreement (Fig. 6.5). Note that in this study we have used repeated EA calculations to improve the statistics; it has also allowed us later to estimate the stability of the obtained values for structural parameters.

To make the analysis more quantitative, we again have estimated the values of

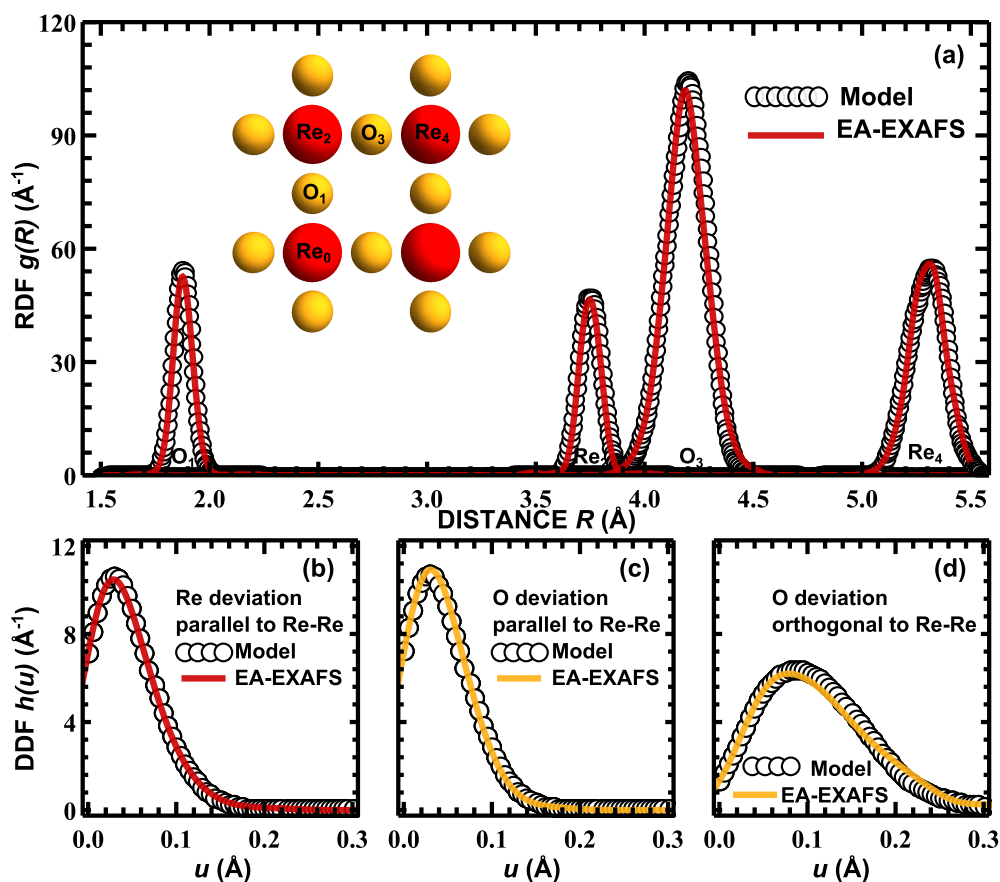


**Figure 6.5: RDF's and atomic displacements for  $\text{ReO}_3$  model**

RDF around Re atom for the first four coordination shells ( $\text{Re}_0\text{-O}_1$ ,  $\text{Re}_0\text{-Re}_2$ ,  $\text{Re}_0\text{-O}_3$ ,  $\text{Re}_0\text{-Re}_4$ , see also the inset), calculated for the MD model by EA method and compared with RDF, obtained directly from MD coordinates (a); distributions of deviations of the oxygen and rhenium atoms from equilibrium positions in the direction parallel and orthogonal to Re–Re bond, calculated using the EA method and obtained directly from MD coordinates (b-d).

average interatomic distances  $\langle R \rangle$  and variances of the distributions of interatomic distances (mean-square relative displacements, MSRD)  $\sigma^2$ , directly calculated from atomic coordinates for the first four coordination shells both for model and for final EA configuration. As one can see in Table 5.1, the RMC/EA-EXAFS method gives accurate values for the average interatomic distances: the difference between the model MD data and the EA results is smaller than  $0.0025 \text{ \AA}$  for the first two coordination shells and smaller than  $0.005 \text{ \AA}$  for next two coordination shells. The MSRD factors are obtained with the accuracy better than  $10^{-4} \text{ \AA}^2$  for the first two coordination shells, and the difference of the MSRD factors for the third and fourth coordination shells is about 5%. A decrease of the accuracy for the outer shells is due to their smaller contribution to the total EXAFS spectrum

relatively to the first shell.

The uncertainties of structural parameters, given in Table 6.2, were estimated by comparing the results obtained in EA simulations with different sequences of pseudo-random numbers and different initial conditions, thus they reflect the statistical uncertainty of the obtained values only. For the analysis of real experimental EXAFS data one should also take into account, for instance, the influence of the uncertainty of chosen values for lattice constant  $a$ , parameters  $S_0^2$  and  $E_0$ . To estimate the importance of these effects, we have carried out additional RMC/EA-EXAFS simulations for the same MD model, but using values of  $a$ ,  $S_0^2$  and  $E_0$ , slightly different from the correct ones ( $a = a_{\text{MD}} = 3.75 \text{ \AA}$ ,  $S_0^2 = 1$  and  $E_0 = 0 \text{ eV}$ ). The results of such calculations have shown that the errors of the obtained values of interatomic distances are very close to the error of the used value of lattice constant. The errors of the obtained values of MSRD factors for the first two coordination shells also depend on the error of lattice constant and are about  $0.0003 \text{ \AA}^2$  for the  $a$  error equal to  $0.003 \text{ \AA}$ . The 10 % error in the value of  $S_0^2$  parameter results in about  $0.0001 \text{ \AA}^2$  large error in the values of MSRD factors for the first two coordination shells, and about ten times larger error in the values of MSRD factors for the distant coordination shells. Small (few electronvolts large) error in the value of parameter  $E_0$ , in turn, does not change the obtained values of structural parameters significantly (obtained differences are smaller than the statistical uncertainty of the results). Note also that the accuracy of the MSRD factors for the first three coordinations shells, obtained using RMC/EA approach, is roughly the same as obtained in the previous section using conventional RMC method (Table 6.1).

The obtained values of structural parameters for the MD model can be compared for the first coordination shell with the ones, calculated using conventional EXAFS analysis: the average  $\text{Re}_0\text{-O}_1$  distance, obtained using FEFFIT code for the model spectrum is  $\langle R \rangle_{\text{Re}_0\text{-O}_1} = 1.875 \pm 0.002 \text{ \AA}$ , the corresponding MSRD is  $\sigma_{\text{Re}_0\text{-O}_1}^2 = 0.0010 \pm 0.0002 \text{ \AA}^2$ . As one can see, these values and their uncertainties are close to that obtained by the RMC/EA-EXAFS method.

Besides MSRD, the RMC/EA-EXAFS method allows us to obtain the mean square displacements (MSD)  $\langle u^2 \rangle$ , which are inaccessible for the conventional EXAFS analysis and are usually measured by the diffraction techniques [235]. The distributions of atomic displacements from equilibrium, described by the displacement distribution functions (DDF)  $h(u)$ , are shown in Fig. 6.5. In  $\text{ReO}_3$

the oscillations of oxygen atoms are essentially anisotropic. Using the RMC/EA-EXAFS method one can discriminate and separately compare the distributions of displacements parallel to the direction, defined by equilibrium positions of  $\text{Re}_0$  and  $\text{Re}_2$  atoms ( $u_{\parallel}$ ), and orthogonal to it ( $u_{\perp}$ ). The quantitative values of the MSD factors  $\langle u^2 \rangle$ , obtained from the MD simulations and the RMC/EA-EXAFS modeling, are compared in Table 5.1. Note that all MSD factors were calculated using MAD approach (see Sec. 4.5) both for original MD model and for the model, obtained in the RMC/EA-EXAFS simulations. In all cases the difference between MSD factors, calculated with the RMC/EA-EXAFS method and from the MD simulations, is below  $2 \times 10^{-4} \text{ \AA}^2$ .

Regarding the true Re–O–Re angle, in our case for the MD model its mean value  $\varphi_{\text{EXAFS}}$  is about  $174^\circ$ , and the EA-EXAFS method estimates it with the accuracy about  $1^\circ$ . As it is also in case of MSD values, small uncertainties of lattice constant  $a$  and parameters  $S_0^2$  and  $E_0$  do not lead to significant changes of the obtained average values for Re–O–Re angle (the changes of MSD and average angle value due to these uncertainties are smaller than the statistical uncertainty).

### 6.3.2 RMC/EA analysis of experimental data

In this section we apply the RMC/EA-EXAFS method to the analysis of the experimental Re  $L_3$ -edge EXAFS spectrum from rhenium trioxide, measured at  $T = 300 \text{ K}$  [231]. The RMC/EA-EXAFS calculations were performed with 32 atomic configurations and during 1500 iterations. The lattice constant was fixed during the calculations at the experimental value  $a_{\text{ReO}_3} = 3.747 \text{ \AA}$  [236]. The comparison of theoretical and experimental EXAFS spectra in this case has been carried out using WT in the  $k$ -space range from 3 to  $18 \text{ \AA}^{-1}$  and in  $R$ -space range from 0.6 to  $5.6 \text{ \AA}$ .

The experimental and reconstructed by the EA method Re  $L_3$ -edge EXAFS spectra are compared in Fig. 6.6. The good agreement between them is supported by their small difference  $\xi = 0.13(1)$  (see Eq. (4.12)), which is only about two times larger than in the analysis of the model MD-EXAFS spectrum.

In Fig. 6.7 we show separately the single-scattering (SS) and multiple-scattering (MS) contributions to the total EA-EXAFS spectrum. As it is expected for  $\text{ReO}_3$ , the MS contribution is very important beyond the first coordination shell [30, 237, 228, 227, 229]. Note that the MS contribution to the FT peak at about  $5.3 \text{ \AA}$  is also significant, although in, for example, [227] and [231] the authors tried

to analyze it using conventional EXAFS analysis in SS approximation, attributing it to the contribution from the fourth coordination shell only. The validity of this approximation and complex structure of this FT peak is analyzed in details in Sec. 6.3.3.

The radial distribution function (RDF) around Re atom, calculated for the final atomic configuration, as well as the corresponding distributions of atomic displacements are compared in Fig. 6.8 and Table 6.2 to those obtained from the MD simulations. As one can see, the force field model, proposed in [59], underestimates the MSRD values for the Re–O bonds that results in the narrower RDF peaks as 1.9 and 4.0 Å. At the same time, the relative displacements of Re atoms in the second and fourth shells (peaks at 3.5 and 4.9 Å, respectively) are well reproduced. Note also that the MSRD value, obtained by the RMC/EA-EXAFS analysis of experimental data, for the first coordination shell agrees well with the previous results for  $\text{ReO}_3$  [227, 229].

Finally, the average value of the true Re–O–Re angle  $\varphi_{\text{EXAFS}}$ , reconstructed by the RMC/EA-EXAFS method for experimental data in Fig. 6.6, is close to that found within the MD simulations (Table 6.2). Also the apparent Re–O–Re angle  $\varphi_{\text{DIFFR}}$  is the same in both cases and is equal to  $180^\circ$ , supporting the conception of cubic  $\text{ReO}_3$  structure.

### 6.3.3 Distant coordination shells in rhenium trioxide

In this section we present the results of temperature-dependent RMC/EA-EXAFS analysis for crystalline  $\text{ReO}_3$ , with the focus on the outer coordination shells (fourth coordination shell  $\text{Re}_0\text{--Re}_4$  and fifth coordination shell  $\text{Re}_0\text{--O}_5$ ). The results of RMC/EA simulations for the temperature-dependent Re  $L_3$ -edge EXAFS data are shown in Fig. 6.9. As one can see, in all cases a very reasonable agreement between experimental and calculated EXAFS spectra has been obtained.

Now we will focus on the analysis of the third peak of the FT, located at about 5.2–5.3 Å. This complex peak consists of contributions from the fourth and fifth coordination shells, as well as of contributions of high order MS effects.

The contribution of the  $\text{Re}_0 - \text{Re}_4$  coordination shell to the total EXAFS spectrum and its temperature dependence is illustrated in Fig. 6.10, while the contribution of the  $\text{Re}_0 - \text{O}_5$  coordination shell to the total EXAFS spectrum and its temperature dependence is shown in Fig. 6.11. As one can see, the fourth



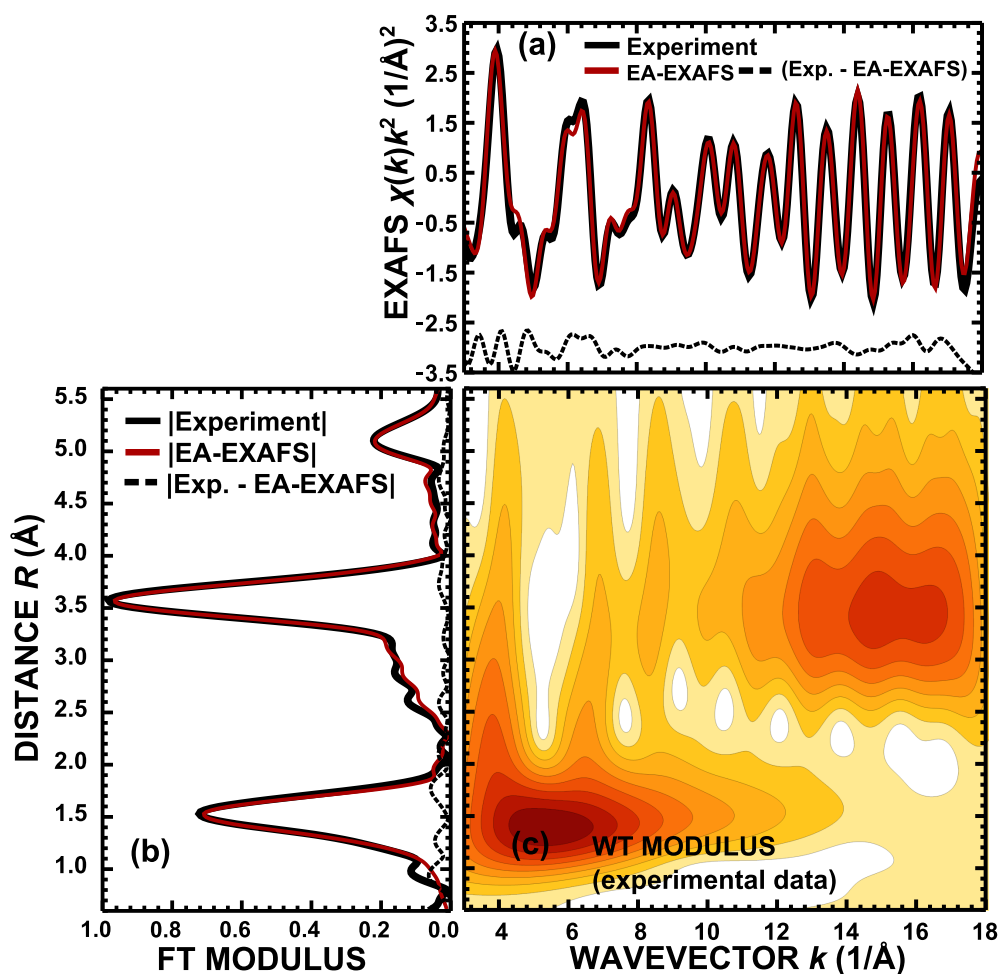


**Figure 6.6:** EA analysis of experimental  $\text{ReO}_3$  EXAFS spectra. Experimental and calculated by the RMC/EA-EXAFS method  $\text{Re L}_3$ -edge EXAFS signals  $\chi(k)k^2$  (a) and their FT moduli (b), and WT modulus of experimental signal (c) at  $T = 300$  K.

coordination shell gives much stronger contribution that, however, is strongly dependent on the temperature.

From atomic coordinates one can also directly calculate the values of structural parameters, such as mean square relative displacements (Table 6.3). At this point one can realize that the fifth coordination shell, i.e.,  $\text{Re}_0 - \text{O}_5$  atomic pairs with equilibrium distance equal to  $5.62 \text{ \AA}$ , consists actually of two very different groups of oxygen atoms: from the 30 oxygen atoms in this coordination shell six are located in the strongly correlated linear  $\text{Re}_0 - \text{O}_1 - \text{Re}_2$  chain, while the 24 remaining oxygens are located off the chain, and their motion is significantly less correlated with the motion of central rhenium atoms. As is revealed by our RMC analysis, both sets of oxygens have very different values of MSRD factors, denoted

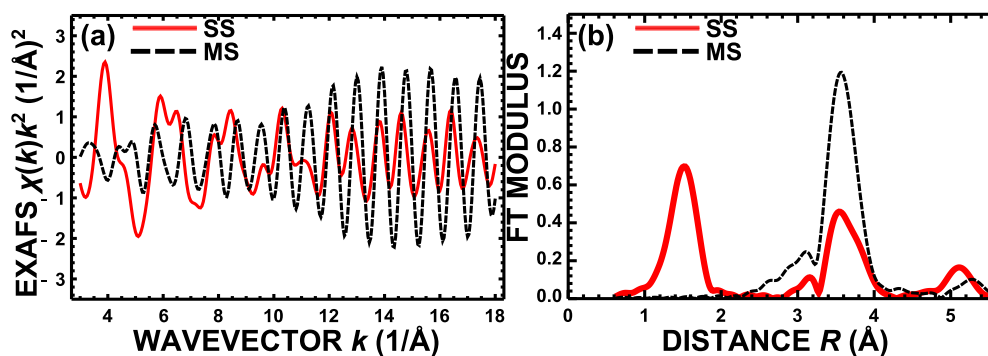


**Figure 6.7:** EA analysis of SS and MS contributions to the experimental  $\text{ReO}_3$  EXAFS spectra

Calculated single-scattering and multiple-scattering contributions to the Re  $L_3$ -edge RMC/EA-EXAFS spectrum (a) and their Fourier transforms (b) for  $\text{ReO}_3$ .

**Table 6.3:** Values of the mean-square relative displacements (MSRD)  $\sigma^2$  (in  $\text{\AA}^2$ ) for the fourth and fifth coordination shells.

	$T = 10$ K	$T = 200$ K	$T = 423$ K
$\sigma_{\text{Re}_0\text{-Re}_4}^2$	0.0027(1)	0.0040(1)	0.0087(2)
$\sigma_{\text{Re}_0\text{-O}_{5,\text{lin}}}^2$	0.0025(1)	0.0026(1)	0.0057(2)
$\sigma_{\text{Re}_0\text{-O}_{5,\text{off-lin}}}^2$	0.0082(1)	0.0096(2)	0.0130(2)
$\sigma_{\text{Re}_0\text{-O}_{5,\text{eff}}}^2$	0.0065(2)	0.0072(1)	0.0107(3)

in Table 6.3 as  $\sigma_{\text{Re}_0\text{-O}_{5,\text{lin}}}^2$  and  $\sigma_{\text{Re}_0\text{-O}_{5,\text{off-lin}}}^2$ , respectively: one can see, the MSRD factors for the in-chain oxygens are relatively small and also relatively slowly increase with temperature, while the MSRD factors for the off-chain oxygens are about 2-3 times larger and their increase with temperature is more pronounced.

The total contribution of the fifth coordination shell to the total EXAFS spectrum (Fig. 6.11) consists of contributions of both of these oxygen groups, and its dependency on temperature can be characterized by effective MSRD factor  $\sigma_{\text{Re}_0\text{-O}_{5,\text{eff}}}^2$ , calculated from atomic coordinates of all 30 oxygen atoms of the fifth coordination shell without separating them in groups (Table 6.3).

Finally, we will discuss the influence of MS effects. The total single-scattering and multiple-scattering contributions to the total  $\text{ReO}_3$   $L_3$ -edge EXAFS spectrum at  $T = 300$  K are shown in Fig. 6.7. As one can see, the MS effects have also significant influence on the shape of the peak of Fourier transform at 5.2  $\text{\AA}$ . More detailed analysis of the contributions of different MS paths is illustrated in Fig. 6.12, where double-scattering (DS), triple-scattering (TS) and higher order MS contributions are shown separately. As one can see, all of these MS paths have strong contribution in the region of our interest and should be calculated

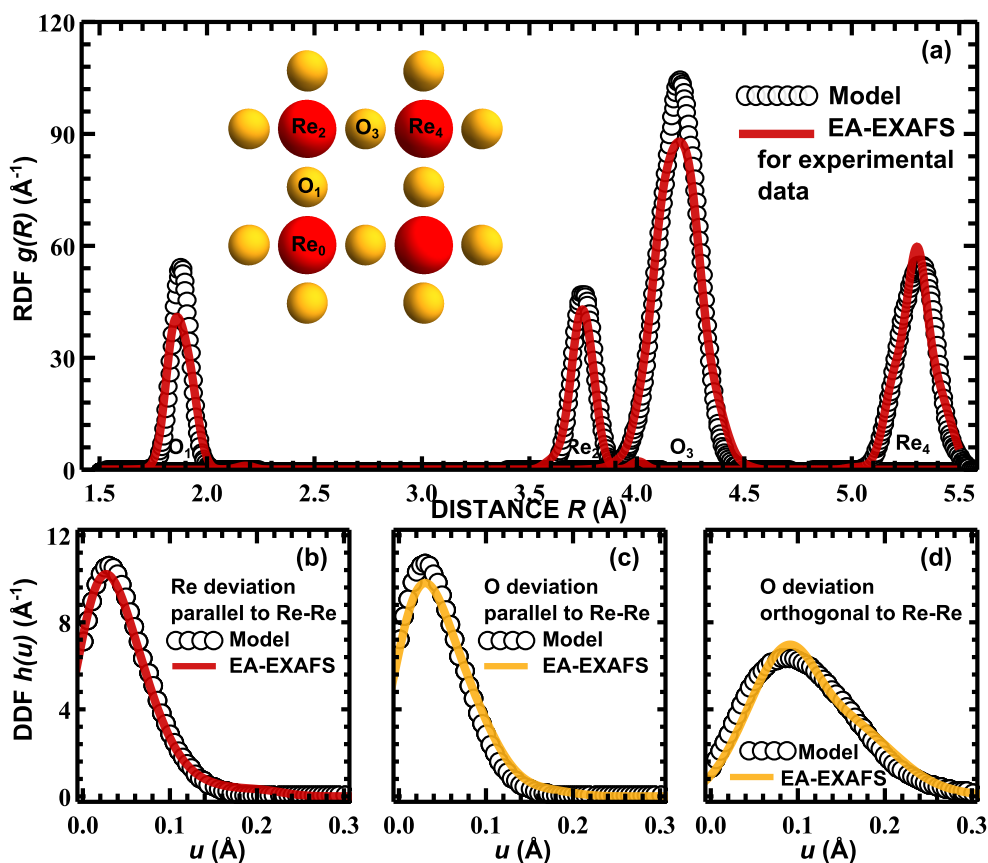
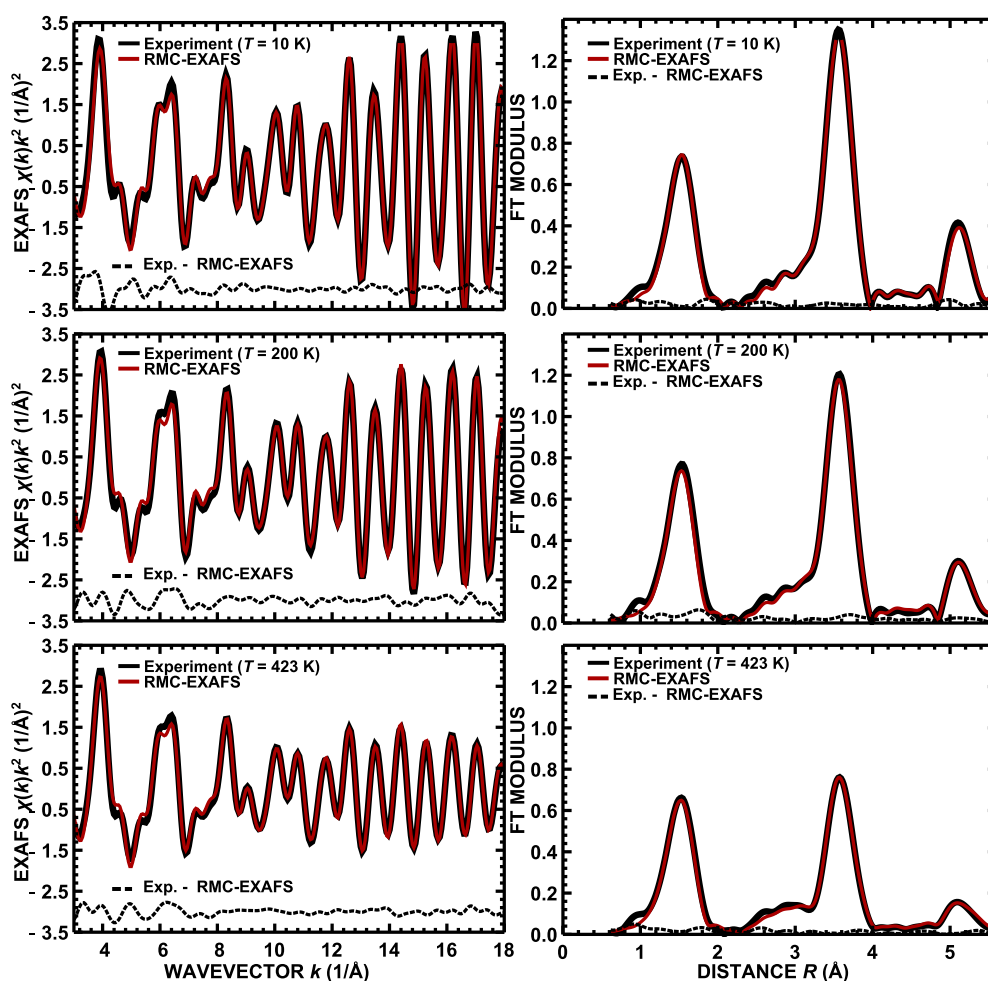


Figure 6.8: RDF's and atomic displacements for experimental  $\text{ReO}_3$  sample

RDF around Re atom, calculated for experimental data and RDF obtained from MD calculations (a); distributions of displacements of the oxygen and rhenium atoms from equilibrium positions in the direction parallel and orthogonal to Re–Re bond, obtained from MD calculations and experimental data using the EvAX code (b)-(d).

accurately for the precise EXAFS analysis. However, one may notice that the intensity of the total MS contribution is actually smaller than, say, the intensity of TS or higher order contributions, indicating that contributions of MS paths interfere here destructively, and a lot of them get cancelled out.

Moreover, as it turns out, the MS contributions interfere destructively also with the SS contribution from the fifth coordination shell: in Fig. 6.13 the temperature dependency of the MS contributions and temperature dependency of the sum of MS contributions and contribution from the fifth coordination shell are compared. As one can see, for every temperature the sum of MS contributions and contribution from the fifth coordination shell has smaller intensity than the one of pure MS contributions. This explains why SS approximation works so well



**Figure 6.9: EA analysis of temperature-dependent experimental  $\text{ReO}_3$  EXAFS spectra**

Experimental temperature-dependent Re  $L_3$ -edge EXAFS data from crystalline  $\text{ReO}_3$ , the EXAFS spectra, corresponding to final RMC/EA configuration, and their Fourier transforms.

for the description of this peak at  $5.2 \text{ \AA}$  - it consists practically of the contribution from the fourth coordination shell ( $\text{Re}_0\text{-Re}_4$ ) only, and all other contributions are almost completely canceled out.

## 6.4 Conclusions

In this chapter we have demonstrated that reverse Monte Carlo (RMC) method can be successfully used to analyze EXAFS spectra of crystalline materials, taking into account multiple-scattering effects, contributions from distant coordination shells and accounting for thermal disorder effects as well as for correlation of

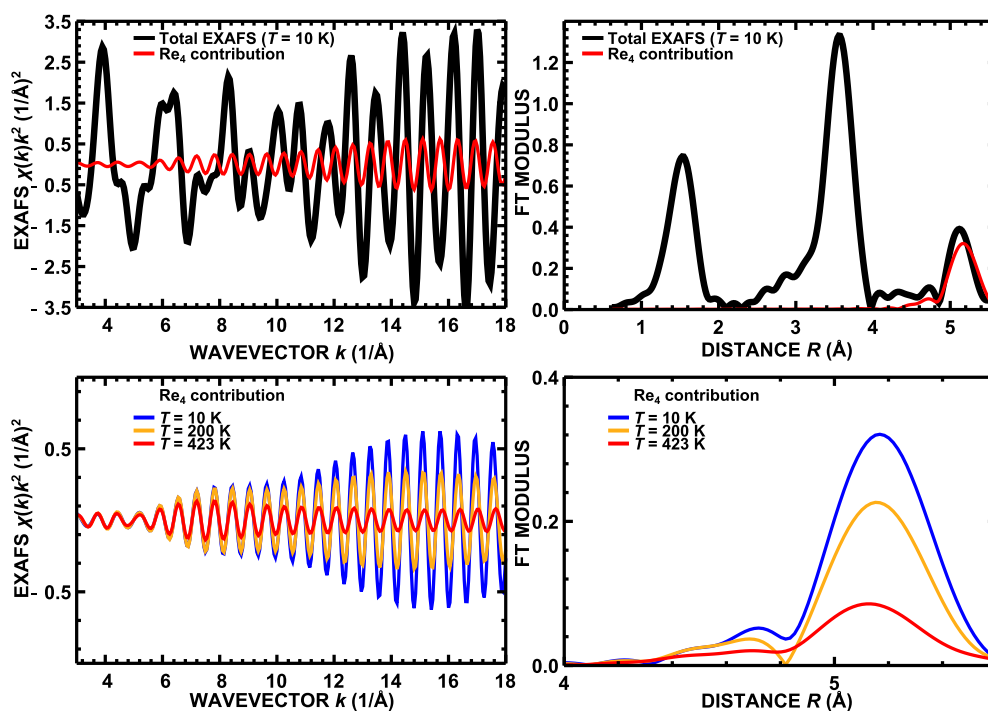


Figure 6.10: Temperature dependence of the  $\text{Re}_0\text{-Re}_4$  contribution to the total EXAFS spectrum.

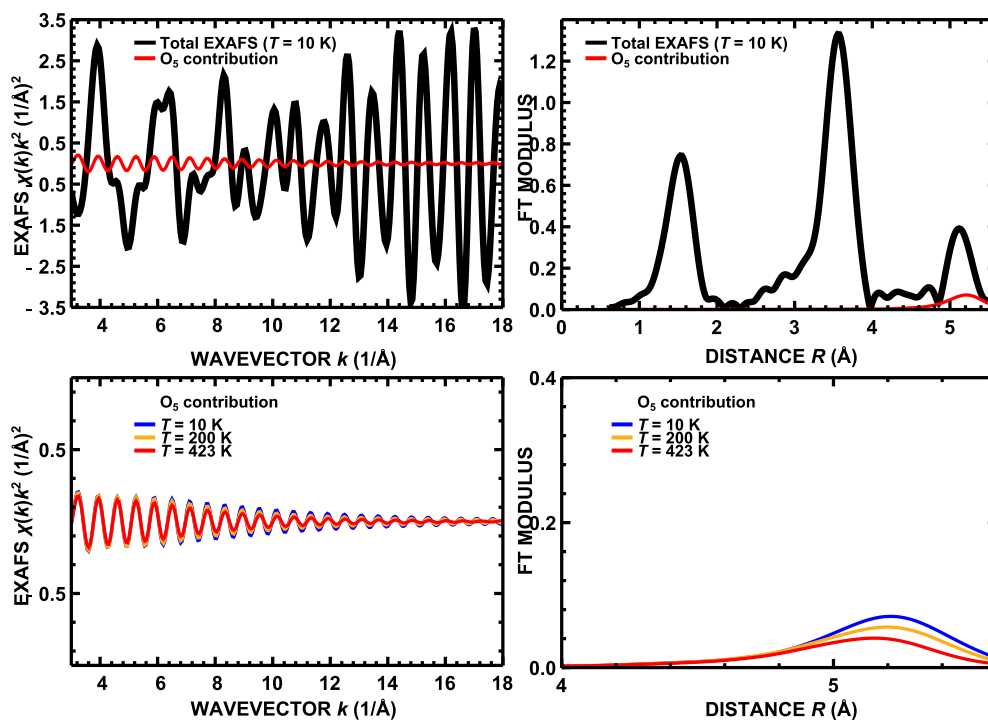
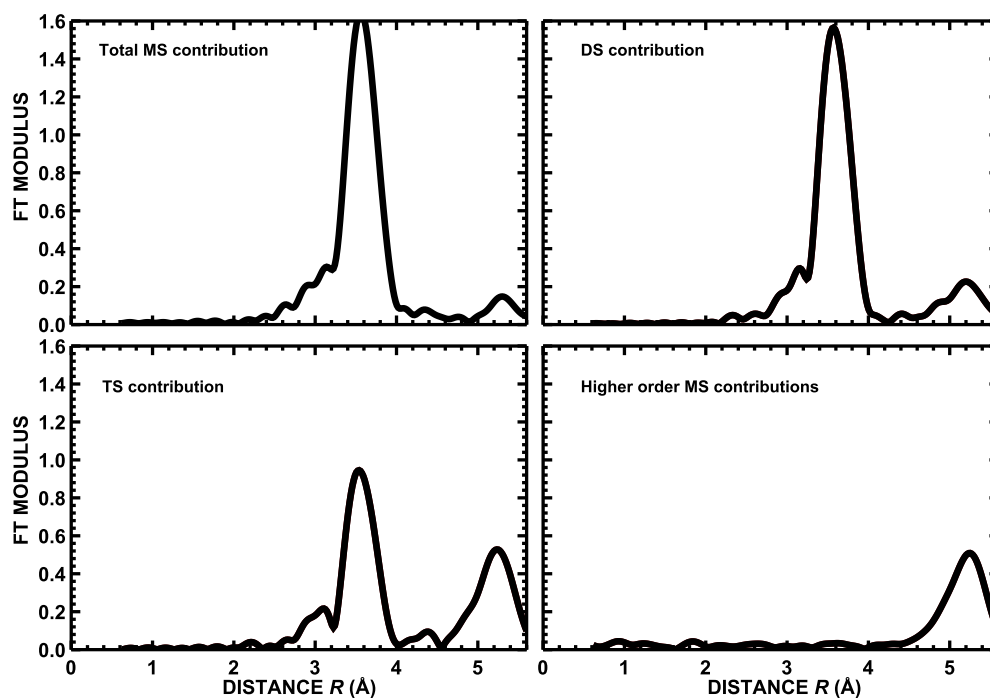
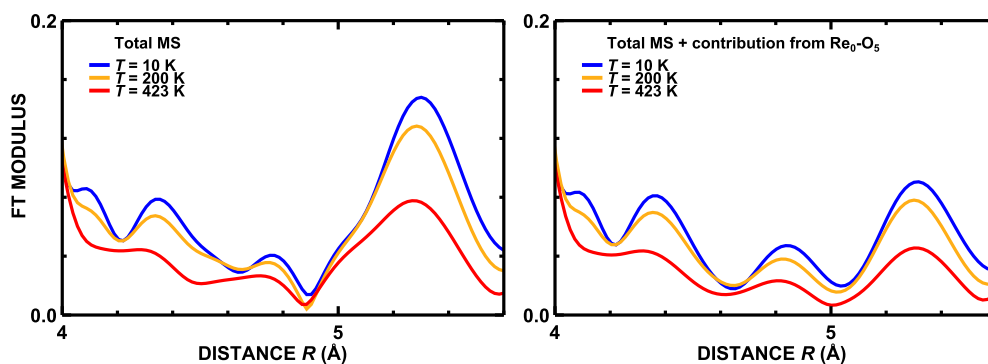


Figure 6.11: Temperature dependence of the  $\text{Re}_0\text{-O}_5$  contribution to the total EXAFS spectrum.



**Figure 6.12: Influence of multiple-scattering effects**

Total multiple-scattering (MS), double-scattering (DS), triple-scattering (TS) and higher order MS contributions to the total  $\text{ReO}_3$   $L_3$ -edge EXAFS spectrum at  $T = 300$  K, calculated in the RMC/EA simulations



**Figure 6.13: Temperature dependence of multiple-scattering contributions**

Decrease of multiple-scattering contributions to the total  $\text{ReO}_3$   $L_3$ -edge EXAFS spectrum with temperature (left panel) and the result of interference of the MS contributions and contribution from the sixth coordination shell (right panel).

atomic motion. The obtained structural models were reconstructed accounting for the behavior of EXAFS spectra in  $k$  and  $R$ -spaces through the use of the Morlet wavelet transform as a criterion for the residual minimization between the experimental and calculated EXAFS data.

We have also shown that the novel approach, based on the use of evolutionary algorithm, is computationally more efficient than conventional reverse Monte Carlo approach. The RMC/EA-EXAFS method allowed us for the first time to extract accurately structural information both from the nearest and distant coordination shells of rhenium. As a result of the RMC/EA simulations, the radial distribution functions for the first five coordination shells, the displacement distribution functions and the bond-angle distribution functions were obtained. Using the obtained structural model we were able to study in details also the different overlapping single-scattering and multiple-scattering contributions to the total EXAFS with characteristic half-path length  $R$  about 5 Å and have validated for the first time the single-scattering approximation commonly used for the analysis of 4th coordination shell (Re<sub>0</sub>–Re<sub>4</sub>).

## 7. HYDROGEN INTERCALATION INTO $\text{ReO}_3$

### 7.1 Introduction<sup>1</sup>

Important advantage of simulation-based approaches to EXAFS data treatment is the possibility to probe directly the many-atomic distribution functions, such as distribution of angles, but also the correlations of different atomic displacements. Thus much more structural information from the EXAFS spectra can be obtained, and, for instance, also the shapes and orientation of coordination polyhedra can be studied straightforwardly. Therefore the simulation-based approaches turn the EXAFS spectroscopy into a powerful tool for the studies of truly local structure, rather than just of distances distribution in the first coordination shell.

A good illustration to this statement is the study of hydrogen intercalation process into crystalline rhenium trioxide  $\text{ReO}_3$ , presented in this chapter.

The process of the intercalation of hydrogen ions in platinized  $\text{ReO}_3$  was studied *in situ*, and EXAFS spectra containing contributions from atoms, located at distances up to 6 Å from the absorbing rhenium atom, have been obtained in [7]. At the same time, the performed conventional EXAFS analysis, presented in [7], was able to provide information on the first coordination shell around rhenium atom only. It revealed some two-modal distribution of the Re–O distances, but it was impossible to find out, for instance, whether this complex distribution is due to the distortion of Re–O<sub>6</sub> octahedra or due to the appearance of two different types of regular octahedra [7].

In the study, presented in this chapter, we employ the RMC/EA method to resolve a contradiction between the results of powder neutron diffraction [238] and X-ray absorption spectroscopy [7, 239], observed during the distortion of the local atomic structure in hydrogen rhenium bronzes  $\text{H}_x\text{ReO}_3$ .

According to the neutron diffraction study [238], the insertion of hydrogen into perovskite-type cubic  $\text{ReO}_3$  induces internal strain, which leads to the tilting and

---

<sup>1</sup>The material, presented in this chapter, has been published as J. Timoshenko, A. Kuzmins, J. Purans, EXAFS STUDY OF HYDROGEN INTERCALATION INTO  $\text{ReO}_3$  USING THE EVOLUTIONARY ALGORITHM; J. Phys.: Condens. Matter 26 (2014) 055401 (15 pages).



slight deformation of originally regular  $\text{ReO}_6$  octahedra and to the increase of the Re–O bond lengths, while the cell volume remains almost constant. In particular, in the case of hydrogen rhenium bronze  $\text{H}_{1.36}\text{ReO}_3$ , having the largest known amount of inserted hydrogen, the Re–O–Re angles between two octahedra, determined by neutron diffraction (i.e., apparent angles [233]), change from  $\varphi_{\text{DIFFR}} = 180^\circ$  to  $169^\circ$ , the O–Re–O angles inside the octahedra become split into two groups of  $\sim 82^\circ$  and  $\sim 98^\circ$ , and the Re–O bonds lengthen by  $0.03 \text{ \AA}$  from  $\sim 1.87 \text{ \AA}$  to  $\sim 1.90 \text{ \AA}$  [238].

Previous X-ray absorption spectroscopy studies [7, 239] also indicate the occurrence of octahedra tilting upon hydrogen insertion, however the analysis of the Re  $L_3$ -edge EXAFS suggests strong distortion of the first coordination shell of rhenium, which was tentatively interpreted as the appearance of two different rhenium sites, both having nearly regular octahedral coordination with the Re–O bond lengths equal to  $1.88 \text{ \AA}$  and  $2.06 \text{ \AA}$ , caused by the charge disproportionation phenomenon ( $2\text{Re}^{5+} \rightarrow \text{Re}^{6+} + \text{Re}^{4+}$ ). Note that the change of the rhenium formal charge seemed to be supported by a shift (about 2 eV) of both Re  $L_1$  and  $L_3$  absorption edges [7].

Thus, the clear contradiction between two experimental results remains unresolved for years and will be addressed in details below, considering both static and dynamic disorder and including correlation effects.

## 7.2 Analysis of $\text{ReO}_3$ lattice distortion induced by intercalation of hydrogen ions

It is known that upon insertion hydrogen ions attach to the oxygen atoms of  $\text{ReO}_3$  lattice, forming the OH bonds [238], and the valence state of formally  $\text{Re}^{6+}$  ions is reduced due to the localization of additional electron [7]. Both effects can lead to the significant distortion of  $\text{ReO}_3$  lattice [240]. Neutron diffraction study of the hydrogen rhenium bronze  $\text{D}_{1.36}\text{ReO}_3$  has revealed that the presence of hydrogen ions leads to the tilting of  $\text{ReO}_6$  octahedra, thus significantly decreasing the average value of apparent Re–O–Re angle  $\varphi_{\text{DIFFR}}$  [7, 238].

The experimental Re  $L_3$ -edge EXAFS data were taken from [7], where the experimental details are also given. Briefly, platinized polycrystalline  $\text{ReO}_3$  has been exposed to hydrogen flow for 2.5 hours at room temperature. Next, the air flow was passed through the sample to oxidize it and to deintercalate the

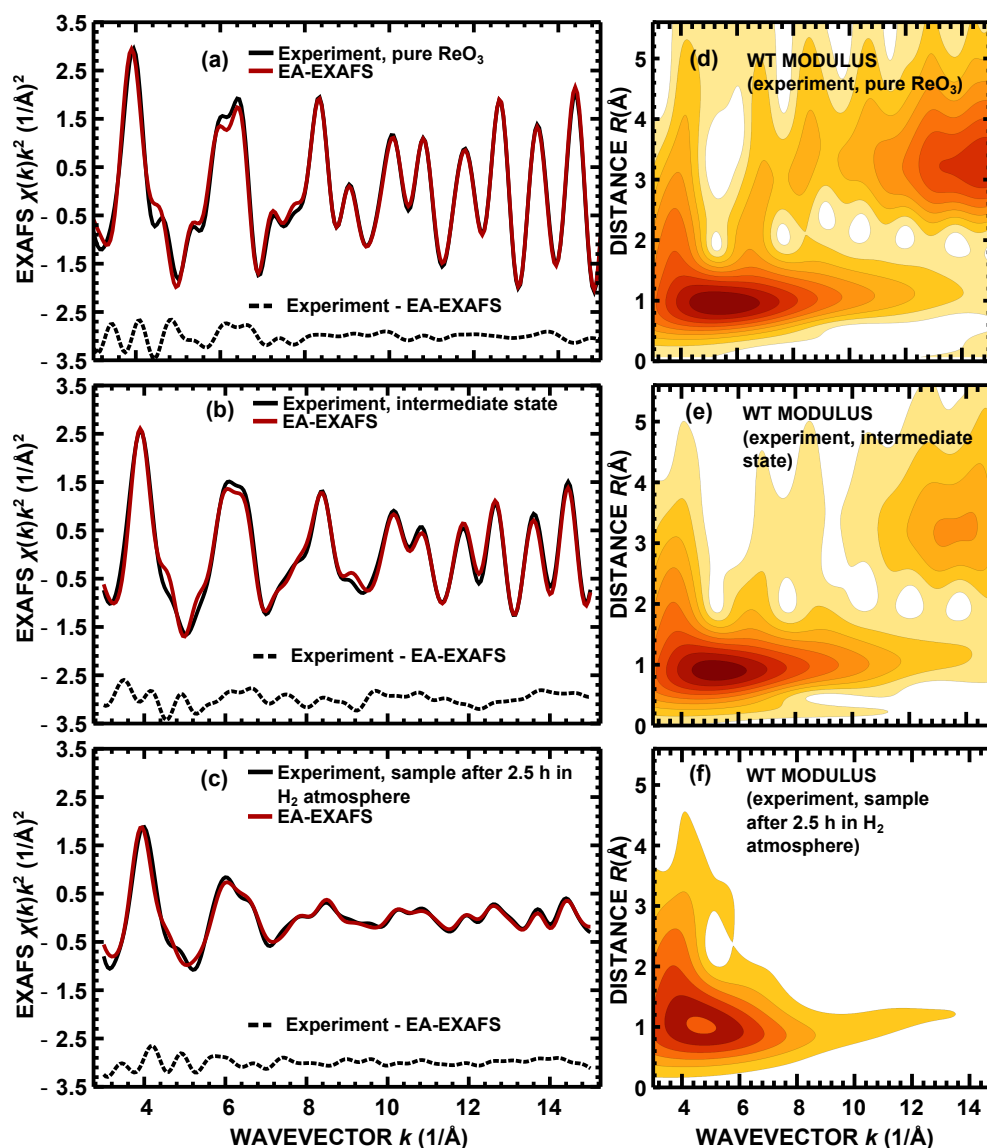


**Figure 7.1: Influence of hydrogen intercalation on EXAFS spectra**  
 Experimental and calculated by the EA-EXAFS method  $\text{Re L}_3$ -edge EXAFS signals  $\chi(k)k^2$  (a, b, c) and the WT moduli of experimental signals (d, e, f) for pure crystalline  $\text{ReO}_3$ , for  $\text{ReO}_3$  after 2.5 hours in  $\text{H}_2$  atmosphere and for intermediate state.

hydrogen ions. The EXAFS spectra have been in-situ measured before the intercalation process, after the intercalation process and continuously during the deintercalation phase.

The analysis of EXAFS spectra for pure crystalline  $\text{ReO}_3$ , for  $\text{ReO}_3$  after 2.5 hours in  $\text{H}_2$  atmosphere and during the de-intercalation process has been carried out using the EA-EXAFS method with the same parameters as used in previous chapter: development of 32 atomic configurations was simulated for

1500 iterations, with the lattice constant, fixed during the calculations at the experimental value  $a_{\text{ReO}_3} = 3.747 \text{ \AA}$  [236]. The comparison of the experimental and calculated spectra has been carried out using WT in the  $k$ -space range from 3 to 15  $\text{\AA}^{-1}$  and in the  $R$ -space range from 0.6 to 5.6  $\text{\AA}$ . In calculations we also assume that the presence of hydrogen ions itself does not have any direct contribution to EXAFS [241], and all observed changes are due to static and thermal distortions of the lattice.

The Fourier filtered experimental EXAFS spectra and the ones, reconstructed by the EA-EXAFS method, are shown in Fig. 7.1. As one can see, the disorder, induced by the presence of hydrogen ions, significantly reduces the amplitude of EXAFS spectra, so that the contribution of the second and further coordination shells to the total spectrum becomes very small after exposure to hydrogen atmosphere for 2.5 hours. Nevertheless, the EA simulations allow us to obtain structure models, for which the theoretical EXAFS is reasonably close to the experimental spectra.

The RDFs around rhenium and DDFs for rhenium and oxygen, calculated from the atomic coordinates obtained in the EA simulations, are shown in Fig. 7.2. Corresponding MSRD factors for the first four coordination shells and the values of the MSD factors for rhenium and oxygen atoms, parallel and orthogonal to the direction, defined by the average positions of  $\text{Re}_0$  and  $\text{Re}_2$ , are given in Fig. 7.3. The bonding angle distribution functions (BADF) for the true  $\text{Re-O-Re}$  angle  $\varphi_{\text{EXAFS}}$  and their mean values are shown in Fig. 7.4. Note that the knowledge of both MSRD  $\sigma^2$  and MSD  $\langle u^2 \rangle$  quantities provides one with the access to correlation effects in atomic motion, since the two parameters are related as  $\sigma^2 = \langle u_A^2 \rangle + \langle u_B^2 \rangle - 2\langle u_A u_B \rangle$ , where  $\langle u_A^2 \rangle$  and  $\langle u_B^2 \rangle$  are corresponding MSD factors for atoms  $A$  and  $B$ , and  $\sigma^2$  is the MSRD factor for A-B bond.

In pure  $\text{ReO}_3$  the MSRD  $\text{Re}_0\text{-O}_3$  for the third coordination shell is large, being several times larger than the corresponding MSRD factors of the first ( $\text{O}_1$ ) and second ( $\text{Re}_2$ ) coordination shells, and also it is about twice as large as the MSRD factor of the fourth ( $\text{Re}_4$ ) coordination shell. The large values of the MSRD factor for the  $\text{Re}_0\text{-O}_3$  pair can be explained by (i) the large amplitude of oxygen oscillations in the direction, orthogonal to the  $\text{Re}_0\text{-Re}_2$  bond, and (ii) relatively weak correlation of motion for  $\text{Re}_0$  and  $\text{O}_3$  atoms. One can estimate that the correlation effects in the  $\text{Re}_0\text{-O}_3$  pair vibrations are negligible, since the MSRD factor  $\sigma_{\text{Re}_0\text{-O}_3}^2$  (Fig. 7.3) is close to the sum of MSD factors for the two atoms  $\tilde{\sigma}_{\text{Re}_0\text{-O}_3}^2 = \langle u_{\text{Re}}^2 \rangle + \langle u_{\text{O}_\perp}^2 \rangle / 2 \approx 0.013 \text{ \AA}^2$ .

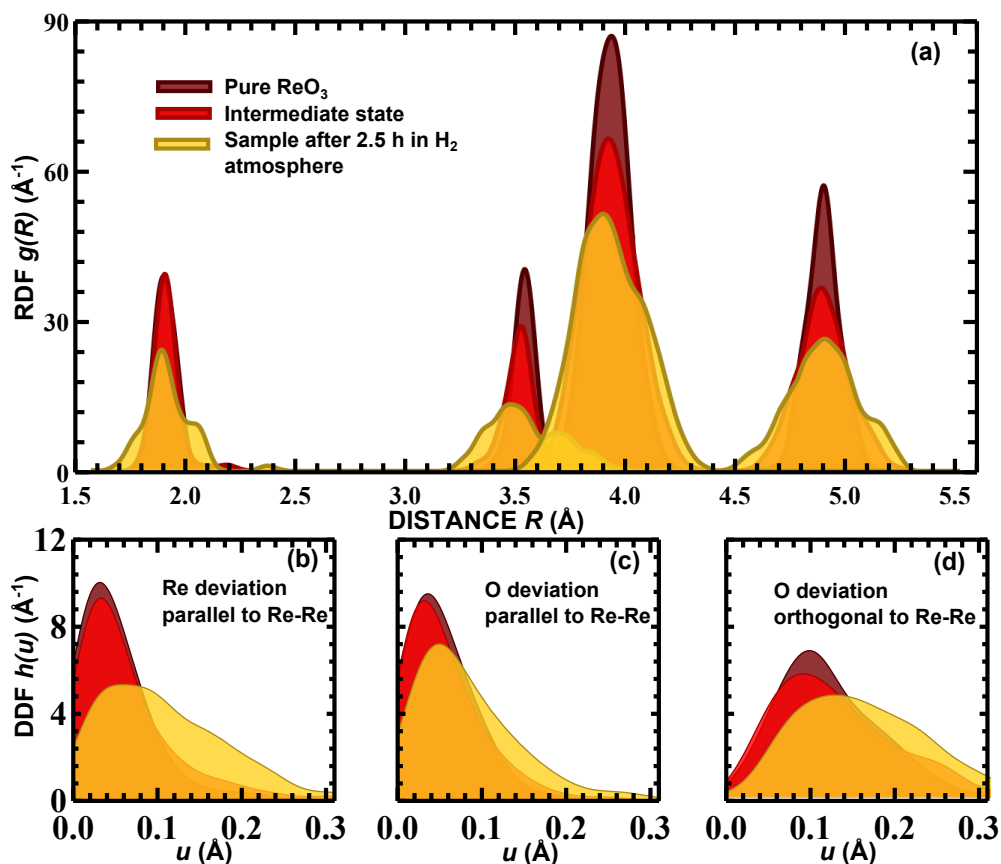


**Figure 7.2: Influence of hydrogen intercalation on lattice structure** RDF around Re atom, calculated for pure crystalline  $\text{ReO}_3$ , for  $\text{ReO}_3$  after 2.5 hours in  $\text{H}_2$  atmosphere and for intermediate state (a), and corresponding distributions of the deviations of the oxygen and rhenium atoms from equilibrium positions in the direction parallel and orthogonal to Re–Re bond, calculated using the EA method (b)-(d).

As one may expect, the presence of hydrogen significantly broadens all peaks of RDF, DDFs and BDF, indicating the occurrence of pronounced disorder in the lattice. The average value of the true Re–O–Re angle  $\varphi_{\text{EXAFS}}$  decreases from about  $172^\circ$  for pure  $\text{ReO}_3$  to  $168^\circ$  for the hydrogen intercalated  $\text{H}_x\text{ReO}_3$ . We have also evaluated the average value of the apparent Re–O–Re angle  $\varphi_{\text{DIFFR}}$ , which decreases from  $180^\circ$  to about  $168^\circ$  indicating a rotation of  $\text{ReO}_6$  octahedra in agreement with previous neutron diffraction study [238]. The MSRD factor ( $0.036 \text{\AA}^2$ ) for the  $\text{Re}_0\text{--Re}_2$  pair increases almost 20 times in  $\text{H}_x\text{ReO}_3$  with respect to that ( $0.0021 \text{\AA}^2$ ) in pure  $\text{ReO}_3$ . It does not mean, however, that the Re lattice is completely distorted. The most significant contribution to the increase of MSRD is attributed to the reduction of the correlation in a motion of two neighboring

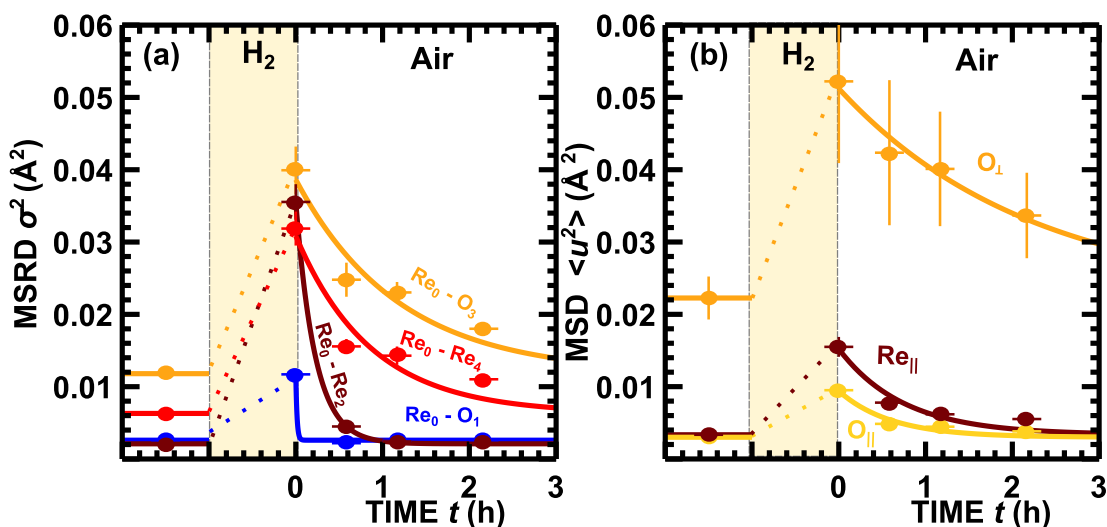


**Figure 7.3: Time-dependencies of MSRD and MSD factors in the hydrogen deintercalation process**

Changes of the MSRDs, calculated for experimental data for the first four coordination shells (a), and MSD factors for the displacements of Re and O atoms in the direction, parallel ( $\dots_{\parallel}$ ) and orthogonal ( $\dots_{\perp}$ ) to the direction, defined by the average positions of  $\text{Re}_0$  and  $\text{Re}_2$ , (b) in the intercalation/deintercalation process.

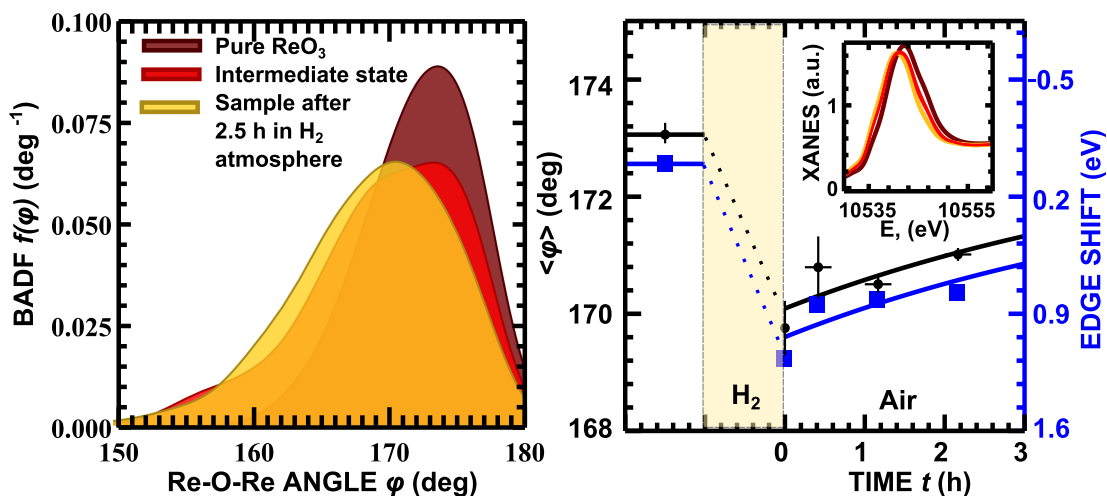


**Figure 7.4: Re–O–Re angle in the hydrogen detintercalation process**

(a) Bonding-angle distribution function (BADF) for the true Re–O–Re angle  $\varphi_{\text{EXAFS}}$ , calculated using the EA method for pure crystalline  $\text{ReO}_3$ , for  $\text{ReO}_3$  after 2.5 hours in  $\text{H}_2$  atmosphere and for intermediate state. (b) The corresponding changes of the average value of the true Re–O–Re angle in the intercalation/deintercalation process that correlate with the shift (blue squares) of  $L_3$  edge (shown in the inset).

rhenium atoms. To estimate correlation effect, one again can compare the MSRD factor  $\sigma_{\text{Re}_0-\text{Re}_2}^2$  for the second coordination shell with the sum of the MSD factors

for rhenium atoms, equal to  $\tilde{\sigma}_{\text{Re}_0-\text{Re}_2}^2 = 2\langle u_{\text{Re}}^2 \rangle \approx 0.0066 \text{ \AA}^2$  for pure  $\text{ReO}_3$  and  $\approx 0.031 \text{ \AA}^2$  for  $\text{H}_x\text{ReO}_3$ . The latter value for  $\text{H}_x\text{ReO}_3$  is close to the actual value of the MSRD factor ( $0.036 \text{ \AA}^2$ ), whereas  $\tilde{\sigma}_{\text{Re}_0-\text{Re}_2}^2$  for pure  $\text{ReO}_3$  is about three times larger than the actual value of  $\sigma_{\text{Re}_0-\text{Re}_2}^2 = 0.0021 \text{ \AA}^2$ . Thus, the motion of two neighbouring rhenium atoms is strongly correlated in pure  $\text{ReO}_3$ , whereas it is mostly uncorrelated in  $\text{H}_x\text{ReO}_3$ .

After the sample is exposed to air, the structural parameters gradually return to the values, characteristic for pure  $\text{ReO}_3$ . One can roughly approximate these trends with exponential functions  $f(t) = f_{\text{pure}} + a \exp^{-t/\tau}$  (solid lines in Figs. 7.3 and 7.4), where  $f_{\text{pure}}$  is the value of corresponding structural parameter (MSD, MSRD or mean Re–O–Re angle) for pure  $\text{ReO}_3$ ,  $a$  is a free parameter,  $t$  is the experimental time, and  $\tau$  is the characteristic relaxation time. One can notice that the times  $\tau$  differ significantly for different coordination shells. In particular, the values of  $\tau$  for MSD and MSRD factors for the third ( $\text{O}_3$ ) and fourth ( $\text{Re}_4$ ) coordination shells, having weak correlation of atomic motion with absorbing rhenium atom, are in the range from 0.7 to 2.5 hours. On the contrary, the values of  $\tau$  for MSRD factors for the first two coordination shells, which are strongly influenced by the correlation of atomic motion, are much smaller, being about 0.16 hours for the MSRD of the second ( $\text{Re}_2$ ) coordination shell and even smaller (0.01 hours) for the first ( $\text{O}_1$ ) coordination shell. We propose that such difference in the characteristic relaxation times is due to the fact that the changes of the structural parameters in both of these sets have different physical origin. The changes of correlation of atomic motion and, correspondingly, of MSRD factors in the first two coordination shells have electronic origin and, thus, short relaxation times. They arise due to additional electrons localized largely at rhenium atoms and introduced together with hydrogen ions to maintain charge neutrality. On the contrary, the variation of the MSD and MSRD parameters in the third and fourth coordination shells reflects static disorder, caused by the presence of hydrogen atoms in the  $\text{ReO}_3$  lattice.

Finally, we will discuss the type of static disorder in the  $\text{ReO}_3$  lattice, induced by hydrogen insertion. Since in hydrogen rhenium bronze  $\text{HReO}_3$  the formal valence state of rhenium atoms is +5, two different models for the possible lattice distortion have been proposed in [7]: (i) the distortion of all  $\text{Re}^{5+}\text{O}_6$  octahedra and (ii) the co-existence of two different types of relatively regular octahedra ( $\text{Re}^{4+}\text{O}_6$  and  $\text{Re}^{6+}\text{O}_6$ ) due to the presence of two different valence states of rhenium atoms (the so-called charge disproportionation model).

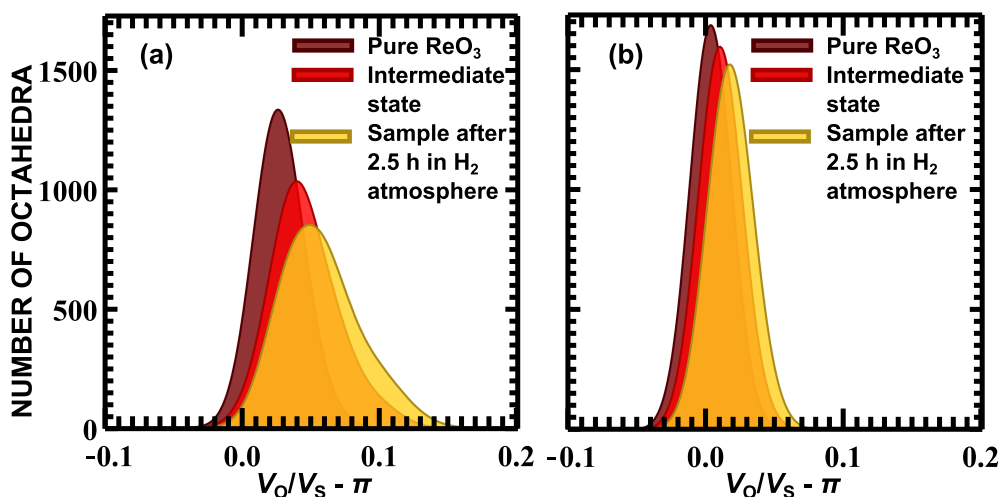


**Figure 7.5: Distortion of  $\text{ReO}_6$  and  $\text{Re}(\text{Re}_2)_6$  octahedra**

Histograms of the ratio of octahedron volume and volume of corresponding circumscribing sphere  $V_O/V_S - \pi$ , characterizing the distortion of the  $\text{ReO}_6$  (a) and  $\text{Re}(\text{Re}_2)_6$  (b) octahedra for pure  $\text{ReO}_3$ , for  $\text{ReO}_3$  after 2.5 hours in  $\text{H}_2$  atmosphere and for the intermediate state.

To characterize the distortion of the  $\text{ReO}_6$  octahedra, as well as the distortion of the octahedra, formed by six  $\text{Re}_2$  atoms of the second coordination shell, we used the approach, proposed in [242]. For each octahedron we calculated its volume  $V_O$  and the volume  $V_S$  of the sphere that is the closest to all vertices of that octahedron. In the case of regular octahedron such sphere is circumscribed sphere, and the ratio  $V_O/V_S$  is equal to  $\pi$ . The histograms of the quantity  $V_O/V_S - \pi$  for both  $\text{ReO}_6$  and  $\text{Re}(\text{Re}_2)_6$  octahedra are shown in Fig. 7.5. They all have a single peak shape independently on hydrogen intercalation, therefore one may conclude that only one type of rhenium-oxygen octahedra is present, thus being favorable to the first model in [7]. The broadening of the histogram peak indicates that the distortion of the  $\text{ReO}_6$  octahedra increases significantly with the increase of the amount of hydrogen ions in the lattice.

Upon hydrogen insertion, the valence state of rhenium ions is reduced that agrees with the  $\text{Re } L_1$  and  $L_3$  absorption edge shift by about 2 eV to smaller energies (Fig. 7.4) [7]. Therefore, the origin of the  $\text{ReO}_6$  octahedra distortion can be tentatively attributed to the change of the rhenium electronic structure.

At the same time, the  $\text{Re}(\text{Re}_2)_6$  octahedra do not distort, although it was pointed out that the MSRD factor  $\sigma_{\text{Re}_0-\text{Re}_2}^2$  for the second coordination shell increases significantly upon hydrogen intercalation. In fact, the histograms in Fig. 7.5 are narrow, and the ratio  $V_O/V_S$  is close to  $\pi$ . It reflects the fact that, as

it was mentioned, the change of the value of the MSD factor  $\sigma_{\text{Re}_0-\text{Re}_2}^2$  is mostly due to the reduction of the correlation of atomic motion, not due to static lattice distortion. This result agrees with the cubic symmetry of hydrogen rhenium bronze [238].

### 7.3 Conclusions

In this study the use of a novel simulation approach, based on the evolutionary algorithm (EA), allowed us to follow structure development at different steps of hydrogen intercalation into  $\text{ReO}_3$  from in-situ EXAFS measurements at the Re  $L_3$ -edge. The employed RMC/EA-EXAFS method allowed us to observe the variation of MSD and MSD as functions of deintercalation time and to determine the characteristic relaxation times for structural parameters in each coordination shell.

We found that atomic motion is strongly correlated in the first and second coordination shells of rhenium in cubic  $\text{ReO}_3$ , whereas it becomes significantly less correlated in  $\text{H}_x\text{ReO}_3$ . The changes in the correlation of atomic motion are attributed to electronic origin, since they have short relaxation time. This effect has been related to additional electrons, localized largely at rhenium atoms and entering into the crystal lattice together with hydrogen ions to maintain charge neutrality.

Besides, the insertion of hydrogen atoms leads to the distortion and tilting of the rhenium-oxygen octahedra. Our analysis revealed that these processes have significantly longer characteristic times.

To conclude, in this chapter on the example of hydrogen intercalation studies we have shown that the use of advanced simulation-based techniques as the RMC/EA-EXAFS method indeed extends potentiality of EXAFS spectroscopy and opens new possibilities for structure determination not accessible by conventional approaches.



## 8. ANISOTROPIC DYNAMICS OF WURTZITE-TYPE ZINC OXIDE

### 8.1 Introduction<sup>1</sup>

Zinc oxide (ZnO) is a wide band-gap ( $E_g = 3.37$  eV [243]) semiconductor, which has many promising technological applications [244, 245, 246, 247] and, therefore, is an extremely popular research topic during the last years [248, 249, 250]. Crystalline lattice of ZnO in most common wurtzite-type phase is essentially anisotropic [251, 252, 253] that is reflected in its piezoelectric [254] and pyroelectric [255] properties. The wurtzite structure has a hexagonal unit cell with two lattice parameters,  $a$  and  $c$ , and belongs to the space group of  $P6_3mc$  [244]. It is composed of two interpenetrating hexagonal-close-packed sublattices, each built up by one type of atoms (Zn or O), which are displaced with respect to each other along the threefold  $c$ -axis by the amount of the internal parameter  $u$ . The Zn and O atoms are in the (2b) Wyckoff positions: Zn  $(0, 0, 0)$ ,  $(1/3, 2/3, 1/2)$ ; O  $(0, 0, u)$ ,  $(1/3, 2/3, 1/2+u)$ . Both Zn and O atoms are tetrahedrally coordinated by four atoms of the other type, and the value of the parameter  $u$  controls the degree of the  $\text{ZnO}_4$  tetrahedra distortion, whereas  $uc$  corresponds to the distance between average positions of nearest Zn and O atoms in the  $[0001]$  direction.

The anisotropy of the ZnO lattice directly influences its lattice dynamics, which is also anisotropic, as revealed by X-ray diffraction measurements of thermal expansion and thermal ellipsoids along  $a$  and  $c$  directions [256, 257, 258]. Obviously, for the design of different nanostructured ZnO-based materials the deep comprehension of such anisotropic properties is essential. However, even in the case of bulk ZnO material the understanding of the local atomic structure and lattice dynamics is still far from complete [259, 260].

---

<sup>1</sup>The material, presented in this chapter, has been published as J. Timoshenko, A. Anspoks, A. Kalinko, A. Kuzmin, LOCAL STRUCTURE AND DYNAMICS OF WURTZITE-TYPE ZnO FROM SIMULATION-BASED EXAFS ANALYSIS, *Phys. Stat. Solidi (c)* (2014), 11 (2014) 1472–1475; and as J. Timoshenko, A. Anspoks, A. Kalinko, A. Kuzmin, TEMPERATURE DEPENDENCE OF THE LOCAL STRUCTURE AND LATTICE DYNAMICS OF WURTZITE-TYPE ZnO, *Acta Mater.* 79 (2014) 194–202.

This issue can be addressed by the extended X-ray absorption fine-structure spectroscopy. The treatment of contributions from the outer shells and many-atom distribution functions using multiple-scattering (MS) theory and simulation-based approaches to EXAFS analysis can give one the access to the information on distributions of bonding angles and, noteworthy, anisotropy of the material structure [261, 119, 120]. In the case of ZnO this means that thermal disorder and interatomic distances within at least the first three coordination shells, containing nearest oxygen and zinc atoms within the *ab*-plane and along the *c*-axis direction, should be determined with high enough accuracy. It is essential to properly account for the MS contributions into the total Zn K-edge EXAFS spectrum: as it will be shown below, they are significant for the outer shells.

Until now only a few EXAFS studies of ZnO have been carried out. The analysis of the first coordination shell around absorbing Zn atom was performed in [262, 263, 264]. It was extended recently up to the third shell of Zn in pure ZnO thin films grown at different nitrogen partial pressures in [265]. Pressure-dependent Zn K-edge EXAFS spectra were analysed in [266], taking into account some multiple-scattering contributions. A number of studies have been devoted to the investigations of doped ZnO thin films and different nanosystems (nanorods, nanoparticles, nanowires). For example, the local environment around Fe [267], Co [268, 269], Ni [270, 271] and Cu [264, 272, 273] in ZnO has been investigated, based on the analysis of the metal K-edge X-ray absorption spectra. An excellent review on the applications of X-ray absorption spectroscopy to the investigations of nanostructured ZnO can be found in [243]. Finally, the study of the O K-edge in single-crystal ZnO has been also carried out in [274].

In this study we employed simulation-based techniques for the analysis of temperature-dependent (10-300 K) Zn K-edge EXAFS data from polycrystalline wurtzite-type ZnO, taking into account all important MS contributions, anisotropy of the system and also the thermal disorder effects. Two techniques, classical molecular dynamics (MD) [4] and reverse Monte Carlo method coupled with evolutionary algorithm (RMC/EA) have been employed for the interpretation of EXAFS spectra with the goals (i) to advance the understanding of the local atomic structure and dynamics of ZnO lattice and (ii) to validate the existing force-field models [275, 276, 277] commonly used in MD simulations.

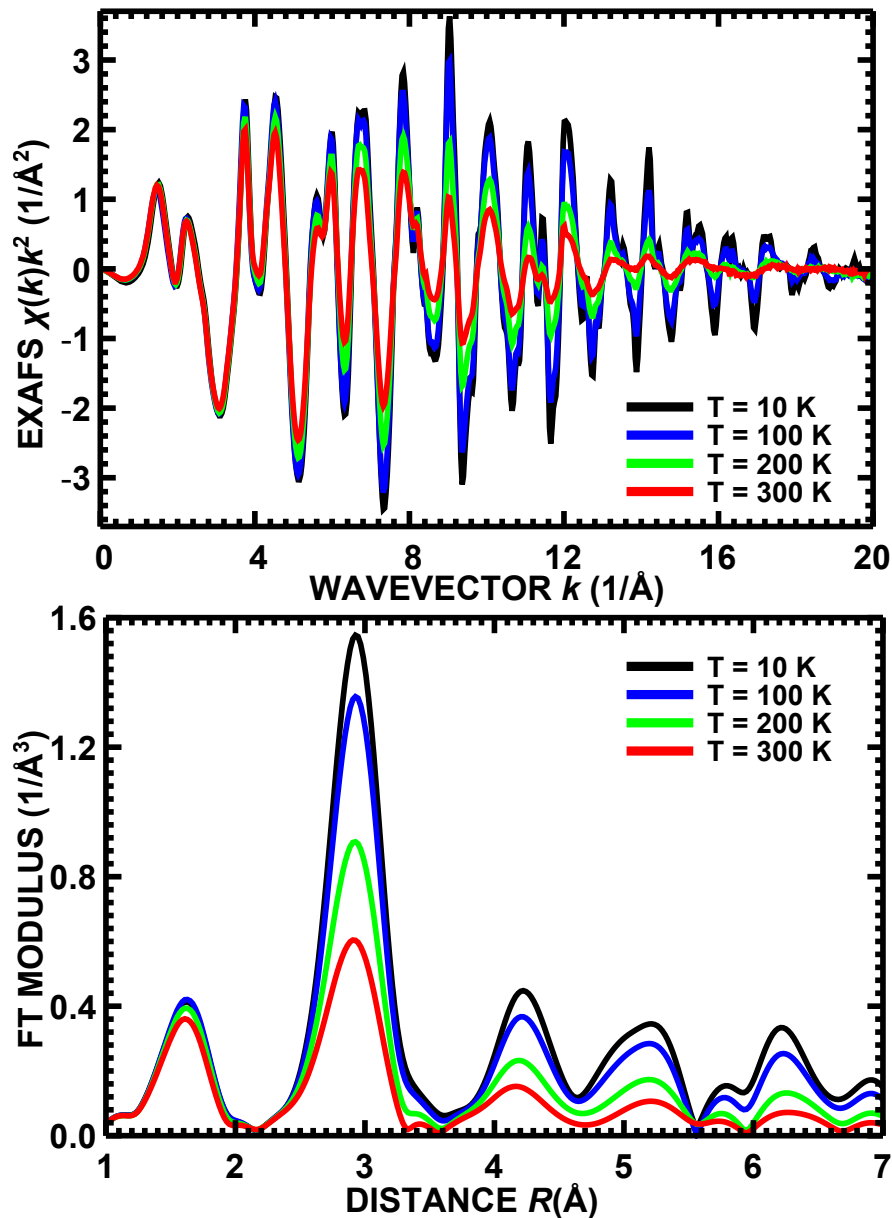


**Figure 8.1:** Experimental Zn K-edge EXAFS spectra for zinc oxide. Experimental spectra  $\chi(k)k^2$  and their Fourier transforms (FT) for polycrystalline wurtzite-type ZnO measured at temperatures from 10 to 300 K.

## 8.2 Experimental and data analysis

X-ray absorption spectra of wurtzite-type ZnO (99.99%, Alfa Aesar) were acquired at the Zn K-edge in transmission mode at the HASYLAB/DESY C bending-magnet beamline [278]. A liquid He flow cryostat was used to perform temperature dependent measurements in the range between 10 and 300 K.

The experimental Zn K-edge EXAFS spectra were extracted using the con-

ventional procedure and are shown together with their Fourier transforms (FT) in Fig. 8.1. The first peak in FT at 1.5 Å is due to the contribution of the first coordination shell (four closest oxygen atoms) around the absorbing zinc atom, whereas the second main peak at 2.9 Å originates mainly due to the outer coordination shells formed by zinc atoms. Due to the overlap of contributions from different coordination shells and due to the mentioned contributions of many-atom distribution functions (the multiple-scattering effects), the analysis of EXAFS data beyond the first coordination shell is a complicated task. Moreover, as it will be shown below, in the case of ZnO even the first coordination shell consists of two separate contributions, which cannot be separated using conventional EXAFS analysis due to the small difference ( $\sim 0.03$  Å) of two non-equivalent Zn–O bond lengths within the  $\text{ZnO}_4$  tetrahedra [251, 252, 253]. To treat these problems, we used two different numerical approaches, based on classical MD and RMC simulations.

### 8.3 Revealing problems of MD force-field models

In classical MD one needs to specify empirical force-field model to calculate interatomic forces. Then the classical Newton's equations of motion can be integrated over time, and the trajectories of atoms can be accumulated. As a result, thousands of different atomic configurations are obtained. For each configuration the EXAFS is calculated using *ab initio* multiple-scattering theory, and the configuration-averaged EXAFS spectrum is obtained [4] and directly compared with the experimental spectrum.

At the moment to our knowledge three different force-field models are used for MD simulations of ZnO (both for crystalline and nanostructured samples) [275, 276, 277]. In all three cases for the description of short-range forces a Buckingham-type potential with different parameters has been used, but for calculations of long-range Coulomb interaction the charges of Zn and O ions were assumed to be equal to formal charges (+2 and -2, correspondingly). Note that the values of parameters in the Buckingham potentials were chosen to have the best possible agreement between calculated and experimentally measured lattice constants, elastic and dielectric properties in [275, 277] and also between corresponding phonon spectra in [276]. Using these three common force-field models, the MD simulations were performed by A. Kuzmin, using the GULP code [279, 280] in the canonical (NVT) ensemble with periodic boundary conditions.

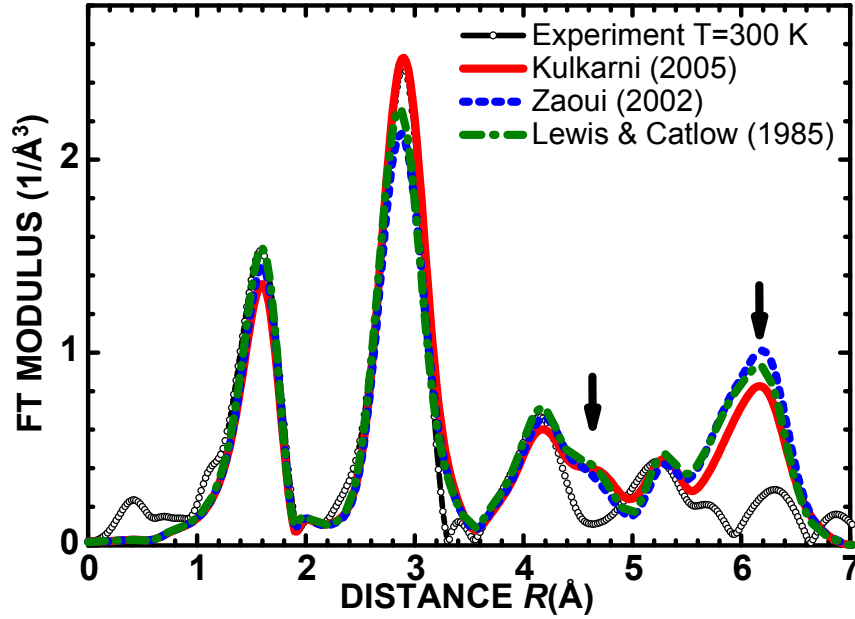


**Figure 8.2:** EXAFS spectra obtained in MD simulations for ZnO. Fourier transforms of the experimental and MD-EXAFS Zn K-edge EXAFS spectra  $\chi(k)k^2$ . The MD-EXAFS spectra were calculated using three different force-field models [275, 276, 277].

The simulation box had a size of the  $5a \times 5a \times 3c$  relaxed supercell ( $a = 3.2706 \text{ \AA}$ ,  $c = 5.1379 \text{ \AA}$ ), containing 300 atoms. The Newton's equations of motion were integrated with the Verlet leapfrog algorithm [281], with a time step of 0.5 fs. The Nosé-Hoover thermostat [282] was used to keep the average temperature around  $T = 300 \text{ K}$  during simulations. For each force-field model a set of 4000 static atomic configurations was generated during a simulation run of 20 ps after system equilibration for 20 ps. These configurations were further used to calculate the Zn K-edge configuration-averaged EXAFS (MD-EXAFS) using ab initio real-space multiple-scattering FEFF8 code. The multiple-scattering contributions were accounted up to the 7th order.

The results of the MD-EXAFS simulations using three different force-field models [275, 276, 277] are compared with the experimental Zn K-edge EXAFS spectrum in Fig. 8.2. As one can see, all three force-field models are able to reproduce rather well the behavior of the zinc coordination shells up to about 4.5 Å, but they fail for outer shells. In particular, the peaks in FT at  $\sim 4.6 \text{ \AA}$  and  $\sim 6.1 \text{ \AA}$  (indicated by arrows in Fig. 8.2) have much higher amplitude in the simulation than in the experiment. However, the detailed analysis of the first two peaks in FT at  $\sim 1.5 \text{ \AA}$  and  $\sim 2.9 \text{ \AA}$  (Fig. 8.2) suggests that also for the

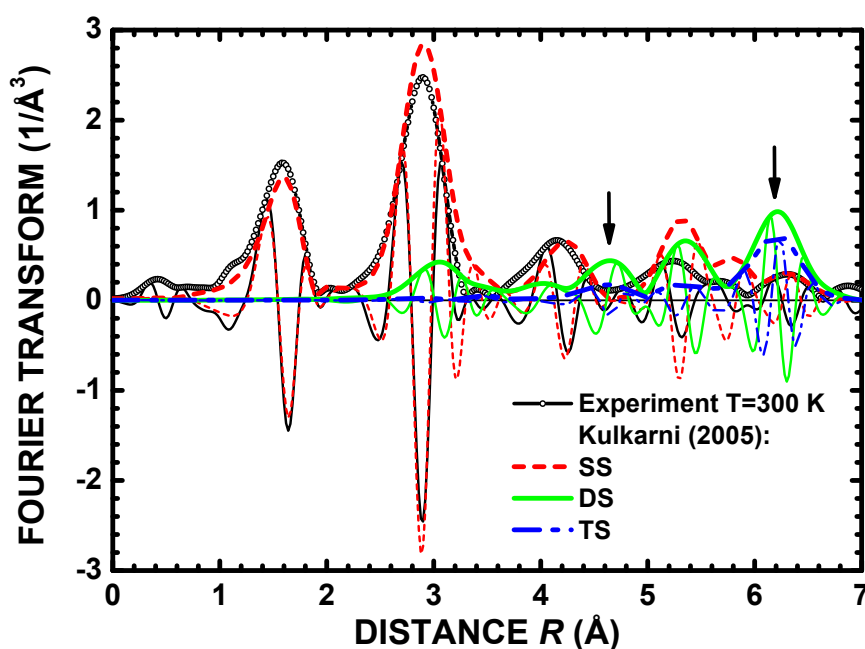


**Figure 8.3: Influence of MS effects on MD-EXAFS spectra for ZnO**

Fourier transforms (imaginary parts and moduli) of the experimental Zn K-edge EXAFS spectrum  $\chi(k)k^2$  ( $T = 300$  K) and MD-EXAFS spectrum, obtained with force-field as in [275], and corresponding total SS, DS and TS contributions to the Zn K-edge MD-EXAFS spectrum.

nearest coordination shells the accuracy of the force-field models is not sufficient to describe properly atom dynamics due to the model simplicity. Note that on average, the model from [275] is slightly better than the other two [276, 277].

The significant differences between the experimental Zn K-edge EXAFS and MD-EXAFS spectra beyond  $4.5$  Å in FT can be attributed to the influence of MS effects, related to the many-atom distribution functions [261]. In Fig. 8.3 the total contributions of the single-scattering (SS), double-scattering (DS) and triple-scattering (TS) events are shown separately. As one can see, the MS (DS and TS) signals dominate in the  $R$ -space ranges where the largest disagreement between the experimental EXAFS and MD-EXAFS spectra is observed, i.e., at  $4.5$ - $4.8$  Å and  $5.6$ - $6.6$  Å. Besides, there is also a prominent DS contribution at  $3.1$  Å (under the second peak in FT) and combined DS and TS contribution at  $5.3$  Å. Note that the MS contributions are substantially out-of-phase with the SS signals, thus leading to the reduction of the total EXAFS amplitude.

To conclude, the force-field models from [275, 276, 277] are able to describe the average structure of ZnO but fail to reproduce accurately its lattice dynamics, i.e., the amplitudes of atom vibrations and correlation effects.

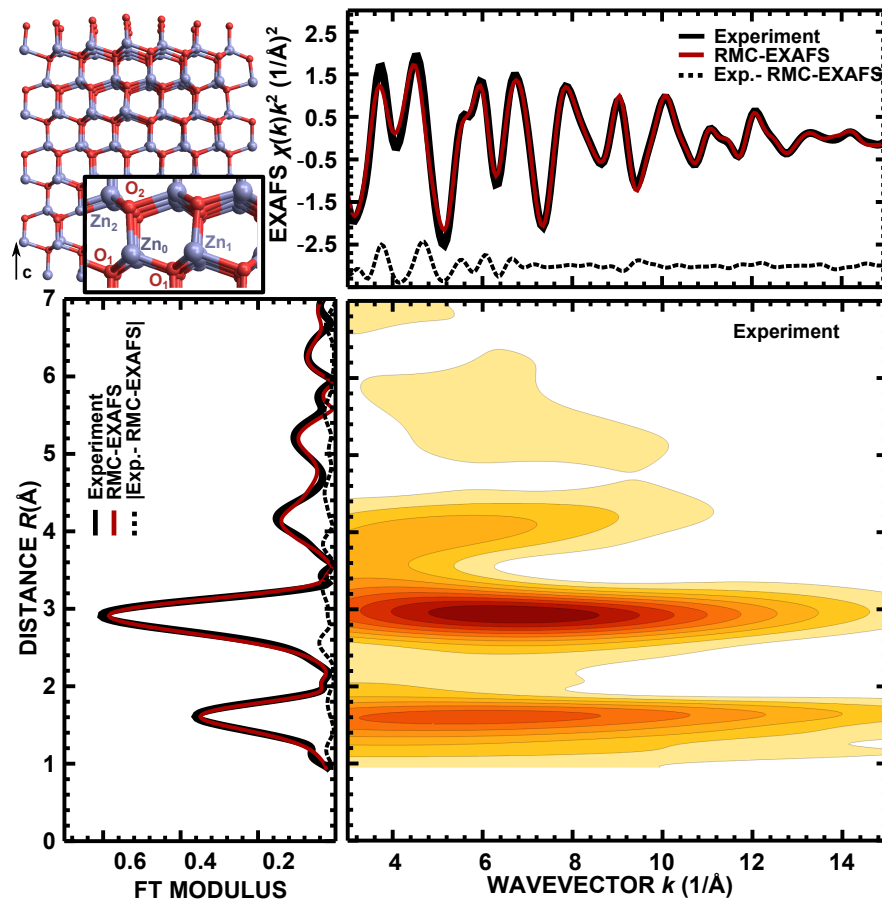


**Figure 8.4:** RMC/EA simulations for the room temperature experimental EXAFS data

Upper left panel: supercell used in the RMC/EA simulation (blue large balls are zinc atoms, red small balls are oxygen atoms). Upper right panel: the experimental ( $T = 300$  K) and calculated (corresponding to the final RMC configuration) Zn K-edge EXAFS spectra and their difference. Bottom left panel: Fourier transforms of the experimental and calculated EXAFS spectra and their difference. Bottom right panel: the Morlet wavelet transform of the experimental EXAFS spectrum.

## 8.4 RMC/EA-EXAFS calculations

Reverse Monte Carlo simulation of EXAFS is potentially capable to achieve better agreement with the experimental data than the MD-EXAFS method due to the possibility to fine tune the structural model. Also, opposite to classical Molecular Dynamics, the RMC method is applicable at low temperatures. In this study RMC/EA simulations with 32 supercells with a size of  $4a \times 4a \times 4c$  ( $a = 3.2496$  Å,  $c = 5.2042$  Å [253]), containing 256 atoms each, have been carried out. Comparison of the experimental and theoretical EXAFS spectra has been performed using Morlet wavelet transform (WT) in the  $k$ -space range from  $3$  Å<sup>-1</sup>

to  $15 \text{ \AA}^{-1}$  and in the  $R$ -space range from  $0.9 \text{ \AA}$  to  $5.5 \text{ \AA}$ .

The supercell, used in the calculations, the experimental ( $T = 300 \text{ K}$ ) EXAFS spectrum and the calculated EXAFS spectrum corresponding to the final RMC configuration (RMC/EA-EXAFS) are shown in Fig. 8.4, along with the Fourier and wavelet images of the experimental and theoretical Zn K-edge EXAFS spectra. Note that the RMC/EA-EXAFS spectrum includes contributions from the scattering paths with the half-path length up to  $6.9 \text{ \AA}$  and the multiple-scattering contributions up to the third order. As one can see, a good agreement between the experimental and calculated Zn K-edge EXAFS spectra is achieved both in  $k$  and  $R$  space, also in the ranges ( $4.5\text{-}4.8 \text{ \AA}$  and  $5.6\text{-}6.6 \text{ \AA}$ ), where the MD-EXAFS models fail (Fig. 8.2). This result suggests that the structural model, obtained by the RMC/EA method, is reliable enough to be used in further analysis for the extraction of more detailed information.

## 8.5 Discussion

### 8.5.1 Comparison of MD and RMC/EA results

First, we will discuss the origin of the problems in the case of the MD models. In Fig. 8.5 (left panel) we show separately the MS and SS contributions to the Fourier transform of the total RMC/EA-EXAFS spectrum. As one can see, here the contribution of the MS effects at  $4.5\text{-}4.8 \text{ \AA}$  is much smaller than in the case of the MD models. Besides, the main interlayer (along  $c$ -axis direction) SS ( $\text{Zn}_0 \rightleftharpoons \text{Zn}$ ,  $R=6.14 \text{ \AA}$ ) and intralayer (along  $a$  or  $b$  axis direction) TS ( $\text{Zn}_0 \rightleftharpoons \text{Zn} \leftrightarrow \text{Zn}$ ,  $R=6.50 \text{ \AA}$ ) signals contributing at  $5.6\text{-}6.6 \text{ \AA}$  in FT are comparable in the RMC/EA model, whereas the TS signal dominates strongly the SS one in the MD models due to the difference in the thermal damping factors (see Fig. 8.5 (right panels)). Therefore, we conclude that the main problem of the MD models [275, 276, 277] is related to the proper accounting for many-atom distribution functions.

The partial radial distribution functions (RDFs) for Zn–O and Zn–Zn atom pairs, obtained from the MD simulations using the force-field model by Kulkarni [275] and from the RMC/EA analysis, are compared in Fig. 8.6 (left panel). At first glance, they are quite close, but differ in details. To highlight the differences, we show (middle and right panels in Fig. 8.6) separately contributions into the partial RDFs from non-equivalent oxygen ( $\text{O}_1$  and  $\text{O}_2$ ) and zinc ( $\text{Zn}_1$  and  $\text{Zn}_2$ ) atoms, located in the first and second coordination shells of absorbing  $\text{Zn}_0$  atom,



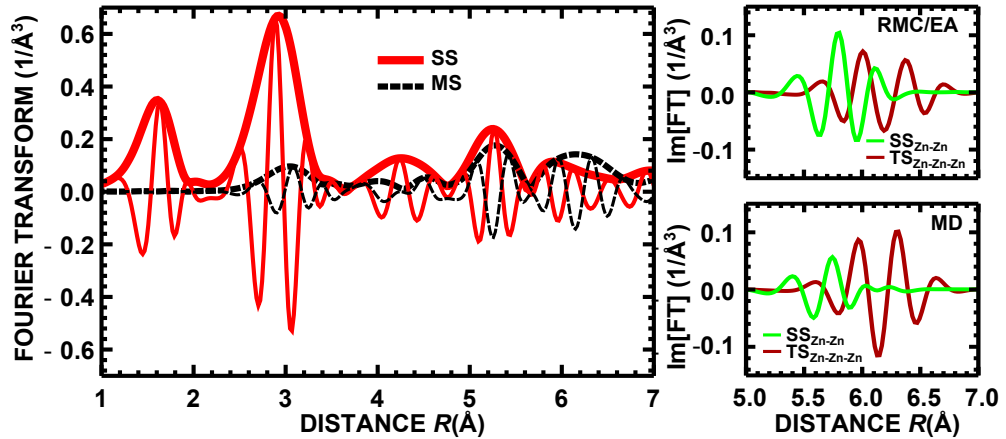


**Figure 8.5: Influence of MS effects on the Zn K-edge EXAFS spectrum for ZnO**

Left panel: Fourier transforms (imaginary parts (thin lines) and moduli (thick lines)) of the total SS and MS contributions to the Zn K-edge RMC/EA-EXAFS spectra, obtained from the best fit of the experimental data measured at  $T = 300$  K. Right panels: Imaginary parts of the Fourier transforms of the SS ( $\text{Zn}_0 \rightleftharpoons \text{Zn}$ ,  $R=6.14$  Å) and TS ( $\text{Zn}_0 \rightleftharpoons \text{Zn} \rightleftharpoons \text{Zn}$ ,  $R=6.50$  Å) EXAFS spectra calculated by RMC/EA and MD methods.

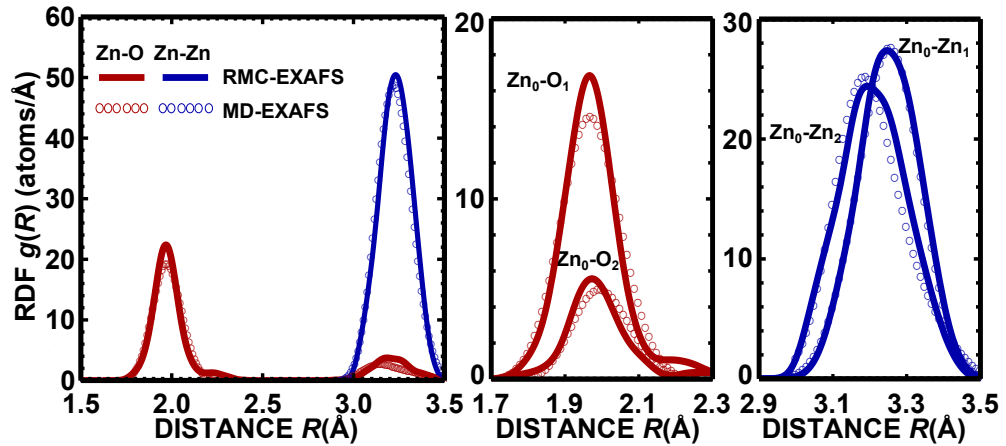


**Figure 8.6: Radial distribution function for atoms around absorbing Zn** Left panel: Partial radial distribution functions (RDFs) for Zn–O (red lines) and Zn–Zn (blue lines) atom pairs, obtained from the MD simulations with the force-field model by Kulkarni [275] (circles) and from the RMC/EA analysis (solid lines) at  $T = 300$  K. Middle and right panels: contributions from non-equivalent oxygen and zinc atoms, located in the first and second shells, respectively.

respectively. As one can see, the Zn–Zn RDFs obtained by the two models are quite close. However, there is clear difference in the amplitude between the  $\text{Zn}_0\text{--O}_1$  contributions from oxygen atoms located in the  $ab$ -plane. Also the width and position of the  $\text{Zn}_0\text{--O}_2$  peaks of oxygen atoms, located along the  $c$ -axis, deviate

appreciably. The failure of the MD simulations comes from the simplicity of the Zn–O pair potential model [275]: it is not able to reproduce accurately the non-centrosymmetric ZnO crystal structure [251, 252, 253], which is responsible for its piezoelectricity.

The partial RDFs, obtained by the RMC/EA method, were used to evaluate the MSRD values for the Zn–O and Zn–Zn atom pairs. At room temperature they are equal to  $\sigma^2(\text{Zn}_0\text{--O}_1) = 0.0040 \pm 0.0003 \text{ \AA}^2$  and  $\sigma^2(\text{Zn}_0\text{--Zn}_1) = 0.0067 \pm 0.0006 \text{ \AA}^2$  along the  $c$ -axis and to  $\sigma^2(\text{Zn}_0\text{--O}_2) = 0.0042 \pm 0.0009 \text{ \AA}^2$  and  $\sigma^2(\text{Zn}_0\text{--Zn}_2) = 0.0088 \pm 0.0009 \text{ \AA}^2$  in the orthogonal direction (in the  $ab$ -plane). These MSRD values indicate that the interactions within Zn–O and Zn–Zn atom pairs differ along the  $c$ -axis and in the  $ab$ -plane.

We will address this difference in details in the next section.

### 8.5.2 Influence of temperature

The RMC/EA-EXAFS method was successfully employed to perform accurate analysis of the Zn K-edge EXAFS spectra for crystalline ZnO at the temperatures  $T \leq 300 \text{ K}$  (Figs. 8.4 and 8.7). Good reproduction of all peaks in FTs up to  $7 \text{ \AA}$  gives us a confidence in the structural information extracted from the outer coordination shells. The final RMC configurations were used to calculate temperature dependencies of the average Zn–O and Zn–Zn interatomic distances and corresponding MSRD factors, characterizing the amplitudes of relative atomic oscillations (Fig. 8.8).

According to the X-ray diffraction data [252, 253] (see dashed lines in Fig. 8.8), the average distances  $\langle R \rangle_{\text{D}}(\text{Zn}_0\text{--Zn}_1)$  and  $\langle R \rangle_{\text{D}}(\text{Zn}_0\text{--Zn}_2)$  should vary little solely due to the lattice thermal expansion. However, the interatomic distances as probed by EXAFS grow with increasing temperature due to the additional contribution caused by thermal vibrations [35]. Note that the average interatomic Zn–Zn distance probed by EXAFS  $\langle R \rangle_{\text{EXAFS}} = \langle R \rangle_{\text{D}} + \langle (\Delta\sigma_{\perp})^2 \rangle / 2\langle R \rangle_{\text{D}}$  should be systematically larger than that  $\langle R \rangle_{\text{D}}$  probed in diffraction experiments [252, 253] due to the second term accounting for the perpendicular MSRD  $\langle (\Delta\sigma_{\perp})^2 \rangle$  of the neighbouring atom in the direction orthogonal to the interatomic bond [35, 36].

At the same time, the average distances between zinc and four nearest oxygen atoms, forming  $\text{ZnO}_4$  tetrahedron (Fig. 8.4), vary differently with increasing temperature. The average distance  $\langle R \rangle_{\text{EXAFS}}(\text{Zn}_0\text{--O}_2)$  between the absorbing zinc and the apical oxygen atom, located along the  $c$ -axis, increases, whereas the average distance  $\langle R \rangle_{\text{EXAFS}}(\text{Zn}_0\text{--O}_1)$  between the absorbing zinc and the three

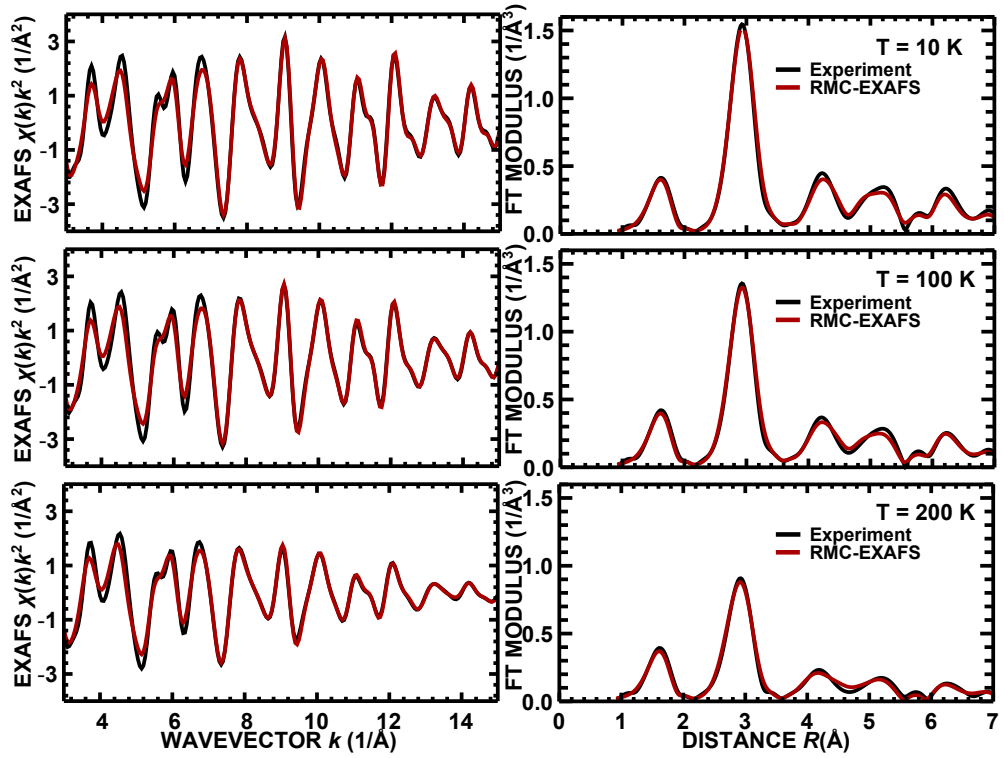
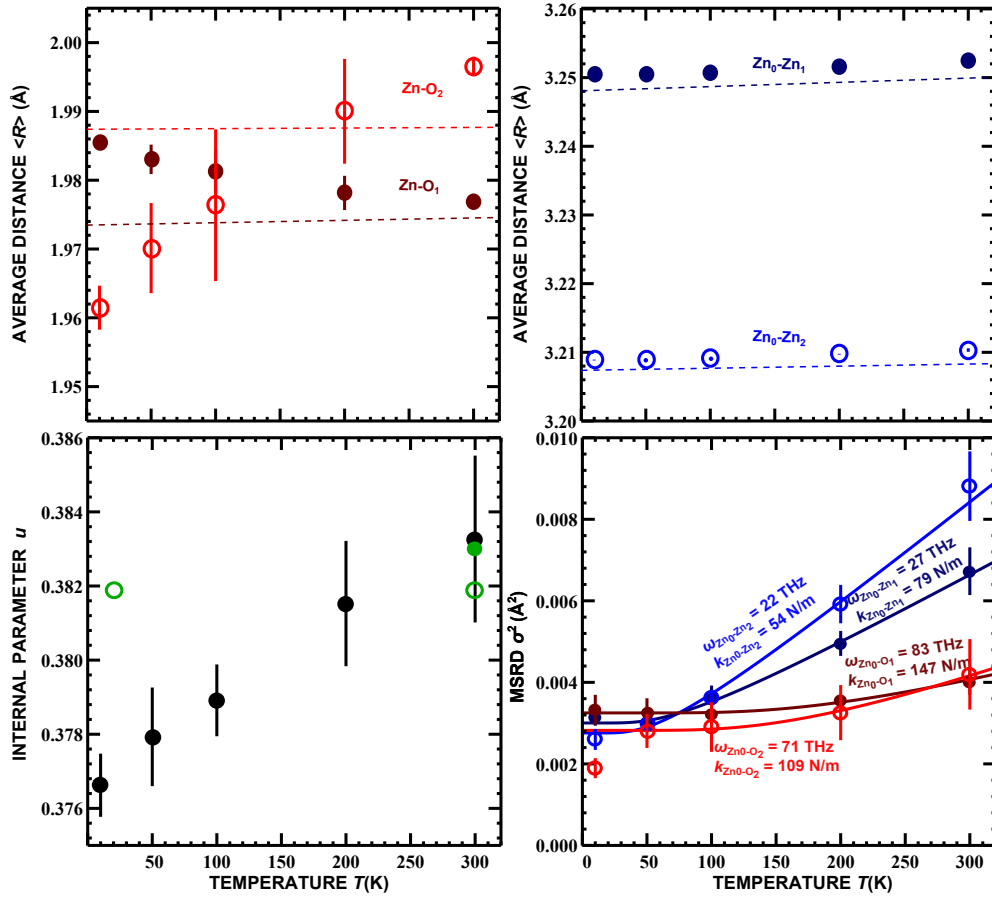


Figure 8.7: Results of the RMC/EA-EXAFS calculations for the experimental Zn K-edge EXAFS spectra in crystalline ZnO at representative temperatures.

basal oxygen atoms, located within the  $ab$ -plane, is slightly reduced. This result implies that the internal parameter  $u$ , giving the equilibrium position of oxygen atom along the  $c$ -axis [283], varies with temperature. The values of the parameter  $u$  as a function of temperature, calculated from the final RMC configurations, are shown in the bottom left panel of Fig. 8.8. It can be seen that the parameter  $u$  increases by about 0.01 with increasing temperature from 10 to 300 K. Clearly, this conclusion should be supported by the diffraction experiments. Surprisingly, to our knowledge up to now there exists only one low temperature study of the parameter  $u$  by neutron diffraction at 20 K [258]. It was concluded in [258] that below room temperature  $u$  does not change significantly. The contradiction between our results, obtained from EXAFS analysis, and neutron diffraction data in [258] is especially intriguing, since it is known that the parameter  $u$  is responsible for pyroelectric properties of wurtzite-type compounds [284].

Temperature dependencies of the parallel MSD's  $\sigma^2$  for the four atom pairs ( $\text{Zn}_0\text{-O}_1$ ,  $\text{Zn}_0\text{-O}_2$ ,  $\text{Zn}_0\text{-Zn}_1$  and  $\text{Zn}_0\text{-Zn}_2$ ) were fitted using correlated Einstein model [37] (bottom right panel of Fig. 8.8). The obtained values of the Einstein



**Figure 8.8: Structure parameters for wurtzite-type ZnO**

Upper panels: temperature dependencies of Zn–O (left panel) and Zn–Zn (right panel) average interatomic distances; dashed lines show X-ray diffraction data in the range from 4.2 to 300 K from [252, 253]. Lower left panel: temperature dependence of the internal parameter  $u$ , obtained from our RMC/EA simulations; the values of parameter  $u$  obtained from diffraction studies are shown by green empty circles (neutron diffraction [258]) and green filled circle (X-ray diffraction [257]). Lower right panel: MSR D factors as a function of temperature for the four atom pairs (Zn<sub>0</sub>–O<sub>1</sub>, Zn<sub>0</sub>–O<sub>2</sub>, Zn<sub>0</sub>–Zn<sub>1</sub> and Zn<sub>0</sub>–Zn<sub>2</sub>) in crystalline ZnO (solid lines – fits by the Einstein model).

frequency ( $\omega$ ) were used to estimate effective bond-strength constants ( $k$ ). They are equal to  $\omega(\text{Zn}_0\text{--O}_1)=83\pm 9$  THz,  $\omega(\text{Zn}_0\text{--O}_2)=71\pm 15$  THz,  $\omega(\text{Zn}_0\text{--Zn}_1)=27\pm 1$  THz,  $\omega(\text{Zn}_0\text{--Zn}_2)=22\pm 1$  THz and  $k(\text{Zn}_0\text{--O}_1)=147\pm 33$  N/m,  $k(\text{Zn}_0\text{--O}_2)=108\pm 28$  N/m,  $k(\text{Zn}_0\text{--Zn}_1)=79\pm 8$  N/m,  $k(\text{Zn}_0\text{--Zn}_2)=54\pm 5$  N/m.

The obtained results suggest that the atoms, located within one  $ab$ -plane (i.e., Zn<sub>0</sub>–Zn<sub>1</sub> and Zn<sub>0</sub>–O<sub>1</sub> atom pairs) are interacting more strongly than the atoms, located in the neighboring layers along the  $c$ -axis (Zn<sub>0</sub>–Zn<sub>2</sub> and Zn<sub>0</sub>–O<sub>2</sub> atom pairs), although the distances between, correspondingly, Zn<sub>0</sub>–Zn<sub>1</sub> and Zn<sub>0</sub>–Zn<sub>2</sub>,

and  $\text{Zn}_0\text{-O}_1$  and  $\text{Zn}_0\text{-O}_2$  are close. Thus it is clear that such system in principle cannot be described accurately by simple pairwise force-field models. Note also that the differences between atom pairs  $\text{Zn}_0\text{-Zn}_1$  and  $\text{Zn}_0\text{-Zn}_2$ , and  $\text{Zn}_0\text{-O}_1$  and  $\text{Zn}_0\text{-O}_2$ , have been already observed in the case of oriented wurtzite-type ZnO nanorods in [285], where the polarization of the synchrotron X-ray beam has been exploited to discriminate contributions of different atom pairs. However, to our knowledge, such strikingly different behaviour is established for the first time for the bulk ZnO in this study.

Finally, we would like to comment on the MSRD value for the  $\text{Zn}_0\text{-O}_2$  bond at 10 K, which is significantly smaller than the one expected from the Einstein model fit to higher temperature experimental data (Fig. 8.8). This fact can be related to very low vibration amplitude of Zn atoms observed previously by neutron diffraction at 20 K in [258]. The origin of such behaviour is unclear and requires further investigations.

## 8.6 Conclusions

The local atomic structure and lattice dynamics in polycrystalline wurtzite-type ZnO were studied by the Zn K-edge X-ray absorption spectroscopy in the temperature range from 10 to 300 K. Temperature dependent EXAFS spectra were analysed using two advanced theoretical approaches based on classical molecular dynamics (MD-EXAFS) and reverse Monte Carlo/evolutionary algorithm (RMC/EA-EXAFS) methods.

The MD-EXAFS method allowed us to use the experimental EXAFS spectra to validate the existing force-field models [275, 276, 277]. We found that the three models are able to reproduce general behaviour of the lattice dynamics in bulk ZnO but fail in the accurate description of thermal motion, especially, the many-atom correlations. Therefore, one should take care when applying them to nanostructured zinc oxide.

The RMC/EA-EXAFS method gives more accurate description of the thermal disorder in ZnO, since it is not limited by any simplified model. As a result, it allowed us to discriminate contributions of non-equivalent Zn and O atoms in the first and second coordination shells around the absorbing Zn atoms. Essential differences between Zn-O and Zn-Zn bonds aligned along the *c*-axis and in the *ab*-plane of ZnO hexagonal crystal lattice were revealed and are responsible for its noncentrosymmetric structure. Our results suggest that both Zn and O atoms,

located inside one atomic layer within the  $ab$ -plane, interact stronger than the atoms at approximately the same distance, but located in the neighboring layers along the  $c$ -axis. The observed changes of the average distances  $Zn_0-O_1$  and  $Zn_0-O_2$  (Fig. 8.4) also imply that with increasing temperature the structure of ZnO becomes more anisotropic, since the oxygen  $O_2$  is pulled closer to the upper  $ab$ -plane (corresponding structural parameter  $u$  increases). The latter result needs to be confirmed by diffraction measurements.

## 9. STRUCTURE OF POLYCRYSTALLINE AND NANOSIZED TUNGSTATES

### 9.1 Introduction<sup>1</sup>.

Transition-metal tungstates  $AWO_4$  are important materials with interesting optical, magnetic and ferroelectric properties, which make them suitable for many practical applications [286, 287, 288]. However, a relation between properties of tungstates and their structure and lattice dynamics is still debatable. Two types of tungstate structure exist depending on the size of the  $A^{2+}$  cation [289]: wolframite-type ( $MnWO_4$ ,  $CoWO_4$ ,  $NiWO_4$ ,  $ZnWO_4$ ,  $CuWO_4$ ,  $FeWO_4$ ) is preferable for small cations, whereas sheelite-type ( $CaWO_4$ ,  $SrWO_4$ ,  $BaWO_4$ ) is adopted for large cations. Tailoring of tungstate properties is possible by producing their solid solutions [290, 291, 292, 293] or reducing the size of crystallites down to nanoscale [294, 295, 296]. In both cases, the knowledge of atomic structure becomes crucial for understanding and controlling of the properties but obtaining this information is a challenging problem.

Bulk  $CoWO_4$  and  $CuWO_4$  are wolframite-type compounds, which order antiferromagnetically at the Néel temperatures of 55 K and 24 K, respectively [297]. Cobalt tungstate has monoclinic structure (space group  $P2/c$ ) [298, 299], while  $CuWO_4$  has even lower, triclinic symmetry (space group  $P\bar{1}$ ) [298, 299, 300]. The low symmetry of  $CuWO_4$  is due to the first-order Jahn-Teller (FOJT) effect that is characteristic also for many other transition-metal complexes. In the case of  $CuWO_4$  it is caused by  $3d^9$  electron configuration of  $Cu^{2+}$  ions [301, 302, 303, 304]:  $d$ -electrons of copper interact with negatively charged oxygen ions and distortion of  $CuO_6$  octahedra gets energetically favorable. This results in the axial distortion ( $4 \times R(Cu-O) \sim 1.97 \text{ \AA}$  and  $2 \times R(Cu-O) \sim 2.4 \text{ \AA}$ ) of  $CuO_6$  octahedra. Note

---

<sup>1</sup>The material, presented in this chapter, has been partially published as J. Timoshenko, A. Anspoks, A. Kalinko, A. Kuzmin, ANALYSIS OF EXAFS DATA FROM COPPER TUNGSTATE BY REVERSE MONTE CARLO METHOD, *Physica Scripta* 89 (2014) 044006 (6 pages); and as J. Timoshenko, A. Anspoks, A. Kalinko, A. Kuzmin, LOCAL STRUCTURE OF NANOSIZED TUNGSTATES REVEALED BY EVOLUTIONARY ALGORITHM (accepted for publication in *Physica Status Solidi A* in 2014)

that the  $\text{CoO}_6$  octahedra in  $\text{CoWO}_4$  are also distorted but in a more subtle way, having 4 short ( $\sim 2.07$  Å) and two longer ( $\sim 2.13$  Å) Co–O bonds.

Tungsten ions, having formally 6+ valence state ( $5d^0$  electron configuration), form partially covalent bonds with six oxygen atoms that results in a distortion of  $\text{WO}_6$  octahedra via the second-order Jahn-Teller (SOJT) effect [305]. In this case the large ionic charge of tungsten reduces the energy of vacant  $d$ -orbitals and the  $p$  electrons from neighboring oxygen atoms may enter. Then, similarly as in the case of FOJT, the deformation of  $\text{WO}_6$  octahedra allows to reduce total energy. In  $\text{CoWO}_4$  this distortion leads to the off-center displacement of tungsten atoms and results in 4 shorter ( $\sim 1.85$  Å) and 2 longer ( $\sim 2.12$  Å) W–O bonds. At the same time,  $\text{WO}_6$  octahedra in  $\text{CuWO}_4$  are more strongly deformed: here 3 nearest ( $\sim 1.8$  Å), 2 intermediate ( $\sim 2.0$  Å) and 1 distant ( $\sim 2.2$  Å) oxygen atoms are present.

Both  $\text{CoWO}_4$  and  $\text{CuWO}_4$  are very promising catalytic materials, for instance, for photocatalytic oxidation of water. Catalytic properties of these compounds are especially pronounced in their nanostructured form: very small sizes of nanoparticles (smaller than 2 nm) are characteristic for both materials that results in high surface-to-volume ratio [306]. Thus the properties of such materials strongly depend on the atomic structure, which, in turn, can significantly differ from that in the bulk.

X-ray absorption spectroscopy may be a proper tool to investigate the structure of wolframite-type compounds due to its local sensitivity and element selectivity [2]. In our recent works [307, 308, 309, 60, 304, 310, 311] we have used EXAFS to study the local structure (first coordination shell) both of microcrystalline and nanocrystalline tungstates ( $\text{ZnWO}_4$ ,  $\text{NiWO}_4$ ,  $\text{MnWO}_4$ ,  $\text{CoWO}_4$ ,  $\text{CuWO}_4$ ,  $\text{CaWO}_4$ ,  $\text{SrWO}_4$ ,  $\text{BaWO}_4$ ,  $\text{SnWO}_4$ ). EXAFS studies of  $\text{AgWO}_4$  (W  $L_3$ -edge) [312],  $\text{CdWO}_4$  (W  $L_3$  and Cd K-edges) [313],  $\text{PbWO}_4$  single crystals (W  $L_3$ -edge) [314] and microcrystalline  $\text{PbWO}_4$  (W and Pb  $L_3$ -edges) [315] are reported in literature. The evolution of the distortion of  $\text{CuO}_6$  octahedra upon applied pressure in  $\text{CuWO}_4$  was analyzed using the Cu K-edge EXAFS in [302]. In all of these cases, however, EXAFS analysis was limited to the first coordination shell of metal atoms only: a complex structure and low symmetry of tungstates complicate the interpretation of EXAFS spectra by conventional methods for the outer coordination shells significantly [316]. Moreover, the use for EXAFS analysis of advanced simulation technique as classical molecular dynamics (MD)



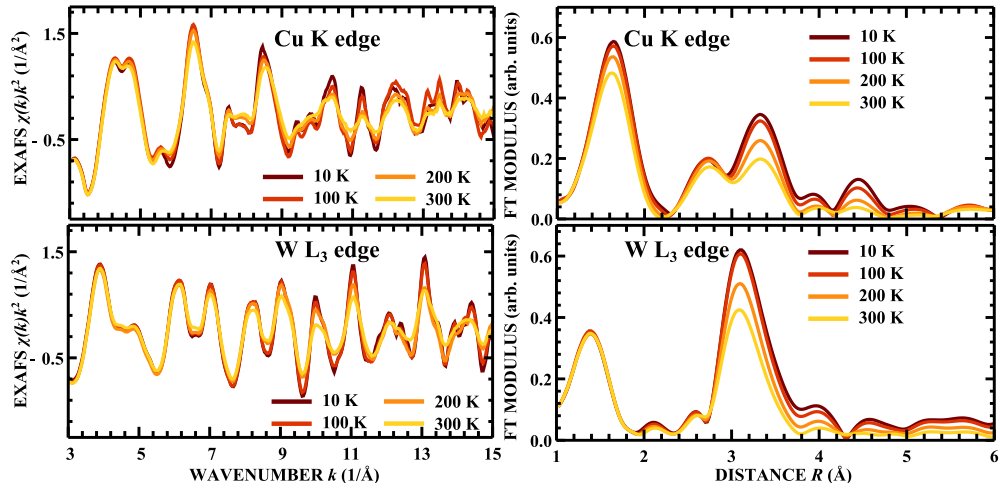


**Figure 9.1: EXAFS spectra for microcrystalline  $\text{CuWO}_4$**   
 $\text{CuWO}_4$  EXAFS spectra at Cu K-edge and W  $L_3$ -edge, measured in the temperature range between 10 K and 300 K, and the corresponding Fourier transforms.

[4, 63, 57] is also not possible in this case due to the lack of the precise force-field model for such complicated structures.

Therefore, in this work we analyze the EXAFS data for copper tungstate  $\text{CuWO}_4$  and for cobalt tungstate  $\text{CoWO}_4$  using the reverse Monte Carlo and evolutionary algorithm (RMC/EA) technique. The RMC/EA-EXAFS approach first is applied to the investigations of microcrystalline  $\text{CoWO}_4$  and  $\text{CuWO}_4$  powders and then is used to reconstruct the 3D structure of nanocrystalline  $\text{CuWO}_4$  and  $\text{CoWO}_4$ .

## 9.2 Experimental data

X-ray absorption measurements were performed in transmission mode at the HASYLAB DESY C1 bending-magnet beamline at the Co K (7709 eV), Cu K (8979 eV) and W  $L_3$  (10207 eV) edges. The X-ray beam intensity was measured by two ionization chambers filled with argon and krypton gases. The higher order harmonics were removed by detuning of the double-crystal monochromator Si(111) to 60% of the rocking curve maximum using the beam-stabilization feedback control.

Nanocrystalline  $\text{CoWO}_4$  and  $\text{CuWO}_4$  powder samples were obtained by coprecipitation method from aqueous solutions of  $\text{Na}_2\text{WO}_4 \cdot \text{H}_2\text{O}$  and  $\text{Co}(\text{NO}_3)_2 \cdot 6\text{H}_2\text{O}$  or  $\text{Cu}(\text{SO}_4)_2 \cdot 5\text{H}_2\text{O}$  at room temperature,  $\text{pH} = 8$  [317, 318]. Microcrystalline powders were obtained from nanopowders by annealing at  $800^\circ\text{C}$  for 4-8 hours. Both

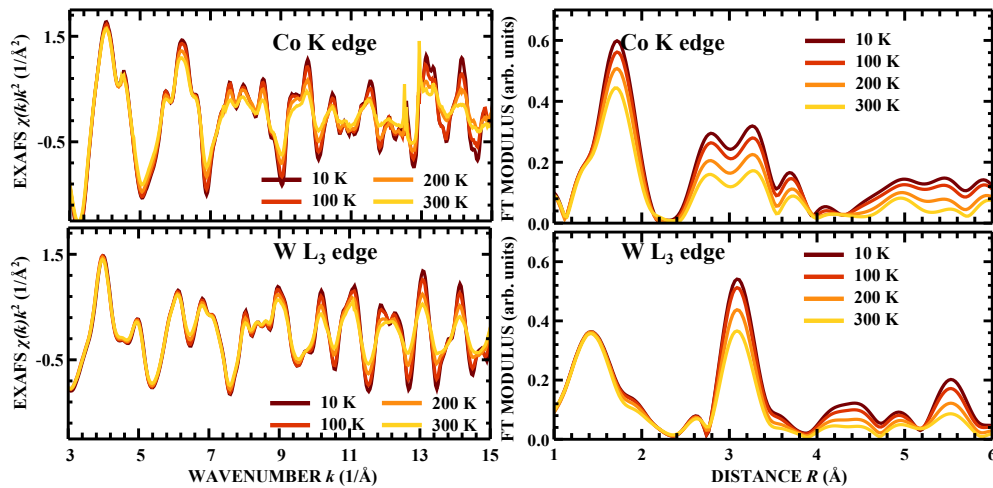


**Figure 9.2: EXAFS spectra for microcrystalline  $\text{CoWO}_4$**

$\text{CoWO}_4$  EXAFS spectra at Co K-edge and W  $L_3$ -edge, measured in the temperature range between 10 K and 300 K, and the corresponding Fourier transforms.

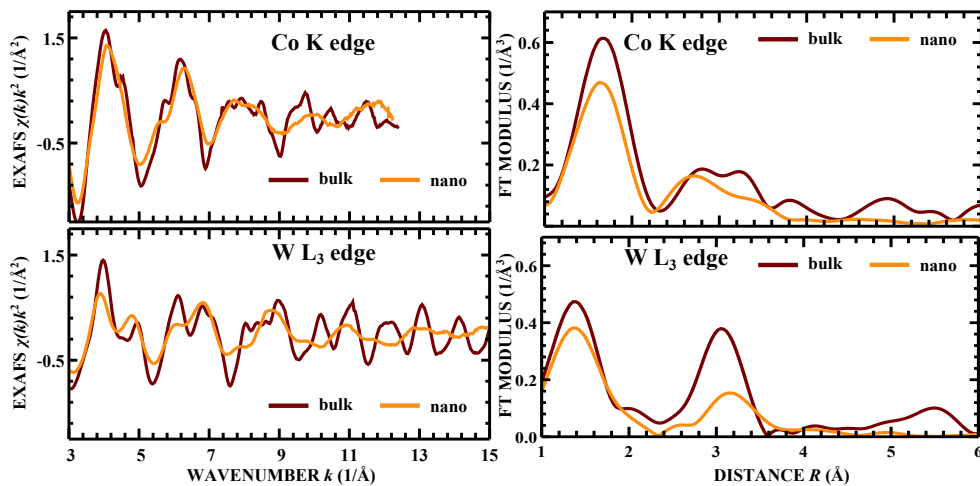


**Figure 9.3: EXAFS spectra for nanocrystalline  $\text{CoWO}_4$**

Experimental Co K-edge and W  $L_3$ -edge room temperature EXAFS spectra for microcrystalline ("bulk") and nanocrystalline ("nano")  $\text{CoWO}_4$  and their Fourier transforms.

microcrystalline and nanocrystalline samples were previously characterized using Raman spectroscopy, FTIR measurements and X-ray diffraction [311]: nanosized tungstates appeared to be X-ray amorphous, which indicates that the synthesized nanocrystallites are just a few nanometers large. The only visible broad band in Raman spectra is located at  $955\text{ cm}^{-1}$  and can be associated with short W-O bond [311].

For XAS measurements both nanocrystalline and microcrystalline powders were deposited on Millipore filter and fixed by Scotch tape.

The sample temperature was maintained using the Oxford Instruments liquid helium flow cryostat. EXAFS data were extracted from the total absorption spectra using conventional procedure (Sec. 2.7.2).

Temperature dependent experimental EXAFS from microcrystalline ("bulk") CoWO<sub>4</sub> and CuWO<sub>4</sub> are shown in Figs. 9.1 and 9.2, while room temperature EXAFS data for microcrystalline and nanocrystalline CoWO<sub>4</sub> and their Fourier transforms (FT) are compared in Fig. 9.3.

As one can see, the thermal disorder has relatively weak influence on the shape of EXAFS of investigated tungstates: with the increase of temperature from 10 K to 300 K the amplitude of EXAFS spectra is only slightly reduced. Especially noteworthy is the first peak of the Fourier transform of W L<sub>3</sub>-edge EXAFS: it is almost completely temperature independent, indicating that the first coordination shell around tungsten is practically insensitive to temperature changes.

At the same time, when one compares the amplitude of EXAFS spectra from microcrystalline and nanocrystalline CoWO<sub>4</sub>, one can note that the amplitude of EXAFS for nanocrystalline CoWO<sub>4</sub> is significantly smaller (especially for W L<sub>3</sub>-edge spectrum) suggesting strong structure distortion due to size reduction and accompanying structure relaxation effects. The FT peaks beyond the second one are almost completely suppressed, indicating the lack of order beyond the first few coordination shells. This may be interpreted as an evidence of the very small size of nanoparticles.

### 9.3 Separate analysis of the Co/Cu K-edge and W L<sub>3</sub>-edge EXAFS for microcrystalline tungstates CoWO<sub>4</sub> and CuWO<sub>4</sub>

#### 9.3.1 CoWO<sub>4</sub> case

In the first calculations we focused on the investigations of microcrystalline tungstates, and initially we analyzed separately the available W L<sub>3</sub>-edge and Co (or Cu) K-edge EXAFS spectra.

The RMC/EA calculations were carried out for population of 32 4×4×4 supercells (768 atoms). A difference between the model and RMC/EA-EXAFS spectra was minimized by the best fit of their wavelet transforms (WT), i.e., simultaneously in *k*-space and in *R*-space (Eq. (4.12)). For CoWO<sub>4</sub> corresponding

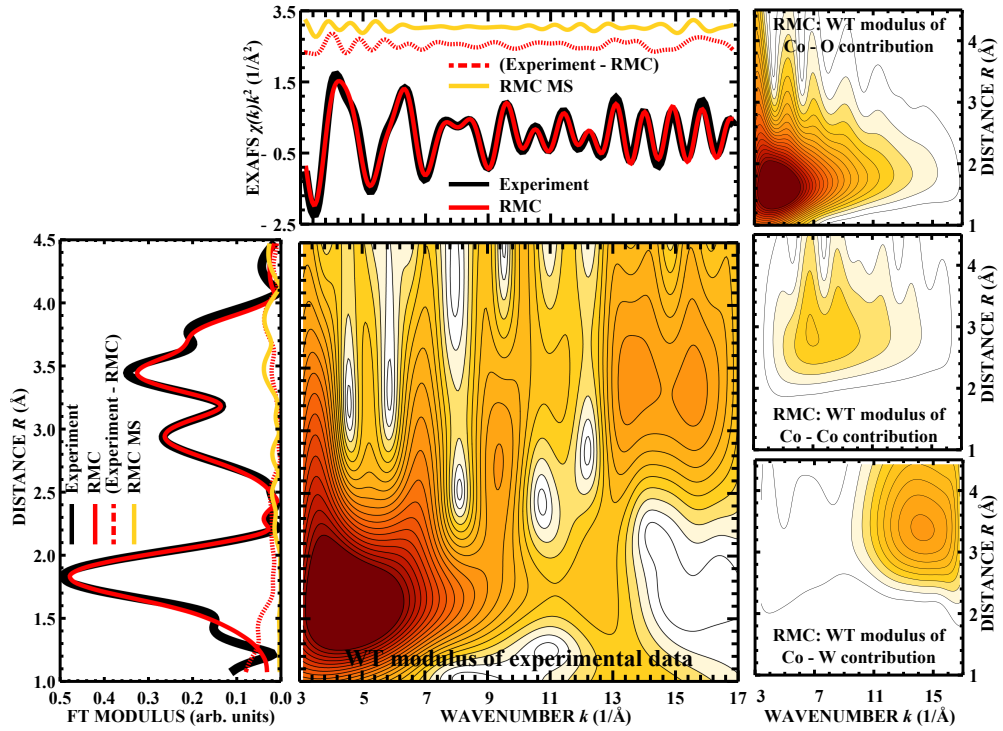


**Figure 9.4:** RMC/EA analysis of the Co K-edge EXAFS spectrum for microcrystalline  $\text{CoWO}_4$

Experimental Co K-edge EXAFS spectrum for  $\text{CoWO}_4$  ( $T = 6$  K), total RMC EXAFS spectrum, a contribution of the MS effects (RMC MS) and the difference between experimental and total RMC EXAFS spectra are shown along with their Fourier transforms. The WT moduli of the experimental spectrum and the Co–O, Co–W and Co–Co contributions to the total RMC EXAFS signal are shown in the central and three right panels, respectively.

WTs have been carried out in the  $k$ -space from 3 to 15  $\text{\AA}^{-1}$  and in  $R$ -space from 1 to 4.5  $\text{\AA}$ . For  $\text{CuWO}_4$  corresponding WTs have been carried out in the  $k$ -space from 3 to 17  $\text{\AA}^{-1}$  and in  $R$ -space from 1 to 3.8  $\text{\AA}$ .

The experimental ( $T = 6$  K) and simulated Co K-edge EXAFS spectra are compared in Fig. 9.4 along with their Fourier and wavelet transforms. The RMC/EA method successfully reconstructs the experimental Co K-edge EXAFS signal, revealing the 3D structure of tungstate and allowing to analyze the influence of different contributions on the total EXAFS. Note that the influence of the multiple-scattering (MS) effects turns out to be almost negligible in the case of the Co K-edge EXAFS in  $\text{CoWO}_4$ . In addition, the contributions of Co–O, Co–Co and Co–W distances are clearly separated in the wavelet image of EXAFS spectrum, making the wavelet transform to be an ideal tool for the analysis of EXAFS in such complex systems.

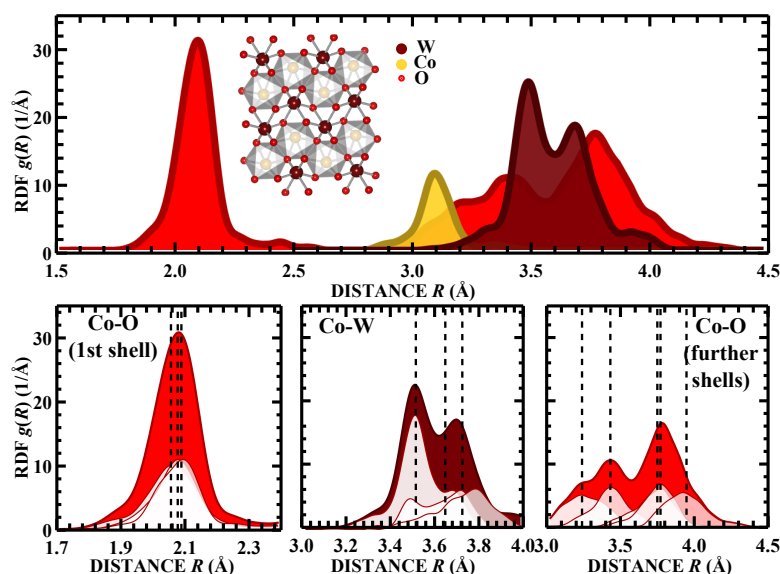


**Figure 9.5:** Radial distribution of atoms around cobalt for microcrystalline  $\text{CoWO}_4$

Partial RDFs (Co–O, Co–Co and Co–W) around cobalt atom, calculated from the RMC/EA results ( $T = 6$  K). The contributions of the Co–O and Co–W atom pairs are separately shown in the bottom panels.

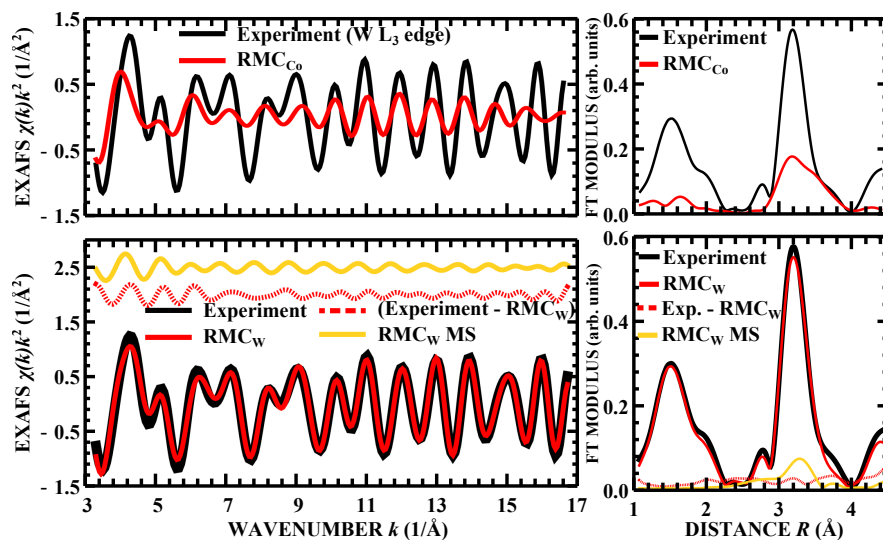


**Figure 9.6:** Checking the obtained structural model for microcrystalline  $\text{CoWO}_4$

The W L<sub>3</sub>-edge EXAFS, calculated for the atomic configuration, obtained from RMC simulations for the Co K-edge EXAFS spectrum, and the corresponding W L<sub>3</sub>-edge experimental EXAFS ( $T = 6$  K), and their FT (upper panels). The results of RMC/EA calculations using the W L<sub>3</sub>-edge experimental EXAFS spectrum (bottom panels).

The atomic radial distribution functions (RDFs) can be calculated straightforwardly from the results of the RMC/EA simulation. The partial RDFs around Co atom are shown in Fig. 9.5, where individual contributions from non-equivalent atoms of the same type (O and W) are also presented in the bottom panels. Note that even the first coordination shell of cobalt in CoWO<sub>4</sub> consists actually of three different Co–O contributions.

To check the structural model, obtained from the RMC/EA simulation of the Co K-edge EXAFS (Fig. 9.4), we employed it further to calculate the W L<sub>3</sub>-edge EXAFS (RMC<sub>Co</sub> curve in Fig. 9.6). In the upper row in Fig. 9.6 we compare this theoretical signal with the experimental EXAFS spectrum. As one can see, the two EXAFS spectra differ significantly: in particular, the amplitude of the RMC<sub>Co</sub> EXAFS is much lower than that of the experimental signal, i.e., our RMC/EA simulation overestimated the mean-square relative displacements for the oxygen atoms around tungsten. At the same time, if RMC/EA simulation is performed using the experimental W L<sub>3</sub>-edge EXAFS spectrum instead of the one from the Co K-edge, the agreement between theoretical and experimental EXAFS spectra becomes very good (lower row in Fig. 9.6). This result suggests that the EXAFS signal from the one absorption edge only does not provide sufficient information to accurately reconstruct the complicated structure of CoWO<sub>4</sub>.

### 9.3.2 CuWO<sub>4</sub> case

Similar results can be obtained also for CuWO<sub>4</sub> system: the results of RMC/EA simulations for the W L<sub>3</sub>-edge are shown in Fig. 9.7. Again, the influence of the multiple-scattering (MS) effects is small, but non-negligible, and they contribute to the large and complex peak of FT at 3.3 Å. Through the MS effects this peak thus contains additional indirect information also about the atoms in the first coordination shell.

The contributions of the W–O, W–W and W–Cu paths are clearly separated in the wavelet image of the EXAFS despite the fact that some of them correspond to similar interatomic distances  $R$ : one can see, for instance, the backscattering from heavy tungsten atoms has larger contribution to the total EXAFS at higher values of wavevector  $k$  than the backscattering from lighter copper or oxygen.

Similarly as in the case of CoWO<sub>4</sub>, the structural model, obtained from the RMC simulation of the W L<sub>3</sub>-edge EXAFS from CuWO<sub>4</sub>, was employed further to calculate the Cu K-edge EXAFS spectrum (RMC<sub>W</sub> curve in Fig. 9.8).

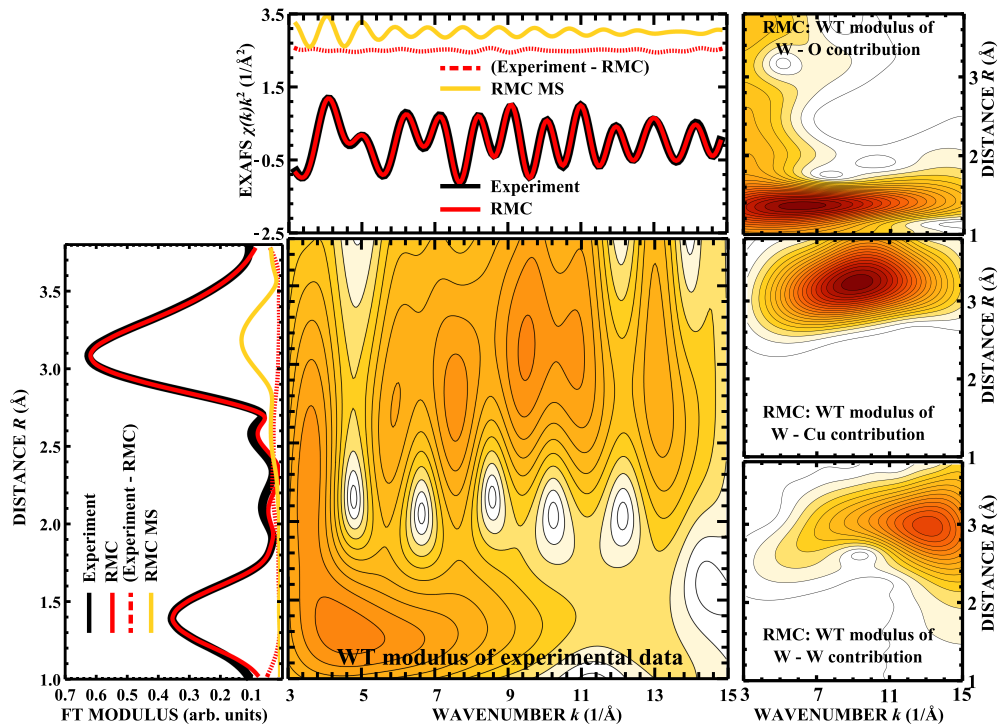


**Figure 9.7: RMC/EA analysis of the W L<sub>3</sub>-edge EXAFS spectrum for microcrystalline CuWO<sub>4</sub>**

Experimental W L<sub>3</sub>-edge EXAFS spectrum ( $T = 10$  K) for CuWO<sub>4</sub>, total RMC-EXAFS spectrum, a contribution of the MS effects (RMC MS) and the difference between experimental and total RMC-EXAFS spectra are shown along with their Fourier transforms. The WT moduli of the experimental spectrum and the W–O, W–W and W–Cu contributions to the total RMC-EXAFS signal are shown in the central and three right panels, respectively.

In the upper row in Fig. 9.8 we compare this theoretical spectrum with the experimental ( $T = 10$  K) EXAFS data. And again one can see, the two EXAFS spectra differ significantly. And, again, if RMC/EA simulation is performed using the experimental Cu K-edge EXAFS spectrum instead of the one from the W L<sub>3</sub>-edge, the agreement between theoretical and experimental EXAFS spectra becomes very good (lower row in Fig. 9.8).

To conclude, the results, obtained both for CoWO<sub>4</sub> and CuWO<sub>4</sub> in studies, where the EXAFS data from tungsten and Co (Cu) absorption edges were treated separately, show that in this case the information from a single absorption edge is not sufficient to unambiguously reconstruct the 3D structure of complex material. As was shown, the influence of multiple-scattering effects is small in the observed systems. Therefore EXAFS is determined practically only by pair-distribution functions of involved atoms in this case and contains no information on angles.

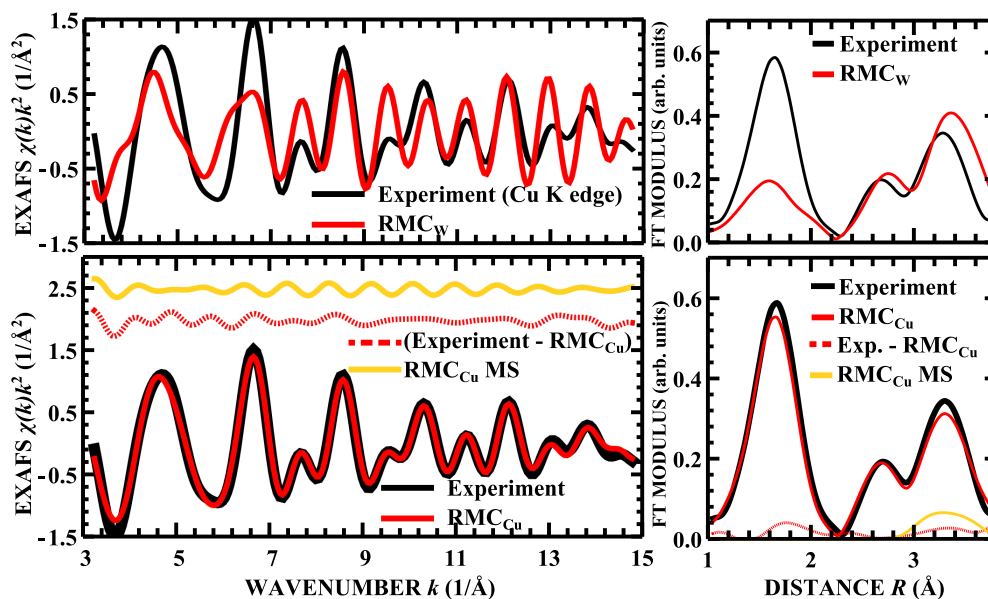


**Figure 9.8:** Checking the obtained structural model for microcrystalline  $\text{CuWO}_4$

The Cu  $K$ -edge EXAFS signal, calculated for the atomic configuration, obtained from RMC/EA simulation for the W  $L_3$ -edge EXAFS spectrum, and the corresponding Cu  $K$ -edge experimental EXAFS spectrum ( $T = 10$  K), and their FT (upper panels). The results of RMC/EA calculations using the Cu  $K$ -edge experimental ( $T = 10$  K) EXAFS spectrum (bottom panels).

Therefore we cannot expect to be able to reconstruct the distribution of oxygens in the first coordination shell around, say, tungsten from the Co/Cu  $K$ -edge EXAFS spectra - there is simply no such information in these data.

Rather obvious solution to the above mentioned problem is to perform RMC/EA fit of the Co (Cu)  $K$ -edge and W  $L_3$ -edge EXAFS spectra simultaneously, using a single structural model for both spectra.

## 9.4 Simultaneous fit of the Co/Cu $K$ -edge and W $L_3$ -edge EXAFS

### 9.4.1 $\text{CoWO}_4$ case

In this section we present the results, obtained by RMC/EA simulations for microcrystalline  $\text{CoWO}_4$  and  $\text{CuWO}_4$ , where at each iteration the quality of structure model was estimated by calculating differences  $\xi$  (Eq. 4.12) between experimental and theoretical EXAFS data both for the W  $L_3$  and Co (Cu)  $K$  absorption edges. The total difference between experimental and calculated EX-



AFS data  $\xi = (\xi_W + \xi_{\text{Co(Cu)}})/2$  was obtained from the difference between the wavelet transforms of experimental and simulated W L<sub>3</sub>-edge EXAFS spectra  $\xi_W$  and the difference between the wavelet transforms of experimental and simulated Co (or Cu) K-edge EXAFS  $\xi_{\text{Co(Cu)}}$ .

The results of such calculations are shown in Fig. 9.9. In this case the EXAFS spectra for both absorption edges were calculated in the single-scattering approximation, since, as it was already pointed out in Figs. 9.4 and 9.6, the contribution of the multiple-scattering effects to the total EXAFS signal in the case of CoWO<sub>4</sub> is small and is of the same order of magnitude as the final difference between experimental and total calculated EXAFS spectra.

One can see from the two left panels in Fig. 9.9 that both the Co K-edge and W L<sub>3</sub>-edge EXAFS spectra, obtained from the simultaneous RMC/EA fit, agree reasonably well with the corresponding experimental EXAFS spectra. This means that the obtained atomic configuration equally well represents the local structure around both cobalt and tungsten atoms. The calculated radial distribution functions around Co and W atoms are shown in the two right panels in Fig. 9.9. Note that while the RDFs for the outer shells above 2.7 Å are close for cobalt and tungsten, as can be expected from CoWO<sub>4</sub> structure, the first coordination shell, composed of six oxygen atoms, differs significantly, being strongly distorted around tungsten atoms and rather regular around cobalt atoms.

#### 9.4.2 CuWO<sub>4</sub> case

The results of RMC/EA modelling of the Cu K-edge and W L<sub>3</sub>-edge EXAFS from CuWO<sub>4</sub> simultaneously, using a single structural model for both spectra are shown in Fig. 9.10. One again can see from the two left panels in Fig. 9.10 that the agreement between experimental EXAFS data and the results of RMC/EA simulations is reasonable both for the Cu K-edge and W L<sub>3</sub>-edge, i.e., the obtained structure model equally describes the local structure around both copper and tungsten atoms.

The calculated radial distribution functions around Cu and W atoms are shown in the two right panels in Fig. 9.10. As in the case of CoWO<sub>4</sub>, first coordination shell around tungsten is strongly distorted due to the second-order Jahn-Teller effect: three different groups of W–O distances can be distinguished (at 1.7 Å, at 2.1 Å and at 2.3 Å). However, in the case of CuWO<sub>4</sub> also the first coordination shell around Cu is significantly distorted: six closest oxygen atoms can be arranged in two groups - one with Cu–O distances about 1.9 Å, the other

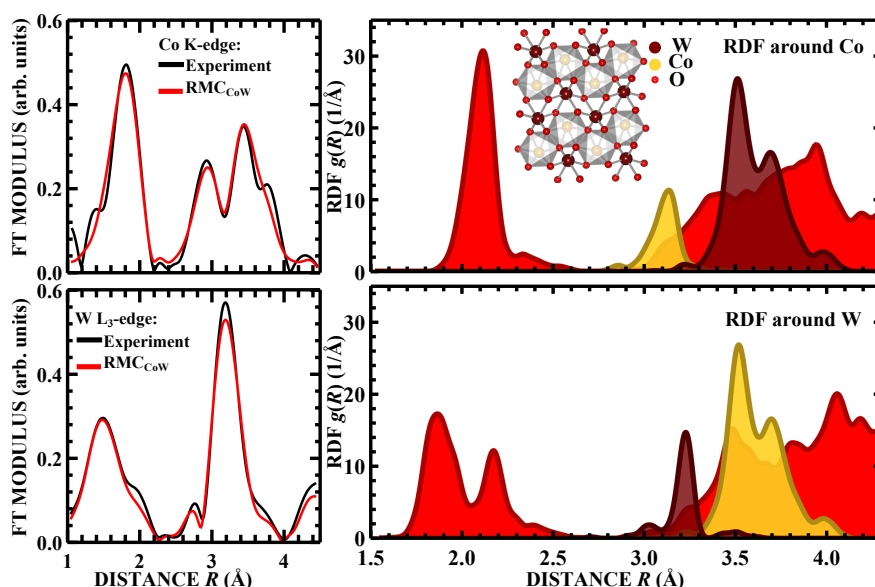


Figure 9.9: RMC/EA simulations for microcrystalline  $\text{CoWO}_4$  using the Co K-edge and W L<sub>3</sub>-edge EXAFS data simultaneously. FT of the calculated and experimental ( $T = 6$  K) spectra (left panels), and corresponding calculated RDF around cobalt and tungsten atoms (right panels).

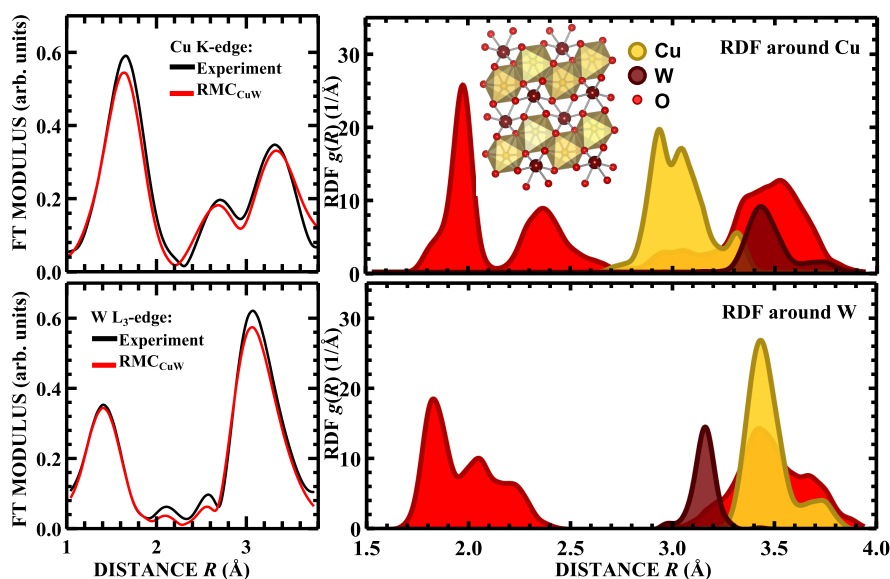
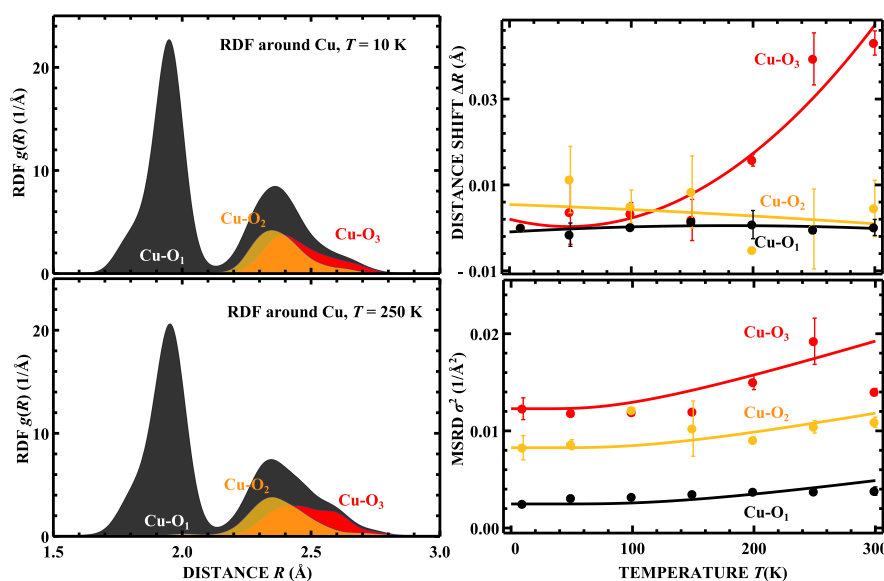


Figure 9.10: RMC/EA simulations for microcrystalline  $\text{CuWO}_4$  using the Cu K-edge and W L<sub>3</sub>-edge EXAFS spectra simultaneously. FT of the calculated and experimental spectra for  $T = 10$  K (left panels), and calculated RDF around copper and tungsten atoms (right panels).

with Cu–O distances about  $2.3 \text{ \AA}$ . This result is consistent with the predictions of *ab-initio* calculations [319].

The temperature dependence of the first coordination shell around tungsten



**Figure 9.11: Temperature-dependence of the local structure of microcrystalline  $\text{CuWO}_4$**

First coordination shells of radial distribution functions around copper atom for low temperature ( $T = 10$  K) and high-temperature ( $T = 250$  K) cases (left panels), and relative changes of the mean Cu–O distances and MSRD factors as functions of sample temperatures (right panels).

atom is weak and is already analyzed in [320]. Therefore here we focus on the distribution of closest oxygen atoms around copper atoms (Fig. 9.11). One can see, the distribution of closest four oxygen atoms, arranged at about  $1.85$  Å from copper atom, practically does not depend on temperature due to very strong Cu–O bond. All four oxygens in this group are also practically equivalent and cannot be distinguished by our analysis. The second peak of RDF around Cu atom consists of contributions from two oxygen atoms. At low temperatures they both are located at about  $2.3$  Å from Cu atom. With the increase of temperature, however, the one, initially slightly more distant atom, moves significantly further from Cu, while the other oxygen atom is pulled closer to the copper. The widths of distribution functions, characterized by the mean-square radial distribution (MSRD) factors, for both of these oxygens also increase with temperature more significantly than it is in case of the four oxygens from the closest group, meaning that the strength of Cu–O bond is much weaker in this case.

## 9.5 Local structure of nanosized tungstates

### 9.5.1 Evolutionary algorithm for the studies of nanostructured systems

In this section for the first time our RMC/EA-EXAFS approach is applied to reconstruct the structure of nanomaterials. Since the experimentally measured  $\text{CoWO}_4$  and  $\text{CuWO}_4$  EXAFS spectra are averaged over large number of nanoparticles, instead of a supercell with periodic boundary conditions for these simulations as a starting configuration an ensemble of 64 identical nanoparticles was used. These nanoparticles consist of four  $\text{WO}_6$  and  $\text{CoO}_6$  (or  $\text{CuO}_6$ ) octahedra and correspond to the one of four proposed nanoparticle models (A, B, C and D, see Fig. 9.12). Note that the models B, C and D involve edge-sharing  $\text{CoO}_6$  or  $\text{CuO}_6$  octahedra, but edge-sharing  $\text{WO}_6$  octahedra are present in the models A, C and D. Note that while atoms are moved randomly during the EA simulations, the maximal displacement of atoms from their starting positions was constrained to be smaller than  $0.5 \text{ \AA}$ . Our approach allows accounting for moderate static and dynamic disorder, while keeping the structural topology of our nanoparticle models unchanged. As a result of the simulation, we can estimate the consistency of the concrete topological model with the experimental EXAFS data. Note also that this approach is similar to the one, presented by Gilbert et al in [115], where RMC method was applied to X-ray scattering data to reconstruct the structure of ferrihydrite nanoparticles.

For each calculation 256 such ensembles have been constructed and optimized via EA procedure. Comparison of experimental and theoretical EXAFS spectra has been performed in the  $k$ -space range from  $3 \text{ \AA}^{-1}$  to  $12 \text{ \AA}^{-1}$  (for the Co and Cu K-edge data) or from  $3 \text{ \AA}^{-1}$  to  $15 \text{ \AA}^{-1}$  (for the W  $L_3$ -edge data) and in the  $R$ -space range from  $1.0 \text{ \AA}$  to  $4.0 \text{ \AA}$  using Morlet wavelet transform. EXAFS data from the W  $L_3$ -edge and the Co (or Cu) K-edge were fitted simultaneously. For the calculations of the Co and Cu K-edge EXAFS up to 150 scattering paths were taken into account, while for the calculations of the W  $L_3$ -edge EXAFS - up to 70 scattering paths with maximal half-path length of  $6.5 \text{ \AA}$ . Multiple-scattering contributions up to the sixth order were included in our analysis. As usually, the calculation of the cluster potential was performed only once at the beginning (before the main RMC/EA-EXAFS calculations) for the average atom configurations, corresponding to the bulk  $\text{CoWO}_4$  and  $\text{CuWO}_4$  crystallographic structures. Also the values of  $E_0$  (the energy reference of the photoelectron kinetic

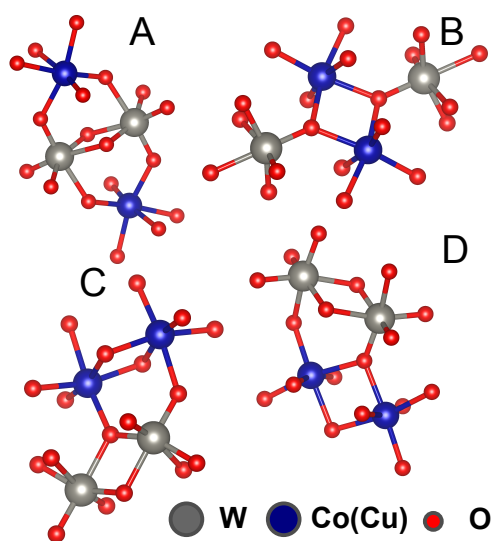


**Figure 9.12:** Suggested structure models of  $\text{CoWO}_4$  and  $\text{CuWO}_4$  nanocrystallites.

energy [2, 321]) and  $S_0^2$  (the amplitude scaling factor [2, 321],  $S_0^2=1$  in this work) parameters were fixed at their values determined for crystalline tungstates [311].

### 9.5.2 Results and discussion

The experimental Cu and Co K-edge and W  $L_3$ -edge EXAFS spectra from nanocrystalline  $\text{CoWO}_4$  and  $\text{CuWO}_4$  at room temperature and at 10 K temperature and their Fourier transforms along with the results of EA simulations starting from four different structural models are shown in Figs. 9.13-9.15. The final residuals, characterizing the difference between simulated and experimental EXAFS data, are summarized in Table 9.1.

First of all, let us note that the experimental W  $L_3$ -edge EXAFS spectra are quite similar for  $\text{CoWO}_4$  and  $\text{CuWO}_4$  at room temperature and for  $\text{CuWO}_4$  at 10 K. Also the influence of temperature, if  $\text{CuWO}_4$  EXAFS spectra for 10 K and for room temperature are compared, appears to be small, similarly as it was for the bulk material. This indicates that (i) the surrounding of W atom in wolframite structure is almost independent on the type of transition metal, and that (ii) thermal disorder (i.e., the disorder due to thermal motion of atoms) for these systems is weak with respect to static disorder.

As one can see, all four models (A, B, C and D) are able to reproduce the experimental EXAFS spectra from the first coordination shell (broad, asymmetric peaks in FTs between 1 and 2 Å) around metal atoms, thus confirming that the

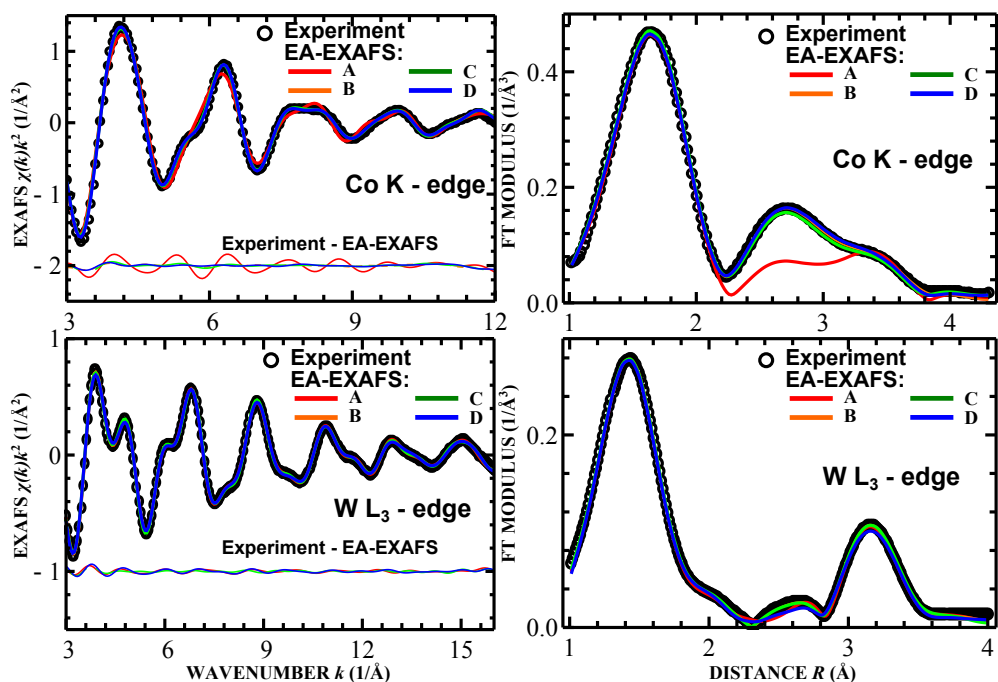


**Figure 9.13:** RMC/EA analysis of EXAFS spectra for nanocrystalline  $\text{CoWO}_4$

Left panels: the experimental Co K-edge and W  $L_3$ -edge EXAFS spectra for nanocrystalline  $\text{CoWO}_4$  at room temperature are shown by circles and the results of EA simulations starting from four different structural models (A, B, C, D as in Fig. 9.12) are represented by solid lines. Thin solid lines in the left panels show the difference between experimental EXAFS and the result of corresponding EA calculation. Right panels: the corresponding Fourier transforms are shown.

building elements of nanosized tungstates are distorted metal-oxygen octahedra. The main differences between the results, obtained for the four proposed models, are observed in the further peaks of FTs that are located between 2 and 4 Å and that correspond to the contribution from the further coordination shells and multiple-scattering effects - i.e., to the part of EXAFS that is difficult to access precisely by conventional methods.

In the FTs in Figs. 9.13 -9.15 it is clearly seen that the model A (i.e., the model without edge-sharing  $\text{CuO}_6$  ( $\text{CoO}_6$ ) octahedra) contradicts the available experimental Cu (Co) K-edge EXAFS data: the amplitude of FT peaks for simulated spectra is much lower than that for the experimental spectra. Thus this model can be excluded from further considerations. Note that the presence of two neighboring Co or Cu atoms is required for Langmuir-Hinshelwood-like mechanisms of water oxidation reaction [322], thus our result is consistent with the observed high catalytic activity of tungstates nanoparticles.

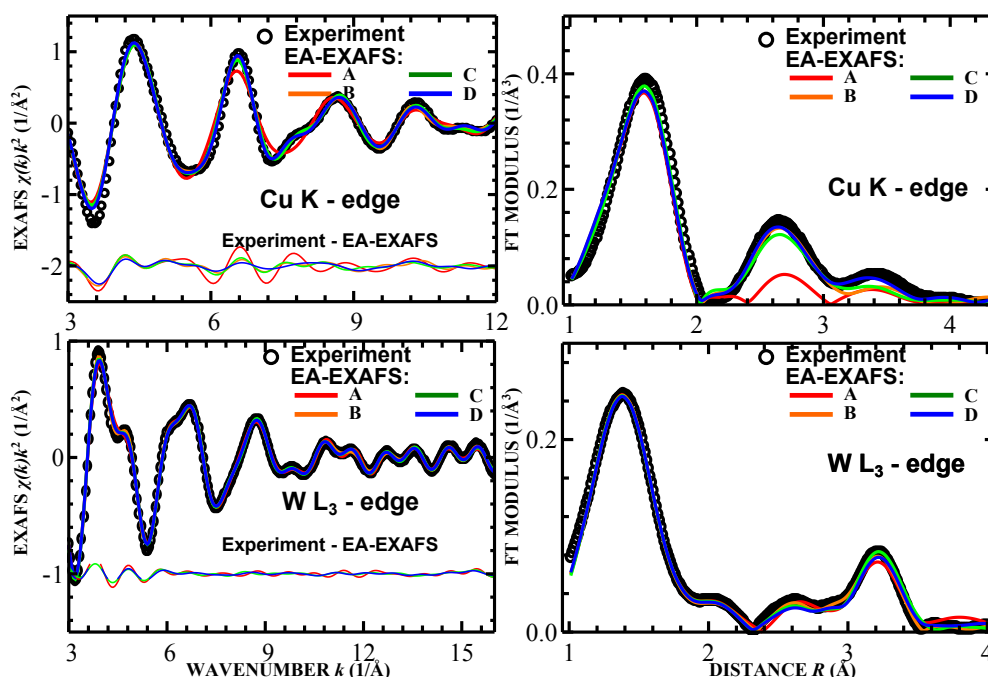


**Figure 9.14:** RMC/EA analysis of EXAFS spectra for nanocrystalline  $\text{CuWO}_4$  at room temperature

Left panels: the experimental Cu K-edge and W  $L_3$ -edge EXAFS spectra for nanocrystalline  $\text{CuWO}_4$  at room temperature are shown by circles and the results of EA simulations starting from four different structural models (A, B, C, D as in Fig. 9.12) are represented by solid lines. Thin solid lines in the left panels show the difference between experimental EXAFS and the result of corresponding EA calculation. Right panels: the corresponding Fourier transforms are shown.

Models B, C and D with edge-sharing  $\text{CoO}_6$  ( $\text{CuO}_6$ ) octahedra, in turn, give similar and quite remarkable results: the agreement between model EXAFS spectra and experimental Co and Cu K-edge, and W  $L_3$ -edge data is excellent even for the complex peaks at 2-4 Å.

Careful examination of the final total differences between calculated and experimental EXAFS at both Co(Cu) K and W  $L_3$  edges (Table 9.1) shows that the model B (i.e., the model without edge-sharing  $\text{WO}_6$  octahedra) describes slightly better the available data both for  $\text{CoWO}_4$  and  $\text{CuWO}_4$  cases: this model provides slightly better agreement for the W  $L_3$ -edge EXAFS. Thus in the remaining part of our discussion we will focus on the results, obtained for the model B.

Local structure of nanosized tungstates can be characterized by radial distribution functions (RDFs) around absorbing atoms that can be constructed in a straightforward way from the final sets of coordinates, obtained in RMC/EA simulations. We present these results in Fig. 9.16: here the distribution of atoms

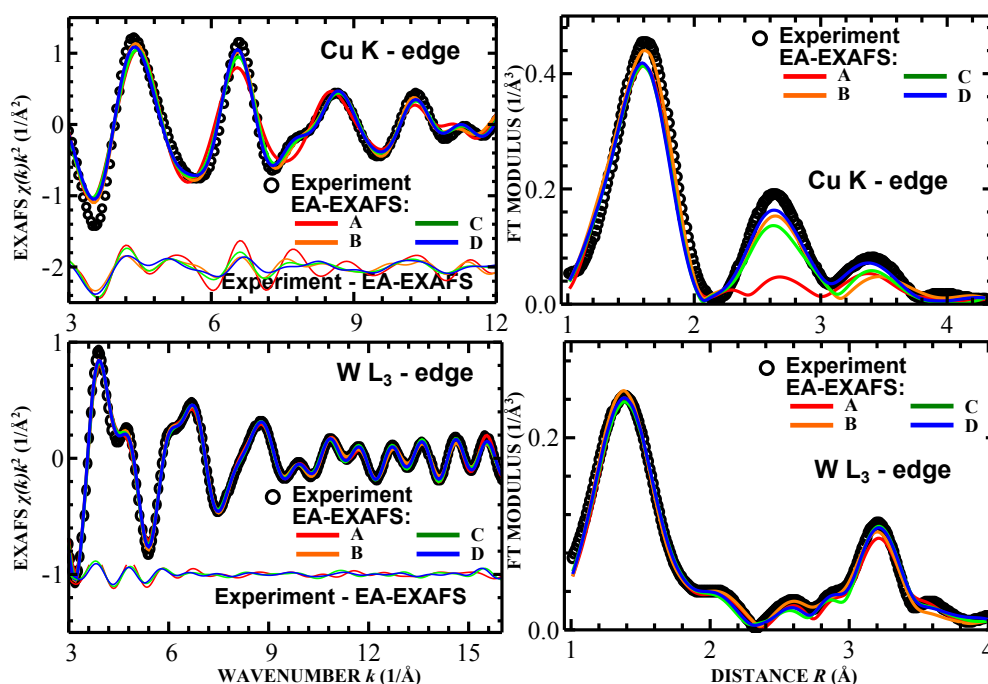


**Figure 9.15:** RMC/EA analysis of EXAFS spectra for nanocrystalline  $\text{CuWO}_4$  at 10 K

Left panels: the experimental Cu K-edge and W  $L_3$ -edge EXAFS spectra for nanocrystalline  $\text{CuWO}_4$  at 10 K are shown by circles and the results of EA simulations starting from four different structural models (A, B, C, D as in Fig. 9.12) are represented by solid lines. Thin solid lines in the left panels show the difference between experimental EXAFS and the result of corresponding EA calculation. Right panels: the corresponding Fourier transforms are shown.

with respect to Co(Cu) and W atoms is plotted. The first coordination shell of Cu in  $\text{CuWO}_4$  (peaks that corresponds to 1.8-2.8 Å distance from Cu atom), unlike the first coordination shell of Co in  $\text{CoWO}_4$ , is strongly split: it is the manifestation of the pronounced first-order Jahn-Teller effect [301, 302, 303, 304]. Note that the distribution of oxygen atoms in the first coordination shell around Cu or Co is close to that in bulk materials (dashed lines in Fig. 9.16). The changes of structure in the further coordination shells are more prominent: one can see that the length of the Co-Co bond that corresponds to the RDF peak at about 3.0 Å is reduced by about 0.2 Å with respect to that in microcrystalline  $\text{CoWO}_4$ . In the case of  $\text{CuWO}_4$  the distribution of the Cu-Cu distances is, in turn, much broader and appears to be even bimodal - for some of the  $\text{CuWO}_4$  nanocrystallites the single Cu-Cu bond is also shorter than Cu-Cu bonds in the bulk material, but there exist also some nanocrystallites with Cu-Cu distance being while in others it is about 0.3-0.4 Å longer than that in polycrystalline sample.



Relaxation of the first coordination shell around tungsten atom is analyzed in more details in Fig. 9.17: here we compare the radial distribution of oxygen atoms in the first coordination shell around W atoms for all three cases (CoWO<sub>4</sub> at room temperature, CuWO<sub>4</sub> at room temperature and CuWO<sub>4</sub> at 10 K temperature). In the first coordination shell of W for nanocrystalline CuWO<sub>4</sub>, similarly as for CoWO<sub>4</sub>, only two different W–O distances can be observed, in contrast to the case of bulk CuWO<sub>4</sub>, where three groups of W–O distances can be clearly distinguished. In both studied tungstates the nearest four oxygen atoms are pulled closer to the tungsten atoms, forming the first peak of RDF at around 1.8-1.9 Å, while the distant two oxygen atoms move slightly away, resulting in the second peak at around 2.3-2.4 Å. Thus the structure relaxation of nanosized tungstates results in the increase of WO<sub>6</sub> octahedra distortion (similar conclusions were drawn by us from the analysis of the EXAFS spectra from the first coordination shell around tungsten using regularization-like method [311].)

In the model B from the six oxygen atoms that surround tungsten atoms one ('bridging' oxygen) is also bonded to the Co or Cu atom, while five remaining oxygen atoms are bonded to the tungsten only. Our analysis has revealed that for all studied nanostructured samples the bridging W–O bond is involved in the group of closest four oxygen atoms (RDF peak at around 1.8-1.9 Å). Three remaining, non-bridging W–O bonds in this group can be considered as double tungsten-oxygen W=O bonds. These W=O bonds can also be associated with the broad peak in Raman spectra at about 955 cm<sup>-1</sup>: a well known correlation between the frequency of stretching vibration and the length of the W–O bond [323] suggests that the bond length corresponding to the observed Raman peak should be about 1.7 Å long.

The second group of non-bridging W–O bonds with the length about 2.3-2.4 Å arguably can be associated with hydrogenated W–OH bonds, as evidenced

**Table 9.1:** The final total residuals at both Co(Cu) K and W L<sub>3</sub> edges, characterizing the difference between simulated and experimental EXAFS data for nanocrystalline CoWO<sub>4</sub> and CuWO<sub>4</sub> and four different structural models.

Structure model	CoWO <sub>4</sub> (300 K)	CuWO <sub>4</sub> (300 K)	CuWO <sub>4</sub> (10 K)
A	0.106(1)	0.176(1)	0.229(1)
B	0.036(1)	0.092(3)	0.135(1)
C	0.044(2)	0.117(2)	0.159(5)
D	0.049(2)	0.104(4)	0.138(2)

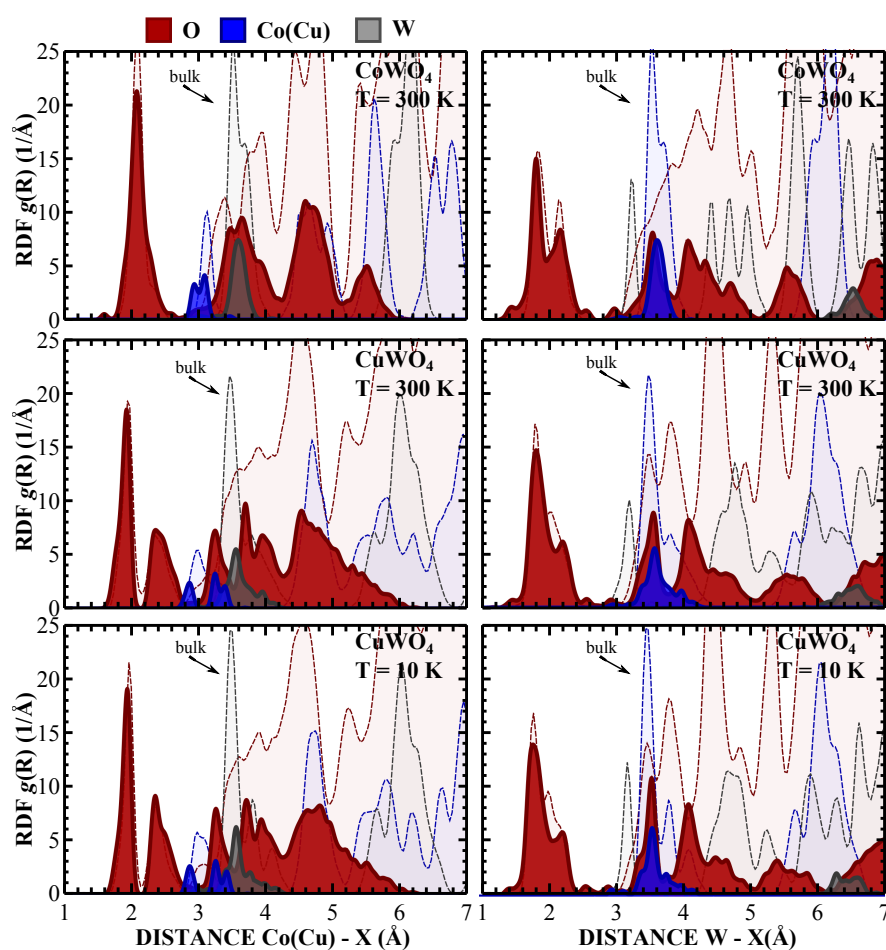


**Figure 9.16:** Radial distribution of atoms around W and Co/Cu in  $\text{CoWO}_4$  and  $\text{CuWO}_4$  nanoparticles (solid lines) and bulk material (dashed lines), obtained by the RMC/EA simulations for the model B (Fig. 9.12).

by FTIR spectra [311], or to bridging and randomly oriented bonds between touching nanoparticles.

## 9.6 Conclusions

Reverse Monte-Carlo method, coupled with evolutionary algorithm, allows us to efficiently analyze EXAFS data both from crystalline and nanocrystalline materials, taking into account multiple-scattering effects as well as static and thermal disorder. Such simulations allowed us to reconstruct the local environment around Cu, Co and W atoms in wolframite-type compounds  $\text{CuWO}_4$  and  $\text{CoWO}_4$ . We found that EXAFS data from a single absorption edge in this case does not contain enough information to precisely reconstruct the local structure

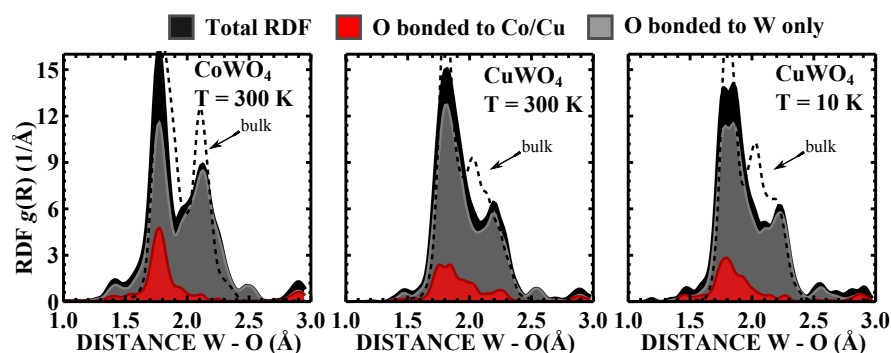


**Figure 9.17:** Radial distribution of atoms (1st coordination shell) around tungsten in  $\text{CoWO}_4$  and  $\text{CuWO}_4$  nanoparticles (solid lines) and bulk material (dashed lines) obtained by the RMC/EA simulations for the model B (Fig. 9.12).

around both metal atoms. However, the RMC/EA calculations using EXAFS data for the W  $L_3$ -edge and Cu (or Co) K-edges simultaneously allowed us to overcome this problem and to obtain a single structure model, consistent with all available experimental EXAFS data.

More detailed analysis of the evolution of local structure upon temperature increase was performed for microcrystalline  $\text{CuWO}_4$ . It was shown that in the first coordination shell around copper the distribution of the closest four oxygen atoms is practically temperature-independent due to strong Cu–O bond, while the distribution of the remaining two oxygens is strongly influenced by temperature.

For the first time evolutionary algorithm method was applied to obtain the structure model for nanostructured materials. The reconstruction of the structure of  $\text{CoWO}_4$  and  $\text{CuWO}_4$  nanoparticles revealed that they consist of  $\text{WO}_6$  and  $\text{CoO}_6$  ( $\text{CuO}_6$ ) octahedra, but the analysis of EXAFS data beyond the first coordination shell, which was made possible by our evolutionary algorithm scheme, has shown that  $\text{CoO}_6$  ( $\text{CuO}_6$ ) octahedra have common edges, while the  $\text{WO}_6$  octahedra probably do not. Further analysis of the obtained results allowed us to characterize in details the structure relaxation in nanosized tungstates.

The obtained results support the presence of two neighboring Co or Cu atoms in tungstate nanoparticles, which are required for the two-site Langmuir-Hinshelwood-like mechanisms of water oxidation reaction [322].

## 10. CONCLUSIONS

In this thesis we have presented a novel reverse Monte Carlo (RMC) - type approach for the advanced analysis of EXAFS data for crystalline and nanocrystalline materials. A number of original features in our approach allows us to outperform other existing methods in this field in the terms of computational efficiency and the complexity of information that can be obtained. Let us emphasize them here once again.

First of all, we considered that the complex structure of EXAFS spectra due to a contribution of the multiple-scattering effects and of distant coordination shells is not an obstacle, but rather a source of valuable structural information that can be treated using simulation-based approaches and possibilities, provided by modern *ab-initio* codes for EXAFS data modelling. While such advanced analysis is computationally expensive, it allows one to discover a new potentiality of the EXAFS spectroscopy as a method not only for local structure studies, but also for probing more distant coordination shells, for revealing the anisotropy and correlations of atomic thermal motion and static displacements, for investigations of bonding angles and more complex many-atom distribution functions. These possibilities can bring new light even to studies of relatively well-known materials, as was demonstrated in this thesis, for instance, on the example of the analysis of EXAFS data for wurtzite-type ZnO, where RMC-type approach allowed us to reveal essential differences between dynamics of Zn–O and Zn–Zn bonds aligned along the *c*-axis and in the *ab*-plane of ZnO hexagonal crystal lattice. When, in turn, applied to the studies of crystalline rhenium trioxide ReO<sub>3</sub>, the developed method allowed us for the first time to extract accurately structural information both from the nearest and distant coordination shells of rhenium and to study in details also the different overlapping single-scattering and multiple-scattering contributions to the total EXAFS.

Secondly, as it was shown, the optimization process that employs the power of evolutionary algorithm (EA), implemented by us for the first time for simulation-based EXAFS analysis, allows much more efficient exploration of the possible configuration space (in our case – configurations of atomic coordinates in 3D structure model). This approach allowed us to make feasible advanced analysis

of complex compounds with low symmetry even with only decent computational resources available. We would like to emphasize that this aspect is very important to make the approach, presented here, broadly available and applicable to many other material studies. Computational efficiency of the method is also an issue, when one considers that to extract the dynamical information from EXAFS measurements it is not enough to interpret a single spectrum. Instead one should analyze a whole series of experimental data, obtained, for instance, at different temperatures. This approach allowed us to estimate the bond strength between nearest atoms in crystalline germanium, rhenium trioxide, zinc oxide and copper and cobalt tungstates. When used for studies of zinc oxide, it also revealed the displacement of equilibrium position of oxygen atoms along  $c$ -axis of hexagonal ZnO lattice. Obviously, the same principle applies to the processing of EXAFS from any in-situ experiment, and within this thesis we presented the results of RMC/EA study of EXAFS data for the in-situ measurements of hydrogen intercalation/deintercalation process into  $\text{ReO}_3$  lattice. We were able to reveal and distinguish two different effects that are caused by insertion of  $\text{H}^+$  ions: the changes in the correlation of atomic motion due to the localization of additional electron and the distortion of rhenium-oxygen octahedra.

Thirdly, the wavelet analysis has been applied for the first time for quantitative EXAFS interpretation. The representation of EXAFS spectra in  $k$ - and  $R$ -spaces simultaneously using Morlet wavelet transform (WT) allowed us to obtain more information from the same experimental data and to have much better control over the difference between the experimental and calculated EXAFS data. Especially useful the WT turns to be for the analysis of EXAFS data from the materials, containing both light and heavy elements, such as transition-metal oxides (e.g.,  $\text{ReO}_3$  and  $\text{ZnO}$ ), tungstates (e.g.,  $\text{CuWO}_4$  and  $\text{CoWO}_4$ ), etc. Note that the usage of WT can be advantageous even for conventional EXAFS analysis (curve-fitting).

As it is with a solution to any inverse ill-posed problem, the information, obtained by RMC-type methods, should be taken cautiously and cross-checked with other available experimental and theoretical data. In our approach we have constrained the allowed atomic displacements from the known equilibrium positions to be smaller than some given value. It allowed us to stabilize the solution and to incorporate indirectly the results of diffraction experiments. This aspect, however, limits the presented approach to the analysis of crystalline materials.

Within this thesis it was also demonstrated that for the analysis of complex materials, such as cobalt and copper tungstates, the use of EXAFS data for both metals (W and Co/Cu) is required to obtain unambiguous solution. Luckily, the RMC/EA-type approach allows simultaneous analysis of several EXAFS spectra in a straightforward way. We have also validated the stability and precision of different structural parameters, obtainable by our RMC/EA approach, by applying it to the analysis of model EXAFS data, based on molecular dynamics (MD) simulations for crystalline germanium and rhenium trioxide: thus MD calculations can be used to check the results of RMC analysis. On the other hand, the RMC/EA-EXAFS approach allows us to identify the problems with the force fields, used for molecular dynamics calculations. Here such combined approach was applied to the studies of wurtzite-type ZnO, and we have found that the existing simple interaction models that are commonly used for MD simulations of crystalline and nanostructured ZnO in the literature are able to reproduce general behaviour of the lattice dynamics in bulk ZnO but fail in the accurate description of thermal motion, especially, the many-atom correlations. One can expect that in the future different combinations of our RMC/EA and other numerical simulations can provide even more insight on the local structure and dynamics of different materials. Especially intriguing is the possibility to use the results, provided by our RMC implementation, i.e., the 3D structural model, consistent with available experimental data, for *ab-initio* calculations of electronic structure, and, hence, chemical and optical properties of materials.

Finally, in this thesis it was shown that the developed RMC/EA approach allows us also to validate the consistency of different structure models with available experimental data: in particular, we have shown that the nanoparticles of  $\text{CoWO}_4$  and  $\text{CuWO}_4$  consist of  $\text{WO}_6$  and  $\text{CoO}_6$  ( $\text{CuO}_6$ ) octahedra. Moreover, our analysis of EXAFS data beyond the first coordination shell that was made possible by presented RMC/EA scheme, has shown that  $\text{CoO}_6$  ( $\text{CuO}_6$ ) octahedra have common edges, while the  $\text{WO}_6$  octahedra probably do not. This example introduces a very promising and broad field of future studies, where the approach, presented in this thesis, is applied to investigation of not only crystalline solids, but also of materials, where the equilibrium structure is not known a-priori: i.e., various nanostructured materials, complex mixtures, solid solutions and disordered solids.

## 11. MAIN THESES

The main results of this thesis are:

1. The developed reverse Monte Carlo/evolutionary algorithm method allows one to efficiently analyze EXAFS data for crystalline and nanocrystalline materials, taking into account static and thermal disorder and multiple-scattering effects.
2. The intercalation of hydrogen ions into  $\text{ReO}_3$  lattice leads to two different effects with different characteristic times: (i) the reduction of correlations in atomic motion that occurs relatively fast and (ii) the tilting of  $\text{ReO}_6$  octahedra that is much slower process. The significant reduction of the Re  $L_3$ -edge EXAFS amplitude from  $\text{H}_x\text{ReO}_3$  compound in comparison with that from pure  $\text{ReO}_3$  mostly is a result of changes of atomic correlations.
3. The analysis of the Zn K-edge EXAFS spectra suggests that the lattice dynamics of ZnO is essentially anisotropic: the interactions of atoms that lies in the same  $ab$ -plane are significantly different from the interactions of atoms that are located at similar distances but in different  $ab$ -planes. As a result, the equilibrium position of oxygen atoms along  $c$ -axis changes upon increasing temperature.
4. Simultaneous analysis of EXAFS spectra at the Co/Cu K-edge and W  $L_3$ -edge in  $\text{CoWO}_4$  and  $\text{CuWO}_4$  nanoparticles allows one to reconstruct their atomic structure. It is shown that the nanoparticles consist of a few distorted  $\text{WO}_6$  and  $\text{Co}(\text{Cu})\text{O}_6$  octahedra, where the latter ones are connected by edges.

# References

- [1] S. J. Billinge and I. Levin. The problem with determining atomic structure at the nanoscale. *Science* 316 (2007) 561. 1
- [2] J. J. Rehr and R. C. Albers. Theoretical approaches to X-ray absorption fine structure. *Rev. Mod. Phys.* 72 (2000) 621. 1, 7, 9, 15, 16, 17, 18, 19, 20, 21, 23, 26, 28, 30, 43, 67, 96, 137, 150
- [3] A. Filipponi. EXAFS for liquids. *J. Phys.: Condens. Matter* 13 (2001) R23. 1, 40
- [4] A. Kuzmin and R. Evarestov. Quantum mechanics–molecular dynamics approach to the interpretation of X-ray absorption spectra. *J. Phys.: Condens. Matter* 21 (2009) 055401. 2, 35, 123, 125, 138
- [5] S. J. Gurman and R. L. McGreevy. Reverse Monte Carlo simulation for the analysis of EXAFS data. *J. Phys.: Condens. Matter* 2 (1990) 9463. 2, 37, 49
- [6] J. Purans, N. D. Afify, G. Dalba, R. Grisenti, S. D. Panfilis, A. Kuzmin, V. I. Ozhogin, F. Rocca, A. Sanson, S. I. Tiutiunnikov and P. Fornasini. Isotopic Effect In Extended X-Ray-Absorption Fine Structure of Germanium. *Phys. Rev. Lett.* 100 (2008) 055901. 4, 30, 89
- [7] J. Gaidelene, A. Kuzmin, J. Purans and C. Guéry. Influence of hydrogen intercalation on the local structure around Re ions in perovskite-type ReO<sub>3</sub>. *Phys. Status Solidi C* 2 (2005) 149. 4, 113, 114, 119, 120
- [8] A. Kuzmin. Application of cluster computing in materials science. *Latvian J. Phys. Tech. Sci.* 2 (2006) 7. 4
- [9] M. Newville. Fundamentals of XAFS (2004). URL <http://xafs.org/Tutorials>. 7, 25
- [10] D. E. Sayers, E. A. Stern and F. W. Lytle. New Technique for Investigating Noncrystalline Structures: Fourier Analysis of the Extended X-Ray Absorption Fine Structure. *Phys. Rev. Lett.* 27 (1971) 1204. 8, 15
- [11] J. J. Rehr, J. J. Kas, M. P. Prange, A. P. Sorini, Y. Takimoto and F. Vila. Ab initio theory and calculations of X-ray spectra. *C. R. Physique* 10 (2009) 548. 9, 67, 68, 69



- [12] J. Bearden and A. Burr. Reevaluation of X-ray atomic energy levels. *Rev. Mod. Phys.* 39 (1967) 125. 10
- [13] J. Baruchel, J. Hodeau, M. Lehmann, J. Regnard and C. Schlenker. *Neutron and synchrotron radiation for condensed matter studies*. Springer (1994). ISBN 978-3-662-22223-2. 11, 12, 22
- [14] In comparison: The European XFEL and FLASH (2014). URL [http://www.xfel.eu/overview/in\\_comparison/](http://www.xfel.eu/overview/in_comparison/). 11
- [15] F. Lehner. "DESY in 2012: a year of light and dust" (2013). URL <http://cds.cern.ch/record/1416008>. 12
- [16] F. Hippert, E. Geissler, J. L. Hodeau, E. Lelièvre-Berna and J.-R. Regnard. *Neutron and X-ray Spectroscopy*. Springer (2005). ISBN 978-1-4020-3337-7. 13, 14, 68, 69
- [17] S. Calvin. *XAFS for Everyone*. CRC Press (2013). ISBN 978-1-4398-7863-7. 13, 15, 18, 21, 22, 23, 25, 26, 30, 60, 61
- [18] L. V. Azároff. Theory of extended fine structure of X-ray absorption edges. *Rev. Mod. Phys.* 35 (1963) 1012. 15
- [19] E. A. Stern. Theory of the extended X-ray-absorption fine structure. *Phys. Rev. B* 10 (1974) 3027. 15
- [20] F. Lytle, D. Sayers and E. Stern. Extended X-ray-absorption fine-structure technique. II. Experimental practice and selected results. *Phys. Rev. B* 11 (1975) 4825. 15
- [21] E. Stern, D. Sayers and F. Lytle. Extended X-ray-absorption fine-structure technique. III. Determination of physical parameters. *Phys. Rev. B* 11 (1975) 4836. 15
- [22] P. Lee, P. Citrin, P. t. Eisenberger and B. Kincaid. Extended X-ray absorption fine structure its strengths and limitations as a structural tool. *Rev. Mod. Phys.* 53 (1981) 769. 15
- [23] L. Campbell, L. Hedin, J. Rehr and W. Bardyszewski. Interference between extrinsic and intrinsic losses in X-ray absorption fine structure. *Phys. Rev. B* 65 (2002) 064107. 19, 20, 21
- [24] K. Klementiev. VIPER: Users Manual and Tutorial with comments on analysis methods in EXAFS (2009). URL <https://www.cells.es/Beamlines/CLAESS/>. 21
- [25] A. L. Ankudinov, B. Ravel, J. J. Rehr and S. D. Conradson. Real-space multiple-scattering calculation and interpretation of X-ray-absorption near-edge structure. *Phys. Rev. B* 58 (1998) 7565. 22, 24, 43, 66, 67, 68, 69, 70, 186, 188
- [26] C. Ashley and S. Doniach. Theory of extended X-ray absorption edge fine structure (EXAFS) in crystalline solids. *Phys. Rev. B* 11 (1975) 1279. 23

- [27] P. Lee and J. Pendry. Theory of the extended X-ray absorption fine structure. *Phys. Rev. B* 11 (1975) 2795. 23
- [28] N. Alberding, E. Crozier, R. Ingalls and B. Houser. Focussed multiple-scattering in compressed  $\text{ReO}_3$ . *Le Journal de Physique Colloques* 47 (1986) C8. 23, 92
- [29] R. Vedrinskii, L. Bugaev and I. Levin. Single and multiple electron scattering description in X-ray absorption spectrum: theory and the problem of solid structure investigation. *Phys. Status Solidi B* 150 (1988) 307. 23
- [30] A. Kuzmin, J. Purans, M. Benfatto and C. R. Natoli. X-ray-absorption study of rhenium  $L_3$  and  $L_1$  edges in  $\text{ReO}_3$ : Multiple-scattering approach. *Phys. Rev. B* 47 (1993) 2480. 23, 24, 92, 93, 104
- [31] A. Kuzmin and P. Parent. Focusing and superfocusing effects in X-ray absorption fine structure at the iron K edge in  $\text{FeF}_3$ . *J. Phys.: Condens. Matter* 6 (1994) 4395. 23
- [32] A. Kuzmin and J. Purans. X-ray absorption spectroscopy study of local structural changes in  $\alpha\text{-WO}_3$  under colouration. *J. Phys.: Condens. Matter* 5 (1993) 2333. 23, 24
- [33] J. Garcia, A. Bianconi, M. Benfatto and C. Natoli. Coordination geometry of transition metal ions in dilute solutions by XANES. *Le Journal de Physique Colloques* 47 (1986) C8. 24
- [34] A. Kuzmin, S. Obst and J. Purans. X-ray absorption spectroscopy and molecular dynamics studies of hydration in aqueous solutions. *J. Phys.: Condens. Matter* 9 (1997) 10065. 24
- [35] P. Fornasini. Study of lattice dynamics via extended X-ray absorption fine structure. *J. Phys.: Condens. Matter* 13 (2001) 7859. 26, 131
- [36] W. R. Busing and H. A. Levy. The effect of thermal motion on the estimation of bond lengths from diffraction measurements. *Acta Crystallogr.* 17 (1964) 142. 26, 131
- [37] E. Sevillano, H. Meuth and J. J. Rehr. Extended X-ray absorption fine structure Debye-Waller factors. I. Monatomic crystals. *Phys. Rev. B* 20 (1979) 4908. 28, 132
- [38] R. Kubo. Generalized cumulant expansion method. *Journal of the Physical Society of Japan* 17 (1962) 1100. 28, 30
- [39] M. Vaccari, R. Grisenti, P. Fornasini, F. Rocca and A. Sanson. Negative thermal expansion in  $\text{CuCl}$ : An extended X-ray absorption fine structure study. *Phys. Rev. B* 75 (2007) 184307. 28, 30
- [40] A. Kuzmin. EDA: EXAFS data analysis software package. *Physica B* 208-209 (1995) 175. ISSN 0921-4526. 29, 30

- [41] E. Schlicht. Estimating the smoothing parameter in the so-called Hodrick-Prescott filter. *Journal of the Japan Statistical Society* 35 (2005) 99. 30
- [42] M. Newville, B. Ravel, D. Haskel, J. Rehr, E. Stern and Y. Yacoby. Analysis of multiple-scattering XAFS data using theoretical standards. *Physica B* 208 (1995) 154. 30, 96
- [43] B. Ravel and M. Newville. ATHENA, ARTEMIS, HEPHAESTUS: data analysis for X-ray absorption spectroscopy using IFEFFIT. *J. Synchrotron Radiat.* 12 (2005) 537. 30
- [44] K. Provost, E. Beret, D. Muller, E. S. Marcos and A. Michalowicz. Impact of the number of fitted Debye-Waller factors on EXAFS fitting. *J. Phys.: Conf. Ser.* 430 (2013) 012015. 31, 33
- [45] R. L. McGreevy. Reverse Monte Carlo modelling. *J. Phys.: Condens. Matter* 13 (2001) R877. 34, 38, 46
- [46] B. Alder and T. Wainwright. Phase transition for a hard sphere system. *J. Chem. Phys.* 27 (1957) 1208. 34
- [47] G. Sutmann. Classical molecular dynamics. *Quantum Simulations of Complex Many-Body Systems: From Theory to Algorithms* 10 (2002) 211. 34
- [48] J.-M. Delaye. Modeling of multicomponent glasses: a review. *Current Opinion in Solid State and Materials Science* 5 (2001) 451. 34, 41
- [49] R. Friedman, K. Boye and K. Flatmark. Molecular modelling and simulations in cancer research. *Biochimica et Biophysica Acta (BBA)-Reviews on Cancer* 1836 (2013) 1. 34
- [50] Y. Okamoto. XAFS simulation of highly disordered materials. *Nucl. Instrum. Meth. A* 526 (2004) 572. 35
- [51] G. Ferlat, J.-C. Soetens, A. S. Miguel and P. A. Bopp. Combining extended X-ray absorption fine structure with numerical simulations for disordered systems. *J. Phys.: Condens. Matter* 17 (2005) S145. 35
- [52] D. Cabaret, M. Le Grand, A. Ramos, A.-M. Flank, S. Rossano, L. Galois, G. Calas and D. Ghaleb. Medium range structure of borosilicate glasses from Si K-edge XANES: a combined approach based on multiple-scattering and molecular dynamics calculations. *J. Non-Cryst. Solids* 289 (2001) 1. 35
- [53] P. Kidkhunthod and A. Barnes. A structural study of praseodymium gallate glasses by combined neutron diffraction, molecular dynamics and EXAFS techniques. *J. Phys.: Conf. Ser.* 190 (2009) 012076. 35
- [54] F. Jalilehvand, D. Spångberg, P. Lindqvist-Reis, K. Hermansson, I. Persson and M. Sandström. Hydration of the calcium ion. An EXAFS, large-angle X-ray scattering, and molecular dynamics simulation study. *J. Am. Chem. Society* 123 (2001) 431. 35

- [55] P. J. Merklings, A. Muñoz-Páez, J. M. Martínez, R. R. Pappalardo and E. S. Marcos. Molecular-dynamics-based investigation of scattering path contributions to the EXAFS spectrum: The  $\text{Cr}^{3+}$  aqueous solution case. *Phys. Rev. B* 64 (2001) 012201. 35
- [56] H. Matsuura, S. Watanabe, H. Akatsuka, Y. Okamoto and A. K. Adya. XAFS analyses of molten metal fluorides. *J. Fluorine Chem.* 130 (2009) 53. 35
- [57] A. Kuzmin, V. Efimov, E. Efimova, V. Sikolenko, S. Pascarelli and I. Troyanchuk. Interpretation of the Co K-edge EXAFS in  $\text{LaCoO}_3$  using molecular dynamics simulations. *Solid State Ionics* 188 (2011) 21. 35, 138
- [58] J. Timoshenko, A. Kuzmin and J. Purans. Molecular dynamics simulations of EXAFS in germanium. *Centr. Eur. J. Phys.* 9 (2011) 710. 35
- [59] A. Kalinko, R. A. Evarestov, A. Kuzmin and J. Purans. Interpretation of EXAFS in  $\text{ReO}_3$  using molecular dynamics simulations. *J. Phys.: Conf. Ser.* 190 (2009) 012080. 35, 93, 94, 99, 105
- [60] A. Kalinko and A. Kuzmin. Interpretation of EXAFS in scheelite-type  $\text{AWO}_4$  (A= Ca, Sr, Ba) compounds using molecular dynamics simulations. *J. Phys.: Conf. Ser.* 430 (2013) 012075. 35, 137
- [61] S. W. Price, N. Zonias, C.-K. Skylaris, T. I. Hyde, B. Ravel and A. E. Russell. Fitting EXAFS data using molecular dynamics outputs and a histogram approach. *Phys. Rev. B* 85 (2012) 075439. 35
- [62] A. Anspoks, A. Kuzmin, A. Kalinko and J. Timoshenko. Probing NiO nanocrystals by EXAFS spectroscopy. *Solid State Commun.* 150 (2010) 2270 . 35
- [63] A. Anspoks and A. Kuzmin. Interpretation of the Ni K-edge EXAFS in nanocrystalline nickel oxide using molecular dynamics simulations. *J. Non-Cryst. Solids* 357 (2011) 2604. 35, 138
- [64] A. Anspoks, A. Kalinko, R. Kalendarev and A. Kuzmin. Atomic structure relaxation in nanocrystalline NiO studied by EXAFS spectroscopy: Role of nickel vacancies. *Phys. Rev. B* 86 (2012) 174114. 35
- [65] A. Anspoks, A. Kalinko, R. Kalendarev and A. Kuzmin. Probing vacancies in NiO nanoparticles by EXAFS and molecular dynamics simulations. *J. Phys.: Conf. Ser.* 430 (2013) 012027. 35
- [66] D. F. Yancey, S. T. Chill, L. Zhang, A. I. Frenkel, G. Henkelman and R. M. Crooks. A theoretical and experimental examination of systematic ligand-induced disorder in Au dendrimer-encapsulated nanoparticles. *Chem. Sci.* 4 (2013) 2912. 35
- [67] A. Hall. On an experimental determination of number Pi. *Messenger of Mathematics* 2 (1873) 113. Available online at [www.cs.xu.edu/math/Sources/Buffon/](http://www.cs.xu.edu/math/Sources/Buffon/). 36

- [68] L. Badger. Lazzarini's lucky approximation of  $\pi$ . *Math. Mag.* 67 (1994) 83. 36
- [69] N. Metropolis. The beginning of the Monte Carlo method. *Los Alamos Science* 15 (1987) 125. 36
- [70] N. Metropolis, A. W. Rosenbluth, M. N. Rosenbluth, A. H. Teller and E. Teller. Equation of State Calculations by Fast Computing Machines. *J Chem. Phys.* 21 (1953) 1087. 36, 48
- [71] R. Rohs, I. Bloch, H. Sklenar and Z. Shakked. Molecular flexibility in ab initio drug docking to DNA: binding-site and binding-mode transitions in all-atom Monte Carlo simulations. *Nucleic Acids Res.* 33 (2005) 7048. 36
- [72] P. Romiszowski and A. Sikorski. The structure of polymer chains in confinement. A Monte Carlo study. *J. Mol. Model.* 15 (2009) 681. 36
- [73] W. L. McMillan. Ground State of Liquid He<sup>4</sup>. *Phys. Rev.* 138 (1965) A442. 36
- [74] W. Young and E. Elcock. Monte Carlo studies of vacancy migration in binary ordered alloys: I. *Proceedings of the Physical Society* 89 (1966) 735. 36
- [75] R. McGreevy and L. Pusztai. Reverse Monte Carlo simulation: a new technique for the determination of disordered structures. *Mol. Simul.* 1 (1988) 359. 37, 46
- [76] D. Keen and R. McGreevy. Structural modelling of glasses using reverse Monte Carlo simulation. *Nature* 344 (1990) 423. 37
- [77] R. L. McGreevy and L. Pusztai. The structure of molten salts. *Proc. Roy. Soc. London A* 430 (1990) 241. 37
- [78] D. Keen, W. Hayes and R. McGreevy. Structural disorder in AgBr on the approach to melting. *J. Phys.: Condens. Matter* 2 (1990) 2773. 37
- [79] B. L. Pusztai and R. McGreevy. The structure of liquid CCl<sub>4</sub>. *Mol. Phys.* 90 (1997) 533. 38
- [80] L. Pusztai and R. McGreevy. The structure of molten CuBr. *J. Phys.: Condens. Matter* 10 (1998) 525. 38
- [81] L. Pusztai. Structural modelling using the reverse Monte Carlo technique: Application to amorphous semiconductors. *J. Non-Cryst. Solids* 227230 (1998) 88. 38
- [82] M. G. Tucker, A. L. Goodwin, M. T. Dove, D. A. Keen, S. A. Wells and J. S. O. Evans. Negative Thermal Expansion in ZrW<sub>2</sub>O<sub>8</sub>: Mechanisms, Rigid Unit Modes, and Neutron Total Scattering. *Phys. Rev. Lett.* 95 (2005) 255501. 38
- [83] M. G. Tucker, D. A. Keen, J. S. Evans and M. T. Dove. Local structure in ZrW<sub>2</sub>O<sub>8</sub> from neutron total scattering. *J. Phys.: Condens. Matter* 19 (2007) 335215. 38

- [84] F. Bridges, T. Keiber, P. Juhas, S. Billinge, L. Sutton, J. Wilde and G. R. Kowach. Local Vibrations and Negative Thermal Expansion in  $ZrW_2O_8$ . *Phys. Rev. Lett.* 112 (2014) 045505. 38
- [85] C. A. Young, E. Dixon, M. G. Tucker, D. A. Keen, M. A. Hayward and A. L. Goodwin. Reverse Monte Carlo study of Cu-O bond distortions in  $YBa_2Cu_3O_{6.93}$ . *Z. Kristallogr.* 227 (2012) 280. 38
- [86] D. S. Keeble, E. R. Barney, D. A. Keen, M. G. Tucker, J. Kreisel and P. A. Thomas. Piezoelectric Materials: Bifurcated Polarization Rotation in Bismuth-Based Piezoelectrics. *Adv. Funct. Mater.* 23 (2013) 184. 38
- [87] R. L. McGreevy and P. Zetterström. Reverse Monte Carlo modelling of network glasses: useful or useless? *J. Non-Cryst. Solids* 293-295 (2001) 297 . 38, 47
- [88] D. A. Keen, M. G. Tucker and M. T. Dove. Reverse Monte Carlo modelling of crystalline disorder. *J. Phys.: Condens. Matter* 17 (2005) S15. 38
- [89] S. Adams and J. Swenson. Bond valence analysis of reverse Monte Carlo produced structural models; a way to understand ion conduction in glasses. *J. Phys.: Condens. Matter* 17 (2005) S87. 38
- [90] T. Kawahara, N. Tabuchi, T. Arai, Y. Sato, J. Morimoto and H. Matsumura. Coordination number constraint models for hydrogenated amorphous Si deposited by catalytic chemical vapour deposition. *J. Phys.: Condens. Matter* 17 (2005) S103. 38
- [91] L. Temleitner and L. Pusztai. Orientational correlations in liquid carbon monoxide and nitric oxide. *J. Phys.: Condens. Matter* 17 (2005) S47. 38
- [92] O. Roik, A. Anikeenko and N. Medvedev. Investigation of the particular features of the structure factor of liquid Al-based alloys. *J. Mol. Liq.* 161 (2011) 78. 38
- [93] O. Roik, V. Kazimirov and S. Galushko. The structure of the liquid  $Al_{62}Cu_{25.5}TM_{12.5}$  (TM= Mn, Ni, Fe) alloys. *Phys. Chem. Liq.* 51 (2013) 21. 38
- [94] O. Roik, V. Kazimirov, V. Sokolskii and S. Galushko. Formation of the short-range order in Al-based liquid alloys. *J. Non-Cryst. Solids* 364 (2013) 34. 38
- [95] S. Tahara, H. Ueno, K. Ohara, Y. Kawakita, S. Kohara, S. Ohno and S. Takeda. Medium-range correlation of Ag ions in superionic melts of  $Ag_2Se$  and  $AgI$  by reverse Monte Carlo structural modelling connectivity and void distribution. *J. Phys.: Condens. Matter* 23 (2011) 235102. 38
- [96] S. Chandrasekaran. Structure Factor and Pair Correlation Function of Liquid Para- $H_2$  and Liquid Hg Using Reverse Monte Carlo Simulation. *J. Comput. Theor. Nanos.* 9 (2012) 986. 38
- [97] O. Yagafarov, Y. Katayama, V. Brazhkin, A. Lyapin and H. Saitoh. Energy dispersive X-ray diffraction and reverse Monte Carlo structural study of liquid gallium under pressure. *Phys. Rev. B* 86 (2012) 174103. 38

- [98] M. Inui, Y. Kajihara, K. Kimura, T. Fukumaru, K. Matsuda and M. Yao. Chemical order in liquid  $\text{As}_2\text{Se}_3$  at high temperatures obtained by X-ray scattering and reverse Monte Carlo modeling. *J. Non-Cryst. Solids* 366 (2013) 22. 38
- [99] M. J. Cliffe, M. T. Dove, D. Drabold and A. L. Goodwin. Structure determination of disordered materials from diffraction data. *Phys. Rev. Lett.* 104 (2010) 125501. 38
- [100] M. J. Cliffe and A. L. Goodwin. Nanostructure determination from the pair distribution function: a parametric study of the INVERT approach. *J. Phys.: Condens. Matter* 25 (2013) 454218. 38
- [101] S. Hosokawa, I. Oh, M. Sakurai, W.-C. Pilgrim, N. Boudet, J.-F. Bérar and S. Kohara. Anomalous X-ray scattering study of  $\text{Ge}_x\text{Se}_{1-x}$  glassy alloys across the stiffness transition composition. *Phys. Rev. B* 84 (2011) 014201. 39
- [102] S. Hosokawa, W.-C. Pilgrim, J.-F. Bérar and S. Kohara. Recent developments of anomalous X-ray scattering for non-crystalline materials with help of reverse Monte Carlo modeling: The example of  $\text{GeSe}_2$  glass. *Phys. Status Solidi A* 208 (2011) 2544. 39
- [103] S. Hosokawa, W.-C. Pilgrim, A. Hohle, D. Szubrin, N. Boudet, J.-F. Bérar and K. Maruyama. Key experimental information on intermediate-range atomic structures in amorphous  $\text{Ge}_2\text{Sb}_2\text{Te}_5$  phase change material. *J. Appl. Phys.* 111 (2012) 083517. 39
- [104] S. Hosokawa, J. Bérar, N. Boudet, S. Kohara, J. Stellhorn, W. Pilgrim, A. Zeidler, H. Kato, Y. Kawakita and T. Otomo. A combination of anomalous X-ray scattering and neutron diffraction for structural characterizations of  $\text{Zr}_{63}\text{Ni}_{25}\text{Al}_{12}$  metallic glass. *J. Phys.: Conf. Ser.* 502 (2014) 012023. 39
- [105] J. de Lima, C. Poffo, S. Souza, K. Machado, D. Trichês, T. Grandi and R. de Biasi. Modeling the amorphous structure of mechanically alloyed  $\text{Ti}_{50}\text{Ni}_{25}\text{Cu}_{25}$  using anomalous wide-angle X-ray scattering and reverse Monte Carlo simulation. *Physica B* 424 (2013) 60. 39
- [106] A. Møllergård, R. L. McGreevy and S. G. Eriksson. Structural and magnetic disorder in  $\text{La}_{1-x}\text{Sr}_x\text{MnO}_3$ . *J. Phys.: Condens. Matter* 12 (2000) 4975. 39
- [107] M. G. Tucker, M. T. Dove and D. A. Keen. Application of the reverse Monte Carlo method to crystalline materials. *J. Appl. Cryst.* 34 (2001) 630. 39
- [108] M. Winterer, R. Delaplane and R. McGreevy. X-ray diffraction, neutron scattering and EXAFS spectroscopy of monoclinic zirconia: analysis by Rietveld refinement and reverse Monte Carlo simulations. *J. Appl. Cryst.* 35 (2002) 434. 39
- [109] M. G. Tucker, D. A. Keen, M. T. Dove, A. L. Goodwin and Q. Hui. RMCProfile: reverse Monte Carlo for polycrystalline materials. *J. Phys.: Condens. Matter* 19 (2007) 335218. 39

- [110] I.-K. Jeong and J. Ahn. The atomic structure of lead-free Ba (Zr<sub>0.2</sub>Ti<sub>0.8</sub>)O<sub>3</sub>-(Ba<sub>0.7</sub>Ca<sub>0.3</sub>)TiO<sub>3</sub> by using neutron total scattering analysis. *Appl. Phys. Lett.* 101 (2012) 242901. 39
- [111] N. Bedford, C. Dablemont, G. Viau, P. Chupas and V. Petkov. 3-D Structure of nanosized catalysts by high-energy X-ray diffraction and Reverse Monte Carlo simulations: Study of Ru. *J. Phys. Chem. C* 111 (2007) 18214. 39
- [112] P. Zetterström, S. Urbonaite, F. Lindberg, R. G. Delaplane, J. Leis and G. Svensson. Reverse Monte Carlo studies of nanoporous carbon from TiC. *J. Phys.: Condens. Matter* 17 (2005) 3509. 39
- [113] V. Petkov, N. Bedford, M. R. Knecht, M. G. Weir, R. M. Crooks, W. Tang, G. Henkelman and A. Frenkel. Periodicity and atomic ordering in nanosized particles of crystals. *J. Phys. Chem. C* 112 (2008) 8907. 39
- [114] N. M. Bedford. Analysis of 3D structures of platinum nanoparticles by high energy X-ray diffraction and reverse Monte Carlo simulations. *Solid State Commun.* 150 (2010) 1505 . 39
- [115] B. Gilbert, J. J. Erbs, R. L. Penn, V. Petkov, D. Spagnoli and G. A. Waychunas. A disordered nanoparticle model for 6-line ferrihydrite. *Am. Mineral.* 98 (2013) 1465. 39, 149
- [116] J. D. Wicks and R. L. McGreevy. RMC: modelling neutron diffraction, X-ray diffraction and EXAFS data simultaneously for amorphous materials. *J. Non-Cryst. Solids* 192-193 (1995) 23. 39
- [117] M. Winterer. Reverse Monte Carlo analysis of extended X-ray absorption fine structure spectra of monoclinic and amorphous zirconia. *J. Appl. Phys.* 88 (2000) 5635. 39
- [118] K. Machado, J. de Lima, C. de Campos, T. Grandi and D. Trichês. EXAFS, X-ray diffraction, and reverse Monte Carlo simulations of an amorphous Ni<sub>60</sub>Ti<sub>40</sub> alloy produced by mechanical alloying. *Phys. Rev. B* 66 (2002) 094205. 39, 40
- [119] A. D. Cicco, A. Trapananti, S. Faggioni and A. Filipponi. Is There Icosahedral Ordering in Liquid and Undercooled Metals? *Phys. Rev. Lett.* 91 (2003) 135505. 39, 40, 123
- [120] A. D. Cicco and A. Trapananti. Reverse Monte Carlo refinement of molecular and Condens. systems by X-ray absorption spectroscopy. *J. Phys.: Condens. Matter* 17 (2005) S135. 39, 40, 123
- [121] M.-V. Coulet, D. Testemale, J.-L. Hazemann, J.-P. Gaspard and C. Bichara. Reverse Monte Carlo analysis of the local order in liquid Ge<sub>0.15</sub>Te<sub>0.85</sub> alloys combining neutron scattering and X-ray absorption spectroscopy. *Phys. Rev. B* 72 (2005) 174209. 39, 40
- [122] G. Evrard and L. Pusztai. Reverse Monte Carlo modelling of the structure of disordered materials with RMC++ : a new implementation of the algorithm in C++. *J. Phys.: Condens. Matter* 17 (2005) S1. 39



- [123] Q. Wang, C. Li, X. Niu, R. Shen, K. Lu, S. Wei, Z. Wu, T. Liu, Y. Xie and T. Hu. Structure of liquid krypton under atmospheric pressure: An EXAFS and reverse Monte Carlo study. *Phys. Rev. B* 72 (2005) 092202. 39
- [124] O. Gereben, P. Jóvári, L. Temleitner and L. Pusztai. A new version of the RMC++ Reverse Monte Carlo programme, aimed at investigating the structure of covalent glasses. *J. Optoelectron. Adv. M.* 9 (2007) 3021. 39, 41
- [125] W. K. Luo and E. Ma. EXAFS measurements and reverse Monte Carlo modeling of atomic structure in amorphous Ni<sub>80</sub>P<sub>20</sub> alloys. *J. Non-Cryst. Solids* 354 (2008) 945 . 39
- [126] P. Jóvári, K. Saksl, N. Pryds, B. Lebech, N. P. Bailey, A. Mellergård, R. G. Delaplane and H. Franz. Atomic structure of glassy Mg<sub>60</sub>Cu<sub>30</sub>Y<sub>10</sub> investigated with EXAFS, X-ray and neutron diffraction, and reverse Monte Carlo simulations. *Phys. Rev. B* 76 (2007) 054208. 39
- [127] P. Jóvári, I. Kaban, J. Steiner, B. Beuneu, A. Schöps and M. Webb. Local order in amorphous Ge<sub>2</sub>Sb<sub>2</sub>Te<sub>5</sub> and GeSb<sub>2</sub>Te<sub>4</sub>. *Phys. Rev. B* 77 (2008) 035202. 39
- [128] I. Kaban, P. Jóvári, M. Stoica, J. Eckert, W. Hoyer and B. Beuneu. Topological and chemical ordering in Co<sub>43</sub>Fe<sub>20</sub>Ta<sub>5.5</sub>B<sub>31.5</sub> metallic glass. *Phys. Rev. B* 79 (2009) 212201. 39
- [129] M. Leetmaa, K. T. Wikfeldt and L. G. M. Pettersson. SpecSwap-RMC: a novel reverse Monte Carlo approach using a discrete set of local configurations and pre-computed properties. *J. Phys.: Condens. Matter* 22 (2010) 135001. 39, 41
- [130] A. Di Cicco, F. Iesari, S. De Panfilis, M. Celino, S. Giusepponi and A. Filipponi. Local fivefold symmetry in liquid and undercooled Ni probed by X-ray absorption spectroscopy and computer simulations. *Phys. Rev. B* 89 (2014) 060102. 39
- [131] L. Rátkai, C. Conseil, V. Nazabal, B. Bureau, I. Kaban, J. Bednarcik, B. Beuneu and P. Jóvári. Microscopic origin of demixing in Ge<sub>20</sub>Se<sub>x</sub>Te<sub>80-x</sub> alloys. *J. Alloy Compd.* 509 (2011) 5190. 39
- [132] I. Kaban, P. Jóvári, T. Wágner, M. Bartoš, M. Frumar, B. Beuneu, W. Hoyer, N. Mattern and J. Eckert. Structural study of AsS<sub>2</sub>-Ag glasses over a wide concentration range. *J. Non-Cryst. Solids* 357 (2011) 3430. 39
- [133] L. Rátkai, A. Gonçalves, G. Delaizir, C. Godart, I. Kaban, B. Beuneu and P. Jóvári. The Cu and Te coordination environments in Cu-doped Ge-Te glasses. *Solid State Commun.* 151 (2011) 1524. 39
- [134] A. Chrissanthopoulos, P. Jóvári, I. Kaban, S. Gruner, T. Kavetsky, J. Borc, W. Wang, J. Ren, G. Chen and S. Yannopoulos. Structure of AgI-doped Ge-In-S glasses: Experiment, reverse Monte Carlo modelling, and density functional calculations. *J. Solid State Chem.* 192 (2012) 7. 39

- [135] I. Kaban, P. J3v3ari, R. Wang, B. Luther-Davies, N. Mattern and J. Eckert. Structural investigations of  $\text{Ge}_5\text{As}_x\text{Se}_{95-x}$  and  $\text{Ge}_{15}\text{As}_x\text{Se}_{85-x}$  glasses using X-ray diffraction and extended X-ray fine structure spectroscopy. *J. Phys.: Condens. Matter* 24 (2012) 385802. 39
- [136] I. Kaban, P. J3v3ari, A. Waske, M. Stoica, J. Bednar3ik, B. Beuneu, N. Mattern and J. Eckert. Atomic structure and magnetic properties of Fe-Nb-B metallic glasses. *J. Alloy Compd.* 586 (2014) S189. 39
- [137] P. J3v3ari, Y. Sutou, I. Kaban, Y. Saito and J. Koike. Fourfold coordinated Te atoms in amorphous phase of  $\text{GeCu}_2\text{Te}_3$  phase change material. *Scripta Mater.* 68 (2013) 122. 39
- [138] I. Kaban, P. J3v3ari, V. Kokotin, O. Shuleshova, B. Beuneu, K. Saksl, N. Mattern, J. Eckert and A. Greer. Local atomic arrangements and their topology in Ni-Zr and Cu-Zr glassy and crystalline alloys. *Acta Mater.* 61 (2013) 2509. 39
- [139] P. J3v3ari, A. Piarristeguy, R. Escalier, I. Kaban, J. Bednar3ik and A. Pradel. Short range order and stability of amorphous  $\text{Ge}_x\text{Te}_{100-x}$  alloys ( $12 < x < 44.6$ ). *J. Phys.: Condens. Matter* 25 (2013) 195401. 39
- [140] P. J3v3ari, P. Lucas, Z. Yang, B. Bureau, I. Kaban, B. Beuneu and J. Bednarik. Short-Range order in GeAsTe glasses. *J. Am. Ceram. Soc.* 97 (2014) 1625. 39
- [141] L. Kumara, K. Ohara, Y. Kawakita, P. J3v3ari, M. Hidaka, N. E. Sung, B. Beuneu and S. Takeda. Local structure of superionic glass  $\text{Ag}_x(\text{GeSe}_3)_{1-x}$ ,  $x = 0.565$ . *EPJ Web of Conferences* 15 (2011) 02007. 39
- [142] E. Oliveira, E. Deflon, K. Machado, T. G. Silva and A. Mangrich. Structural, vibrational and optical studies on an amorphous  $\text{Se}_{90}\text{P}_{10}$  alloy produced by mechanical alloying. *J. Phys.: Condens. Matter* 24 (2012) 115802. 39
- [143] G. Antipas, E. Mangiorou and E. Hristoforou. Solute-solvent interactions and atomic cohesion in  $\text{GeSe}_4$  and  $\text{GeSe}_4\text{In}_5$  metallic glasses. *Mater. Res. Express* 1 (2014) 015202. 39
- [144] L. Yang, G. Guo, L. Chen, C. Huang, T. Ge, D. Chen, P. Liaw, K. Saksl, Y. Ren, Q. Zeng et al. Atomic-scale mechanisms of the glass-forming ability in metallic glasses. *Phys. Rev. Lett.* 109 (2012) 105502. 39
- [145] L. Yang, T. Ge, G. Guo, C. Huang, X. Meng, S. Wei, D. Chen and L. Chen. Atomic and cluster level dense packing contributes to the high glass-forming ability in metallic glasses. *Intermetallics* 34 (2013) 106. 39
- [146] L. Yang, G.-Q. Guo, L.-Y. Chen, B. LaQua and J.-Z. Jiang. Tuning local structures in metallic glasses by cooling rate. *Intermetallics* 44 (2014) 94. 39
- [147] S. A. Tupy, A. M. Karim, C. Bagia, W. Deng, Y. Huang, D. G. Vlachos and J. G. Chen. Correlating ethylene glycol reforming activity with *in situ* EXAFS detection of Ni segregation in supported NiPt bimetallic catalysts. *ACS Catalysis* 2 (2012) 2290. 39

- [148] H. Kurt, K. Rode, P. Stamenov, M. Venkatesan, Y.-C. Lau, E. Fonda and J. Coey. Cubic  $\text{Mn}_2\text{Ga}$  thin films: crossing the spin gap with ruthenium. *Phys. Rev. Lett.* 112 (2014) 027201. 39
- [149] V. Krayzman, I. Levin and M. G. Tucker. Simultaneous Reverse Monte Carlo refinements of local structures in perovskite solid solutions using EXAFS and the total scattering pair-distribution function. *J. Appl. Cryst.* 41 (2008) 705. 40, 41
- [150] V. Krayzman, I. Levin, J. C. Woicik, T. Proffen, T. A. Vanderah and M. G. Tucker. A combined fit of total scattering and extended X-ray absorption fine structure data for local-structure determination in crystalline materials. *J. Appl. Cryst.* 42 (2009) 867. 40
- [151] V. Krayzman and I. Levin. Reverse Monte Carlo refinements of local displacive order in perovskites:  $\text{AgNbO}_3$  case study. *J. Phys.: Condens. Matter* 22 (2010) 404201. 40
- [152] K. Németh, K. W. Chapman, M. Balasubramanian, B. Shyam, P. J. Chupas, S. M. Heald, M. Newville, R. J. Klingler, R. E. Winans, J. D. Almer et al. Efficient simultaneous reverse Monte Carlo modeling of pair-distribution functions and extended X-ray-absorption fine structure spectra of crystalline disordered materials. *J. Chem. Phys.* 136 (2012) 074105. 40
- [153] I. Levin, V. Krayzman and J. C. Woicik. Local-structure origins of the sustained Curie temperature in (Ba, Ca)  $\text{TiO}_3$  ferroelectrics. *Appl. Phys. Lett.* 102 (2013) 162906. 40, 41
- [154] M. G. Tucker, D. A. Keen, M. T. Dove, A. L. Goodwin and Q. Hui. RMCProfile: reverse Monte Carlo for polycrystalline materials. *J. Phys.: Condens. Matter* 19 (2007) 335218. 41
- [155] A. P. Lyubartsev and A. Laaksonen. Calculation of effective interaction potentials from radial distribution functions: A reverse Monte Carlo approach. *Phys. Rev. E* 52 (1995) 3730. 41
- [156] G. Tóth and A. Baranyai. On the theoretical aspects of inverse methods: reverse Monte Carlo simulation or potential determination? *J. Phys.: Condens. Matter* 17 (2005) S159. 41
- [157] G. Opletal, T. Petersen, B. O'Malley, I. Snook, D. G. McCulloch, N. A. Marks and I. Yarovsky. Hybrid approach for generating realistic amorphous carbon structure using metropolis and reverse Monte Carlo. *Mol. Simulat.* 28 (2002) 927. 41
- [158] O. Bouty, J. Delaye and S. Peugnet. Europium structural effect on a borosilicate glass of nuclear interest. *Procedia Chemistry* 7 (2012) 540. 41
- [159] A. K. Soper. Computer simulation as a tool for the interpretation of total scattering data from glasses and liquids. *Mol. Simulat.* 38 (2012) 1171. 41

- [160] I. Harsanyi and L. Pusztai. Hydration structure in concentrated aqueous lithium chloride solutions: A reverse Monte Carlo based combination of molecular dynamics simulations and diffraction data. *J. Chem. Phys.* 137 (2012) 204503. 41
- [161] G. Cobourne, G. Mountjoy, J. Rodriguez-Blanco, L. Benning, A. Hannon and J. Plaisier. Neutron and X-ray diffraction and empirical potential structure refinement modelling of magnesium stabilised amorphous calcium carbonate. *J. Non-Cryst. Solids* 401 (2014) 154. 41
- [162] I. Voleská, J. Akola, P. Jóvári, J. Gutwirth, T. Wágner, T. Vasileiadis, S. N. Yannopoulos and R. O. Jones. Structure, electronic, and vibrational properties of glassy  $\text{Ga}_{11}\text{Ge}_{11}\text{Te}_{78}$ : Experimentally constrained density functional study. *Phys. Rev. B* 86 (2012) 094108. 41
- [163] G. Opletal, R. P. Wang and S. P. Russo. Bonding trends within ternary isocoordinate chalcogenide glasses  $\text{Ge}_x\text{As}_y\text{Se}_{1-xy}$ . *Phys. Chem. Chem. Phys.* 15 (2013) 4582. 41
- [164] G. Opletal, R. Wang and S. Russo. Investigation of bonding within ab initio models of GeAsSe glasses. *Chem. Phys. Lett.* 575 (2013) 97. 41
- [165] J. Akola, S. Kohara, K. Ohara, A. Fujiwara, Y. Watanabe, A. Masuno, T. Usuki, T. Kubo, A. Nakahira, K. Nitta et al. Network topology for the formation of solvated electrons in binary  $\text{CaO-Al}_2\text{O}_3$  composition glasses. *P. Natl. Acad. Sci.* 110 (2013) 10129. 41
- [166] J. Kalikka, J. Akola, R. Jones, S. Kohara and T. Usuki. Amorphous  $\text{Ge}_{15}\text{Te}_{85}$ : density functional, high-energy X-ray and neutron diffraction study. *J. Phys.: Condens. Matter* 24 (2012) 015802. 41
- [167] A. Filipponi, A. D. Cicco and C. R. Natoli. X-ray-absorption spectroscopy and n-body distribution functions in condensed matter. I. Theory. *Phys. Rev. B* 52 (1995) 15122. 43, 67
- [168] M. T. Dove, M. G. Tucker, S. A. Wells and D. A. Keen. Reverse Monte Carlo methods. *EMU Notes Mineral.* 4 (2002) 59. 46
- [169] M. Matsumoto and T. Nishimura. Mersenne Twister: a 623-dimensionally equidistributed uniform pseudo-random number generator. *ACM Trans. Model. Comput. Simul.* 8 (1998) 3. 48
- [170] S. Hoops, S. Sahle, R. Gauges, C. Lee, J. Pahle, N. Simus, M. Singhal, L. Xu, P. Mendes and U. Kummer. COPASIA COMplex PATHway SIMulator. *Bioinformatics* 22 (2006) 3067. 48
- [171] O. Narayan and A. Young. Convergence of Monte Carlo simulations to equilibrium. *Phys. Rev. E* 64 (2001) 21104. 49
- [172] S. Kirkpatrick, C. D. Gelatt and M. P. Vecchi. Optimization by Simulated Annealing. *Science* 220 (1983) 671. 50

- [173] L. Ingber and B. Rosen. Genetic algorithms and very fast simulated reannealing: A comparison. *Math. Comput. Model.* 16 (1992) 87. 50
- [174] S. Rajasekaran. On the convergence time of simulated annealing. *Tech. Reports (CIS)* 1 (1990) 356. 50, 51
- [175] D. Bertsimas and J. Tsitsiklis. Simulated Annealing. *Statist. Sci.* 8 (1993) 10. 53
- [176] B. Hajek. Cooling Schedules for Optimal Annealing. *Math. Oper. Res.* 13 (1988) 311. 53
- [177] D. Goldberg and J. Holland. Genetic algorithms and machine learning. *Mach. Learn.* 3 (1988) 95. 55
- [178] T. Bäck and H. Schwefel. An overview of evolutionary algorithms for parameter optimization. *Evol. Comput.* 1 (1993) 1. 55
- [179] J. Holland. *Adaptation in natural and artificial systems: an introductory analysis with applications to biology, control, and artificial intelligence*. MIT Press (1992). ISBN 978-0262581110. 55
- [180] D. Whitley. An overview of evolutionary algorithms: practical issues and common pitfalls. *Inform. Software Tech.* 43 (2001) 817. 55, 57
- [181] K. Shankland, W. David and T. Csoka. Crystal structure determination from powder diffraction data by the application of a genetic algorithm. *Z. Kristall.* 212 (1997) 550. 55
- [182] B. Kariuki, H. Serrano-González, R. Johnston and K. Harris. The application of a genetic algorithm for solving crystal structures from powder diffraction data. *Chem. Phys. Lett.* 280 (1997) 189. 55
- [183] P. Chacón, J. Diaz, F. Morán and J. Andreu. Reconstruction of protein form with X-ray solution scattering and a genetic algorithm. *J. Mol. Biol.* 299 (2000) 1289. 55
- [184] P. Chacon, F. Moran, J. Diaz, E. Pantos and J. Andreu. Low-resolution structures of proteins in solution retrieved from X-ray scattering with a genetic algorithm. *Biophys. J.* 74 (1998) 2760. 55
- [185] Y. Xiao and D. Williams. Genetic algorithm: a new approach to the prediction of the structure of molecular clusters. *Chem. Phys. Lett.* 215 (1993) 17. 55
- [186] D. Deaven and K. Ho. Molecular geometry optimization with a genetic algorithm. *Phys. Rev. Lett.* 75 (1995) 288. 55
- [187] W. Cai, L. Wang, Z. Pan and X. Shao. Analysis of extended X-ray absorption fine structure spectra using annealing evolutionary algorithms. *Anal. Commun.* 36 (1999) 313. 55
- [188] D. Thierens and D. Goldberg. Convergence models of genetic algorithm selection schemes. *Lect. Notes Comput. Sc.* 866 (1994) 119. 57

- [189] T. Blickle and L. Thiele. A comparison of selection schemes used in evolutionary algorithms. *Evol. Comput.* 4 (1996) 361. 57
- [190] IXS Standards and Criteria Committee. Error Reporting Recommendations: A Report of the Standards and Criteria Committee (2000). URL [http://ixs.iit.edu/subcommittee\\_reports/sc/err-rep.pdf](http://ixs.iit.edu/subcommittee_reports/sc/err-rep.pdf). 60
- [191] S. Muto. Application of spline wavelet transformation to the analysis of extended energy-loss fine structure. *J. Electron Microsc.* 49 (2000) 525. 61
- [192] L. Shao, X. Lin and X. Shao. a Wavelet Transform and its Application to Spectroscopic Analysis. *Appl. Spectrosc. Rev.* 37 (2002) 429. 61
- [193] M. Muñoz, P. Argoul and F. Farges. Continuous Cauchy wavelet transform analysis of EXAFS spectra: A qualitative approach. *Am. Mineral.* 88 (2003) 694. 61, 63
- [194] H. Funke, A. Scheinost and M. Chukalina. Wavelet analysis of extended X-ray absorption fine structure data. *Phys. Rev. B* 71 (2005) 094110. 61, 62, 64
- [195] G. Brown, J. Catalano, A. Templeton, T. Trainor, F. Farges, B. Bostick, T. Kendelewicz, C. Doyle, A. Spormann, K. Revill et al. Environmental interfaces, heavy metals, microbes, and plants: applications of XAFS spectroscopy and related synchrotron radiation methods to environmental science. *Phys. Scripta* 2005 (2005) 80. 61
- [196] M. Munoz, F. Farges and P. Argoul. Continuous Cauchy wavelet transform of XAFS spectra. *Phys. Scripta* 2005 (2005) 221. 61
- [197] M. Harfouche, E. Wieland, R. Dähn, T. Fujita, J. Tits, D. Kunz and M. Tsukamoto. EXAFS study of U (VI) uptake by calcium silicate hydrates. *J. Colloid Interf. Sci.* 303 (2006) 195. 61
- [198] M. Vespa, R. Dähn, D. Grolimund, E. Wieland and A. Scheidegger. Spectroscopic investigation of Ni speciation in hardened cement paste. *Eviron. Sci. Technol.* 40 (2006) 2275. 61
- [199] H. Funke, M. Chukalina and A. Scheinost. A new FEFF-based wavelet for EXAFS data analysis. *J. Synchrotron. Radiat.* 14 (2007) 426. 61
- [200] H. Funke, M. Chukalina and A. Scheinost. Application of wavelet transform to extended X-ray absorption spectroscopy. In *Proceedings of the 7th WSEAS international conference on Wavelet analysis & multirate systems*, pp. 117–121. World Scientific and Engineering Academy and Society (WSEAS) (2007). 61
- [201] M. Sahnoun, C. Daul and O. Haas. Wavelet investigation of  $\text{La}_{0.5}\text{Ca}_{0.5}\text{CoO}_{3-\delta}$  X-ray absorption data. *J. Appl. Phys.* 101 (2007) 014911. 61
- [202] C. K. Chui. *An introduction to wavelets*, volume 1. Academic press (1992). ISBN 978-0-1217-4584-4. 64

- [203] I. Daubechies. *Ten Lectures on Wavelets*. Society for Industrial and Applied Mathematics (1992). ISBN 978-0-8987-1274-2. 64
- [204] J. Kas. *Toward Quantitative Calculation and Analysis of X-Ray Absorption Near Edge Spectra*. Ph.D. thesis, University of Washington (2009). 69, 70
- [205] S. Lloyd. Least squares quantization in PCM. *IEEE T. Inform. Theory* 28 (1982) 129. 72
- [206] E. Parzen. On estimation of a probability density function and mode. *Ann. Math. Stat.* 33 (1962) 1065. 77
- [207] F. Hampel. Robust estimation: A condensed partial survey. *Probab. Theory Relat. Field* 27 (1973) 87. 78
- [208] M. Daszykowski, K. Kaczmarek, Y. Vander Heyden and B. Walczak. Robust statistics in data analysis a review: basic concepts. *Chemometrics Intell. Lab. Syst.* 85 (2007) 203. 78
- [209] G. Dalba, P. Fornasini, M. Grazioli and F. Rocca. Local disorder in crystalline and amorphous germanium. *Phys. Rev. B* 52 (1995) 11034. 81
- [210] G. Dalba, P. Fornasini, R. Grisenti and J. Purans. Sensitivity of extended X-ray-absorption fine structure to thermal expansion. *Phys. Rev. Lett.* 82 (1999) 4240. 81
- [211] J. Purans, N. Afify, G. Dalba, R. Grisenti, S. De Panfilis, A. Kuzmin, V. Ozhogin, F. Rocca, A. Sanson, S. Tiutiunnikov et al. Isotopic Effect In Extended X-Ray-Absorption Fine Structure of Germanium. *Phys. Rev. Lett.* 100 (2008) 55901. 81, 82
- [212] J. Purans, J. Timoshenko, A. Kuzmin, G. Dalba, P. Fornasini, R. Grisenti, N. D. Afify, F. Rocca, S. D. Panfilis, I. Ozhogin and S. I. Tiutiunnikov. Femtometer accuracy EXAFS measurements: Isotopic effect in the first, second and third coordination shells of germanium. *J. Phys.: Conf. Series* 190 (2009) 012063. 81, 82, 90, 91
- [213] J. Timoshenko. *Lattice dynamics of crystalline germanium: isotopic effect*. Master's thesis, University of Latvia (2010). 81, 82
- [214] F. Stillinger and T. Weber. Computer simulation of local order in condensed phases of silicon. *Phys. Rev. B* 31 (1985) 5262. 81
- [215] K. Ding and H. Andersen. Molecular-dynamics simulation of amorphous germanium. *Phys. Rev. B* 34 (1986) 6987. 81
- [216] J. Tersoff. Empirical interatomic potential for silicon with improved elastic properties. *Phys. Rev. B* 38 (1988) 9902. 81
- [217] J. Tersoff et al. Modeling solid-state chemistry: Interatomic potentials for multicomponent systems. *Phys. Rev. B* 39 (1989) 5566. 81

- [218] J. Timoshenko, A. Kuzmin and J. Purans. Molecular dynamics simulations of EXAFS in germanium. *Centr. Eur. J. Phys.* 9 (2011) 710. 82, 83, 90
- [219] A. Smakula, J. Kalnajs and V. Sils. Densities and Imperfections of Single Crystals. *Phys. Rev.* 99 (1955) 1747. 83, 90
- [220] A. Ferretti, D. Rogers and J. Goodenough. The relation of the electrical conductivity in single crystals of rhenium trioxide to the conductivities of  $\text{Sr}_2\text{MgReO}_6$  and  $\text{Na}_x\text{WO}_3$ . *J. Phys. Chem. Solids* 26 (1965) 2007. 92
- [221] J. D. Greiner and H. R. Shanks. The magnetic susceptibility of rhenium trioxide. *J. Solid State Chem.* 5 (1972) 262. 92
- [222] E. Cazzanelli, M. Castriota, S. Marino, N. Scaramuzza, J. Purans, A. Kuzmin, R. Kalendarev, G. Mariotto and G. Das. Characterization of rhenium oxide films and their application to liquid crystal cells. *J. Appl. Phys.* 105 (2009) 114904. 92
- [223] T. Chatterji, P. F. Henry, R. Mittal and S. Chaplot. Negative thermal expansion of  $\text{ReO}_3$ : Neutron diffraction experiments and dynamical lattice calculations. *Phys. Rev. B* 78 (2008) 134105. 92, 96
- [224] T. Chatterji, T. C. Hansen, M. Brunelli and P. F. Henry. Negative thermal expansion of  $\text{ReO}_3$  in the extended temperature range. *Appl. Phys. Lett.* 94 (2009) 241902. 92
- [225] E. E. Rodriguez, A. Llobet, T. Proffen, B. C. Melot, R. Seshadri, P. B. Littlewood and A. K. Cheetham. The role of static disorder in negative thermal expansion in  $\text{ReO}_3$ . *J. Appl. Phys.* 105 (2009) 114901. 92
- [226] B. K. Greve, K. L. Martin, P. L. Lee, P. J. Chupas, K. W. Chapman and A. P. Wilkinson. Pronounced negative thermal expansion from a simple structure: cubic  $\text{ScF}_3$ . *J. Am. Chem. Society* 132 (2010) 15496. 92
- [227] G. Dalba, P. Fornasini, A. Kuzmin, J. Purans and F. Rocca. X-ray absorption spectroscopy study of  $\text{ReO}_3$  lattice dynamics. *J. Phys.: Condens. Matter* 7 (1995) 1199. 92, 96, 104, 105
- [228] B. Houser, R. Ingalls and J. J. Rehr. XAFS study of  $\text{ReO}_3$  under pressure. *Physica B* 208-209 (1995) 323. 92, 104
- [229] A. Kuzmin, J. Purans, G. Dalba, P. Fornasini and F. Rocca. A high-temperature X-ray absorption spectroscopy study of  $\text{ReO}_3$ . *J. Phys.: Condens. Matter* 8 (1996) 9083. 92, 104, 105
- [230] B. Houser and R. Ingalls. X-ray-absorption fine structure determination of pressure-induced bond-angle changes in  $\text{ReO}_3$ . *Phys. Rev. B* 61 (2000) 6515. 92, 97
- [231] J. Purans, G. Dalba, P. Fornasini, A. Kuzmin, S. D. Panfilis and F. Rocca. EXAFS and XRD Studies with Subpicometer Accuracy: The Case of  $\text{ReO}_3$ . *AIP Conf. Proc.* 882 (2007) 422. 92, 95, 104



- [232] J. Tao and A. Sleight. The role of rigid unit modes in negative thermal expansion. *J. Solid State Chem.* 173 (2003) 442. 96, 97
- [233] G. D. Barrera, J. A. O. Bruno, T. H. K. Barron and N. L. Allan. Negative thermal expansion. *J. Phys.: Condens. Matter* 17 (2005) R217. 97, 114
- [234] M. G. Tucker, M. T. Dove and D. A. Keen. Direct measurement of the thermal expansion of the Si-O bond by neutron total scattering. *J. Phys.: Condens. Matter* 12 (2000) L425. 97
- [235] K. N. Trueblood, H.-B. Bürgi, H. Burzclaff, J. D. Dunitz, C. M. Gramaccioni, H. H. Schulz, U. Shmueli and S. C. Abrahams. Atomic Displacement Parameter Nomenclature. Report of a Subcommittee on Atomic Displacement Parameter Nomenclature. *Acta Crystallogr. A* 52 (1996) 770. 103
- [236] T. Chatterji, P. F. Henry, R. Mittal and S. L. Chaplot. Negative thermal expansion of  $ReO_3$  : Neutron diffraction experiments and dynamical lattice calculations. *Phys. Rev. B* 78 (2008) 134105. 104, 116
- [237] A. Kuzmin and J. Purans. A new fast spherical approximation for calculation of multiple-scattering contribution in the X-ray absorption fine structure and its application to  $ReO_3$ ,  $NaWO_3$  and  $MoO_3$ . *J. Phys.: Condens. Matter* 5 (1993) 267. 104
- [238] P. Dickens and M. Weller. The structure of a cubic hydrogen rhenium bronze,  $H_{1.36}ReO_3$ . *J. Solid State Chem.* 48 (1983) 407. 113, 114, 117, 121
- [239] J. Purans, A. Kuzmin, P. Parent and C. Laffon. Study of the electronic structure of rhenium and tungsten oxides on the O K-edge. *Physica B* 259-261 (1999) 1157. 113, 114
- [240] M. Hanawa, Y. Muraoka, T. Tayama, T. Sakakibara, J. Yamaura and Z. Hiroi. Superconductivity at 1 K in  $Cd_2Re_2O_7$ . *Phys. Rev. Lett.* 87 (2001) 187001. 114
- [241] B. Lengeler. Lattice site location of hydrogen by use of extended X-ray absorption fine structure. *Phys. Rev. Lett.* 53 (1984) 74. 116
- [242] E. Makovicky and T. Balić-Žunić. New Measure of Distortion for Coordination Polyhedra. *Acta Crystallogr. B* 54 (1998) 766. 120
- [243] L. Mino, G. Agostini, E. Borfecchia, D. Gianolio, A. Piovano, E. Gallo and C. Lamberti. Low-dimensional systems investigated by X-ray absorption spectroscopy: a selection of 2D, 1D and 0D cases. *J. Phys. D: Appl. Phys.* 46 (2013) 423001. 122, 123
- [244] U. Özgür, Y. I. Alivov, C. Liu, A. Teke, M. A. Reshchikov, S. Doğan, V. Avrutin, S.-J. Cho and H. Morkoç. A comprehensive review of ZnO materials and devices. *J. Appl. Phys.* 98 (2005) 041301. 122

- [245] M. Willander, O. Nur, Q. X. Zhao, L. L. Yang, M. Lorenz, B. Q. Cao, J. Z. Perez, C. Czekalla, G. Zimmermann, M. Grundmann, A. Bakin, A. Behrends, M. Al-Suleiman, A. El-Shaer, A. C. Mofor, B. Postels, A. Waag, N. Boukos, A. Travlos, H. S. Kwack, J. Guinard and D. L. S. Dang. Zinc oxide nanorod based photonic devices: recent progress in growth, light emitting diodes and lasers. *Nanotech.* 20 (2009) 332001. 122
- [246] A. I. Hochbaum and P. Yang. Semiconductor Nanowires for Energy Conversion. *Chem. Rev.* 110 (2010) 527. 122
- [247] P. D. C. King and T. D. Veal. Conductivity in transparent oxide semiconductors. *J. Phys.: Condens. Matter* 23 (2011) 334214. 122
- [248] S. Pearton, D. Norton, K. Ip, Y. Heo and T. Steiner. Recent progress in processing and properties of ZnO. *Prog. Mat. Sci.* 50 (2005) 293. 122
- [249] S. Singh, P. Thiyagarajan, K. Mohan Kant, D. Anita, S. Thirupathiah, N. Rama, B. Tiwari, M. Kottaisamy and M. S. Ramachandra Rao. Structure, microstructure and physical properties of ZnO based materials in various forms: bulk, thin film and nano. *J. Phys. D: Appl. Phys.* 40 (2007) 6312. 122
- [250] A. Janotti and C. G. Van de Walle. Fundamentals of zinc oxide as a semiconductor. *Rep. Prog. Phys.* 72 (2009) 126501. 122
- [251] S. C. Abrahams and J. L. Bernstein. Remeasurement of the structure of hexagonal ZnO. *Acta Crystall. B* 25 (1969) 1233. 122, 125, 131
- [252] R. R. Reeber. Lattice parameters of ZnO from 4.2 to 296 K. *J. Appl. Phys.* 41 (1970) 5063. 122, 125, 131, 133
- [253] H. Karzel, W. Potzel, M. Köfferlein, W. Schiessl, M. Steiner, U. Hiller, G. M. Kalvius, D. W. Mitchell, T. P. Das, P. Blaha, K. Schwarz and M. P. Pasternak. Lattice dynamics and hyperfine interactions in ZnO and ZnSe at high external pressures. *Phys. Rev. B* 53 (1996) 11425. 122, 125, 128, 131, 133
- [254] Z. L. Wang and J. Song. Piezoelectric Nanogenerators Based on Zinc Oxide Nanowire Arrays. *Science* 312 (2006) 242. 122
- [255] Y. Yang, W. Guo, K. C. Pradel, G. Zhu, Y. Zhou, Y. Zhang, Y. Hu, L. Lin and Z. L. Wang. Pyroelectric Nanogenerators for Harvesting Thermoelectric Energy. *Nano Lett.* 12 (2012) 2833. 122
- [256] H. Schulz and K. Thiemann. Structure parameters and polarity of the wurtzite type compounds  $\text{SiC}_2\text{H}$  and ZnO. *Solid State Commun.* 32 (1979) 783. 122
- [257] K. Kihara and G. Donnay. Anharmonic thermal vibrations in ZnO. *Can. Mineral.* 23 (1985) 647. 122, 133
- [258] J. Albertsson, S. Abrahams and Å. Kvik. Atomic displacement, anharmonic thermal vibration, expansivity and pyroelectric coefficient thermal dependences in ZnO. *Acta Crystallogr. B* 45 (1989) 34. 122, 132, 133, 134

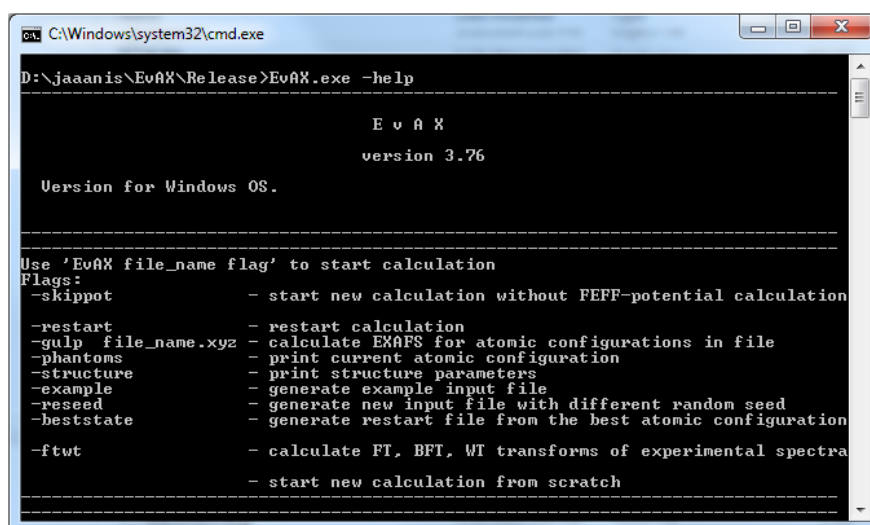
- [259] A. Shalimov, W. Paszkowicz, K. Graszka, P. Skupiski, A. Mycielski and J. Bak-Misiuk. X-ray characterisation of a bulk ZnO crystal. *Phys. Stat. Sol. (b)* 244 (2007) 1573. 122
- [260] J. Serrano, F. J. Manjón, A. H. Romero, A. Ivanov, M. Cardona, R. Lauck, A. Bosak and M. Krisch. Phonon dispersion relations of zinc oxide: Inelastic neutron scattering and *ab initio* calculations. *Phys. Rev. B* 81 (2010) 174304. 122
- [261] A. Filipponi and A. Di Cicco. X-ray-absorption spectroscopy and  $n$ -body distribution functions in condensed matter. II. Data analysis and applications. *Phys. Rev. B* 52 (1995) 15135. 123, 127
- [262] A. Yoshiasa, H. Maeda, T. Ishii, S. Emura, T. Moriga and K. Koto. XAFS study on Debye-Waller factor in tetrahedrally coordinated binary crystals. *Solid State Ionics* 78 (1995) 31. 123
- [263] T. Nedoseikina, A. Shuvaev and V. Vlasenko. X-ray absorption fine structure study on the anharmonic effective pair potential in ZnO and Zn<sub>0.1</sub>Mg<sub>0.9</sub>O. *J. Phys.: Condens. Matter* 12 (2000) 2877. 123
- [264] Q. Ma, J. T. Prater, C. Sudakar, R. A. Rosenberg and J. Narayan. Defects in room-temperature ferromagnetic Cu-doped ZnO films probed by X-ray absorption spectroscopy. *J. Phys.: Condens. Matter* 24 (2012) 306002. 123
- [265] J. Haug, A. Chassé, M. Dubiel, C. Eisenschmidt, M. Khalid and P. Esquinazi. Characterization of lattice defects by X-ray absorption spectroscopy at the Zn K-edge in ferromagnetic, pure ZnO films. *J. Appl. Phys.* 110 (2011) 063507. 123
- [266] F. Decremps, F. Datchi, A. Saitta, A. Polian, S. Pascarelli, A. Di Cicco, J. Itié and F. Baudelet. Local structure of condensed zinc oxide. *Phys. Rev. B* 68 (2003) 104101. 123
- [267] X. X. Wei, C. Song, K. W. Geng, F. Zeng, B. He and F. Pan. Local Fe structure and ferromagnetism in Fe-doped ZnO films. *J. Phys.: Condens. Matter* 18 (2006) 7471. 123
- [268] Z.-L. Lu, H.-S. Hsu, Y. Tzeng, F.-M. Zhang, Y.-W. Du and J.-C. A. Huang. The origins of ferromagnetism in Co-doped ZnO single crystalline films: From bound magnetic polaron to free carrier-mediated exchange interaction. *Appl. Phys. Lett.* 95 (2009) 102501. 123
- [269] L. Bin-Bin, S. Hong-Lie, Z. Rong, X. Xiang-Qiang and X. Zhi. Structural and magnetic properties of codoped ZnO based diluted magnetic semiconductors. *Chin. Phys. Lett.* 24 (2007) 3473. 123
- [270] G. Venkataiah, M. R. Huang, H. Su, C. Liu and J. Huang. Microstructure and magnetic properties of Ni: ZnO nanorod/Zn: NiO nanowall composite structures. *J. Phys. Chem. C* 114 (2010) 16191. 123

- [271] L. Mino, D. Gianolio, F. Bardelli, C. Prestipino, E. S. Kumar, F. Bellarmine, M. Ramanjaneyulu, C. Lamberti and M. R. Rao. EXAFS and XANES investigation of (Li, Ni) codoped ZnO thin films grown by pulsed laser deposition. *J. Phys.: Condens. Matter* 25 (2013) 385402. 123
- [272] Q. Ma, D. B. Buchholz and R. P. H. Chang. Local structures of copper-doped ZnO films. *Phys. Rev. B* 78 (2008) 214429. 123
- [273] P. S. Vachhani, G. Dalba, R. K. Ramamoorthy, F. Rocca, O. Šilewis1985potentialpr and A. K. Bhatnagar. Cu doped ZnO pellets: study of structure and Cu specific magnetic properties. *J. Phys.: Condens. Matter* 24 (2012) 506001. 123
- [274] L. Tröger, T. Yokoyama, D. Arvanitis, T. Lederer, M. Tischer and K. Baberschke. Determination of bond lengths, atomic mean-square relative displacements, and local thermal expansion by means of soft-X-ray photoabsorption. *Phys. Rev. B* 49 (1994) 888. 123
- [275] A. Kulkarni, M. Zhou and F. Ke. Orientation and size dependence of the elastic properties of zinc oxide nanobelts. *Nanotechnology* 16 (2005) 2749. 123, 125, 126, 127, 129, 130, 131, 134
- [276] A. Zaoui and W. Sekkal. Pressure-induced softening of shear modes in wurtzite ZnO: A theoretical study. *Phys. Rev. B* 66 (2002) 174106. 123, 125, 126, 127, 129, 134
- [277] G. Lewis and C. Catlow. Potential models for ionic oxides. *J. Phys. C: Solid* 18 (1985) 1149. 123, 125, 126, 127, 129, 134
- [278] K. Rickers, W. Drube, H. Schulte-Schrepping, E. Welter, U. Brüggmann, M. Herrmann, J. Heuer and H. Schulz-Ritter. New XAFS facility for in-situ measurements at beamline C at HASYLAB. *AIP Conf. Proc.* 882 (2007) 905. 124
- [279] J. D. Gale. Empirical potential derivation for ionic materials. *Phil. Mag. B* 73 (1996) 3. 125
- [280] J. D. Gale and A. L. Rohl. The General Utility Lattice Program (GULP). *Mol. Simul.* 29 (2003) 291. 125, 204
- [281] R. W. Hockney. The Potential Calculation and Some Applications. *Methods Comput. Phys.* 9 (1970) 136. 126
- [282] W. G. Hoover. Canonical dynamics: Equilibrium phase-space distributions. *Phys. Rev. A* 31 (1985) 1695. 126
- [283] E. H. Kisi and M. M. Elcombe.  $u$  parameters for the wurtzite structure of ZnS and ZnO using powder neutron diffraction. *Acta Crystallogr. C* 45 (1989) 1867. 132
- [284] S. L. Mair and Z. Barnea. Anharmonic thermal vibrations in wurtzite structures. *Acta Crystallogr. A* 31 (1975) 201. 132

- [285] S.-W. Han, H.-J. Yoo, S. J. An, J. Yoo and G.-C. Yi. Orientation-dependent X-ray absorption fine structure of ZnO nanorods. *Appl. Phys. Lett.* 86 (2005) 021917. 134
- [286] H. Li, S. Zhou and S. Zhang. The relationship between the thermal expansions and structures of ABO<sub>4</sub> oxides. *J. Solid State Chem.* 180 (2007) 589. 136
- [287] R. Lacomba-Perales, J. Ruiz-Fuertes, D. Errandonea, D. Martínez-García and A. Segura. Optical absorption of divalent metal tungstates: Correlation between the band-gap energy and the cation ionic radius. *Europhys. Lett.* 83 (2008) 37002. 136
- [288] A. Kalinko, A. Kuzmin and R. Evarestov. Ab initio study of the electronic and atomic structure of the wolframite-type ZnWO<sub>4</sub>. *Solid State Commun.* 149 (2009) 425. 136
- [289] A. W. Sleight. Accurate cell dimensions for ABO<sub>4</sub> molybdates and tungstates. *Acta Crystall. B* 28 (1972) 2899. 136
- [290] S. A. T. Redfern. Hard-mode infrared study of the ferroelastic phase transition in CuWO<sub>4</sub>-ZnWO<sub>4</sub> mixed crystals. *Phys. Rev. B* 48 (1993) 5761. 136
- [291] S. L. González-Cortés, T.-C. Xiao, P. M. Costa, S. M. Rodolfo-Baechler and M. L. Green. Relevance of the Co<sub>1-x</sub>Ni<sub>x</sub>WO<sub>4</sub> wolframite-type mixed oxide compositions on the synthesis and catalytic properties of W-based carbides. *J. Mol. Catal. A* 238 (2005) 127. 136
- [292] R. K. Selvan and A. Gedanken. The sonochemical synthesis and characterization of Cu<sub>1-x</sub>Ni<sub>x</sub>WO<sub>4</sub> nanoparticles/nanorods and their application in electrocatalytic hydrogen evolution. *Nanotechnology* 20 (2009) 105602. 136
- [293] J. E. Yourey, J. B. Kurtz and B. M. Bartlett. Structure, optical properties, and magnetism of the full Zn<sub>1-x</sub>Cu<sub>x</sub>WO<sub>4</sub> (0 ≤ x ≤ 1) composition range. *Inorg. Chem.* 51 (2012) 10394. 136
- [294] C.-L. Li and Z.-W. Fu. Nano-sized copper tungstate thin films as positive electrodes for rechargeable Li batteries. *Electrochim. Acta* 53 (2008) 4293. 136
- [295] X. Song, E. Yang, R. Ma, H. Chen and Y. Zhao. Sodium dodecyl sulfate-assisted synthesis of CoWO<sub>4</sub> nanorods. *J. Nanopart. Res.* 10 (2008) 709. 136
- [296] M. Denk, D. Kuhness, M. Wagner, S. Surnev, F. R. Negreiros, L. Sementa, G. Barcaro, I. Vobornik, A. Fortunelli and F. P. Netzer. Metal tungstates at the ultimate two-dimensional limit: fabrication of a CuWO<sub>4</sub> nanophase. *ACS Nano* 8 (2014) 3947. 136
- [297] H. Weitzel. Magnetische struktur von CoWO<sub>4</sub>, NiWO<sub>4</sub> und CuWO<sub>4</sub>. *Solid State Commun.* 8 (1970) 2071. 136
- [298] S. Naik and A. Salker. Solid state studies on cobalt and copper tungstates nano materials. *Solid State Sci.* 12 (2010) 2065. 136

- [299] J. B. Forsyth, C. Wilkinson and A. I. Zvyagin. The antiferromagnetic structure of copper tungstate  $\text{CuWO}_4$ . *J. Phys.: Condens. Matter* 3 (1991) 8433. 136
- [300] A. Anders, A. Zvyagin, M. Kobets, L. Pelikh, E. Khats'ko and V. Yurko. Effect of short range order on the magnetic properties of copper tungstates. *Sov. Phys. JETP* 35 (1972). 136
- [301] J. Ruiz-Fuertes, D. Errandonea, R. Lacomba-Perales, A. Segura, J. González, F. Rodríguez, F. J. Manjón, S. Ray, P. Rodríguez-Hernández, A. Muñoz, Z. Zhu and C. Y. Tu. High-pressure structural phase transitions in  $\text{CuWO}_4$ . *Phys. Rev. B* 81 (2010) 224115. 136, 153
- [302] J. Ruiz-Fuertes, A. Friedrich, J. Pellicer-Porres, D. Errandonea, A. Segura, W. Morgenroth, E. Haussühl, C.-Y. Tu and A. Polian. Structure solution of the high-pressure phase of  $\text{CuWO}_4$  and evolution of the Jahn–Teller distortion. *Chem. Mater.* 23 (2011) 4220. 136, 137, 153
- [303] J. Ruiz-Fuertes, A. Segura, F. Rodríguez, D. Errandonea and M. N. Sanz-Ortiz. Anomalous High-Pressure Jahn-Teller Behavior in  $\text{CuWO}_4$ . *Phys. Rev. Lett.* 108 (2012) 166402. 136, 153
- [304] A. Kuzmin, A. Kalinko and R. Evarestov. Ab initio {LCAO} study of the atomic, electronic and magnetic structures and the lattice dynamics of triclinic  $\text{CuWO}_4$ . *Acta Mater.* 61 (2013) 371. 136, 137, 153
- [305] M. Kunz and I. D. Brown. Out-of-center distortions around octahedrally coordinated  $d_0$  transition metals. *J. Solid State Chem.* 115 (1995) 395. 137
- [306] P. Schmitt, N. Brem, S. Schunk and C. Feldmann. Polyol-mediated synthesis and properties of nanoscale molybdates/tungstates: color, luminescence, catalysis. *Adv. Funct. Mater.* 21 (2011) 3037. 137
- [307] A. Kalinko and A. Kuzmin. Static and dynamic structure of  $\text{ZnWO}_4$  nanoparticles. *J. Non-Cryst. Solids* 357 (2011) 2595. 137
- [308] A. Kuzmin, A. Kalinko and R. A. Evarestov. First-principles LCAO study of phonons in  $\text{NiWO}_4$ . *Cent. Eur. J. Phys.* 9 (2011) 502. 137
- [309] A. Kuzmin, A. Anspoks, A. Kalinko and J. Timoshenko. Effect of cobalt doping on the local structure and dynamics of multiferroic  $\text{MnWO}_4$  and  $\text{Mn}_{0.7}\text{Co}_{0.3}\text{WO}_4$ . *J. Phys.: Conf. Ser.* 430 (2013) 012109. 137
- [310] A. Kuzmin, A. Anspoks, A. Kalinko, J. Timoshenko and R. Kalendarev. Extended X-ray absorption fine structure spectroscopy and first-principles study of  $\text{SnWO}_4$ . *Phys. Scripta* 89 (2014) 044005. 137
- [311] A. Anspoks, A. Kalinko, J. Timoshenko and A. Kuzmin. Local structure relaxation in nanosized tungstates. *Solid State Commun.* 183 (2014) 22. 137, 139, 150, 154, 155

- [312] L. Cavalcante, M. Almeida, W. Avansi Jr, R. Tranquilin, E. Longo, N. Batista, V. Mastelaro and M. S. Li. Cluster coordination and photoluminescence properties of  $\alpha$ -Ag<sub>2</sub>WO<sub>4</sub> microcrystals. *Inorg. Chem.* 51 (2012) 10675. 137
- [313] S. Novais, M. Valerio and Z. Macedo. X-ray-excited optical luminescence and X-ray absorption fine-structures studies of CdWO<sub>4</sub> scintillator. *J. Synchrotron Radiat.* 19 (2012) 591. 137
- [314] W. Zhu, X. Feng, Z. Wu and Z. Man. On the annealing mechanism in PbWO<sub>4</sub> crystals. *Physica B* 324 (2002) 53 . 137
- [315] Z. Qi, C. Shi, D. Zhou, H. Tang, T. Liu and T. Hu. The green emission and local structure of the scintillator PbWO<sub>4</sub>. *Physica B* 307 (2001) 45 . 137
- [316] A. Kalinko, A. Kotlov, A. Kuzmin, V. Pankratov, A. Popov and L. Shirmane. Electronic excitations in ZnWO<sub>4</sub> and Zn<sub>x</sub>Ni<sub>1-x</sub>WO<sub>4</sub> (x = 0.1 - 0.9) using VUV synchrotron radiation. *Cent. Eur. J. Phys.* 9 (2011) 432. 137
- [317] A. Kalinko and A. Kuzmin. Raman and photoluminescence spectroscopy of zinc tungstate powders. *J. Lumin.* 129 (2009) 1144. 138
- [318] A. Kalinko and A. Kuzmin. Static and dynamic structure of ZnWO<sub>4</sub> nanoparticles. *J. Non-Cryst. Solids* 357 (2011) 2595. 138
- [319] A. Kuzmin, A. Kalinko and R. Evarestov. Ab initio LCAO study of the atomic, electronic and magnetic structures and the lattice dynamics of triclinic CuWO<sub>4</sub>. *Acta Mater.* 61 (2013) 371. 147
- [320] A. Kuzmin, A. Anspoks, A. Kalinko and J. Timoshenko. Influence of thermal and static disorder on the local atomic structure in CuWO<sub>4</sub>. *J. Phys.: Conf. Series* (2014). (2014) in press. 148
- [321] V. L. Aksenov, A. Y. Kuzmin, J. Purans and S. I. Tyutyunnikov. EXAFS spectroscopy at synchrotron-radiation beams. *Phys. Part. Nucl.* 32 (2001) 675. 150
- [322] H. Jia, J. Stark, L. Q. Zhou, C. Ling, T. Sekito and Z. Markin. Different catalytic behavior of amorphous and crystalline cobalt tungstate for electrochemical water oxidation. *RSC Advances* 2 (2012) 10874. 151, 156
- [323] M. F. Daniel, B. Desbat, J. C. Lassegues, B. Gerand and M. Figlarz. Infrared and Raman study of WO<sub>3</sub> tungsten trioxides and WO<sub>3</sub>·H<sub>2</sub>O tungsten trioxide hydrates. *J. Solid State Chem.* 67 (1987) 235. 154
- [324] K. Momma and F. Izumi. VESTA 3 for three-dimensional visualization of crystal, volumetric and morphology data. *J. Appl. Crystallogr.* 44 (2011) 1272. 186, 188
- [325] J. J. Rehr, A. L. Ankudinov and Ravel. FEFF8.40 User Guide (2006). URL <http://www.feffproject.org/>. 188, 191



```
C:\Windows\system32\cmd.exe
D:\jaaaanis\EvAX\Release>EvAX.exe -help

-----
                E v A X
                version 3.76

Version for Windows OS.

-----

Use 'EvAX file_name flag' to start calculation
Flags:
-skipptot          - start new calculation without FEFF-potential calculation
-restart          - restart calculation
-gulp file_name.xyz - calculate EXAFS for atomic configurations in file
-phantoms         - print current atomic configuration
-structure        - print structure parameters
-example          - generate example input file
-reseed           - generate new input file with different random seed
-beststate        - generate restart file from the best atomic configuration
-ftwt             - calculate FT, BFT, WT transforms of experimental spectra
                 - start new calculation from scratch

-----
```

Figure A.1: Screenshot of EvAX program

## Appendix A. EVAX CODE: USER'S GUIDE

### A.1 Introduction

EvAX (Evolutionary Algorithms for XAS analysis) is a program for EXAFS analysis using reverse Monte Carlo and evolutionary algorithm methods. Program is written in object-oriented C++ language and consists of 41 code and header files and contains about 10000 lines of code. It can be used both with Windows (Windows XP and newer) and Linux operating systems. The most time-consuming parts of calculations (clustering of atoms, EXAFS *ab-initio* calculations, wavelet transform of EXAFS spectra) can be automatically divided into smaller problems and performed in parallel (in different threads of execution), taking advantage of multi-processor systems. For this purpose for Linux version of the program the *pthread*s library is used, and for Windows version - *CreateThread()* and related functions from standard Windows library *windows.h*. Number of threads to use can be specified by command `Number_of_threads` in the parameter file.



## A.2 Starting new calculation

### A.2.1 Required files and programs

For calculations following files and programs should be prepared:

1. **EvAX program**, compiled for a given operating system<sup>1</sup>.
2. **FEFF program** [25] by Ankudinov, Ravel, Rehr and Conradson (version FEFF8-lite is recommended);
3. For calculations within Linux OS - the auxiliary **runFEFF.exe program**;
4. **Parameter file** - text file, containing values of the parameters for calculations (to get example of such file with default values for all parameters, run EvAX program with a keyword *-example*);
5. **Structure file** - text file, defining the lattice and types of atoms in the crystalline structure. This file can be created, for instance, by VESTA program [324];
6. File with experimental extracted **EXAFS data**.

Structure file, file with experimental EXAFS data and path to FEFF program are specified within the parameter file. The name of parameter file is supplied to EvAX program as a command-line argument. Thus, to start calculations, just type something like

```
EvAX.exe parameters.dat
```

For calculations on Linux cluster the use of *screen* window manager is strongly recommended.

### A.2.2 FEFF program

EvAX program employs as an inner routine the FEFF8-lite code by Ankudinov, Ravel, Rehr and Conradson [25]. FEFF is a copyrighted software, therefore we are not distributing it together with EvAX. FEFF8-lite can be downloaded free of charge from the project's webpage <http://feffproject.org/>.

Follow these instructions:

---

<sup>1</sup>The operating system can be specified using preprocessor directives (*# define*) in the *mssystem.h* file: to choose the operating system either keyword WINDOWS or LINUX should be defined

1. Download the Fortran source code feff85L.f from <http://feffproject.org/>
2. By default the number of atoms that can be used for ab-initio EXAFS calculations in FEFF8-lite is limited by 1000, and it is not sufficient for a realistic crystalline structure model. To increase the allowed number of atoms for FEFF calculations, edit the feff85L.f file: find ALL 130 definitions of parameters `natx` and `nattx`, and set the values of these parameters to, for example, 10000.
3. Use, for instance, Intel *ifort* compiler to create a new FEFF executable.
4. Specify the path and name of your FEFF program in the input file for EvAX calculations.

### A.2.3 Experimental data

Experimental data - extracted EXAFS spectrum is given to EvAX program as a simple two-column text-file. The name of this file should be specified in the parameter file (parameter `File_with_experimental_EXAFS_signal`). The first column of file contains the values of EXAFS signal  $\chi(k)k^n$  and the second column - the corresponding values of wavenumber  $k$ . The power  $n$  used to emphasize contributions to the total EXAFS spectrum at large values of wavenumber  $k$  should be specified in the parameter file (parameter `k_power`). The experimental data are re-interpolated within the EvAX simulations on the mesh from  $k_{\min}$  (parameter `k_min`) to  $k_{\max}$  (parameter `k_max`) with a step, specified by parameter `dk`). If necessary, experimental data can be corrected for amplitude reduction factor  $S_0^2$  and shift of energy reference  $E_0$  (parameters `S02` and `dE0`, correspondingly).

### A.2.4 Structure file

The lattice parameters and types of atoms in the structure are specified in a separate text file. The name of this file should be specified in the parameter file (parameter `File_with_structure`). An example of such file is given below:

```
ZnO Wurtzite structure from H. Karzel et al., Phys. Rev. B 53,
  3.2495999336      0.0000000000      0.0000000000
 -1.6247999668      2.8142360947      0.0000000000
  0.0000000000      0.0000000000      5.2041997910

0.333333343        0.666666687        0.000000000  Zn
```

0.666666627	0.333333313	0.500000000	Zn
0.333333343	0.666666687	0.381900012	O
0.666666627	0.333333313	0.881900012	O

Such file can be created manually, or exported from program VESTA as *\*.p1*-type file [324]. The structure of this file is strict: the order of parameters in the file is important, and also no additional lines can be added. File starts with some arbitrary title, then follows the description of the lattice vectors in form of  $n_x$ ,  $n_y$ ,  $n_z$ , where  $n_x$ ,  $n_y$ ,  $n_z$  are the components of the lattice vectors. Further follows the list of fractional coordinates of all atoms, where entry for each atom ends with its label. As a label one can use the chemical symbol of atom (Zn, O, etc.) or its chemical symbol with one additional digit appended (Zn1, O2, etc.): the atomic label will be used by EvAX program to identify atomic numbers for FEFF calculations.

### A.3 FEFF calculations

#### A.3.1 Common FEFF keywords

For EXAFS calculations we use FEFF code [25], which is employed as an internal routine by EvAX program. The input file *feff.inp*, required for FEFF calculations, is created and the FEFF program is started automatically by EvAX. Normally there is no need to modify this file manually. However, at some situations user may want to have more control over, for example, self-consistent cluster potential calculations. Therefore here we give a brief description of the main keywords in the *feff.inp* file, used as an input file by program FEFF for EXAFS calculations. Information, provided in this Subsection, is based on FEFF user's guide [325].

To start potential calculations, one should specify the atomic cluster. The all types of atoms in the cluster are described after POTENTIALS keyword. Each line corresponds to one distinct atom, and contains integer number (a label, assigned to this atom), the corresponding atomic number and then four optional arguments, where first two limit the angular momentum for the calculations of the self-consistent potential (if they are set to -1, the default values are used) and the third one specifies the stoichiometry, i.e., the relative quantity of the atoms of this kind in the structure. Fourth optional argument is used for the spin-dependent calculations only. One line of the POTENTIALS card is always devoted

to the absorbing atom - its label is always 0 and stoichiometric number can also be set to 0.

In our approach the potential is calculated for equilibrium structure, known, for instance, from diffraction experiments, thus the cluster is set by the list of equilibrium atomic coordinates. The listing of atomic coordinates is started by keyword **ATOMS**, after which each line corresponds to one atom and contains its  $x$ ,  $y$  and  $z$  coordinates and integer number - label - that specifies the type of the atom accordingly to the definitions given in **POTENTIALS** card.

The parameters of the self-consistent potential calculations are given after **SCF** keyword. Four arguments follows: (i) the radius of the cluster for full multiple-scattering calculations (should be larger than the radius of the second coordination shell), (ii) the parameter that specifies the origin of this cluster (should be 0 for solids), (iii) the maximal number of iterations for self-consistent calculations and (iv) a convergence acceleration factor (number between 0 and 1) .

Command **EDGE** specifies the location of the hole - **EDGE K** means that absorption for K-edge is calculated, **EDGE L3** - that absorption for L<sub>3</sub>-edge is calculated, etc.

After keyword **EXCHANGE** follow the parameters that specify, which exchange correlation function will be used. **EXCHANGE 0 0 0** means that Hedin-Lundqvist (HL) model will be used with additional edge shift equal to zero (second argument) and the additional experimental broadening of the spectrum also equal to zero (third argument).

After **S02** the value of the amplitude reduction factor due to many-electronic processes  $S_0^2$  is given. If it is not specified, the value of  $S_0^2$  is calculated from the overlap integrals.

EXAFS calculations are started, if the keyword **EXAFS** is present. After the cluster potential is calculated, one can evaluate the contribution of all scattering paths to the total absorption coefficient and to EXAFS spectrum. These paths are listed by FEFF in *list.dat* and, in more details, in *paths.dat* files. Of course, not all paths have the same importance, and the relative amplitude of the contributions with respect to the first path (usually, the most important) is given in *list.dat* file. To use in further calculations (and to include in *paths.dat* file) only paths with importance, say, larger than 1.5%, one can use **CRITERIA 0 1.5** command. The number of the considered scattering paths can also be reduced by command **NLEGS** that specifies the maximal allowed order of the MS path (**NLEGS 2** means calculations in single-scattering approximation, **NLEGS 3** means

that also the double-scattering effects will be considered, etc.). The command RMAX sets the half-length of the longest scattering path that still will be used for FEFF calculations. Very important aspect that is exploited within EvAX code is that *paths.dat* file can be edited outside FEFF code. This allows us to group all scattering paths and significantly speed up the calculations using clustering algorithm.

The operations that are carried out by FEFF code can be controlled by keyword CONTROL and its six arguments, each of them can be set either to 1 (carry out this step) or to 0 (skip this step). First argument determines whether to perform the potential calculations, second argument is responsible for the calculations of the absorption cross-sections, third - for the full multiple-scattering calculations of XANES part, fourth - for the enumeration of all scattering paths (generation of *paths.dat* file), fifth - for the calculations of effective scattering functions for each of the paths in *paths.dat* file, sixth - for the calculations of total EXAFS spectra.

An example of *feff.inp* file is given below:

```
TITLE    FEFF.inp for ReO3
EDGE     L3
S02      1.000000000000
*        pot    xsph  fms   paths genfmt ff2chi
CONTROL  0      0     0     1     1     1
PRINT    1      0     0     0     0     2
*        r_scf  [ l_scf n_scf ca ]
SCF      5.38997  0     15    0.1
*        ixc   [ Vr  Vi ]
EXCHANGE 0      0     0
EXAFS
RPATH    7.000000000000
NLEGS    8
CRITERIA 0.0  0.000000000000
POTENTIALS
*   ipot  z [ label  l_scm  l_fms  stoichiometry ]
      0  75  Re   -1    -1     0
      1  75  Re   -1    -1     1
      2   8   0   -1    -1     2
ATOMS
0.000000000000 0.000000000000 0.000000000000 0
0.000000000000 0.000000000000 3.747000000000 1
```

```

...
-3.747000000000 -3.747000000000 -1.873500000000 2
END

```

After FEFF calculations are finished, the total EXAFS spectra is saved to *chi.dat* file. Additionally, if the sixth argument of PRINT command is set to be equal to 2, then files *chipNNNN.dat* are generated that contain the contributions to the total EXAFS spectrum from the *NNNN*-th path.

More detailed information related to the control of FEFF calculations can be obtained from FEFF8 manual [325].

### A.3.2 Running FEFF from EvAX code

*feff.inp* files are created and FEFF program is launched several times at each of the RMC/EA iteration. The parameters for FEFF calculations (values for EDGE, CRITERIA, NLEGS, RMAX) are given by user in this case in the input file for EvAX program. Atomic coordinates are given correspondingly to the current RMC/EA atomic configuration. Atomic types, atomic numbers and stoichiometric numbers are obtained together with equilibrium geometry from the structure describing file.

At the first RMC/EA iteration the full FEFF calculation is performed for equilibrium geometry (all six arguments in the CONTROL card are set to 1), hence the self-consistent potential is obtained. Following values for self-consistent calculations are used as default: HL model for the calculations of complex self-energy is applied, maximal number of self-consistent iterations is 15, value of relaxation parameter *c* is set to 0.1, radius of cluster for potential calculations is set to be equal to 1.25 times the length of the longest elementary translation vector that defines the unit cell of crystal. After this FEFF run for equilibrium configuration the *paths.dat* file that contains the description of all relevant paths is created. This file is used by EvAX program to define all non-equivalent types of paths that will be used in further calculations. In general, this first FEFF calculation can be quite time-consuming and can be skipped, if the potentials are already calculated, for example, if interrupted calculations are restarted; one also can use the pre-calculated FEFF potentials, if the better control over different options for self-consistent potential calculations is needed. To skip potential calculations, use *-skippot* command-line keyword for EvAX program.

Further on the *paths.dat* files are created by the EvAX program, and first four arguments of the CONTROL card are set to zero - potential is not recalculated and the FEFF program uses *paths.dat* file, provided by EvAX. Obtained *chi.dat* and/or *chipNNNN.dat* files with the total EXAFS signal and contributions from separate paths are read by EvAX and used for further calculations.

Parameters, used by EvAX code to perform FEFF calculations, are summarized in Sec. A.4.3.

## A.4 Parameters

### A.4.1 Example of parameter file

An example of parameter file is given below, with all parameters set to their default values. File starts with BEGIN keyword and ends, unsurprisingly, with END keyword. Lines starting with # are neglected. The order of parameters in the file is arbitrary. If a parameter is not specified, the default value is used.

```
BEGIN
Title                               EXAMPLE
#####
##### COMMON_PARAMETERS #####
#####
# integers
    Froze_in:                        1500
    Number_of_states:                32
    Number_of_spectra:               1
# strings
    File_with_structure:             structure.p1
# integers_(spectra)
    N_legs                           8
    Max_paths                         100
# doubles_(spectra)
    k_min:                           0
    k_max:                           20
    k_power:                          2
    R_min:                            0
    R_max:                            5
    R_max_for_FEFF:                  6
# strings_(spectra)
    Edge:                             Ge
    Edge_type:                        K
    File_with_experimental_EXAFS_signal: expEXAFS.dat
# misc
    Supercell                        4 4 4
```

```

#####
##### ADVANCED_PARAMETERS #####
#####
# integers
    time1:                10
    time2:                1000
    Update_basis_every_...: 3
    Number_of_threads:    12
# doubles
    Maximal_step_length:  0.005
    Maximal_displacement: 0.4
    Initial_displacement: 0.1
    'Temperature':        1
    Target_dicarding_rate: -1
    Clustering_precision: 0.1
# strings
    Space:                 k
    Norm_type:             L2
    Structure:             p1
    Move_type:             move_all
    File_for_actual_geometry: output.xyz
    File_for_residuals:   output.dat
    File_for_restart:     restart
    FEFF_path:            feff8.exe
    File_for_final_xyz:   phantoms.xyz
    File_for_equilibrium_xyz phantoms_eq.xyz
# doubles_(spectra)
    S02:                  1
    dE0:                  0
    dk:                   0.05
    FEFF_criteria         0
    R0_for_WT:            -1
# strings_(spectra)
    File_for_i-pol._exp._signal: ipolEXAFS.dat
    File_for_BFT_of_exp._signal: expBFT.dat
    File_for_FT_of_exp._signal:  expFT.dat
    File_for_WT_of_exp._signal:  expWT.dat
    File_for_calculated_EXAFS_signal: EXAFS.dat
    File_for_FT:             ft.dat
    File_for_BFT:            bft.dat
    File_for_WT:             wt.dat
# misc_(spectra)
    Window                0
# flags
    pbc:                  1

```



```

        crossoverT                1
        adjust_T                  1
        adjust_step                0
        non_equiv_absorbers        0
# misc
        MT_seed                    291 564 837 1110
#####
END

```

In the EvAX program it is also possible to analyze several EXAFS spectra simultaneously and to try to find a structural model that equally well describes available EXAFS data from absorbing atoms of different types. If different values of some parameter should be used for the analysis of different spectra, one can just list them all in the line corresponding to this parameter. If only one value is given, it will be applied for the analysis of all spectra. Fragment of parameter file for the analysis of two spectra simultaneously is given below:

```

BEGIN
Title                                TWO SPECTRA
#####
##### COMMON_PARAMETERS #####
#####
        Number_of_spectra:          2
# doubles_(spectra)
        k_min:                      0
        k_max:                      20
        R_min:                      0 1
        R_max:                      4 5
# strings_(spectra)
        Edge:                        Cu W
        Edge_type:                   K L3
        File_with_experimental_EXAFS_signal: cuEXAFS.dat wEXAFS.dat
# strings_(spectra)
        File_for_i-pol._exp._signal:  ipolEXAFS.dat
        File_for_BFT_of_exp._signal:  Cu/expBFT.dat W/expBFT.dat
        File_for_FT_of_exp._signal:   Cu/expFT.dat W/expFT.dat
        File_for_WT_of_exp._signal:   Cu/expWT.dat W/expWT.dat
        File_for_FT:                  Cu/ft.dat W/ft.dat
        File_for_BFT:                  Cu/bft.dat W/bft.dat
        File_for_WT:                  Cu/wt.dat W/wt.dat
# flags
        non_equiv_absorbers          0
#####
END

```

Finally, it is also possible to carry out RMC/EA simulations for crystalline systems, where the absorbing atom is located at two (or more) non-equivalent sites. An example of such systems is cubic yttrium oxide. In this case during the RMC/EA run we again need to carry out separate EXAFS calculations for each of the non-equivalent sites, but now the obtained spectra should be added with the correct weights before compared with experimental data, which, of course, contains the signals from all absorbing sites simultaneously. For such calculations one should set the parameter `Number_of_spectra` to the number of non-equivalent sites, but also to change the value of flag `non_equiv_absorbers` to 1.

#### A.4.2 Parameters for structure model construction

Parameter	Description
<code>File_with_structure</code>	name of file with crystal structure definition;
<code>Structure</code>	format of the file with crystal structure definition; currently only one option ( <i>p1</i> ) is supported;
<code>Supercell</code>	size of used supercell;
<code>pb</code>	flag that specifies whether to apply periodic boundary conditions.

#### A.4.3 Parameters for FEFF calculations:

Parameter	Description
<code>FEFF_path</code>	name and location of FEFF program;
<code>Edge</code>	absorbing atom or site (Ge, Re, Y1, Y2, etc.);
<code>Edge_type</code>	absorption edge (K, L3, etc.);
<code>FEFF_criteria</code>	value for FEFF CRITERIA command, minimal relative importance of the scattering path to be considered;
<code>N_legs</code>	value for FEFF NLEGS command, maximal order of the scattering path to be considered;
<code>R_max_for_FEFF</code>	value for FEFF RMAX command, maximal half-length of the scattering path to be considered;
<code>Max_paths</code>	maximal number of scattering paths to include in the EvAX calculations.

## A.4.4 Parameters for spectra comparison

Parameter	Description
space	set the value of this parameter to $k$ , $q$ , $r$ or $w$ to carry out the comparisons of theoretical and experimental EXAFS spectra in $k$ -, $q$ -, $R$ - or wavelet spaces, correspondingly;
Norm_type	set the value of this parameter to $L2$ (default) or $L1$ to use $L_2$ or $L_1$ - type Euclidian norms for the comparisons of theoretical and experimental EXAFS spectra;
R_min and R_max	$R_{\min}$ and $R_{\max}$ : correspondingly the minimal and maximal values of $R$ (in $\text{\AA}$ ) used for residual calculation in $R$ -, $q$ - or wavelet space;
k_min and k_max	$k_{\min}$ and $k_{\max}$ : correspondingly minimal and maximal values of wavenumber $k$ (in $\text{\AA}^{-1}$ ), used for residual calculations in $k$ -, $q$ - or wavelet space; keep $k_{\max}$ smaller than $20.0 \text{\AA}^{-1}$ , and $k_{\min}$ larger than $0.0 \text{\AA}^{-1}$ to avoid interpolation errors;
k_power	the power $n$ used to emphasize contributions at large values of wavenumber $k$ to the total experimental EXAFS spectrum $\chi(k)k^n$ ;
S02	amplitude reduction factor $S_0^2$ (experimental data are divided by $S_0^2$ before compared with calculated EXAFS);
dE0	energy shift $\Delta E_0$ in eV (experimental data are converted to energy space, shifted by $-\Delta E_0$ units and then converted back to wavenumber space, before compared with calculated EXAFS);
dk	sampling step $\Delta k$ (before comparison, experimental data and theoretical data are re-interpolated on a wavenumber mesh in the range between $k_{\min}$ and $k_{\max}$ with step $\Delta k$ );
R0	scaling parameter for wavelet transform; if not specified or set to negative value, default value for R0 is used: $(R_{\min} + R_{\max})/2$ ;
window	command to set different weights to different data points. Two arguments, $k_0$ and $R_0$ , are required. The 2D gaussian function $\rho(k, R)$ is created with half-widths $\sigma_k = (k_{\max} - k_{\min})/2$ in the $k$ -space and $\sigma_R = (R_{\max} - R_{\min})/2$ in the $R$ -space, and the centrum at $((1 - k_0) \cdot k_{\min} + k_0 \cdot k_{\max}; (1 - R_0) \cdot R_{\min} + R_0 \cdot R_{\max})$ , and for calculations of residual then equation (4.13) is used.

## A.4.5 Parameters for RMC and EA calculations and simulated annealing schemes

Number_of_states	number of atomic configurations (i.e., number of individuals) in the population used for EA simulations; if this parameter is set to 1, conventional RMC simulations will be carried out;
Maximal_step_length	(initial) value of parameter $\delta$ - maximal allowed step length;
Move_type	set this parameter to <i>move_all</i> to move all atoms in the configuration at each iteration, or to <i>move_one</i> to move only one randomly selected atom;
'Temperature'	(initial) value of scaling parameter $T$ for Metropolis algorithm; if set to negative value, default (very large) value is used;
Target_discarding_rate	(initial) value of parameter $1 - p$ that determines the expected ratio of accepted and discarded moves;
adjust_T	flag to allow the adjusting the value of parameter $T$ during the simulation;
adjust_step	flag to allow the adjusting the value of parameter $\delta$ during the simulation;
Froze_in	maximal number of iterations ( $t_{\max}$ ); if it is not specified or is set to a negative value, the simulation will be continued with a fixed value of $p$ till there is no significant improvement of residual $\xi$ ; if it is positive, the value of $p$ will be changed linearly from 1 to 0;
Convergence_criteria	parameter that determines the convergence of calculations: if the average change of difference between experiment and simulated data $\xi$ during the last <code>time2</code> iterations are larger than <code>Convergence_criteria</code> , the calculations will be continued; otherwise the parameter $\delta$ will be reduced (if <code>adjust_step</code> is 1) or calculations will be stopped;
Maximal_displacement	maximal allowed displacement $\delta_{\max}$ for atoms from their equilibrium positions;
Initial_displacement	maximal initial displacement for atoms from their equilibrium positions; if <code>Initial_displacement</code> is set to a negative value, the program will try out different values of <code>Initial_displacement</code> and calculations will be started with the value that corresponds to the smallest $\xi$ ;

<code>crossoverT</code>	if set to zero, tournament selection within evolutionary algorithm will be used, otherwise proportional selection will be applied.
-------------------------	--

#### A.4.6 Parameters for clustering algorithm

<code>Clustering_precision</code>	parameter $\varepsilon_c$ that determines the number of clusters for the each type of paths. If the ratio of clustering error for this type of paths $\xi_c$ and current difference between theoretical and experimental EXAFS spectra $\xi$ is larger than $\varepsilon_c$ , the number of clusters is doubled;
<code>time2</code>	frequency of clustering precision check: if the clustering precision is insufficient with respect to the value, determined by parameter <code>Clustering_precision</code> , the number of clusters for the given type of paths is increased;
<code>Update_basis_every...</code>	frequency of recalculations of cluster centra and corresponding partial contributions to EXAFS, the values larger than 3 or 4 may lead to significant errors in the approximation of EXAFS spectra;

#### A.4.7 Other parameters and flags

<code>Number_of_spectra</code>	number of experimental EXAFS spectra, used for the analysis. If <code>non_equiv_absorbers</code> is set to 1 - the number of absorbers of the same type, but located at non-equivalent sites;
<code>non_equiv_absorbers</code>	flag that specifies, whether the absorbing atoms are located at non-equivalent sites;
<code>Number_of_threads</code>	number of threads to use, typically should be set equal to number of CPUs of your machine;
<code>MT_seed</code>	random seed for Mersenne-Twister algorithm;

## A.5 Output

### A.5.1 Introduction

As an output, EvAX produces a number of text-type files. The names of these files can be changed (for instance, to redirect output to some other directory), by changing the value of corresponding parameter in the parameter file. All

output files can be divided in three groups: (i) general output files (only one file per calculation is produced), (ii) spectrum-specific output files (one file per each analyzed EXAFS spectrum is produced, i.e., if, for instance, EXAFS data from two absorption edges are used simultaneously, different names for each of the corresponding output files should be given), and (iii) restart files.

Additionally, each `time1` iterations EvAX prints to the standard output basic information on the current system state: current value of difference between experimental and simulated EXAFS data, calculated in  $k$ -,  $q$ -,  $R$ - and wavelet spaces (`BEST-STATE RESIDUAL`), average change of such difference per iteration (`Delta`), current value of scaling parameter  $T$  for Metropolis algorithm (`Temperature`) and maximal step length for atomic displacements (`Step`) etc:

```

...
-----14.05.2014 13:40:13-----
GENERATION:
1110
BEST-STATE RESIDUAL:
K Q R [W]
0.459614 0.204085 0.140646 0.193367
GA:
Crossovers Mutations Evolutions
30 34 23
REGULATION:
Delta Temperature Step
0.00124913 0.000927289 0.005
-----
-----14.05.2014 13:58:32-----
GENERATION:
1120
BEST-STATE RESIDUAL:
K Q R [W]
0.460606 0.206681 0.140429 0.19519
GA:
Crossovers Mutations Evolutions
33 33 22
REGULATION:
Delta Temperature Step
0.00119698 0.000871764 0.005
...

```

At the end of simulations EvAX prints to the standard output the values of the most important structure parameters. An example of such output is given below: first of all, the effective isotropic mean-square deviations (MSD) for all types of atoms in the structure are calculated. Then the average interatomic distances

( $\langle r_{leg} \rangle$ ), average values of bonding angles ( $\langle \beta \rangle$ ), mean-square relative displacements ( $MAD[r_{leg}]$ ) and variances of angles ( $MAD[\beta]$ ) are calculated. The output is organized similarly as the *paths.dat* file, generated by FEFF program: all photoelectron paths, used in calculations, are listed and can be identified by half-length  $r$  and equilibrium positions of involved atoms with respect to absorbing atoms, and then the calculated values of corresponding structure parameters are given:

-----  
17.05.2014 12:15:08MSD  $\langle u^2 \rangle$   
-----

Sr 0.0263751

Ti 0.0239545

O 0.0282375  
-----

17.05.2014 12:15:08

STRUCTURE PARAMETERS  
-----

		1	2	4	index, nleg, degeneracy, r=					
x	y	z	ipot	label	$\langle r_{leg} \rangle$	$\langle \beta \rangle$	MAD[rleg]	MAD[ $\beta$ ]		
1.410867	1.344733	0.000000	3	0	1.960401	180.000000	0.007944	0.000000		
0.000000	0.000000	0.000000	0	Ti	1.960401	180.000000	0.007944	0.000000		
		2	2	2	index, nleg, degeneracy, r=					
0.000000	0.000000	1.951425	3	0	1.963847	180.000000	0.007397	0.000000		
0.000000	0.000000	0.000000	0	Ti	1.963847	180.000000	0.007397	0.000000		
		3	3	8	index, nleg, degeneracy, r=					
1.344733	-1.410867	0.000000	3	0	1.960401	134.945124	0.007944	14.897332		
1.410867	1.344733	0.000000	3	0	2.764355	134.945124	0.019318	14.897332		
0.000000	0.000000	0.000000	0	Ti	1.960401	90.109753	0.007944	37.715437		
		4	3	16	index, nleg, degeneracy, r=					
0.000000	0.000000	1.951425	3	0	1.963847	134.930775	0.007397	12.520714		
1.410867	1.344733	0.000000	3	0	2.765467	134.859831	0.018703	11.804484		
0.000000	0.000000	0.000000	0	Ti	1.960401	90.209394	0.007944	35.853390		
		5	2	8	index, nleg, degeneracy, r=					
0.000000	2.755600	1.951425	1	Sr	3.382742	180.000000	0.009615	0.000000		
0.000000	0.000000	0.000000	0	Ti	3.382742	180.000000	0.009615	0.000000		

...

### A.5.2 General output files

`File_for_actual_geometry` specifies \*.xyz-type file, where the intermediate atomic configurations are saved. This file is updated with frequency, set by parameter `time1`. If evolutionary algorithm is used and several supercells are simulated, then only the atomic coordinates that correspond to the supercell that currently provides the best description of experimental EXAFS are saved. Coordinates for atoms in all other supercells can be obtained from restart files.

`File_for_residuals` specifies a file, where the current value of the difference between experimental and calculated EXAFS spectra is saved, but also the number of accepted and discarded moves, current value of scaling parameter for Metropolis algorithm and other relevant information. This file is updated with frequency, also set by parameter `time1`.

`File_for_equilibrium_xyz` and `File_for_final_xyz` specify the names of files, created at the end of EvAX calculations, where the coordinates of all atoms for the equilibrium and for the actual atomic configuration, respectively, taking into account periodic boundary conditions, are saved. If evolutionary algorithm is used and several supercells are simulated, then only the atomic coordinates that correspond to the supercell that provides the best description of experimental EXAFS are saved. These files can be used to perform advanced analysis of the obtained structure model.

### A.5.3 Spectrum-specific output files

`File_for_i-pol._exp._signal` specifies the file, where the re-interpolated and corrected for specified  $S_0^2$  and  $\Delta E_0$  values experimental EXAFS spectrum is saved.

`File_for_FT_of_exp._signal` and `File_for_BFT_of_exp._signal` specify the files where the results of Fourier transform and inverse Fourier transform respectively, of the experimental data are saved. `File_for_WT_of_exp._signal` sets the name of file for the results of Morlet wavelet transform for experimental data.

`File_for_calculated_EXAFS_signal` specifies the file, where the calculated EXAFS signal is saved. This file is updated with frequency, set by parameter `time1`. If evolutionary algorithm is used and several supercells are simulated, then only the EXAFS spectrum that is the closest to the experimental data is saved. EXAFS spectra corresponding to the other supercells can be obtained from restart files.



`File_for_FT`, `File_for_BFT` and `File_for_WT` specify the files where the results of Fourier transform, inverse Fourier transform and Morlet wavelet transform, respectively, of the calculated EXAFS data are saved. These files are also rewritten with frequency, set by parameter `time1`.

#### A.5.4 Restart files

Restart files are created with frequency, set by parameter `time2`. The name of restart file is a string, set by parameter `File_for_restart`, to which integer number, corresponding to the number of current iteration, is appended. Restart files are text-type files that consist of two large blocks: the first block has the same structure as the input parameter file, where all current values of system parameters are given. Thus any restart file, produced by EvAX, can be used directly to start a new calculation. The second block contains information on the number of current iteration, current value of differences between experimental and calculated EXAFS spectra, parameters for SA algorithm, and, of course, the current coordinates of all atoms in all simulated supercells. At the end of file the current calculated EXAFS spectra are recorded. Thus EvAX calculations can be restarted from the point, at which the corresponding restart file was created.

The current positions of clusters centra, used by clustering algorithm for EXAFS calculations, are saved to *restartClusters.dat* file. If this file is missing, clustering algorithm will start from scratch after the restart of calculations.

## A.6 EvAX keywords

Together with (or in a few cases - instead of) the name of parameter file some additional command line arguments (keywords) can be specified. All keywords starts with hyphen and several keywords in arbitrary order can be specified.

Already mentioned is the keyword *-example*: running

```
EvAX.exe -example
```

one obtains the example of parameter file.

Brief overview of all possible keywords can be obtained by running

```
EvAX.exe -help
```

The important keywords are *-skippot* and *-restart*:

```
EvAX.exe parameters.dat -skippot
```

starts a new calculation with parameters from the file *parameters.dat*, but the self-consistent FEFF potential is not recalculated. This option may be useful, since the calculations of potential are very time consuming. Besides, it allows to use a pre-calculated potential, created with parameters, specified by user.

```
EvAX.exe restart0001 -restart
```

in turn, continues an existing calculation: in this case the parameters are taken from the file *restart0001* and FEFF potential is not recalculated, but the important difference is that also the current positions of all atoms are read from *restart0001* file. This option can be used to continue an interrupted calculation, but also in the case if user wants to modify the current atomic configuration, i.e., the positions of all atoms, by hand.

For the post-processing of the results of EvAX calculations keywords *-phantoms* and *-structure* can be used.

```
EvAX.exe restart0001 -phantoms
```

creates files, whose names are set by parameters *File\_for\_equilibrium\_xyz* and *File\_for\_final\_xyz*, where the coordinates of all atoms for the equilibrium and for the actual atomic configuration, respectively, taking into account periodic boundary conditions, are saved. These files can be used, for instance, to calculate radial distribution function.

```
EvAX.exe restart0001 -structure
```

forces EvAX to print to the standard output the values of structure parameters. Note that regardless of *-phantoms* and *-structure* keywords this information on is printed out also at the end of simulations.

```
EvAX.exe restart0001 -beststate
```

let EvAX to read the restart file *restart0001*, containing EXAFS spectra and atomic coordinates for all supercells, used for evolutionary algorithm simulations, then the supercell that gives the best description of experimental EXAFS data

is found, and a new restart file is created, containing information on this specific supercell only.

EvAX program can be also used to calculate configurations-averaged EXAFS spectrum for a given set of atomic coordinates, obtained, for instance, in molecular dynamics (MD) simulations with GULP program [280]. To do this, keyword *-gulp* can be used:

```
EvAX.exe parameters.dat -gulp MDdata.xyz
```

calculates EXAFS spectrum with parameters, taken from file *parameters.dat*, for a set of atomic coordinates (MD trajectories) in *MDdata.xyz* file.

Finally, let us note that EvAX program can be used to simply calculate Fourier and wavelet transforms of given EXAFS spectrum:

```
EvAX.exe parameters.dat -ftwt
```

command calculates Fourier, inverse Fourier and Morlet wavelet transforms for EXAFS data with parameters taken from *parameters.dat*. The name of file with analyzed data is set by `File_with_experimental_EXAFS_signal` parameter.

## Appendix B. AUTHOR'S PUBLICATION LIST

### B.1 Published papers

1. J. Timoshenko, A. Kuzmin, WAVELET DATA ANALYSIS OF EXAFS SPECTRA, *Computer Physics Communications* 180 (2009) 920–925.
2. J. Purans, J. Timoshenko, A. Kuzmin, G. Dalba, P. Fornasini, R. Grisenti, N. D. Afify, F. Rocca, S. De Panfilis, I. Ozhogin, and S. I. Tiutiunnikov, FEMTOMETER ACCURACY EXAFS MEASUREMENTS: ISOTOPIC EFFECT IN THE FIRST, SECOND AND THIRD COORDINATION SHELLS OF GERMANIUM, *Journal of Physics.: Conference Series* 190 (2009) 012063 (6 pages).
3. A. Anspoks, A. Kuzmin, A. Kalinko, J. Timoshenko, PROBING NiO NANOCRYSTALS BY EXAFS SPECTROSCOPY, *Solid State Communications* 150 (2010) 2270–2274.
4. J. Timoshenko, A. Kuzmin, J. Purans, MOLECULAR DYNAMICS SIMULATIONS OF EXAFS IN GERMANIUM, *Central European Journal of Physics* 9 (2011) 710–715.
5. J. Timoshenko, A. Kuzmin, J. Purans, REVERSE MONTE CARLO MODELLING OF THERMAL DISORDER IN CRYSTALLINE MATERIALS FROM EXAFS SPECTRA, *Computer Physics Communications* 183 (2012) 1237–1245.
6. J. Timoshenko, A. Kuzmin, J. Purans, AN EFFICIENT IMPLEMENTATION OF THE REVERSE MONTE CARLO METHOD FOR EXAFS ANALYSIS IN CRYSTALLINE MATERIALS, *Journal of Physics.: Conference Series* 430 (2013) 012012 (4 pages).
7. A. Kuzmin, A. Anspoks, A. Kalinko, J. Timoshenko, EFFECT OF COBALT DOPING ON THE LOCAL STRUCTURE AND DYNAMICS OF MULTIFERROIC  $\text{MnWO}_4$  and  $\text{Mn}_{0.7}\text{Co}_{0.3}\text{WO}_4$ , *Journal of Physics.: Conference Series* 430 (2013) 012109 (4 pages).
8. J. Timoshenko, A. Anspoks, A. Kalinko, A. Kuzmin, ANALYSIS OF EXAFS DATA FROM COPPER TUNGSTATE BY REVERSE MONTE CARLO METHOD, *Physica Scripta* 89 (2014) 044006 (6 pages).

9. J. Timoshenko, A. Kuzmins, J. Purans, EXAFS STUDY OF HYDROGEN INTERCALATION INTO  $\text{ReO}_3$  USING THE EVOLUTIONARY ALGORITHM, *Journal of Physics: Condensed Matter* 26 (2014) 055401 (15 pages). **IOP Editor Selected Article.**
10. A. Anspoks, A. Kalinko, J. Timoshenko, A. Kuzmin, LOCAL STRUCTURE RELAXATION IN NANOSIZED TUNGSTATES, *Solid State Communications* 183 (2014) 22–26.
11. A. Kuzmin, A. Anspoks, A. Kalinko, J. Timoshenko, R. Kalendarev, X-RAY ABSORPTION SPECTROSCOPY OF CU-DOPED  $\text{WO}_3$  FILMS FOR USE IN ELECTROCHEMICAL METALLIZATION CELL MEMORY, *Journal of Non-Crystalline Solids* 401 (2014) 87–91. (5 pages).
12. A. Kuzmin, A. Anspoks, A. Kalinko, J. Timoshenko, R. Kalendarev, EXAFS SPECTROSCOPY AND FIRST-PRINCIPLES STUDY OF  $\text{SnWO}_4$ , *Physica Scripta* 89 (2014) 044005 (5 pages).
13. J. Timoshenko, A. Anspoks, A. Kalinko, A. Kuzmin, TEMPERATURE DEPENDENCE OF THE LOCAL STRUCTURE AND LATTICE DYNAMICS OF WURTZITE-TYPE  $\text{ZnO}$ , *Acta Materialia* 79 (2014) 194–202.
14. J. Timoshenko, A. Anspoks, A. Kalinko, A. Kuzmin, LOCAL STRUCTURE AND DYNAMICS OF WURTZITE-TYPE  $\text{ZnO}$  FROM SIMULATION-BASED EXAFS ANALYSIS, *Physica Status Solidi C* 11 (2014) 1472–1475.
15. J. Timoshenko, A. Anspoks, A. Kalinko and A. Kuzmin, LOCAL STRUCTURE OF NANOSIZED TUNGSTATES REVEALED BY EVOLUTIONARY ALGORITHM; accepted for publication in *Physica Status Solidi A* in 2014.

## B.2 Papers, submitted for publication

1. J. Timoshenko, A. Anspoks, A. Kalinko and A. Kuzmin, ANALYSIS OF EXAFS DATA FROM COBALT TUNGSTATE  $\text{CoWO}_4$ : REVERSE MONTE CARLO APPROACH; submitted for publication in *Journal of Physics: Conference Series*.
2. J. Timoshenko, A. Anspoks, A. Kalinko, I. Jonane, A. Kuzmin, LOCAL STRUCTURE OF MULTIFERROIC  $\text{Mn}_{1-c}\text{Co}_c\text{WO}_4$  SOLID SOLUTIONS REVEALED BY THE EVOLUTIONARY ALGORITHM submitted for publication in *Ferroelectrics*.

### **B.3 Published papers that are not related to the topic of the thesis**

1. V. Kashcheyevs, J. Timoshenko, QUANTUM FLUCTUATIONS AND COHERENCE IN HIGH-PRECISION SINGLE-ELECTRON CAPTURE, *Physical Review Letters* 109 (2012) 216801 (5 pages).
2. L. Fricke, M. Wulf, B. Kaestner, V. Kashcheyevs, J. Timoshenko, P. Nazarov, F. Hohls, P. Mirovsky, B. Mackrodt, R. Dolata, T. Weimann, K. Pierz, H.W. Schumacher, COUNTING STATISTICS FOR ELECTRON CAPTURE IN A DYNAMIC QUANTUM DOT, *Physical Review Letters* 110 (2013) 126803 (5 pages). **PRL Editor Suggested Article.**

## Appendix C. PARTICIPATION IN CONFERENCES

### C.1 Poster presentations at international conferences

1. *Functional materials and nanotechnologies-2008* (01.04.2008 - 04.04.2008, Riga, Latvia, poster presentation WAVELET DATA ANALYSIS OF EXAFS SPECTRA (J. Timoshenko, A.Kuzmin)), abstract published in *Abstract of International Conference on Functional materials and nanotechnologies (FM&NT-2008)*.
2. *Functional materials and nanotechnologies-2009* (31.03.2009 - 03.04.2009, Riga, Latvia, poster presentation ISOTOPIC EFFECT IN SECOND AND THIRD COORDINATION SHELLS OF GERMANIUM (J. Timoshenko, A. Kuzmin, J. Purans)), abstract published in *Abstract of International Conference on Functional materials and nanotechnologies (FM&NT-2009)*.
3. *Functional materials and nanotechnologies-2010* (16.03.2010 - 19.04.2010, Riga, Latvia, poster presentation MOLECULAR DYNAMICS SIMULATIONS OF EXAFS IN GERMANIUM (J. Timoshenko, A. Kuzmin, J. Purans)), abstract published in *Abstract of International Conference on Functional materials and nanotechnologies (FM&NT-2010)*, p. 193.
4. *Functional materials and nanotechnologies-2010* (16.03.2010 - 19.04.2010, Riga, Latvia, poster presentation PROBING NiO NANOCRYSTALS STRUCTURE BY EXAFS SPECTROSCOPY (A. Anspoks, A. Kuzmin, A. Kalinko, J. Timoshenko)), abstract published in *Abstract of International Conference on Functional materials and nanotechnologies (FM&NT-2010)*, p. 191.
5. *Functional materials and nanotechnologies-2010* (16.03.2010 - 19.04.2010, Riga, Latvia, poster presentation EXAFS STUDY OF ZnWO<sub>4</sub> ON THE W L<sub>3</sub> AND Zn K EDGES (A. Kalinko, A. Kuzmin, J. Timoshenko)), abstract published in *Abstract of International Conference on Functional materials and nanotechnologies (FM&NT-2010)*, p. 192.
6. *Functional materials and nanotechnologies-2011* (05.04.2011 - 08.04.2011, Riga, Latvia, poster presentation REVERSE MONTE-CARLO MODELLING OF STRUCTURAL AND THERMAL DISORDER IN CRYSTALLINE MATERIALS (J. Timoshenko, A. Kuzmin, J. Purans)), abstract published in *Abstract of*

*International Conference on Functional materials and nanotechnologies (FM&NT-2011)*, p. 177.

7. *Functional materials and nanotechnologies-2012* (17.04.2012 - 20.04.2012, Riga, Latvia, poster presentation X-RAY ABSORPTION SPECTROSCOPY OF Cu-DOPED  $\text{WO}_3$  FOR USE IN ELECTROCHEMICAL METALLIZATION CELL MEMORY (A. Kuzmin, A. Anspoks, A. Kalinko, J. Timoshenko, R. Kalendarev)), abstract published in *Abstract of International Conference on Functional materials and nanotechnologies (FM&NT-2012)*, p. 231.
8. *Functional materials and nanotechnologies-2012* (17.04.2012 - 20.04.2012, Riga, Latvia, poster presentation X-RAY ABSORPTION SPECTROSCOPY STUDY OF LOCAL ATOMIC STRUCTURE AND LATTICE DYNAMICS IN COPPER NITRIDE  $\text{Cu}_3\text{N}$  (A. Kalinko, A. Kuzmin, A. Anspoks, J. Timoshenko, R. Kalendarev)), abstract published in *Abstract of International Conference on Functional materials and nanotechnologies (FM&NT-2012)*, p. 233.
9. *Functional materials and nanotechnologies-2012* (17.04.2012 - 20.04.2012, Riga, Latvia, poster presentation X-RAY ABSORPTION SPECTROSCOPY OF LOCAL STRUCTURE AND LATTICE DYNAMICS IN MULTIFERROIC  $\text{MnWO}_4$  AND  $\text{Mn}_{1-c}\text{Co}_c\text{WO}_4$  (A. Kalinko, A. Kuzmin, A. Anspoks, J. Timoshenko, R. Kalendarev)), abstract published in *Abstract of International Conference on Functional materials and nanotechnologies (FM&NT-2012)*, p. 234.
10. *Functional materials and nanotechnologies-2012* (17.04.2012 - 20.04.2012, Riga, Latvia, poster presentation X-RAY ABSORPTION SPECTROSCOPY OF THE LOCAL ATOMIC STRUCTURE IN PbS QUANTUM DOTS (A. Anspoks, A. Kalinko, P. Kulis, A. Kuzmin, B. Polakov, J. Timoshenko)), abstract published in *Abstract of International Conference on Functional materials and nanotechnologies (FM&NT-2012)*, p. 235.
11. *E-MRS 2014 Spring Meeting* (26.05.2014 - 30.05.2014, Lille, France, poster presentation RECONSTRUCTION OF NANOSIZED TUNGSTATE STRUCTURE FROM EXAFS SPECTRA BY EVOLUTIONARY ALGORITHM (J. Timoshenko, A. Anspoks, A. Kalinko, A. Kuzmin)), abstract published in Book of Abstracts, Symposium F.
12. *Functional materials and nanotechnologies-2014* (29.09.2014 - 02.10.2014, Riga, Latvia, poster presentation LOCAL STRUCTURE OF MULTIFERROIC  $\text{Mn}_{1-c}\text{Co}_c\text{WO}_4$  SOLID SOLUTIONS REVEALED BY THE EVOLUTIONARY ALGORITHM (J. Timoshenko, A. Anspoks, A. Kalinko, A. Kuzmin)), abstract will be published in *Abstract of International Conference on Functional materials and nanotechnologies (FM&NT-2014)*.



13. *Functional materials and nanotechnologies-2014* (29.09.2014 - 02.10.2014, Riga, Latvia, poster presentation EXAFS STUDY OF THE LOCAL STRUCTURE OF CRYSTALLINE AND NANOCRYSTALLINE  $Y_2O_3$  USING EVOLUTIONARY ALGORITHM METHOD (I. Jonane, J. Timoshenko, A. Kuzmin)), abstract will be published in *Abstract of International Conference on Functional materials and nanotechnologies (FM&NT-2014)*.

## C.2 Oral presentations at international conferences

1. *Functional materials and nanotechnologies-2012* (17.04.2012 - 20.04.2012., Riga, Latvia, oral presentation LATTICE DYNAMICS AND STRUCTURAL DISORDER IN RHENIUM TRIOXIDE: REVERSE MONTE CARLO STUDY (J. Timoshenko, A. Kuzmin, J. Purans)), abstract published in *Abstract of International Conference on Functional materials and nanotechnologies (FM&NT-2012)*, p. 96.
2. *15th International Conference on X-ray Absorption Fine Structure*, (22.07.2012 - 28.07.2012, Beijing, China, oral presentation AN EFFICIENT IMPLEMENTATION OF THE REVERSE MONTE CARLO (RMC) METHOD FOR EXAFS ANALYSIS IN CRYSTALLINE MATERIALS (J. Timoshenko, A. Kuzmin, J. Purans)), abstract published in *Abstract of 15th International Conference on X-ray Absorption Fine Structure (XAFS15)*, p. 147.
3. *Functional materials and nanotechnologies-2013* (21.04.2013 - 24.04.2012., Tartu, Estonia, oral presentation ANALYSIS OF EXAFS DATA FROM COPPER TUNGSTATE BY REVERSE MONTE CARLO METHOD (J. Timoshenko, A. Anspoks, A. Kalinko, A. Kuzmin)), abstract published in *Abstract of International Conference on Functional materials and nanotechnologies (FM&NT-2013)*, p. 53.
4. *E-MRS-2013* (16.09.2013 - 20.09.2013., Warsaw, Poland, oral presentation LOCAL STRUCTURE AND DYNAMICS OF WURTZITE-TYPE  $ZnO$  FROM SIMULATION-BASED EXAFS ANALYSIS (J. Timoshenko, A. Anspoks, A. Kalinko, A. Kuzmin)), abstract published in Book of Abstracts, Symposium K.

## Appendix D. PARTICIPATION IN INTERNATIONAL SCHOOLS

1. *XAFS for beginners* (01.09.2008 - 10.09.2008, MAX-lab, Lund, Sweden).
2. *Summer School on Atomistic Simulation Techniques* (04.07.2010 - 25.07.2010, Trieste, Italy).
3. *Ultrafast X-Ray Science with X-Ray Free-Electron Lasers* (29.03.2011 - 02.04.2011, DESY synchrotron radiation center, Hamburg, Germany).
4. *32nd Berlin School on neutron scattering* (07.03.2012 - 16.03.2012, Helmholtz Zentrum Berlin, Germany).
5. *First Baltic School on Application of Neutron and Synchrotron Radiation* (01.10.2012 - 04.10.2012, Riga, Latvia); poster presentation ANALYSIS OF EXAFS DATA FROM COBALT TUNGSTATE  $\text{CoWO}_4$ : REVERSE MONTE CARLO APPROACH (J.Timoshenko, A.Anspoks, A.Kalinko and A.Kuzmin).
6. *Higher European Research Course for Users of Large Experimental systems (HERCULES)-2013* (24.02.2013 - 28.03.2013, Grenoble and Paris, France); poster presentation ANALYSIS OF EXAFS DATA FROM CRYSTALLINE MATERIALS: REVERSE MONTE CARLO APPROACH (J.Timoshenko, A.Anspoks, A.Kalinko and A.Kuzmin).
7. *HERCULES Specialised Course on Dynamical properties investigated by neutrons and synchrotron X-rays* (15.09.2014 - 19.09.2014, Grenoble, France); poster presentation INVESTIGATIONS OF THE LATTICE DYNAMICS OF CRYSTALLINE MATERIALS USING SIMULATION-BASED EXAFS ANALYSIS (J.Timoshenko and A.Kuzmin).

## Appendix E. PARTICIPATION IN EXPERIMENTS AT SYNCHROTRON RADIATION FACILITIES

1. 23.11.2009 - 30.11.2009 EXAFS measurements at DESY synchrotron radiation center, Hamburg, Germany, *Local structure and lattice dynamics in nanocrystalline Zn(Ni)WO<sub>4</sub> and Zn<sub>c</sub>Ni<sub>1-c</sub>WO<sub>4</sub> solid solutions.*
2. 08.07.2011 - 11.07.2011 EXAFS measurements at DESY synchrotron radiation center, Hamburg, Germany, *Local structure and lattice dynamics in multiferroic MnWO<sub>4</sub> and Mn<sub>1-c</sub>Co<sub>c</sub>WO<sub>4</sub>.*
3. 30.11.2011 - 06.12.2011 EXAFS measurements at DESY synchrotron radiation center, Hamburg, Germany, *Study of local atomic and electronic structure in Cu-doped WO<sub>3</sub> programmable metallization cell (PMC) device.*
4. 18.06.2012 - 20.06.2012 EXAFS measurements at DESY synchrotron radiation center, Hamburg, Germany, *EXAFS study of negative thermal expansion in cubic scandium trifluoride ScF<sub>3</sub>.*
5. 06.07.2012 - 09.07.2012 EXAFS measurements at DESY synchrotron radiation center, Hamburg, Germany, *EXAFS study of local structure and lattice dynamics in copper nitride Cu<sub>3</sub>N.*
6. 25.08.2013 - 02.09.2013 EXAFS measurements at ELETTRA synchrotron radiation center, Trieste, Italy, *EXAFS study of local structure and lattice dynamics in ODS steels.*
7. 26.11.2013 - 02.12.2013 IR measurements at SOLEIL synchrotron radiation center, Paris, France, *Investigation of magnetic and structural phase transitions in Zn<sub>x</sub>Ni<sub>1-x</sub>WO<sub>4</sub> and Co<sub>x</sub>Cu<sub>1-x</sub>WO<sub>4</sub> solid solutions.*
8. 03.02.2014 - 10.03.2014 IR measurements at SOLEIL synchrotron radiation center, Paris, France, *Infra-red spectroscopy of lattice dynamics in alpha- and beta-SnWO<sub>4</sub>.*
9. 18.03.2014 - 24.03.2014 EXAFS measurements at SOLEIL synchrotron radiation center, Paris, France, *XAS study of pressure-induced phase transition in SnWO<sub>4</sub>.*

10. 01.09.2014 - 07.09.2014 EXAFS measurements at ELETTRA synchrotron radiation center, Trieste, Italy, *Local structure studies of oxide nanoparticles in austenitic ODS steels.*
11. 11.11.2014 - 17.11.2014 EXAFS measurements at SOLEIL synchrotron radiation center, Paris, France, *XAS study of pressure-induced metallization in antiperovskite-type copper nitride.*